Evaluation of an Active Acoustic Waveguide Sensor for Embedded Structural Monitoring

David Atkinson

Submitted in January 2000
for the Degree of Doctor of Philosophy

Centre for Ultrasonic Engineering
Department of Electronic and Electrical Engineering
The University of Strathclyde
204 George Street, Glasgow, G1 1XW
Scotland, United Kingdom

Table of Contents

Acknowledgements

I would like to thank my supervisor Professor Gordon Hayward for his continual guidance, encouragement, and enthusiasm, and in particular for sending me to so many conferences thereby allowing me to achieve the status of 'the golden boy' from other jealous members of the group! I would like to thank all members of CUE for their general assistance during this time and for providing an enjoyable working environment. Additional thanks to Anthony Gachagan, Jamie Hyslop, and Tommy McCunnie for much appreciated technical support, and the EPSRC for the provision of research funds.

With respect to making my time at CUE a very memorable experience I would like to thank (in no particular order): Simon Whiteley for being a great mate, and keeping the rent low. Richard O'Leary for many good times away from university and for his sharp sense of humour. Robbie Banks for his patter and keenness to collect bacon rolls from Jamiesons. Jamie Hyslop for providing many a fish for my dinner when times were tight, and helping me with Flex by showing me the way to the nearest manual! Stephen Kelly for being one of the greatest joke tellers I've ever encountered. Tommie McCunnie for the inside football information, tea room chats, and continually ridiculing me in public. Anthony Gachagan his for perfect sock co-ordination and other photogenic qualities. Trisha Leggat for keeping the email jokes coming. Graham 'old spice' Benny for adding a wealth of experience that only a man in his twilight years could provide. Randy Reynolds for providing general entertainment. Ian Hall for his enthusiasm! Roger Farlow for defying the laws of visible matter. Saint Walter Galbraith for his optimism, short stories, and general words of wisdom. Kathy O'Gorman for always being so cheerful. Nicola, Agnes and Grant for making me the subject of my last Christmas surprise.

I would like to express my deepest thanks to my Mum and Dad for being fantastic parents and everything they have done for me during my time as a student, my brothers Gareth and Owen, and sister Rhian. I would also like to thank Beverley Wood for her love, encouragement, and friendship. Finally, cheers to all my mates for still hanging about with a student, and making Glasgow a cool place to be.

Abstract

This Thesis describes research aimed towards the realisation of an embedded ultrasonic monitoring system for operation in a *smart structure* environment. Alien fibres embedded within carbon fibre reinforced composite plates could be utilised to guide ultrasound to strategic release points for the interrogation of the test sample, with minimal structural degradation. In particular, an array of fibre waveguides could be utilised to deliver periodic stresses to a plate-type structure to excite Lamb wave propagation. With such a system several problems need to be addressed. Firstly, identification of an appropriate mode of propagation to transport the acoustic energy along the waveguide and meet the requirements of the system is required. Theoretical analysis of elastic wave propagation in cylinders is provided to establish the characteristics of the various supported modes. Subsequently, the longitudinal (axisymmetric) modes are highlighted as being the most appropriate for the proposed system. Ideally, such a mode should be singly generated to provide increased control on the coupling of ultrasound from the waveguide to the desired Lamb wave mode. Therefore, the transducer-fibre interface utilised for efficient single mode generation in the fibre waveguides is essential. This Thesis investigates a novel, cheap, simple, and robust coupling strategy, which employs a conical polymer bond to behave as a mechanical transformer efficiently coupling the lateral displacements of a piezoceramic transducer into longitudinal displacements in the waveguide. Theoretical and experimental analysis of this technique are described and design guidelines detailed.

The Thesis then goes on to provide experimental and theoretical evidence of the fibre waveguide's ability to transport acoustic energy to and from plate-type structures for subsequent Lamb wave generation and detection. Initially, a surface mount strategy is adopted, whereby the ends of several thin cylindrical waveguides are bonded to the surface of aluminium plates to behave as a line array. Generation and detection of the fundamental symmetric (S_0) and asymmetric (A_0) Lamb wave modes is demonstrated. Following this, the Thesis details considerations concerning the realisation of an embedded fibre waveguide monitoring system. Here, the choice of waveguide material and geometry is crucial to ensure the guided ultrasound does not leak into the structure at undesirable locations and that the structural integrity of the test sample is maintainable. Consequently, various waveguide configurations are investigated to establish an arrangement capable of meeting the system requirements. An embedded fibre waveguide Lamb wave system is then presented in a hard-setting polymer plate confirming the basic design methodology. Finally, S_0 Lamb wave generation and detection in a carbon fibre reinforced composite plate is demonstrated utilising embedded acoustic waveguides sensors.

List of Symbols

The following symbols are utilised throughout this Thesis, unless otherwise stated in the text.

Symbol	*Definition*	*Unit*
u	Displacement	m
ε	Strain	-
σ	Stress	Nm^{-2}
ν	Poisson Ratio	-
ρ	Density	Kgm^{-3}
E	Young's Modulus	Nm^{-2}
μ	Lamℳ Constant (Shear Modulus)	Nm^{-2}
λ	Lamℳ Constant	Nm^{-2}
F	Force	N
C	Phase Velocity	ms^{-1}
C_g	Group Velocity	ms^{-1}
C_0	Bar Velocity	ms^{-1}
C_s	Shear Velocity	ms^{-1}
C_l	Longitudinal Velocity	ms^{-1}
f	Frequency	Hz
ω	Angular Frequency	Radians
a	Radius	m
Ω	Dimensionless Frequency ($\omega a/C_s$)	-
Λ	Wavelength	m
γ	Propagation Constant	m^{-1}

Chapter 1

Introduction

1.1. Background

With increasing requirements for relatively remote and less invasive ultrasonic systems, this Thesis endeavours to highlight the potential of ultrasonic delivery via embedded fibre waveguides for subsequent non-invasive structural condition monitoring. The concept of transporting mechanical energy along a cylindrical (or other) waveguide is well established [1]. With regard to ultrasonic systems, such waveguides normally comprise of an inner core, along which the wave energy is confined, and an outer cladding that is designed to minimise acoustic leakage and offer a degree of mechanical protection. Important application issues include the wave mode dispersion characteristics, the waveguide geometry and materials, and the electro-mechanical interface required to generate the particular mode of interest.

Incorporating continual monitoring capabilities, and therefore a degree of intelligence into structures is of considerable current interest to the aerospace, hydrocarbon, and automobile industries. Moreover, ultrasound is a prime candidate to perform this monitoring function, since it has a well-established track record in NDT [2]. In addition, the associated sensor technology has reached a relatively high degree of refinement due to advances in material science and improved modelling techniques [3]. However, it is essential that any instrumentation does not detract from the integrity of the structure and is cost effective in terms of implementation and subsequent operation. Consequently, optical fibre sensors offer distinct advantages for integration into certain structures, due to their immunity to electrical interference, resistance to corrosion, and

relatively small unobtrusive dimensions [4]. The implementation of this sensor technology into so-called *smart structures* has reached a significant level of maturity. However a limitation of optical fibre sensors is that they are essentially passive devices and consequently do not possess the resolution and discrimination afforded by alternative, ultrasonic techniques. That is, an optical fibre will take a measurement local to its sensor gauge region, whereas an ultrasonic equivalent could actively introduce mechanical energy to a structure to interrogate areas that are not in contact with the sensor itself. This introduces significant advantages for the monitoring of large structural areas.

Consequently, it will be demonstrated that fibres can be utilised to guide ultrasound to load structures for their subsequent interrogation. The inspection of plate-type geometries is of specific interest since they form many practical structural components. An appropriate monitoring technique for this geometry, with recognised potential for smart structure applications is the generation and detection of Lamb waves [5], which are guided acoustic plate waves capable of propagating over large distances. Consequently, the major thrust of this Thesis is to propose and evaluate a novel sensor system utilising embedded fibre waveguides to transport acoustic energy to and from plate-type structures for subsequent Lamb wave excitation and detection. Nevertheless, the technology discussed in the course of the Thesis is not limited to this particular waveguide application.

1.2. Aims and Contributions of Thesis

1.2.1. Aims of Thesis

- Investigate contemporary sensor technology currently receiving interest for smart structure applications. Consequently, establish the context of an unobtrusive acoustic fibre waveguide system for condition health monitoring within this field of research.

- Investigate elastic wave propagation in isotropic cylinders, obtaining information on the character of the various modes that can be supported, and the associated dispersion relations, thereby determining a suitable waveguide mode for ultrasonic delivery.

- Investigate an appropriate coupling technique to generate and detect the desired fibre waveguide mode in terms of efficiency and mode selectivity.

- Establish the capability of fibre waveguides to deliver acoustic energy to plate-type structures for subsequent Lamb wave generation and detection.

- Explore the feasibility of an embedded fibre waveguide Lamb wave monitoring system, in terms of the waveguide and system requirements.

- Demonstrate Lamb wave generation and detection in a carbon fibre reinforced composite plate utilising embedded fibre waveguides to transport the mechanical energy to and from the structure.

1.2.2. Contributions of Thesis

- A comprehensive literature review on smart structure sensor research is provided. This review is particularly concerned with experimental research on sensor technologies suitable for integration into structural components for so-called smart structures. In addition, a review of waveguide applications is provided to demonstrate the novel nature of the proposed system.

- A detailed theoretical discussion of elastic wave propagation in isotropic cylinders is presented, outlining the pertinent relations for dispersion analysis. The characteristics of the various acoustic mode types that are supported by such a geometry are detailed, and the axisymmetric longitudinal modes are highlighted as being particular suited to the requirements of the proposed monitoring system.

- Theoretical modelling and experimental verification of a mechanism to couple ultrasonic energy from a piezoceramic transducer, into a longitudinal fibre waveguide mode, via a simple conical polymer interface is introduced. Close correlation between the resonant characteristics of the ceramic and frequency response of the coupled acoustic energy is demonstrated. Moreover, activation of

the lateral resonances of the transducer, which are associated with the width (for a plate) or radial (for a disc) dimensions are shown to provide the most efficient coupling response. As such, the polymer cone coupling mechanism is shown to behave as a mechanical transformer, efficiently converting lateral displacements at its base into longitudinal displacements at its apex. A systematic theoretical analysis is subsequently presented to evaluate the influence of the various design parameters on the coupling efficiency, and an experimental analysis is detailed to investigate uni-modal operation. In reaction to this, design guidelines are outlined for efficient, uni-modal coupling into the fundamental longitudinal fibre waveguide mode utilising this technique.

- A review of Lamb wave excitation methodology is provided to establish the significance of a non-invasive fibre waveguide delivery system. Subsequently, a novel acoustic, fibre waveguide, sensor system, capable of generating and detecting Lamb wave propagation in plates is established. An initial surface mount strategy for operation in metallic plates is adopted to confirm the viability of the concept.

- An embedded fibre waveguide system for operation in non-metallic plates is discussed and demonstrated. Here the requirements of the waveguide are considered, and homogeneous, clad, and *tube-fibre* waveguides are investigated. Consequently, tube-fibre waveguides are embedded within an epoxy plate, and Lamb wave generation and detection is demonstrated.

- Finally, the construction of a carbon fibre reinforced composite plate with embedded tube-fibre waveguides is detailed. Lamb wave generation and detection is demonstrated revealing the potential of a fibre waveguide system for the condition monitoring of practical structural components.

1.2.3. Publications and Conference Papers Arising From Thesis

Journal Publication

D. Atkinson and G. Hayward, "Fibre Waveguide Transducers For Lamb Wave NDE", *IEE Proc.-Sci. Meas. Technol.*, Vol. 145, No. 5, 1998, pp 260-268

D. Atkinson and G. Hayward, "The Generation and Detection of Longitudinal Guided Waves in Thin Fibres Using a Conical Transformer", submitted to *IEEE Transactions on Ultrasonics Ferroelectrics and Frequency Control*

D. Atkinson and G. Hayward, "An Active Fibre Waveguide Sensor for Embedded Structural Condition Monitoring", submitted to *IEEE Transactions on Ultrasonics Ferroelectrics and Frequency Control*

Conference Papers

D. Atkinson, A. Cochran, and G. Hayward, "Lamb Wave Generation and Detection via Propagation of Ultrasound Along Fibres", Presented at Ultrasonics International, 2-4 July 1997, Het Aula Congrescentrum, TU Delft, The Netherlands

D. Atkinson, and G. Hayward, "Propagation of Ultrasound along Fibres for the Non-Destructive Testing of Plates", *Proceedings of the IEEE Ultrasonics Symposium,* Toronto October 1997, pp 797-800

D. Atkinson, A. Gachagan, and G. Hayward, "Transducers for Guided Wave NDE", Presented at 1998 Office of Naval Research Transducers Materials and Transducers Workshop, 12-14 May 1998, The Penn Stater Conference Centre, State College, Pennsylvania, USA.

D. Atkinson, and G. Hayward, "Coupling of Ultrasonic Energy to and from Fibres for the Non-Destructive Testing of Plates", Presented at the 4th European and 2nd MIMR Conference, 6-8 July 1998, Harrogate, UK.

D. Atkinson, and G. Hayward, "Embedded Acoustic Fibre Waveguides For lamb Wave NDE", Presented at the British Institute of Non-Destructive Testing, NDT '99 and UK Corrosion '99, 14-16 September, 1999, The Sandbanks Hotel, Poole Dorset, UK.

D. Atkinson, and G. Hayward, "Embedded Fibres Waveguides for Lamb Wave Condition Monitoring", *Proceedings of the IEEE Ultrasonics Symposium,* Lake Tahoe, Nevada, October 1999, (in press).

1.3. Overview of Thesis

Chapter 2

An introduction to the concept of *smart structures* is provided in Chapter 2 detailing what they are and pertinent considerations concerning their implementation. Particular attention is paid to contemporary sensor technology suitable for integration into host materials for subsequent structural monitoring. Suitable optical fibre sensors merit detailed consideration since they are arguably the most mature smart structure sensor and also due to their geometrical similarity to the proposed acoustic fibre waveguide option. Furthermore, a review of current applications employing cylindrical acoustic waveguides is provided to demonstrate the novel nature of the work presented within this Thesis.

Chapter 3

This Chapter details the relevant theory associated with elastic wave propagation in homogeneous, isotropic cylinders. Initially, a simplified analysis is presented on the fundamental waveforms that propagate in the low frequency regime. Following this, the exact equations of motion for elastic wave propagation are provided and solved to demonstrate dispersion information on the various supported modes. Finally, the characteristics of each mode type and their suitability for the proposed monitoring system are considered.

Chapter 4

The development of a coupling mechanism for longitudinal ultrasonic propagation along fibre waveguides is discussed. Here electric stimulation of a piezoceramic transducer generates the initial mechanical energy, which is subsequently coupled into the fibre waveguide via a polymer cone. This technique is considered in terms of its ability to couple the various resonances of the piezoceramic into the waveguide. It is revealed through spectral analysis that the lateral harmonics of the transducer (those normal to the thickness mode) are coupled most efficiently into the waveguide. Consequently, the nature of the coupling mechanism is theoretically investigated utilising finite element analysis (FEA) and experimental verification is provided, revealing that the polymer cone behaves as a mechanical transformer. Further FEA demonstrates the significance of the polymer cone dimensions on the coupling efficiency.

The requirement for unimodal axisymmetrical propagation along fibre waveguides is then considered. An experimental programme is described, which initially investigates ultrasonic propagation along a steel rod. Here uni-modal longitudinal and flexural propagation is demonstrated using various transducer configurations. The rod experiments reveal considerations applicable to uni-modal longitudinal propagation along fibre waveguides. Following this design guidelines are provided for efficient, longitudinal uni-modal coupling into the waveguide utilising the described polymer cone technique.

Chapter 5

This Chapter discusses elastic wave propagation in plates (Lamb waves), describing relevant theory and current Lamb wave excitation methodology, revealing the significance of a fibre waveguide based Lamb wave monitoring system. The realisation of such a system is subsequently described, and experimental and modelling results are presented. The design concept utilises a line array of waveguides surface bonded to an aluminium plate to deliver a series of periodic stresses for the generation of a particular Lamb wave mode. Similarly, surface bonded fibre waveguides are utilised to detect the generated Lamb wave. These preliminary surface mount results provide a *proof of concept*, showing that fibre waveguides can be utilised to transport mechanical energy to and from structures for the remote generation and detection of ultrasonic signals with structural health monitoring capabilities. As such these results provide the first step to establishing the feasibility an embedded ultrasonic fibre waveguide sensor system.

Chapter 6

This Chapter investigates the feasibility of an embedded fibre Lamb wave system. Firstly, the requirements of the waveguide are stated for successful implementation of the proposed Lamb wave monitoring system. Various waveguide geometries are considered through theoretical, modelling, and experimental analysis. Experimental results are then presented for an embedded waveguide Lamb wave system. Initaly, the waveguides are embedded within a hard-setting polymer plate to confirm the basic design methodology. Subsequently, an embedded fibre waveguide monitoring system in a carbon fibre reinforced composite plate is described. Here successful generation and

detection of the fundamental symmetric Lamb wave mode is demonstrated. Finally, implementation considerations are discussed and conclusions drawn.

Chapter 7

To conclude this Thesis an overview of the findings and achievements is provided. Additionally, suggestions for further work are detailed to illustrate the potential the system and other avenues of investigation still to be addressed.

Chapter 2

Smart Structure Sensors & Acoustic Fibre Waveguides

2.1. Overview of Chapter

A major aim of this Thesis is to demonstrate an innovative sensor technology, utilising ultrasonic fibre waveguides embedded within composite materials to perform condition monitoring. Sensors with the ability to be successfully embedded within structures commonly fall into an area of research termed *smart structures*. Subsequently, this Chapter will introduce the concept of smart structures, describing what they are and the current sensor technologies relevant to their implementation. Particular attention will be paid to contemporary optical fibre and piezoelectric devices suitable for embedding into structures, to quantify the value of non-invasive ultrasonic fibre waveguide sensors. In addition, this Chapter will review applications that have utilised cylindrical ultrasonic waveguides, including wire delay lines, acousto-optic modulators, medical instrumentation, process monitoring and non-destructive testing.

2.2. Smart Structure Overview - What are they?

The natural world provides innumerable examples of living things with the ability to sense, react, and adapt to their immediate environment. Over the last decade or so a new interdisciplinary field of research termed *smart structures* has emerged, which strives to mimic this intrinsic biological survival quality in order to optimise operational conditions and enhance the functionality of structural designs. This area of research evolved from the development of *smart skins* in the US in the mid 1980s, which aimed to integrate radar antennas into the skins of military aircraft [6]. The idea of further developing the smart skin concept into something that included the

entire structure has been attributed to Eric Udd of Blue Road Research, formerly of McDonnell Douglas [6]. The idea of health monitoring and other functions inherent to structural design took hold within the Air Force and the smart structure field was born.

By 1992, the field had achieved much global interest and the first European conference on smart structures and materials was held in Glasgow [7]. In 1993 Rogers [8] pointed out that smart structure research to date was often described by one of two prevalent paradigms. The first he described as a *technological paradigm:* "the integration of actuators, sensors, and controls with a material or structural component". This description offers the technological method to achieve a smart structure but provides no actual goal or design guidance. The second definition was termed a *science paradigm:* "material systems with intelligence and life features integrated in the microstructure of the material system to reduce mass and energy and produce adaptive functionality". Importantly, this description focuses on the goals of the smart structure, but offers little guidance on the technology required to achieve the goals. This seems to provide a more useful basis for a definition since, once decided on, the goals should be longer lasting than the required technology, which will necessarily evolve over the years.

More recently (1996), a formal definition for smart structures was provided by Spillman *et al.* [9], in an attempt to focus the attention of the research field and stimulate an assessment on the commercial potential of smart structures. The definition offered was as follows:

"A smart structure is a non-biological physical structure having the following attributes:

(i) a definite purpose;

(ii) means and imperative to achieve that purpose;

(iii) a biological pattern of functioning."

It can be seen that this definition falls into the science paradigm category but more importantly yields a design philosophy. Considering a biological method of functioning provides a working model for the focus of smart structure technology. Take for example the case of the human being: the sensing capabilities include, sight, hearing, smell, and touch; data links are provided by nerves; actuation by muscles and hormones; and data processing via the brain. Therefore, it is evident that an interdisciplinary integration of technologies is required to emulate a biological pattern of functioning.

Furthermore, to follow the outlined design philosophy it is crucial to evaluate how biology would overcome a problem and follow this approach rather than a conventional engineering solution. For example Rogers [8] considers the case of drawing a straight line on a piece of paper placed on an unstable table. He points out that a standard engineering approach to this problem would be to mathematically model the dynamics of the table, establish the mechanism to be used to draw the line, and the various interactions between paper, pen and table, and any other issues considered relevant. A control algorithm would then be established to move the pen

across the paper while calculating the expected response of the unstable table at each pen location. This plan would provide a solution that would yield the same response time and time again, never getting better nor worse. A smart structure solution to the same problem would first consider the biological approach. For example a human drawing a straight line usually only needs to employ one muscle, however, on a rickety table would use co-contraction of the tricep and bicep muscles to gain control. This is highly energy intensive as the muscles are acting against each other to do no work. As the human draws more lines, the dynamics of the table would be increasingly understood and therefore, the body would increasingly conserve energy tending towards no co-contraction of the muscles. However, the introduction of an unknown parameter, such as a small child entering the room would once again induce co-contraction to gain control. It is this dynamic learning approach that needs to be considered at the design stage of a smart structure. Following this, decisions can be made on what technology should be utilised to best perform each of the various sensing, actuating, controlling, communicating and processing functions.

Therefore, smart structures provide the opportunity to access new sensing, signal processing, data interpretation, and material technologies in an integrated fashion at a structural design level. This introduces a major impact on conventional design philosophies, for example: the maintenance of a structure would be carried out on demand rather than scheduled to meet conservative estimations of failure [10]. The structure could also be designed to anticipate varying loading conditions to actively provide structural modifications as and when required. Such factors are evidently

cost driven, both reducing unnecessary maintenance, and increasing the structure's life cycle time.

A smart structure will therefore monitor itself, or perhaps its immediate environment, so that it may respond to changes in order to optimise its operation conditions. The response of the structure could take many forms depending on the nature of its operation. For example: a structure could respond by calling an external 'doctor' to repair damage; it may be self-repairing e.g. a healing fluid released from a corroded container, or a mechanical arm induced to weld a cracking joint; or embedded actuators being utilised to control abnormal vibrational conditions, say in a building during an earthquake or perhaps in a rocket during lift-off [10]. Ideally, the progress of smart structure methodology will create structures that are capable of learning, growing, surviving, and even retiring at the end of their life cycle through continual intrinsic monitoring [8].

The multifunctional nature of this field has naturally led to the majority of smart structure work being carried out in a modular fashion, i.e. research establishments tend to solve individual smart structure related problems or forward novel smart structure components such as suitable sensors or actuators. Obviously, the realisation of smart structures demands focused research in each area to be performed thereby arming the structural design engineer with a diverse arsenal of technologies for each set of problems. This Thesis looks at developing a novel sensor system suitable for embedding into composite materials for structural health monitoring in a smart

structure environment. Consequently, the following Section will discuss the sensor technologies currently receiving the most attention from the smart structure community.

2.3. Contemporary Smart Structure Sensor Technology

For a structure to be able to react to its environment it must be capable of obtaining information on how its environment is affecting that structure. Therefore, sensor technology is the starting point of any smart structure design. Obviously different types of structures, or even similar structures under diverse conditions, will encounter different problems requiring differing sensing systems matched to the structural requirements. For example concrete structures require sensors that can withstand a very high pH environment, and in some cases sensors that can be pretensioned to allow for compressive loading [10]. On the other hand, sensors embedded within carbon or glass fibre composite materials must be able to withstand the curing process, be unobtrusive to the host, and also allow the material to maintain its characteristic elastic properties. Metallic structures pose yet another set of problems, in that generally embedded sensors are impractical, and so a surface mount strategy needs to be adopted. Here the sensor may be required to endure a harsh environment, e.g. on an oil rig in the north sea, deeming a robust choice of sensor paramount. Therefore, it is clear that there is no generic smart structure technology, and each smart structure requires specific sensor capabilities designed for its individual needs. These requirements can be extremely wide ranging, demanding compatibility with the operating environment.

2.3.1. Optical Fibres

2.3.1.1. Overview

Optical fibre sensor development is arguably the most mature area of research within the smart structure field. Their evolution as a smart structure sensor can be largely attributed to the following characteristics [4].

- Small overall diameters (often less than 125μm), providing them with the potential to be embedded with no overall structural degradation.

- Ability to withstand environmental factors such as the high temperatures and pressures associated with composite manufacture.

- Immunity to electromagnetic interference.

- They are passive dielectric devices, which is of importance when operating in an electrically hazardous environment.

- High bandwidth.

- They can be multiplexed to form a distributed sensor along one fibre.

- The increased interest in fibre optic technology within the telecommunications industry is driving down the cost of components.

Furthermore, optical fibres are conceptually attractive since they provide a structural analogue to a biological nervous system, thereby conforming to the biological pattern of functioning specified by the formal definition. More importantly, continual

reduction in component prices, coupled with improvements in quality, has led to the development of fibre optic sensors capable of monitoring a number of parameters including: acceleration, electric and magnetic field measurement, temperature, pressure, acoustic waves, vibration, linear and angular position, strain, humidity, viscosity, and chemical measurements [11]. The reader is referred to Udd [11] for a detailed review of these various sensor configurations. With this variety in measurement capability, their employment within industry is fairly diverse, and with respect to smart structures, their sensing functions fall into four categories [4]. These are:

(1) *Manufacturing process monitoring*; here parameters such as pressure, viscosity, water content and temperature can be measured to improve structural manufacture quality.

(2) *Non destructive evaluation* of fabricated parts; where an external source, for example acoustic or electromechanical, may be utilised in conjunction with an embedded optical fibre sensor to measure say, acoustic signature changes, or delamination.

(3) *Continual health monitoring*; where the structural integrity of a system is assessed through the integration of optical fibre sensors.

(4) *Active control sensors*; environmentally induced structural changes are monitored and utilised to activate a reaction in real time. For example sensing vibration, to induce suppression actuation, or sensing structural variations in an aeroplane to induce automatic changes in the flight envelope.

There are, in general, a number of different strategies that can be employed to sense a desired parameter with optical fibres [12]. The sensor may be configured as a *point sensor,* monitoring a sample of the measurand at a specific point defined by the effective cross-sectional area of the sensing element. A larger area can be monitored using an *integrated sensor,* where the sensor takes an average measurement over its active length. Such sensors may measure integrated strain or an average temperature over a significant length of a structure. Sensing can also be carried out by *distributed sensors,* which evaluate the parameter of interest throughout the geometry of the sensor element as a function of position [10]. Multiplexed sensors can also be realised by combining a number of point, integrated, or distributed sensors into a single system. Multiplexed *integrated sensors* are often termed *quasi-distributed sensors.*

Out of the various options available for fibre optic sensing, three configurations of strain sensor are currently attracting the most attention within the smart structure field [12]. These are Fibre Fabry-Perot Interferometers (FFPI), Fibre Bragg Grating sensors (FBGS), and very long gauge length sensors. The first two sensor arrangements have received particular interest and are therefore worthy of further consideration.

2.3.1.2. Fibre Fabry-Perot Interferometer

The FFPI sensor can be configured in either an extrinsic or intrinsic fashion, as illustrated in Figure 2.1. The extrinsic sensor utilises a hollow glass sleeve to align a

single mode and multimode optical fibre. An air gap separates the reflective cleaved ends of the two optical fibres to form a cavity region. Each fibre is free to move longitudinally in the region near the cavity, but is constrained at some point along its length by bonding to the glass tube. The distance between the bonding points is known as *the gauge length,* since perturbations over this region will affect the cavity length (L) and consequently the sensor output. Longitudinal strain, or temperature variation can be measured local to the gauge length since it will introduce changes in length L, resulting in shifts in the cavity mode frequencies [13]. This sensor is more typically utilised for surface mount experiments.

The intrinsic form is known to have the advantage for smart structure applications since it is more robust and less obtrusive [13]. In this case, internal mirrors parallel to each other, and perpendicular to the fibre axis, form an integral part of the continuous length of fibre, thereby creating a cavity region of length L and refractive index n. The gauge length of this sensor is the distance L, since changes in the optical path between the mirrors leads to detectable shifts in the cavity mode frequencies. Longitudinal (parallel to fibre axis) strain (ε_L) measurements can therefore be calculated from a knowledge of this change in cavity length (ΔL) using the relationship, $\varepsilon_L = \Delta L/L$. ε_L is a unitless parameter, which is often referred to in terms of *microstrain* ($\mu\varepsilon$) due to the small strains being measured. Here, the change in gauge length, ΔL, is measured in micrometers (μm), and the original gauge length, L, is measured in metres (m).

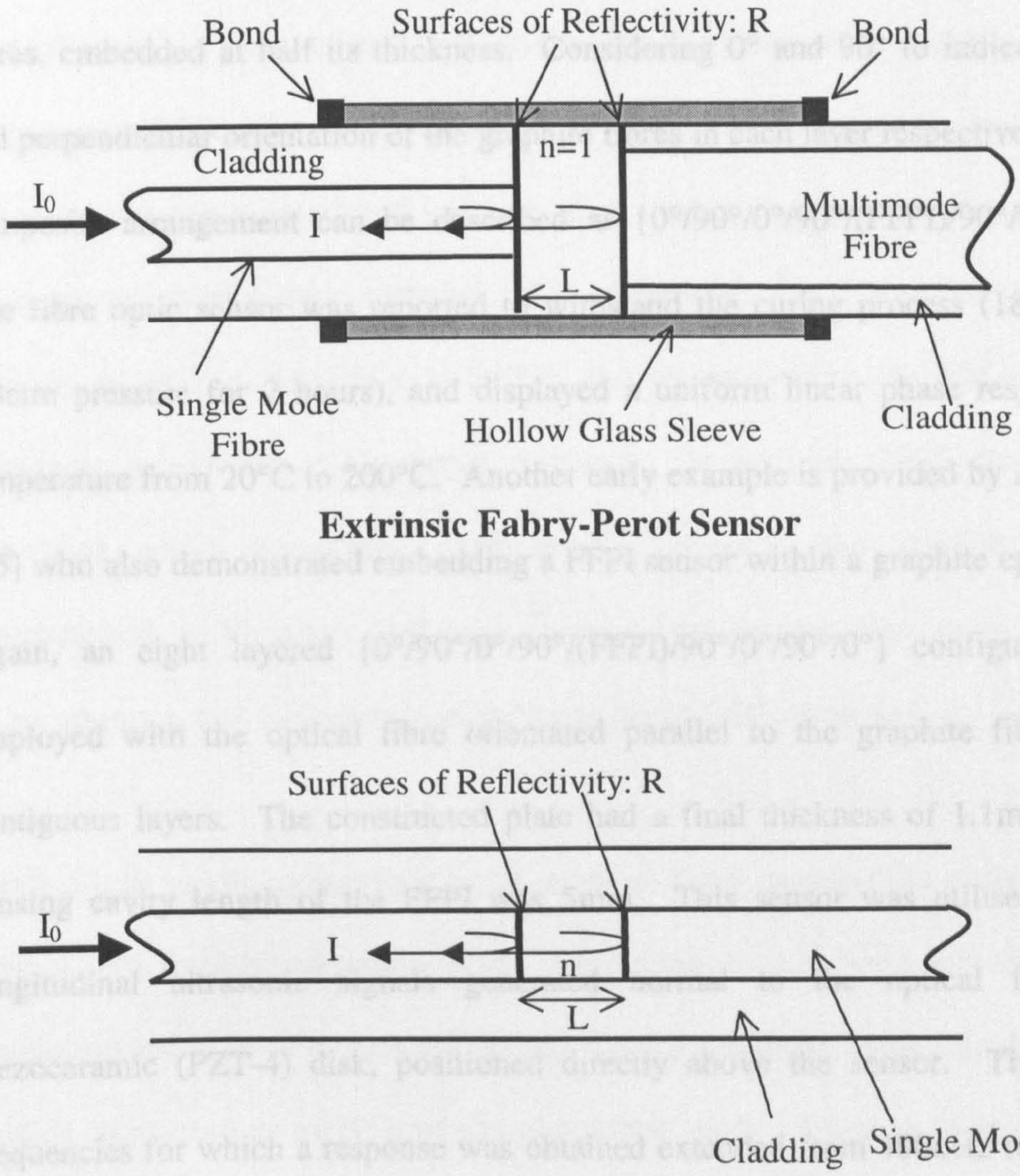

Figure 2.1: *Fabry-Perot Sensor Configurations*

The first reported example of an FFPI embedded within a composite structure was provided in 1989 by Lee *et al.* [14], who utilised the sensor to measure temperature. The constructed composite was a 15cm square, 1.1mm thick, graphite epoxy plate

comprising of eight layers with the FFPI sensor, parallel to adjacent reinforcement fibres, embedded at half its thickness. Considering 0° and 90° to indicate parallel and perpendicular orientation of the graphite fibres in each layer respectively then the composite arrangement can be described as {0°/90°/0°/90°/(FFPI)/90°/0°/90°/0°}. The fibre optic sensor was reported to withstand the curing process (180°C under 5.3atm pressure for 2 hours), and displayed a uniform linear phase response with temperature from 20°C to 200°C. Another early example is provided by Alcoz *et al.* [15] who also demonstrated embedding a FFPI sensor within a graphite epoxy panel. Again, an eight layered {0°/90°/0°/90°/(FFPI)/90°/0°/90°/0°} configuration was employed with the optical fibre orientated parallel to the graphite fibres of the contiguous layers. The constructed plate had a final thickness of 1.1mm, and the sensing cavity length of the FFPI was 5mm. This sensor was utilised to detect longitudinal ultrasonic signals generated normal to the optical fibre by a piezoceramic (PZT-4) disk, positioned directly above the sensor. The range of frequencies for which a response was obtained extended from 100kHz to 5MHz. It was noted that the ability to perform time multiplexing would permit the incorporation of several sensing cavity regions into one fibre for a pseudo-distributed acoustic sensor.

Strain measurements made by embedded FFPIs in both, graphite, and Kevlar composites have also been described by Valis *et al.* [16]. The sensors were shown to display a linear response over the range, 0 to 500με when a flexural force was applied to the structure under test. Further experiments were described for a 16-layer

graphite composite panel incorporating an embedded FFPI between the second and third layers [17]. To provide a comparison with conventional techniques an electric strain gauge (ESG) was bonded to each side of the composite, above and below the FFPI. Strains were introduced via an applied load to the centre of the sample and strain measurements were recorded. The embedded sensor was demonstrated to perform as well as the ESGs at 200°F, and to outperform the ESGs at 300°F, displaying a superior stable linear response. In addition, FFPI strain sensors embedded within composites such as Kevlar/epoxy, and graphite/epoxy are demonstrated by Measures [18] who discusses the devices high strain sensitivity, linear response, low hysteresis, and ability to match ESG responses.

Finally, it is worth mentioning that Lee *et al.* have successfully embedded FFPI sensors into metallic structures [19]. Here such devices were embedded within aluminium and utilised to measure both temperature and ultrasonic signals. Graphite moulds were used in air to cast the aluminium parts. Stainless-steel stress relief tubes were extending a short distance into the cast in order to pass the fibres though, thereby avoiding breakage at the air-metal interface. The embedded FFPI was shown to be 2.9 times more sensitive to temperature than when operated in air due to thermal expansions in the aluminium. The same sensor was utilised to detect ultrasonic signals launched into the aluminium via a surface mounted piezoceramic transducer over the frequency range of 100kHz to 8MHz, and to detect a noise burst generated by breaking a pencil on the surface of the cast aluminium.

2.3.1.3. Fibre Bragg Grating Sensor

Consider the Fibre Bragg Grating Sensor (FBGS), shown in Figure 2.2, which is also being intensively developed for smart structure applications. This sensor utilises a single mode optical fibre which has a grating written into its core by high intensity, short wavelength optical radiation, with a periodic intensity distribution [12]. The grating creates a region of periodic variation in the index of refraction, which generates a narrowband reflection. The reflected signal has a centre wavelength, termed the Bragg wavelength, which is linearly dependent on the period of the grating and the mean core index of refraction. Therefore, the Bragg wavelength is shifted when the fibre grating is subjected to variations in strain (or temperature), which results in a wavelength encoded optical measurement [13].

FBGS have a few advantages over other fibre optic sensing techniques, particularly their ability to make localised, distributed and absolute measurements with good linearity [20], as well as offering the potential of a low cost sensor that can be mass produced during the standard manufacturing process [21]. However, to ensure that an embedded FBGS demonstrates a linear relation between Bragg wavelength shifts, and longitudinal strain in the host, two assumptions have to be made [20]. Firstly, the fibre's axial strain is equal to that of the host material in the optical fibre direction; and secondly, there is no transverse strain coupled from the host to the optical fibre. Work published by Tang *et al.* [20] investigates these issues of measurement effectiveness through numerical analysis, and concludes that a thick

host, large embedded length of fibre, and optimum elastic modulus for the coating all improve the effectiveness of this sensor.

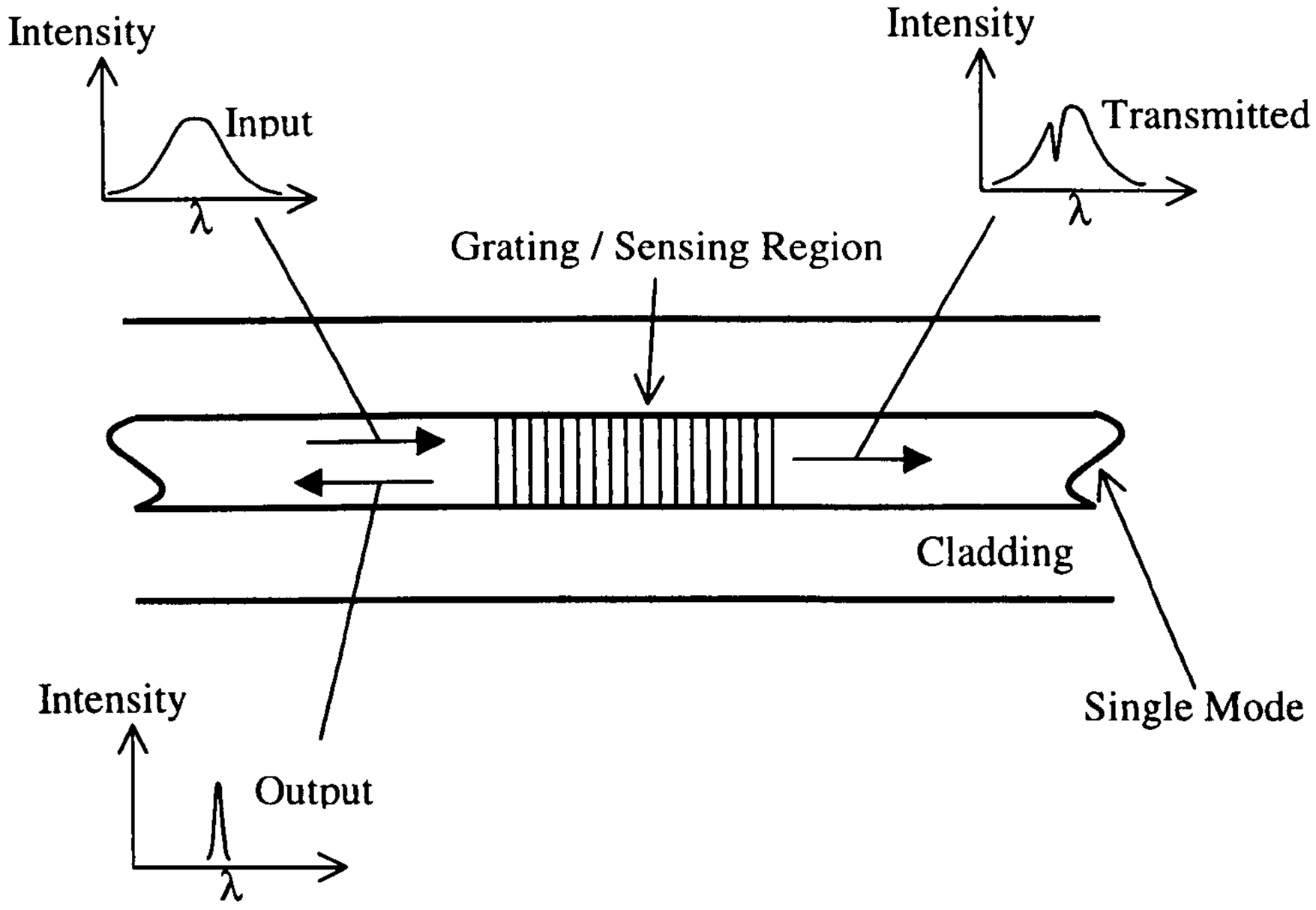

Figure 2.2: Fibre Bragg Grating Sensor

While dynamic measurements with FBGS yield very high strain detection sensitivities, accurate quasi-static strain measurements provide a significant challenge [21]. This is further complicated by the requirement to compensate for inevitable temperature variations. However, an example of a hybrid in-line fibre Etalon/Bragg grating sensor (ILFE/BG) that can simultaneously measure strain and temperature is provided by Jin *et al.* [22]. This sensor uses a ILFE sensor (essentially an intrinsic fibre Fabry-Perot) cascaded with a Bragg grating in one fibre. This enables the different sensing capabilities of each sensor to be combined into one

transducer capable of decoding temperature and strain information simultaneously. The sensor was demonstrated by embedding it into a unidirectional graphite/epoxy composite cantilever beam. The beam was of dimensions, 150mm x 25mm x 1.8mm, and the sensor was embedded 0.5mm from the surface parallel to the reinforcement fibres. A semi-conductor thermistor, and a resistance strain gauge were adhered to the surface of the beam, directly above the embedded sensor, to provide measurement verification. Once constructed the beam was subjected to a simultaneous combination of both strain and temperature fields. The embedded sensor was considered to achieve a measurement accuracy of 0.5°C for temperature and 5με for strain. It was also proposed that this sensor arrangement could be configured as a quasi-distributed sensor by introducing several gratings, with different Bragg wavelengths, along the length of one fibre. Here, identification of information from each grating would be achieved using wavelength mutilplexing techniques.

Furthermore, in work carried out by Udd *et al.* [23], four FBGS were embedded into a 22 ft fibre glass utility pole. The pole consisted of three 8ft sections that were tapered and bonded together after insertion. The successfully embedded sensors were utilised to measure tension and compression above and below one of the joints. Surface mount strain gauges were also used to enable a comparison. A variety of three-point bend loading conditions were applied to the 22 ft fibre glass utility pole. Extremely good agreement was demonstrated between the embedded sensors and surface mount strain gauges up to an 8000lbs load. The pole was designed to fail at

25,000lbs and was tested to failure, which occurred at 25,700lbs. It was therefore, concluded that the fibre gratings had been successfully embedded within the utility pole with no structural degradation. It was also highlighted that the environmentally robust nature of these sensors allows them to be successfully embedded at temperatures that would destroy conventional electrical strain gauges.

In addition to the utility pole experiments, Udd *et al.* [23] describe work carried out by Blue Road Research, and Production Products on embedding FBGSs into a cylindrical carbon epoxy, simulated missile casing. Here, three FBGSs were embedded approximately 2mm under the surface of the test structure, and again two electrical strain gauges were surface mounted for comparison. The structure was subjected to three-point bend tests and the embedded fibre optic grating sensor, in conjunction with a sophisticated demodulation system was shown to provide a performance equivalent to the conventional stain gauge demodulation system utilised.

In addition to integration into advanced composite materials, these devices have drawn considerable attention from civil engineers. For example, Maaskant *et al.* [24] describe a FBGS array that has been installed in the Beddington Trail Bridge in Calgary (Alberta, Canada) to monitor prestressing tendons. The strain sensors are attached to both steel and carbon-fibre-reinforced plastic (CFRP) prestressing tendons, which are embedded in the precast girders of the bridge. Measurement of traffic loads and the relaxation behaviour of the tendons are presented, revealing

significant differences in the behaviour of the two tendon materials. Another example is provided by Davis *et al.* [25] who describe the use of a prototype FBGS array system by successfully embedding sensors into reinforced concrete beams and deck panels to monitor the strain at several locations. The system demonstrated approximately 1με resolution and about a 10,000με range. The concrete samples were tested to failure and it is reported that all the FBGS survived, continuing to measure even after failure had occurred.

2.3.1.4. Mach-Zender and Michelson Interferometers

As previously mentioned other types of optical sensor that have received interest from the smart structure field are those in the very long gauge length category, which include interferometer fibre sensors such as the Mach-Zender, and Michelson. Both these sensors display an extremely flexible geometry, high sensitivity, and ease of fabrication and demodulation. However, in order to implement them effectively it is often necessary to optimise the coating with respect to acoustic, electric or magnetic field responses [11].

The Mach-Zender interferometer utilises both a sensing and a reference leg (see Figure 2.3) where the entire length of the embedded sensing leg acts as the sensor. This leg, which is subjected to the parameter of interest, generates detectable optical phase shifts, which are compared with the reference leg to provide a measurement. An example of a Mach-Zender fibre configuration embedded in a 3mm, carbon fibre reinforced composite plate is provided by Pierce *et al.* [26]. Here the embedded fibre

optic sensor was utilised to detect guided acoustic plate waves (Lamb waves) propagating along the structure. Detection of Lamb waves was demonstrated and shown to be up to 20 times more efficient than a similar surface bonded device.

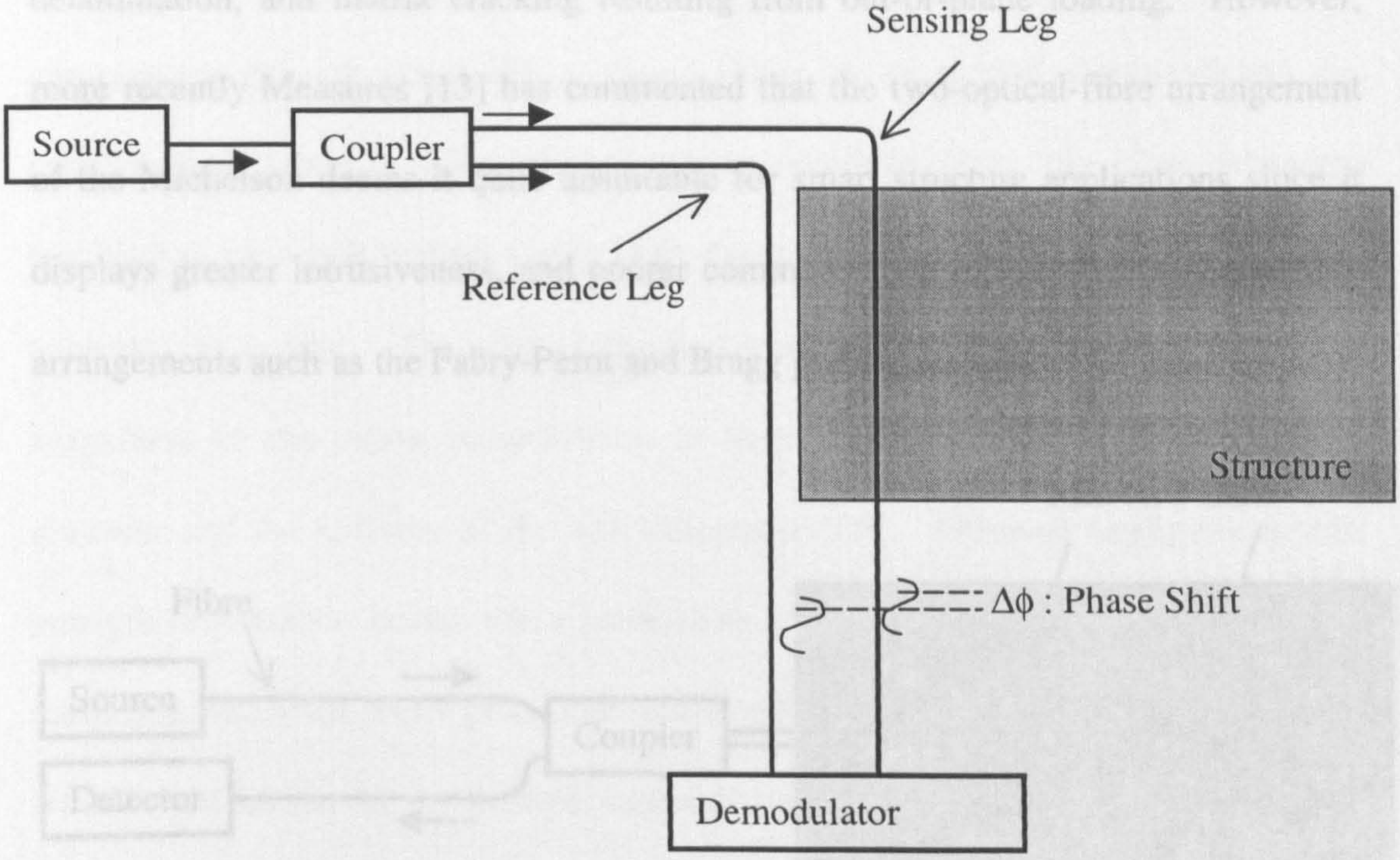

Figure 2.3: *Mach-Zender Interferometer*

The Michelson sensor configuration also employs two fibre legs, where one beam coupler is utilised to both split, and combine the propagating signals, as depicted in Figure 2.4. Both fibres, which are of differing lengths, are terminated with highly reflective ends to generate return signals. The gauge region of the sensor is determined by the difference in length of the two fibre legs, which when subjected to the parameter of interest introduces a detectable optical phase shift. Such Michelson sensors have also been embedded within composite materials for acoustic related measurements. For example, Measures [18] describes such a sensor utilised to detect

acoustic emission (AE) in both Kevlar/epoxy, and graphite/epoxy multilaminated panels, which is of interest since this phenomena can result from matrix cracking, fibre breakage, or delamination. Moreover, Measures illustrates examples of delamination, and matrix cracking resulting from out-of-plane loading. However, more recently Measures [13] has commented that the two-optical-fibre arrangement of the Michelson deems it quite unsuitable for smart structure applications since it displays greater intrusiveness, and poorer common mode rejection than single fibre arrangements such as the Fabry-Perot and Bragg grating sensors.

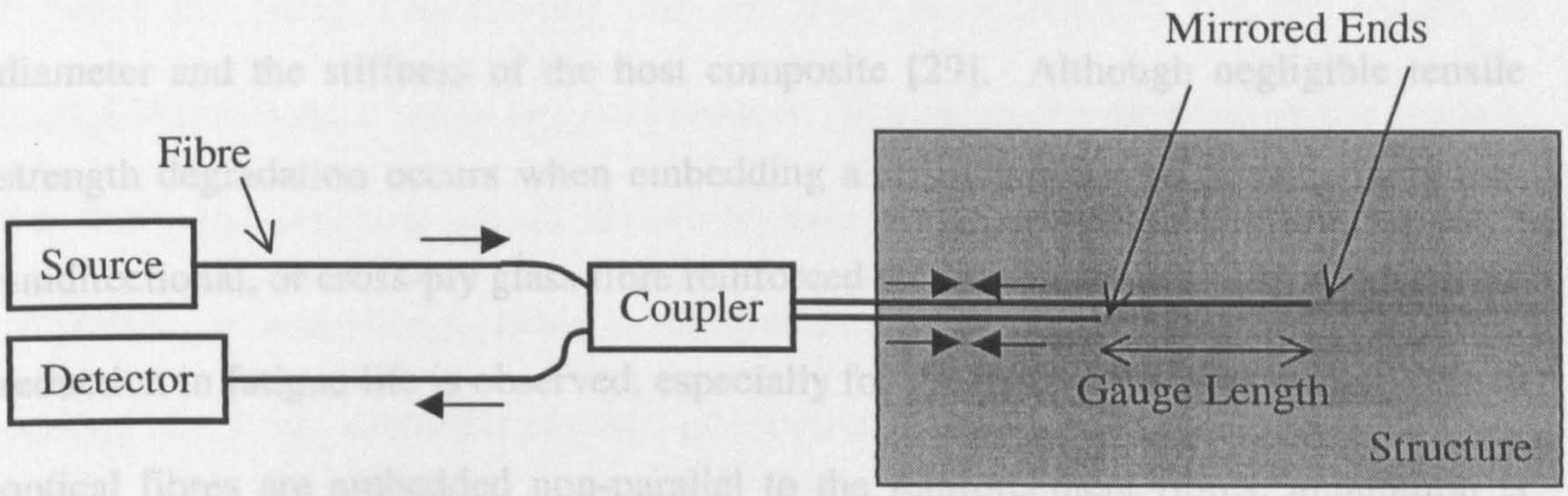

Figure 2.4: *Michelson Interferometer*

2.3.1.5. General Considerations when Embedding Optical Fibres

To avoid inducing degradation in structural strength, several important factors must be considered when embedding any form of fibre optic sensor into a composite. These include the coating of the fibre (which is crucial to successful sensing), and placement of the fibre [4]. Carmen and Sendeckyj [27] have comprehensively reviewed the pertinent literature concerning the obtrusiveness of embedded optical fibres, and more recently this area has been discussed by Jeon *et al.* [28]. There are

two fundamental static mechanical properties that can be affected by embedded optical fibres, namely longitudinal compressive strength, and transverse tensile strength. The introduction of optical fibres into host composites, in general has little influence on the tensile strength of the structure, however it does often degrade the compressive strength [28]. When optical fibres are embedded non-parallel to the reinforcement fibres a local disturbance is introduced into the fibre geometry resulting in resin rich regions where large strain concentrations can take place when subjected to a load. The size of the perturbed strain region and, therefore, the magnitude of the stress concentration is largely dependent on the optical fibre diameter and the stiffness of the host composite [29]. Although negligible tensile strength degradation occurs when embedding a small number of optical fibres into unidirectional, or cross-ply glass fibre reinforced epoxy composites [28], a significant reduction in fatigue life is observed, especially for the cross-ply configuration. When optical fibres are embedded non-parallel to the reinforcement fibres, undulation is created in the matrix, which reduces the buckling strength of the host under compression. The extent of this effect is widely varied, depending on the host material, matrix configuration, and optical fibre diameter. For example, near to no buckling strength degradation has been reported for unidirectional Kevlar/epoxy plates [30], while degradation up to and in excess of 60% has been demonstrated for cross-ply graphite/bismaleimide composites [27, 31]. Here, the degree of degradation was shown to be linearly proportional to the number of embedded optical fibres. In addition, the low-velocity impact and delamination buckling behaviour of composite laminates with embedded optical fibres has been studied [28]. It has been

reported that the presence of embedded optical fibres in cross-ply glass fibre/epoxy matrices has negligible effect on the shape of the impact damage, irrespective of the orientation or number of optical fibres. However, the extent of the damage is influenced significantly by fibre orientation, with fibres embedded at 45°, producing far more damage than those embedded in-line with adjacent reinforcement fibre layers.

Furthermore, Haslach and Whipple [32] discuss coating (which acts as the interface between the fibre core/cladding and the host) considerations for the design of embedded fibre optic strain and load sensors. The material properties of the coating, the fibre, and the host are all shown to have an influence on the fibre's optical response. It was shown, using a mathematical model, that the proper choice of coating eliminates detection of transverse strains, thereby permitting a single fibre to be used to confidently measure axial strain. In addition, it was shown that for one fibre not to induce a significant stain in a neighbouring fibre they should be separated by at least four coating diameters. Furthermore, modelling has shown that a careful selection of coating for an embedded fibre can minimise its obtrusive characteristics [33, 34]. It was demonstrated that for a given host and fibre material, optimal thickness and material properties exist for the coating to reduce the stress concentration in the host material surrounding the fibre.

2.3.2. Piezoelectric Sensors

Piezoelectric materials have found a variety of sensor applications within smart structure systems due to their ability to produce measurable electrical charges in response to mechanical stresses. These materials can generally be categorised into one of two groups, namely piezoceramics, such as Lead Zirconate Titanate (PZT), and piezopolymers such as polyvinyldenefluoride (PVDF). Piezoceramics typically display high stiffness characteristics, and are capable of generating large displacements with quick response times, making them more suited to actuator applications [8]. The brittleness of these materials does place restrictions on their minimum thickness, which can be of significance for embedded systems. On the other hand, materials such as PVDF are flexible, can be configured as thin films to conform to a variety of shapes, have low stiffness, display high damping and are wideband making them a better sensor candidate [35]. The majority of research performed on piezoelectric smart structure applications has involved theoretical or modelling analysis, and a good review of such work is provide by Chee *et al.* [35], however, experimental investigation has been more limited.

While piezoceramics are more suited to actuation than sensing, in some cases they have been shown to perform both functions. For example, Kumar *et al.* investigate a piezoceramic system for broadband vibration control [36], where a collocated piezoceramic sensor and actuator is utilised to sense and react to pressure fluctuations and actively dampen vibration. A critical parameter of such a system is the feedback circuitry, which ensures a 180° phase shift between the sensing voltage

and the voltage applied to the actuator over the frequency range of interest. The described system utilised Modified Lead Titanate (MPT) as the sensor material and was demonstrated reducing pressure fluctuation induced on a steel block (by a shaker) over a frequency bandwidth of 3.5kHz.

Yang and Bian report an experimental analysis of the effectiveness of vibration suppression by embedded piezoelectric sensor/actuators in composite laminated plates [37]. In this study two fibre-glass-reinforced composite samples of dimensions 300mm x 140mm x 1.2mm were constructed, with ply configurations of $\{0/90\}_{6s}$, and $\{45/-45\}_{6s}$, where the subscript '6s' indicates that the plate is symmetrical about its central axis with six layers on either side, as depicted in Figure 2.5(a). Each plate had 6 PZT5H elements of size 25mm x 25mm x 0.3mm embedded within them, 3 on each side of the central axis. Square cut-outs were fabricated into the plates to accommodate the transducers in the 3rd to 5th, and 8th to 10th plies. Figure 2.5(a) and (b) reveals the layout as an elevation cross-section and plan cross section respectively. The PZT5H material was utilised for both sensing and actuation due to its low temperature sensitivity, high strain sensitivity, and quick response. The embedded piezoelectric elements were shown to display approximately linear actuation from 0 to 110με for a direct voltage (DC) range of 0-500 Volts. Additionally, Finite Element Analysis indicated that the influence of the embedded transducers on the natural bending and torsional frequencies of the plates is negligible. Moreover, experimental results demonstrated that the embedded devices increase the structural damping by a factor of 7 for the $[0/90]_{6s}$ plate and a factor of 9

for the $[45/-45]_{6s}$ when configured with one of the six piezoelectric elements as a sensor and the other five as actuators. Furthermore, torsional vibration suppression was shown to be most effective when two elements were utilised as sensors, and two as actuators with a 180° phase difference. Here damping was increased by a factor of 90 in the $[0/90]_{6s}$ plate, and a factor of 70 in the $[45/-45]_{6s}$.

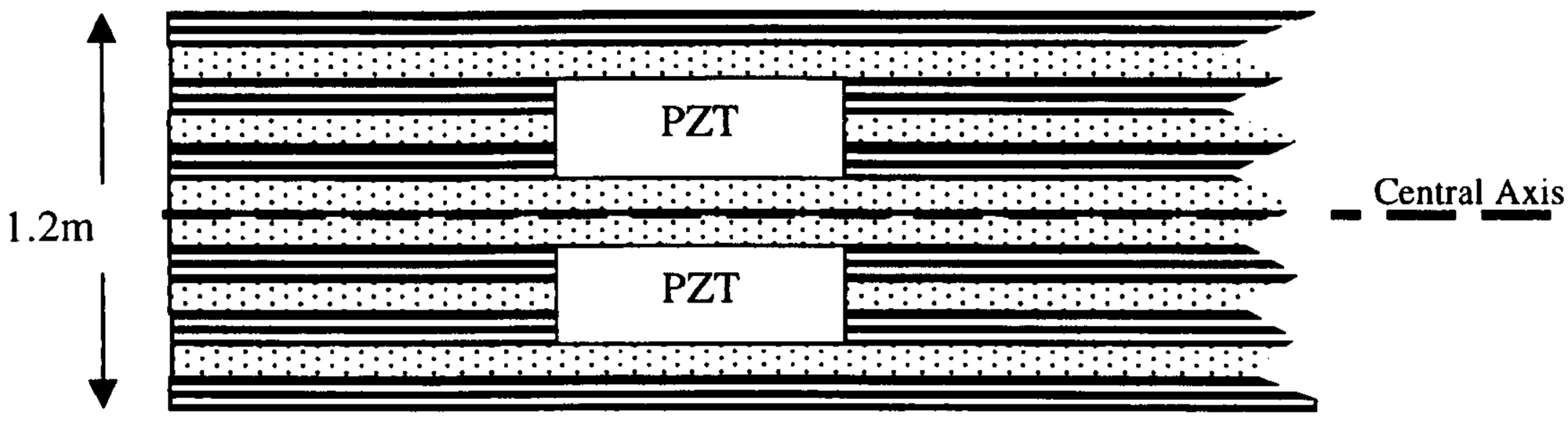

Figure 2.5(a): *Elevation: Composite Plate Layout with Embedded PZT Elements*

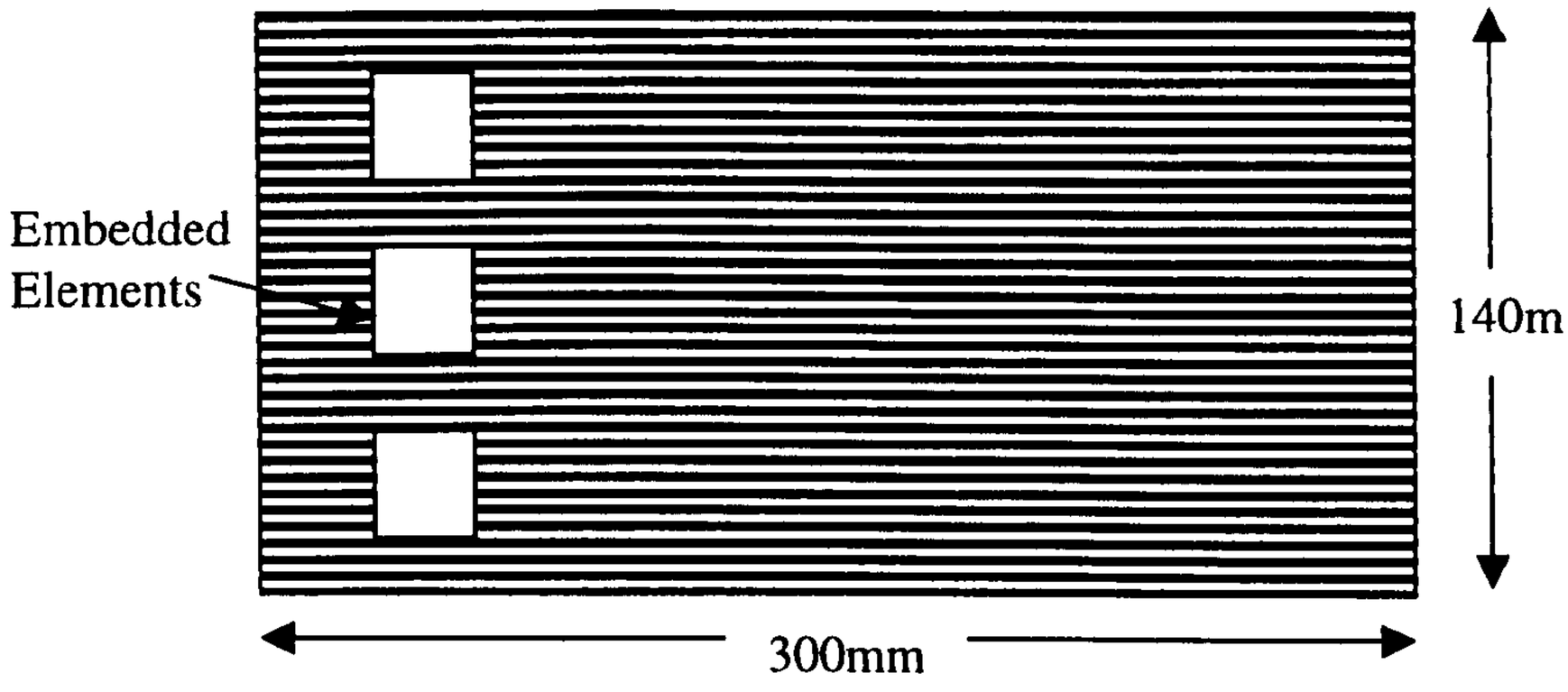

Figure 2.5(b): *Plan: Composite Plate Layout with Embedded PZT Elements*

As mentioned previously, piezopolymers (such as PVDF) make a more suitable piezoelectric sensor since they can be fashioned into thin sheets and formed to adhere to most surfaces. Moreover, they exhibit a flat response over a wide frequency range and possess excellent mechanical strength [38]. Importantly, they display low acoustic impedance, which enables a number of devices to be distributed over a structure with minimal impact on its mechanical properties. Chui *et al.* describe research on the characterisation of piezoelectric thin films, and its use for crack growth monitoring in metallic structures, and damage detection in composite plates [38]. Experimental results were presented for a 12.5mm thick Aluminium Alloy centre-cracked (6mm diameter hole with two 4mm notches protruding from it) specimen, which had a number of 28μm thick, by 4mm x 20mm Nickel Chromium (NiCr) sputtered PVDF thin films adhered to it. The specimen, which was clamped at one end, was subjected to constant amplitude cyclic loading and the resultant crack growth was measured using a vernier microscope. Repeated comparisons were made between the measured crack length and the recorded peak-peak sensor voltage after a specified number of loading cycles. It was shown that the sensitivity of the devices (defined as the measured peak-peak voltage, divided by the peak-peak voltage across a reference device adhered away from the crack) increases with crack growth, and that the gradient of the response changes as the crack passes under, and beyond the sensor. The sensors were therefore shown to be capable of detecting changes in the strain field due to the presence cracks. Furthermore, Chiu *et al.* go on to report damage detection in a cross-ply graphite/epoxy sample with two, 30mm 'barely visible impact damages' (BVID). In this experiment comparisons were made

between measurements from PVDF sensors (28μm thick NiCr sputtered) adhered to damaged and undamaged regions of the sample. It was shown that under cyclic loading conditions the sensors behaved differently revealing their capacity to detect BVID. Similarly, PVDF thin film sensors were utilised to detect BVID in a carbon fibre/epoxy resin skin, honeycomb core structure, which represented a "realistic" aircraft component.

A further piezoelectric sensor option for structural health monitoring is that of piezoelectric paint, which has been evaluated by Egusa and Iwasawa [39]. The paint is prepared using PZT ceramic powder as a pigment and epoxy resin as a binder, and can be cured at room temperature to establish films as thin as 25μm. This sensor can therefore be conveniently applied to large structures without drastically affecting their mechanical properties. The paint is then poled at room temperature under electric fields of up to 450kVcm^{-1}. Compared with piezopolymers the paint film sensor has the advantage of being even more suitable for complex structural shapes. Egusa and Iwasawa go on to describe experimental results that reveal the paint's ability to sense the vibration modes of an underlying aluminium cantilever beam.

When inspecting large structures an attractive approach is to utilise piezoelectric sensors configured to generate and detect ultrasonic waves that can propagate large distances in the structure. For example, of particular interest to this Thesis are Lamb waves (guided acoustic plate waves discussed in detail in Chapter 5), which are capable of propagating over large distances in plate-type structures [5]. Here

interaction with mechanical flaws in the structures affects the wave propagation allowing one sensor to inspect several metres, along the acoustic path. This approach maximises the area monitored, to the number of sensors utilised, which is obviously a desirable feature for smart structure monitoring since it enables a significant reduction in the number of embedded sensors required. Ideally, one transducer would be able to send, and receive a particular Lamb wave mode for the interrogation of a section of the structure, and also be capable of operating in a number of directions [5].

To permit unobtrusive integration into a host material, the Lamb wave transducer requires to be both thin, and flexible. Two transducer technologies have emerged with this in mind, namely flexible low profile piezoplatelet devices [40], which incorporate active piezoceramic platelets embedded within a lithe epoxy matrix; and flexible piezopolymer devices made of materials such as PVDF [5]. Both designs display controlled wavelength bandwidths through interdigital (ID) electrode patterns, and controlled frequency bandwidths through narrowband excitation to enable uni-modal operation, which is required for unambiguous data interpretation. A comparative study of the two technologies is provided by Gachagan *et al.* [40], who show that the piezopolymer devices are cost effective, simple to manufacture, and exhibit good uni-modal operation, however, the piezoplatelet configuration is far more efficient. This factor is of particular significance when operating in highly attenuative composite materials. Gachagan *et al.* [41] demonstrate the low profile piezoplatelet configuration surface mounted to carbon fibre reinforced composite

plates. Here, efficient Lamb wave generation and detection was presented with propagation distances of approximately 1m reported. An example of an embedded piezoelectric transducer for Lamb wave generation in composite plates is provided by Moulin *et al.* [42]. Here two piezoceramic (PZT) disc transducers of diameter 5mm and thickness 2mm were embedded in a 3.85mm cross ply composite plate. The devices were embedded by simply machining two 3mm deep blind holes into the plate, placing the discs in the holes then filling the remaining void with epoxy. It was reported that the radial vibration modes of the embedded piezoceramic discs provided the most efficient coupling for Lamb wave excitation.

Unlike these discussed active Lamb wave devices, Wenger *et al.* report on the evaluation of a passive composite piezoelectric Lamb wave sensor, which is proposed for *in-situ* acoustic emission (AE) detection in plate-type structures [43]. The devices consist of a piezoelectric powder dispersed in a polymer matrix, which takes advantage of the mechanical strength and low dielectric permittivity of the polymer and the strong piezoelectric and electromechanical properties of the ceramic. A single film of this composite material is often referred to as a monomorph. Two such layers can be configured into one device to form a bimorph, which provides the ability to operate in one of two modes (thickness or bending) depending on the relative polarisation and electrode configuration of the constituent monomorphs. Wenger *et. al* report on two 25-ply unidirectional S-glass fibre/epoxy composite plates of thickness 3mm, constructed with bimorphs embedded within them. The sensors were investigated with respect to their ability to detect an AE source, which

can result from matrix cracking, fibre breakage, or delamination. In this case a simulated AE source was realised by snapping a pencil lead on the surface of the plate to induce a sudden release of stress, which subsequently stimulates Lamb wave propagation in the plate. The sensors were demonstrated detecting the acoustic activity in the plates 100mm from the source, indicating their potential as passive AE sensors.

Another sensor that utilises the generation and detection of acoustic waves is the surface acoustic wave (SAW) device. Here changes in the surface wave's travelling time between the SAW device and a reflector are used to indicate changes in the physical variable of interest. The operating frequency of such devices is generally from ten megahertz to a few gigahertz, which interestingly matches the radio and radar frequency range. As a result of this, Varadan *et al.* [44] have demonstrated a passive SAW strain sensor, which uses electromagnetic waves to wirelessly excite the device. This sensor is being developed for the realisation of a new smart material system for wireless sensing and control of helicopter rotor blades. This passive device resembles a large credit card and is constructed from a piezoelectric lithium niobate crystal and an integral silk-screened antenna. The antenna captures an incoming electromagnetic signal and propagates it across the lithium niobate crystal, which efficiently converts it into a surface acoustic wave. Each sensor reflects the surface wave off a uniquely pattered layer of aluminium to create an identifiable phase modulated encoded signal. The reflected signal is retransmitted and is utilised to measure strain variations. Demonstration of such devices adhered to a Plexiglass

cantilever beam (to approximate a helicopter blade) for strain measurement was presented. A linear response between measured phase angle shift and applied strain was presented, with a resolution of 0.0009mm/mm strain per degree of phase angle change.

2.3.3. Inherent Reinforcement Fibre Sensors

An area of common concern for all sensor technologies to be embedded within composite materials is that of resultant structural degradation. Therefore, one very attractive concept is to utilise the inherent material, for example the reinforcement fibres within the composite structure, to also behave as the sensor. Techniques employing this concept have been devised and shall be discussed in this Section.

2.3.3.1 Reinforcement Fibres as Ultrasonic Waveguide Sensors

Kent and Ruddell [45, 46, 47] describe a system utilising the reinforcement fibres of, glass/matrix composites (GMC), ceramic/matrix composites (CMC), and metal/matrix composites (MMC) as acoustic waveguides to monitor the fibre/matrix interface during the manufacturing process. This concept utilises direct monitoring of the ultrasonic signal propagating in the fibre, to provide an indication of the mechanical integrity of the interface along the fibre's length. As such, the reinforcement fibre provides a channel for the exchange of ultrasonic information transfer. Consider an embedded reinforcement fibre that is constrained at its axial-radial boundaries, here some of the ultrasonic energy propagating in the fibre will

leak into the surrounding media across the fibre/matrix interface. Therefore, this rate of leakage provides a direct indication of the stress wave transfer from the fibre to the matrix within the elastic regime, which in turn determines the mechanical characteristics of the composite material. In this work, both piezoceramic and laser methods for generation and detection of the ultrasonic energy were described. The results presented reveal that the both the velocity, and the frequency content of the propagating ultrasound, can provide a direct indication of the pertinent interface characteristics during the manufacturing process cycle. Therefore, it was proposed that this in-situ technique be utilised on-line for improved interfacial properties and performance.

2.3.3.2. Reinforcement Fibres as Electrical Resistance Sensors

At a more elementary level, the electrical resistance of carbon fibres has been measured and used to successfully detect damage in unidirectional carbon fibre reinforced plastic (CFRP) laminates [48]. There are three conduction direction paths formed in such composites, namely: (1) the Longitudinal direction, along the carbon fibres; (2) the transverse direction, by fibre-to-fibre contact paths between adjacent fibres; and (3) in the thickness of the sample, by contacts between plies of the laminates. These various electrical conductivity paths permit the measurement of damage evolutions such as fibre fractures, matrix cracking, and delamination.

2.3.3.3. Reinforcement Fibres as Optical Waveguide Sensors

In Section 2.3.1 the potential for optical fibre sensors to be embedded in composites was highlighted. Although the optical fibres do not degrade the tensile strength of

the composite when properly embedded, concerns still remain on the resultant structure's ability to withstand compressive loading [29]. This is largely due to the diameter mismatch between the optical fibres (typically 125μm), and the reinforcing fibres such as glass or carbon (typically 7-12μm). A possible solution to this problem is to use the reinforcement fibre as the light guiding medium. Recent developments in the manufacture of quartz reinforcement fibres, which offer low dielectric constant, high heat resistance, and importantly the ability to guide light when properly coated, has initiated Hayes *et al.* [49] to develop the realisation of this very concept. Bundles of quartz reinforcement fibres were coated with silicone resin to form *self-sensing* 70μm thick layers. Composite panels were then constructed from 16 plies of Ciba/Geigy carbon fibre prepregs in the sequence $\{0°/90°/90°/0°/0°/90°/0°/90°\}_s$, to produce a 300mm square panel. The self-sensing fibres were embedded within the composite between layers 1 and 2, and layers 15 and 16. Similar composites were also constructed with conventional optical fibres embedded within them to provide a comparison. It was demonstrated that, unlike the plates incorporating the conventional embedded optical fibres, the self-sensing fibre composite plates produced no undesirable resin rich areas. Furthermore, it was proposed that the self-sensing fibres should induce no detrimental effect on the properties on the composite, due to diameter compatibility, and the ability to engineer the interface as required. In addition, the fibres were demonstrated to detect impact damages as low as 2 Joules, out performing the conventional optical fibres, which were only capable of detecting impacts greater than 4 Joules.

2.4. Acoustic Fibre Waveguide Applications

Section 2.3. discussed various contemporary sensor technologies being considered for smart structure applications. This Thesis introduces a new sensor technology concept based on the delivery of ultrasonic energy to a structure via embedded acoustic fibre waveguides. Consequently, to put this application into context, the following Section will describe the various areas of technology that have previously employed cylindrical acoustic waveguides.

2.4.1. Delay Lines

In the early days of telephony, electric circuits were required to introduce short time delays. However, increasing demands made on these circuits to achieve higher bandwidths, and longer delay times resulted in the development of acoustic delay lines. Systems based on ultrasonic propagation along wires were considered particularly attractive because, they were relatively simple structures, and could be made of inexpensive materials compared with acoustic solid or liquid delay lines [50]. This early application for acoustic wire waveguides was widely investigated in the 1950s and 1960s, [51, 52, 53], and subsequently in the 1970s for clad waveguides [1, 54, 55], where the cladding offered a loss-free mechanical support enabling long delay lines to be coiled.

The transducers used to induce ultrasonic propagation along wire delay lines are usually based on magnetostriction in the wire itself, or in a short length of different material joined to the wire. Consider a delay line of a magnetostrictive wire material with a small coil of conducting wire wound round a section of it as depicted in Figure 2.6. When a current is passed though the coil, the waveguide section beneath it is magnetised, and by magnetostriction an extensional packet of strain is produced, which propagates along the delay line [50].

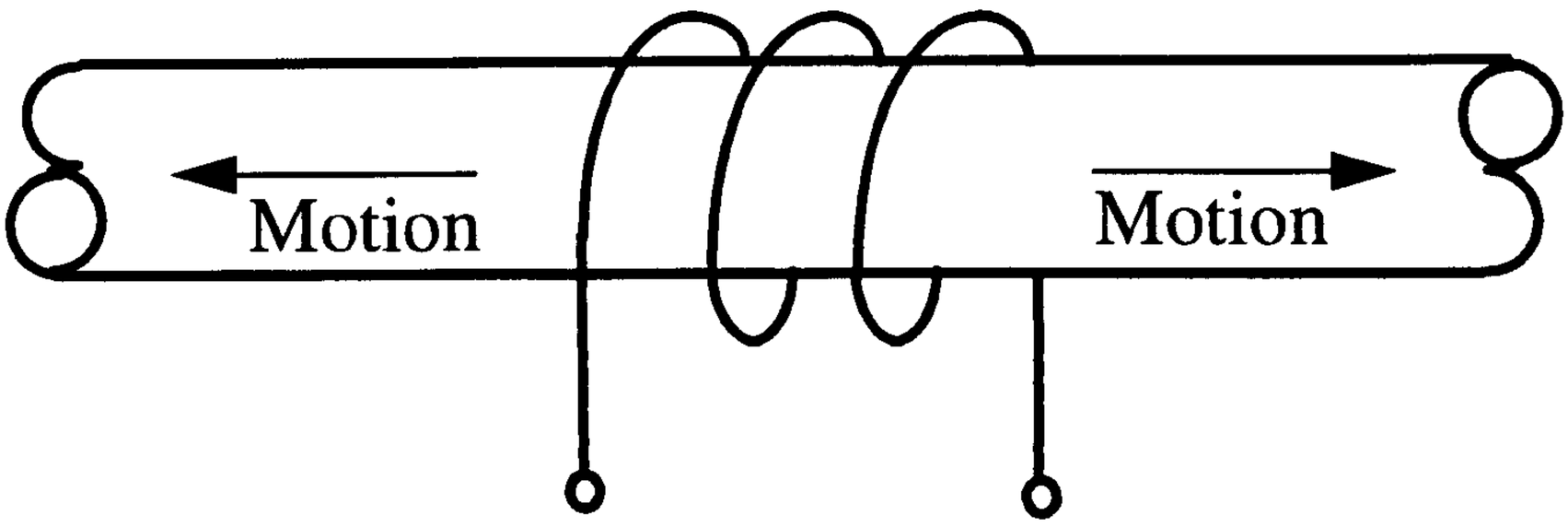

Figure 2.6: *Extensional wave generation using magnetostrictive transduction*

However, torsional propagation is most frequently used in wire delay lines because of its non-dispersive qualities, (i.e. all frequencies propagate at the same velocity). This type of waveform is typically generated by attaching two separate wires or tapes to the delay line at right angles, as in the Scarrott and Naylor transducer, as depicted in Figure 2.7. Here longitudinal tension is generated in the separate wires or strips using magnetostrictive methods, which in turn applies torque to the main wire, thus generating torsional motion. Another magnetostrictive method, which directly

generates torsional propagation in the wire delay line, relies on the Wiedemann effect [50]. Here a helical magnetic field is produced in the delay line wire by combining an axial field (generated by a current flowing in a coil wrapped around the wire) with a circumferential field (generated by a current flowing in the delay wire itself) to induce a twisting strain.

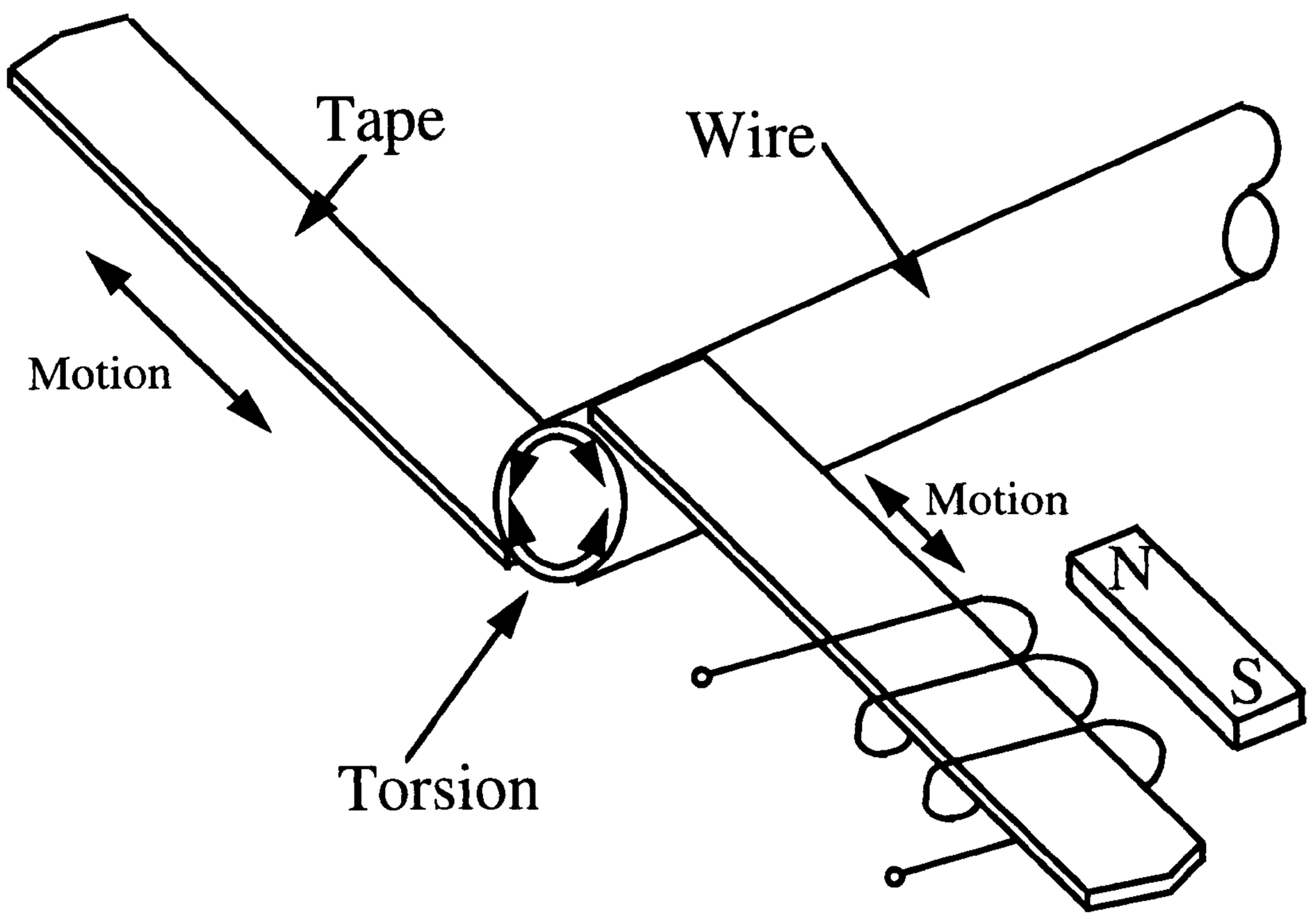

Figure 2.7: *Scarrott and Naylor generation of torsional modes in a wire delay line*

2.4.2. Acousto-Optic Modulators

In optical engineering there is much interest in devices that provide coupling between two orthogonally polarised modes of a birefringent optical fibre [56]. Acoustic

energy is often used in such devices to apply uniform stress to optical fibres at periodic intervals. Frequency shifters [57, 58], polarisation couplers [56], and tuneable optical fibres [59] have all used acoustic energy for this function. Travelling surface acoustic waves are typically used to stress the fibre periodically, producing a frequency shift in the light by causing phase-matched coupling between two orthogonally polarised modes of the birefringent optical fibre. Phase matching requires that an acoustic wave propagating along the direction of the fibre has a periodic length equal to the fibre beat length (L_B) [57]. The beat length of the fibre is given by $L_B = L_0/\Delta n$, where L_0 is the optical wavelength in free space and Δn is the birefringence of the fibre [56].

The periodic stress required for fibre-optic frequency shifters has also been realised using acoustic flexural modes propagating in the optical fibre. Kim *et al.* [60] have demonstrated an all-fibre optical frequency shifter using mode coupling between the two lowest-order optical modes in a weakly guiding fibre (that is LP_{01} and LP_{11}). These two optical modes are orthogonal to one another in an unperturbed straight fibre and consequently will not exchange optical power as they propagate along it. However optical coupling between these modes can be induced by periodic microbending, at a distance given by the beat length of the fibre. This is achieved by exciting an acoustic flexural mode to propagate in the fibre.

The coupling method used to introduce flexural motion into the optical fibre involves the employment of an acoustic horn attached at one end to an unclad section of the

optical fibre and at the other end to a piezoceramic transducer, as revealed in Figure 2.8. The plastic jacket is removed from the section in which the flexural wave is to propagate to reduce attenuation of the acoustic wave to insignificant levels. Theoretical studies of acoustic horns have been extensively undertaken, for example see Mason [61]. Such structures transform low amplitude acoustic waves at their base into high amplitude acoustic waves at the apex via a change in the cross section. Silica horns are typically used in fibre-optic applications for good acoustic matching to the fibre. The tip of the horn, which is bonded to the fibre, should be of approximately the same diameter as the fibre for a good acoustic transfer of energy [60]. Acoustic dampers are often wrapped around the fibre at one side of the horn to prevent acoustic energy propagating in both directions.

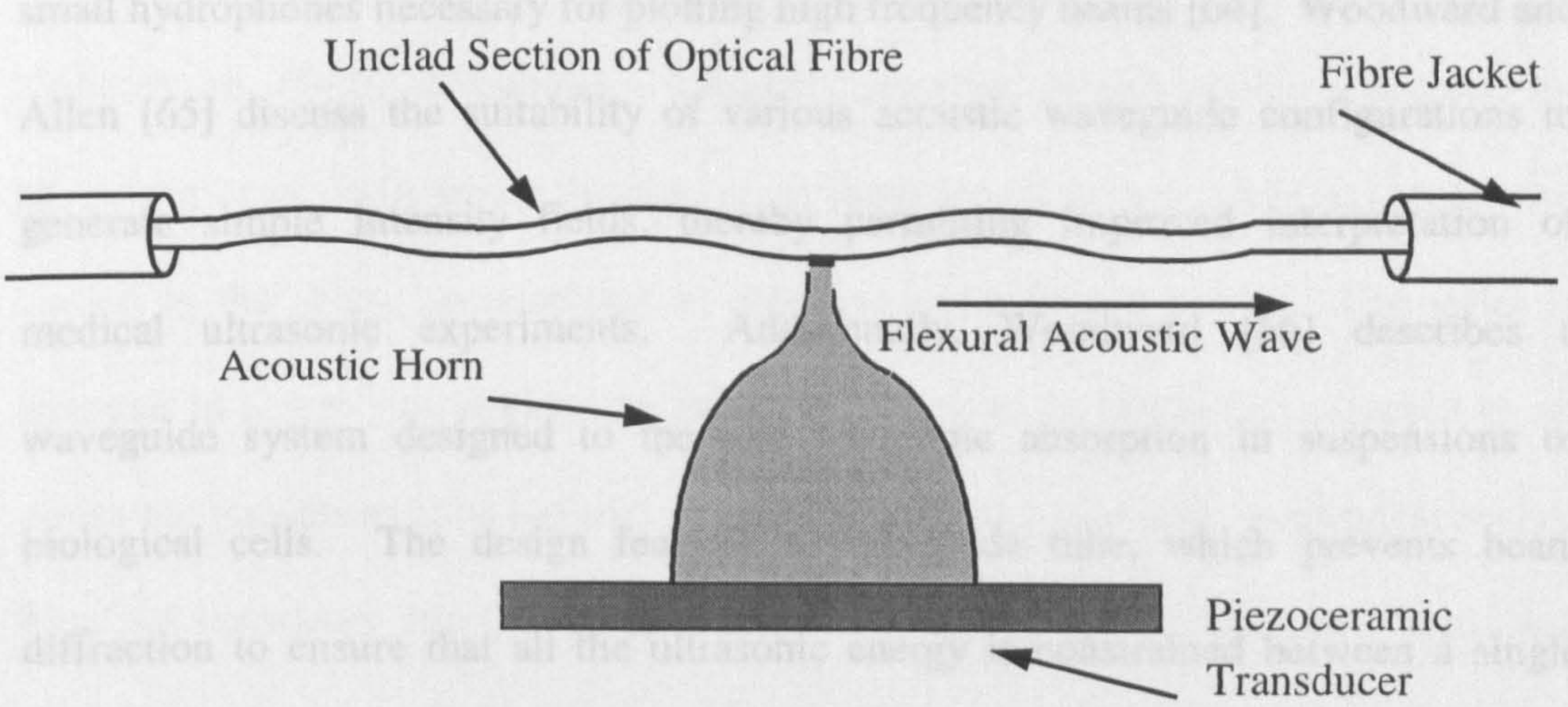

Figure 2.8: *Coupling of a Flexural Acoustic Mode into an Optical Fibre*

Theoretical and experimental investigations into the coupling of acoustic energy from acoustic horns into optical fibres have been carried out in an effort to improve frequency shifters [62]. New configurations of acoustic horn optical fibre coupling have also been examined where the acoustic horn is collinearly, rather than transversely, bonded to the optical fibre [63]. Such a configuration is reported to improve the robustness of the fibre-to-horn bond, the compactness, efficiency at a given RF power level, and acoustic bandwidth.

2.4.3. Medical Applications

Acoustic waveguides have been used in the design of several medical instruments, including, sonically sensitive needles and catheters used in tissue biopsy, and very small hydrophones necessary for plotting high frequency beams [64]. Woodward and Allen [65] discuss the suitability of various acoustic waveguide configurations to generate simple intensity fields, thereby permitting improved interpretation of medical ultrasonic experiments. Additionally, Woodward [66] describes a waveguide system designed to measure ultrasonic absorption in suspensions of biological cells. The design features a waveguide tube, which prevents beam diffraction to ensure that all the ultrasonic energy is constrained between a single transducer and a moveable air-backed reflector, and is lost only by absorption into the sample.

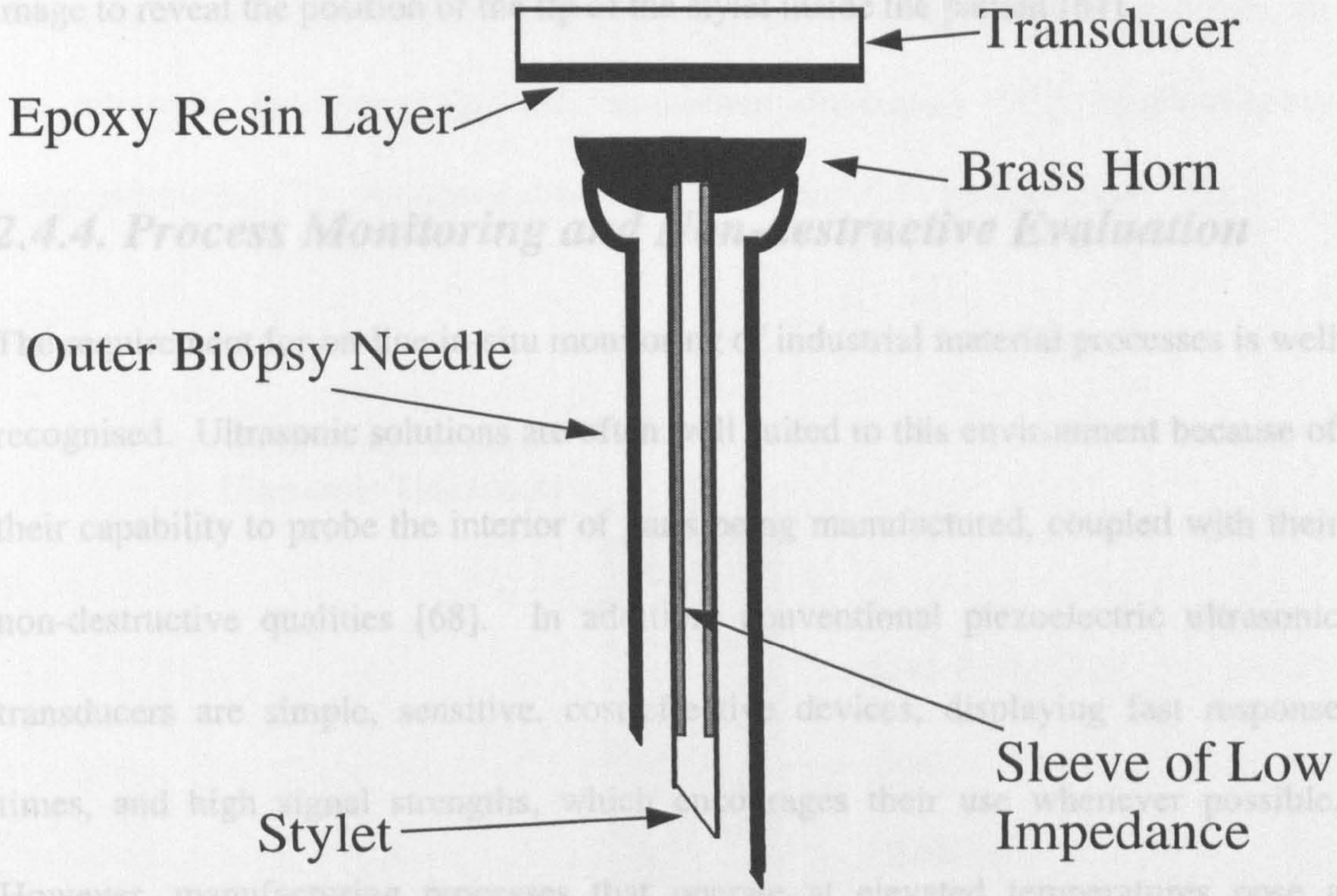

Figure 2.9: *Sonically sensitive biopsy needle*

Furthermore, Figure 2.9 shows a sonically sensitive biopsy needle discussed by Nicholson *et al.* [64], which consists of an inner length of solid stainless steel wire known as the stylet, encapsulated in a hollow outer biopsy needle. The stylet is wrapped in a very low impedance material (except at its tip) and is clamped to an ultrasonic transducer at its top end. A brass horn is used to couple mechanical energy from the transducer into the stainless steel wire with an epoxy resin layer providing electrical insulation. The stylet is glued to the horn and the horn is mechanically clamped onto the transducer. The needle is used in conjunction with an ultrasonic imaging system, which introduces ultrasound to the tip of the stylet. This acoustic energy is transported by the waveguide to the transducer where it is converted into an

electrical signal. Subsequently, a flashing spot is superimposed onto the real-time image to reveal the position of the tip of the stylet inside the patient [67].

2.4.4. Process Monitoring and Non-destructive Evaluation

The requirement for on-line in-situ monitoring of industrial material processes is well recognised. Ultrasonic solutions are often well suited to this environment because of their capability to probe the interior of parts being manufactured, coupled with their non-destructive qualities [68]. In addition, conventional piezoelectric ultrasonic transducers are simple, sensitive, cost-effective devices, displaying fast response times, and high signal strengths, which encourages their use whenever possible. However, manufacturing processes that operate at elevated temperatures pose a significant problem to such transducers, which display performance degradation or even complete failure. Here an attractive option is to employ a clad waveguide as a buffer rod, which isolates the piezoelectric element from the process being monitored, see Figure 2.10 [68]. In such a configuration one end of the buffer rod is brought into contact with the high temperature environment to be monitored, while the other end is attached to a piezoelectric transducer to excite guided waves in the rod. The transducer end is air or water cooled to permit the use of conventional high performance ambient temperature piezoelectrics and couplants. The buffer cladding provides mechanical isolation for the ultrasonic energy propagating in the rod's core, and is typically made of a material that can be readily machined for ease of incorporation into the process environment. These devices tend to be utilised in pulse-echo mode (one transducer transmits and receives) with reflection times and

magnitudes delivering the required information on the material under investigation. Examples of processes that have demonstrated these devices for high-temperature on-line ultrasonic monitoring include, aluminium die-casting [69], graphite/epoxy composite curing [70], polymer extrusion [70, 71], and flow measurement [72].

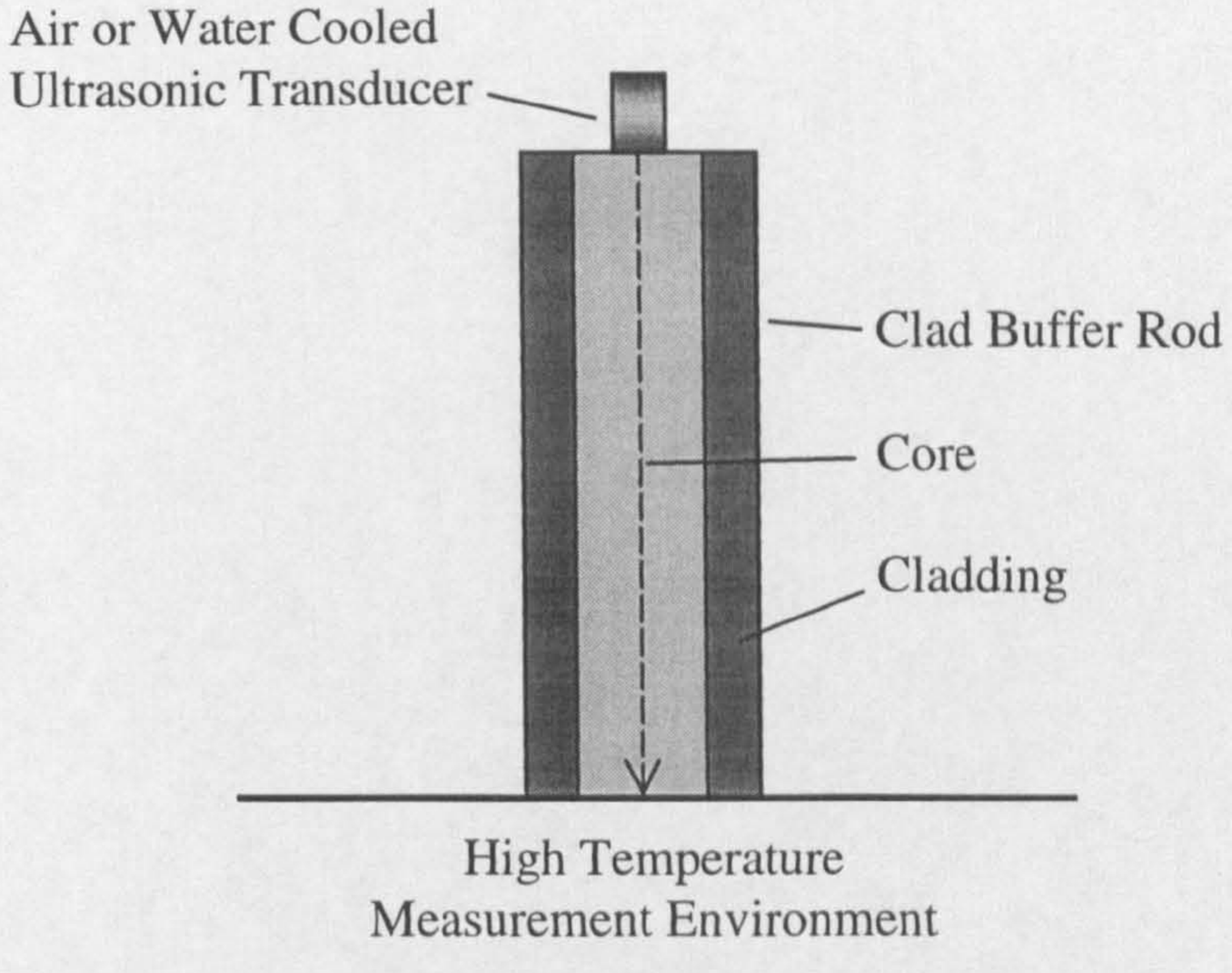

Figure 2.10: *Clad Buffer Rod For High Temperature Process Monitoring*

Unclad ultrasonic waveguides have also been utilised for process monitoring applications. For example Journeau and Ducret [73] describe a feasibility study on a waveguide device capable of performing ultrasonic characterisation of liquid metals. Here two stainless steel waveguides (of diameter 3mm) are utilised, one to deliver ultrasound to the test sample and the other to receive. The feasibility of the probe was demonstrated in solidifying lead and liquid mercury. The device, which is very much in its embryonic state, is being developed for operation at 2000°C for the characterisation of the liquid metal mix that would result from a severe nuclear

reactor accident where the core itself would melt. The behavioural characteristics of this melt would provide valuable safety information for the nuclear industry.

Wire waveguides have also been adopted to perform in-situ measurements of polymeric cure procedures. When such a waveguide is embedded in epoxy, or a fibre-reinforced/epoxy composite, the surrounding media acts as an infinite cladding. Therefore, as it cures the viscosity and temperature vary, which directly influence the attenuation and velocity of ultrasonic propagation in the guide yielding information on the state of cure. Sun and Winfree [74], and Harrold and Sanjana [75] provide experimental examples of such techniques for epoxy, and graphite fibre/epoxy composite cure procedures respectively. Furthermore, Costley *et al.* [76] discuss a robust acoustic wire waveguide sensor for measuring the viscosity of highly viscous liquids. This sensor utilises torsional wave propagation, generated in the waveguide by the Wiedemann effect (discussed in Section 2.4.1), and was reported to take viscosity measurements of molten glass at temperatures up to 1060°C.

In addition, waveguide rods have been demonstrated with non-destructive evaluation (NDE) applications. For example Yamaguchi *et al.* [77] utilise a fused quartz rod of length 50cm, and diameter 1mm as a waveguide, excited by a PZT piezoceramic transducer, to deliver longitudinal waves to aluminium and glass test samples for subsequent NDE. The waveguide was adhered to each sample via a matching layer at various locations and detection of hidden flaws close to the surface was demonstrated by monitoring the variance in acoustic impedance. Furthermore, a

movable, dry-contact, waveguide transducer design has been developed at Stanford University for the NDE of plate-type structures [78]. Here longitudinal waves are generated in a steel rod by a piezoceramic element while the other end, which is tapered, is brought into contact with the test plate under force to generate a Lamb wave. These devices are described in detail in Chapter 5, which investigates Lamb wave technology.

2.5. Proposed Acoustic Fibre Waveguide Sensor for Smart Structures

It has been shown in this Chapter that the implementation of optical fibre sensor technology into smart structures has reached a significant level of maturity, with their small, lightweight nature enabling them to be successfully integrated into composite structural components. Nevertheless, a limitation of optical fibre sensors for condition monitoring applications is that they are essentially passive devices, only capable of inspecting regions local to their sensing gauge. Consequently, many embedded optical fibre sensors would be required to monitor the health of a large structural area, thereby increasing the likelihood of structural degradation.

As previously discussed, a solution to this problem is to utilise an active sensor that can generate and detect ultrasonic waves capable of propagating over large distances (i.e. several metres), such as Lamb waves in plate-type structures. Unfortunately, such acoustic sensors have yet to be successfully integrated into composite materials. However, it has been shown in this Chapter that acoustic fibre waveguides can be

utilised to deliver ultrasonic energy to and from test samples. Therefore, it is proposed that an embedded active acoustic fibre waveguide sensor be developed, which is capable of transporting ultrasonic energy to and from structures to induce and detect ultrasonic propagation within the structure. Such a sensor would combine the geometrical and low cost advantages of the optical fibre sensors, with the resolution and long distance monitoring capabilities offered by alternative ultrasonic techniques. Furthermore, a group of such embedded fibre waveguide sensors could be utilised as an ultrasonic array with the ability to focus or beam steer for greater structural coverage and improved resolution. The realisation of such a diverse, flexible, low cost, long range, active (or passive) sensor would be a significant contribution to the field of continual structural health monitoring.

2.6. Conclusions

This Chapter has introduced the concept of smart structures and discussed various applicable contemporary sensor technologies. In particular, experimental work on suitable embedded optical fibre configurations, such as the FFPI and FBGS has been presented. The influence of embedded optical fibres on the host structure has also been discussed indicating that while the compressive strength often degrades the tensile strength remains largely unaffected. Various piezoelectric sensors appropriate for integration into smart structure components have been reviewed. Additionally, the attractive option of utilising an inherent structural component (such as the reinforcement fibres) as the sensor has been highlighted, and several systems utilising this concept have been discussed.

Moreover, this Chapter has reviewed a diverse range of technologies that employ cylindrical acoustic waveguides, thereby establishing the novel nature of the proposed monitoring system application, which utilises embedded acoustic fibre waveguides to transport ultrasonic energy to and from a structure for its interrogation. As such, the proposed technique strives to introduce a low cost remote active sensor that combines the advantages of optical fibres, i.e. small size for potentially unobtrusive integration into a host, immunity to electromagnetic interference, and the ability to withstand environmental factors such as high temperatures and pressures associated with composite manufacture, along with the advantages of acoustic wave propagation sensors, which permit large areas of a structure to be monitored with a minimal number of sensors.

CHAPTER 3

THEORY OF ELASTIC WAVE PROPAGATION IN CYLINDERS

3.1. Overview of Chapter

There are three families of waves that can propagate in solid isotropic cylinders, these are called: longitudinal; torsional; and flexural. In the longitudinal case, elements of the rod extend and contract, and there is no lateral motion along the axis of the rod. For torsional vibrations, each transverse section of the rod remains in its own longitudinal plane and rotates about its centre, the axis of the rod remaining undisturbed. Finally, flexural vibrations correspond to the flexure of portions of the rod, with elements of the central axis moving laterally during the motion [79]. This Chapter provides a review of relevant theory on the propagation of such stress waves in cylindrical bars as outlined by Kolsky [79], Redwood [80], Morse and Freshback [83], and Meeker and Meitzer [53].

Firstly, an introduction to the relationships between stress and strain, and equations of motion in an isotropic solid will be provided for clarity. This leads on to a simplified examination of cylindrical bars for the case when the propagating wavelength is large compared with the lateral dimensions of the bar. The problem is then considered in terms of the exact elastic equations. Dispersion curves will be presented and modal characteristics discussed. Consequently, the mode most suited to the requirements of the proposed Lamb wave monitoring system will be discussed.

3.2. *Basis for Mechanical Wave Propagation*

The propagation of elastic waves in solid isotropic cylinders derives from knowledge of the stress-strain relationships and equations of motion in an infinite isotropic solid.

3.2.1. *Stress, Strain and Displacement Relations*

Consider a point in a solid body at location (x, y, z) which is displaced to location ($x+u_x$, $y+u_y$, $z+u_z$). This will result in a neighbouring point ($x+\delta x$, $y+\delta y$, $z+\delta z$) being displaced to location ($x+u_x+\delta x+\delta u_x$, $y+u_y+\delta y+\delta u_y$, $z+u_z+\delta z+\delta u_z$) [79] where:

$$\delta u_x = \frac{\partial u_x}{\partial x}\delta x + \frac{\partial u_x}{\partial y}\delta y + \frac{\partial u_x}{\partial z}\delta z$$

$$\delta u_y = \frac{\partial u_y}{\partial x}\delta x + \frac{\partial u_y}{\partial y}\delta y + \frac{\partial u_y}{\partial z}\delta z \qquad \textbf{3.1}$$

$$\delta u_z = \frac{\partial u_z}{\partial x}\delta x + \frac{\partial u_z}{\partial y}\delta y + \frac{\partial u_z}{\partial z}\delta z$$

The partial derivatives in Equation 3.1 may be defined such that:

$$\varepsilon_{xx} = \frac{\partial u_x}{\partial x} \qquad \varepsilon_{xy} = \varepsilon_{yx} = \frac{\partial u_y}{\partial x} + \frac{\partial u_x}{\partial y}$$

$$\varepsilon_{yy} = \frac{\partial u_y}{\partial y} \qquad \varepsilon_{yz} = \varepsilon_{zy} = \frac{\partial u_z}{\partial y} + \frac{\partial u_y}{\partial z} \qquad \textbf{3.2}$$

$$\varepsilon_{zz} = \frac{\partial u_z}{\partial z} \qquad \varepsilon_{zx} = \varepsilon_{xz} = \frac{\partial u_x}{\partial z} + \frac{\partial u_z}{\partial x}$$

The quantities ε_{xx}, ε_{yy}, and ε_{zz}, represent extensional strains in the x, y, and z axes respectively, while ε_{xy}, ε_{yz}, ε_{zz} correspond to components of shear strain.

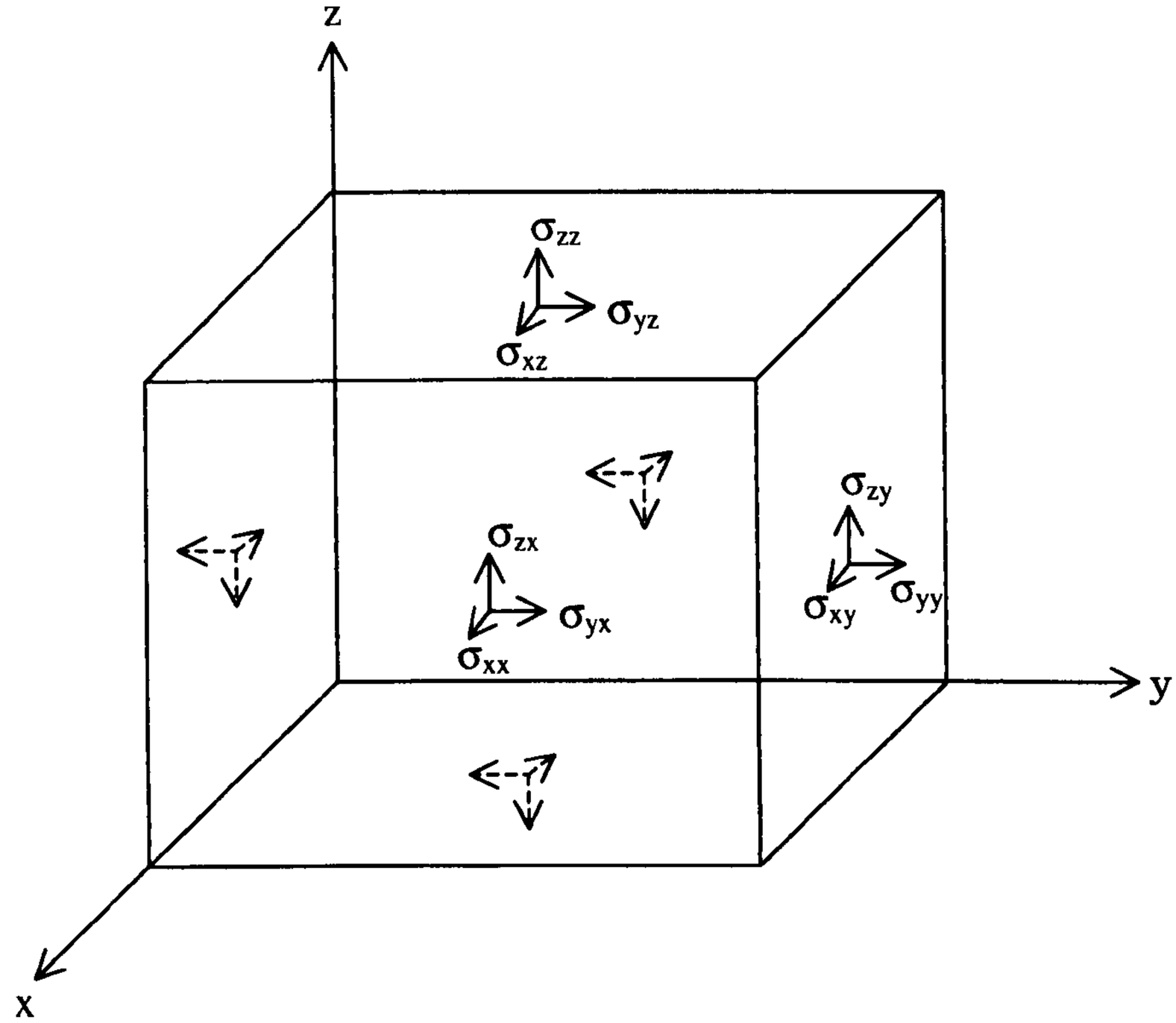

Figure 3.1: *Infinitesimal cubic element*

Now consider an infinitesimal cubic element in a solid body under static equilibrium (Figure 3.1). Stress on a surface of the element comprises both a normal stress component perpendicular to the surface and shear stress components in plane with the surface. Therefore, there are nine components of stress acting on the element: σ_{xx}, σ_{yx}, σ_{zx}, σ_{xy}, σ_{yy}, σ_{zy}, σ_{xz}, σ_{yz}, σ_{zz}, where the first subscript denotes the direction of the stress and the second subscript defines the axis normal to the plane on which the

stress is acting. If it is assumed that the cubic volume element is small enough that there is negligible stress change over the faces, then the summation of moments about the various axes reduces the nine components of stress to six ($\sigma_{ij} = \sigma_{ji}$ where $i \neq j$).

3.2.2. Generalised form of Hooke's Law and Elastic Constants

From the general form of Hooke's law, it is assumed that each of the six components of stress is a linear function of the six components of strain resulting in 36 elastic constants c_{ij} [80].

$$\sigma_{xx} = c_{11}\varepsilon_{xx} + c_{12}\varepsilon_{yy} + c_{13}\varepsilon_{zz} + c_{14}\varepsilon_{yz} + c_{15}\varepsilon_{zx} + c_{16}\varepsilon_{xy}$$

$$\sigma_{yy} = c_{21}\varepsilon_{xx} + c_{22}\varepsilon_{yy} + c_{23}\varepsilon_{zz} + c_{24}\varepsilon_{yz} + c_{25}\varepsilon_{zx} + c_{26}\varepsilon_{xy}$$

$$\sigma_{zz} = c_{31}\varepsilon_{xx} + c_{32}\varepsilon_{yy} + c_{33}\varepsilon_{zz} + c_{34}\varepsilon_{yz} + c_{35}\varepsilon_{zx} + c_{36}\varepsilon_{xy}$$

$$\sigma_{yz} = c_{41}\varepsilon_{xx} + c_{42}\varepsilon_{yy} + c_{43}\varepsilon_{zz} + c_{44}\varepsilon_{yz} + c_{45}\varepsilon_{zx} + c_{46}\varepsilon_{xy}$$

$$\sigma_{zx} = c_{51}\varepsilon_{xx} + c_{52}\varepsilon_{yy} + c_{53}\varepsilon_{zz} + c_{54}\varepsilon_{yz} + c_{55}\varepsilon_{zx} + c_{56}\varepsilon_{xy}$$

$$\sigma_{xy} = c_{61}\varepsilon_{xx} + c_{62}\varepsilon_{yy} + c_{63}\varepsilon_{zz} + c_{64}\varepsilon_{yz} + c_{65}\varepsilon_{zx} + c_{66}\varepsilon_{xy} \qquad \textbf{3.3}$$

Love[81] shows that if the elastic energy is to be a single valued function of the strain any coefficient c_{ij} must be equal to the coefficient c_{ji}, therefore the 36 elastic constants reduce to 21. Furthermore, for an isotropic solid the coefficient values should be independent of the set of axes chosen, therefore, only two constants are required to define the elastic properties. These are known as the lamé constants λ and μ (*shear modulus*), therefore:

$$c_{12} = c_{13} = c_{21} = c_{23} = c_{31} = c_{32} = \lambda$$

$$c_{44} = c_{55} = c_{66} = \mu \qquad \textbf{3.4}$$

$$c_{11} = c_{22} = c_{33} = \lambda + 2\mu$$

The other 24 coefficients all become zero and therefore Equation 3.3 reduces to:

$$\sigma_{xx} = \lambda\Delta + 2\mu\varepsilon_{xx} \qquad \sigma_{yy} = \lambda\Delta + 2\mu\varepsilon_{yy} \qquad \sigma_{zz} = \lambda\Delta + 2\mu\varepsilon_{zz}$$

$$\sigma_{yz} = \mu\varepsilon_{yz} \qquad \sigma_{zx} = \mu\varepsilon_{zx} \qquad \sigma_{xy} = \mu\varepsilon_{xy} \qquad \textbf{3.5}$$

or, in shorthand notation $\sigma_{ii} = \lambda\Delta + 2\mu\varepsilon_{ii}$, and $\sigma_{ij} = \mu\varepsilon_{ij}$

Here $\Delta = \varepsilon_{xx} + \varepsilon_{yy} + \varepsilon_{zz}$; this quantity is termed dilation and represents volume change over a unit cube. Although λ and μ completely define the elastic behaviour of an isotropic solid, three other constants are often utilised. These are: Poisson's ratio (ν) which is the ratio of lateral contraction to longitudinal extension ($-\varepsilon_{yy}/\varepsilon_{xx}$); Young's Modulus ($E$) which is the ratio between applied stress and resultant strain on a bar specimen; and Bulk Modulus (B) which is the ratio between applied pressure and the fractional change in volume when a solid is subjected to a uniform hydrostatic compression ($-\sigma_{xx}/\Delta$). From Equation 3.5 these can be defined in terms of λ and μ [79]:

$$\nu = \frac{\lambda}{2(\lambda+\mu)} \qquad E = \frac{\mu(3\lambda+2\mu)}{\lambda+\mu} \qquad B = \lambda + \frac{2\mu}{3} \qquad \textbf{3.6}$$

3.2.3. Equations of Motion in an Isotropic Solid

The elastic equations of motion for a solid are obtained by considering the variation of stress across the faces of a small cubic element, and take the following form [79]:

$$\rho\frac{\partial^2 u_x}{\partial t^2}=\frac{\partial \sigma_{xx}}{\partial x}+\frac{\partial \sigma_{xy}}{\partial y}+\frac{\partial \sigma_{xz}}{\partial z}$$

$$\rho\frac{\partial^2 u_y}{\partial t^2}=\frac{\partial \sigma_{yx}}{\partial x}+\frac{\partial \sigma_{yy}}{\partial y}+\frac{\partial \sigma_{yz}}{\partial z} \qquad \textbf{3.7}$$

$$\rho\frac{\partial^2 u_z}{\partial t^2}=\frac{\partial \sigma_{zx}}{\partial x}+\frac{\partial \sigma_{zy}}{\partial y}+\frac{\partial \sigma_{zz}}{\partial z}$$

Equation 3.7 holds true for both isotropic and anisotropic media. For the case of an isotropic solid, substitute Equation 3.5 into Equation 3.7:

$$\rho\frac{\partial^2 u_x}{\partial t^2}=\frac{\partial}{\partial x}(\lambda\Delta+2\mu\varepsilon_{xx})+\frac{\partial}{\partial y}(\mu\varepsilon_{xy})+\frac{\partial}{\partial z}(\mu\varepsilon_{xz})$$

$$\rho\frac{\partial^2 u_y}{\partial t^2}=\frac{\partial}{\partial x}(\mu\varepsilon_{yx})+\frac{\partial}{\partial y}(\lambda\Delta+2\mu\varepsilon_{yy})+\frac{\partial}{\partial z}(\mu\varepsilon_{yz}) \qquad \textbf{3.8}$$

$$\rho\frac{\partial^2 u_z}{\partial t^2}=\frac{\partial}{\partial x}(\mu\varepsilon_{zx})+\frac{\partial}{\partial y}(\mu\varepsilon_{zy})+\frac{\partial}{\partial z}(\lambda\Delta+2\mu\varepsilon_{zz})$$

Therefore, from the relations of Equation 3.2, the equations of motion for an unbound isotropic solid may be defined as:

$$\rho \frac{\partial^2 u_x}{\partial t^2} = (\lambda + \mu)\frac{\partial \Delta}{\partial x} + \mu \nabla^2 u_x$$

$$\rho \frac{\partial^2 u_y}{\partial t^2} = (\lambda + \mu)\frac{\partial \Delta}{\partial y} + \mu \nabla^2 u_y \qquad \textbf{3.9}$$

$$\rho \frac{\partial^2 u_z}{\partial t^2} = (\lambda + \mu)\frac{\partial \Delta}{\partial z} + \mu \nabla^2 u_z$$

The Laplacian operator ∇^2 denotes $\frac{\partial^2}{\partial x^2} + \frac{\partial^2}{\partial y^2} + \frac{\partial^2}{\partial z^2}$.

3.3. Simplified Analysis of Elastic Wave Propagation in Solid Cylinders

For the theoretical study that will follow it is prudent to state the one dimensional (1D) wave equation (Equation 3.10) which describes linear time varying wave propagation in the *x*-direction [82].

$$\frac{\partial^2 y}{\partial x^2} = \left(\frac{1}{C^2}\right)\frac{\partial^2 y}{\partial t^2} \qquad \textbf{3.10}$$

Here y is a linear function and *C* is a constant of the propagation medium. A general solution to this equation is described by Equation 3.11.

$$y = f_1(Ct - x) + f_2(Ct + x) \qquad \textbf{3.11}$$

where f_1 and f_2 are distinct solutions to the wave equation and describe waves travelling in the positive and negative x directions respectively. Therefore, the general solution corresponds to two waves travelling in opposite directions.

3.3.1. Longitudinal motion in a bar

Consider a bar to be made up of a number of planar cross-sections. Now if, during motion, each section has uniform stress over it and remains planar, then the equation of motion may be obtained [79]. Consider Figure 3.2, which shows a small element PQ of length δx, where the cross-sectional area of the rod is A.

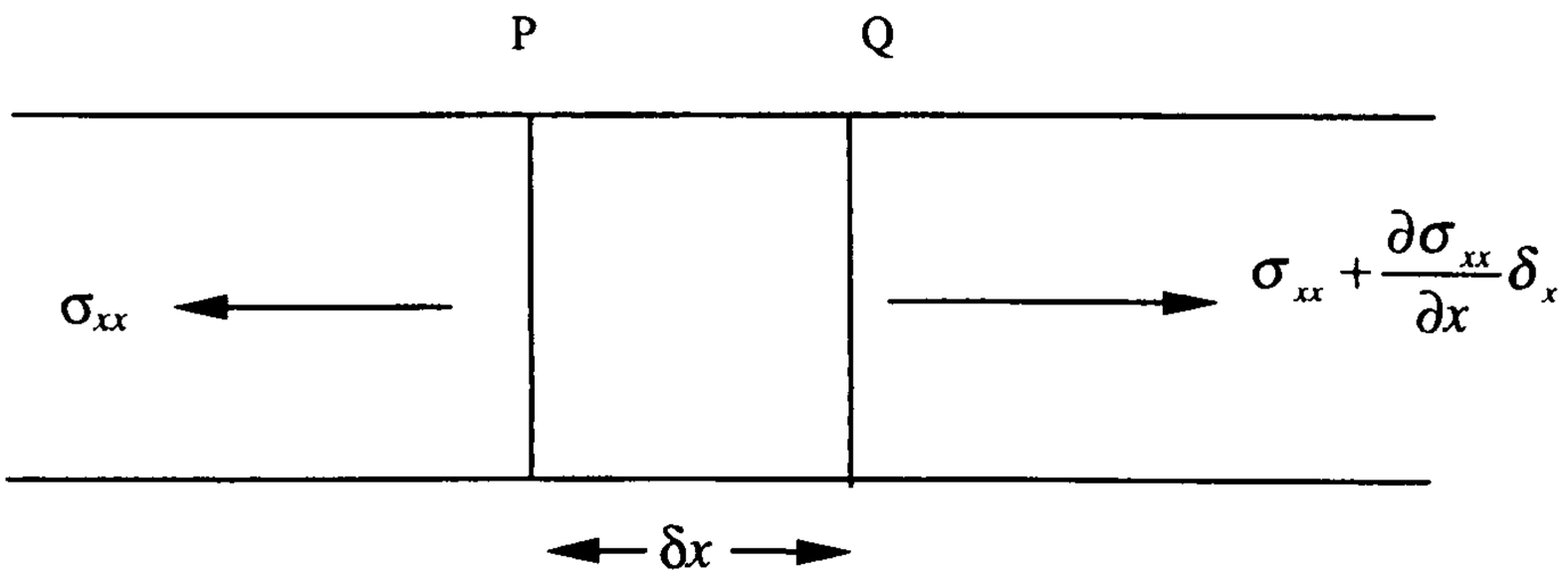

Figure 3.2: *Element of a bar with longitudinal forces acting on it*

Now if σ_{xx} is the stress acting on the face passing through P, then the stress on the other face will be given by $\sigma_{xx} + (\partial \sigma_{xx} / \partial x)\, \delta x$. Therefore, from Newton's second law of motion (the change of momentum per second is proportional to applied force in the direction of the force),

$$\rho A \delta x \left(\frac{\partial^2 u_x}{\partial t^2} \right) = A \left(\frac{\partial \sigma_{xx}}{\partial x} \right) \delta x \qquad \textbf{3.12}$$

Here ρ is the density of the rod and the displacement of the element is given by u_x. Young's modulus, E, is defined as the ratio between stress σ_{xx} and strain ($\partial u_x/\partial x$). Therefore Equation 3.12 may be written as:-

$$\rho\left(\frac{\partial^2 u_x}{\partial t^2}\right) = E\left(\frac{\partial^2 u_x}{\partial x^2}\right) \qquad \textbf{3.13}$$

Now this equation can be seen to be of the form of the 1D wave equation (Equation 3.10), a solution of which is:

$$u_x = B(C_0 t - x) + F(C_0 t + x) \qquad \textbf{3.14}$$

therefore,

$$C_0 = \sqrt{\frac{E}{\rho}} \qquad \textbf{3.15}$$

B and F are arbitrary functions dependant on initial conditions. F corresponds to a forward travelling wave (increasing x) and B to a backward travelling wave (decreasing x). Thus this form of motion has a propagation velocity corresponding to the bar velocity of the material, C_0, given by Equation 3.15.

The analysis so far has not assumed that the rod is cylindrical, and holds true for any uniform cross-section. It assumes that stress acts uniformly over each section, and that plane transverse sections of the rod remain plane during the passage of the stress waves. It is, therefore, only approximate since longitudinal strains on the rod will

result in lateral strains governed by Poisson's ratio (ν). The effect of this lateral motion in cylindrical bars becomes significant when the operative wavelengths are of the same order as the diameter of the bar.

3.3.2. Torsional motion in a bar

Consider torsional motion within a cylindrical bar, where each transverse section remains in its own plane and rotates about its centre. The equation of motion may be obtained from analysis of such a section, PQ, of length δx (see Figure 3.3) as $\delta x \rightarrow 0$ [79].

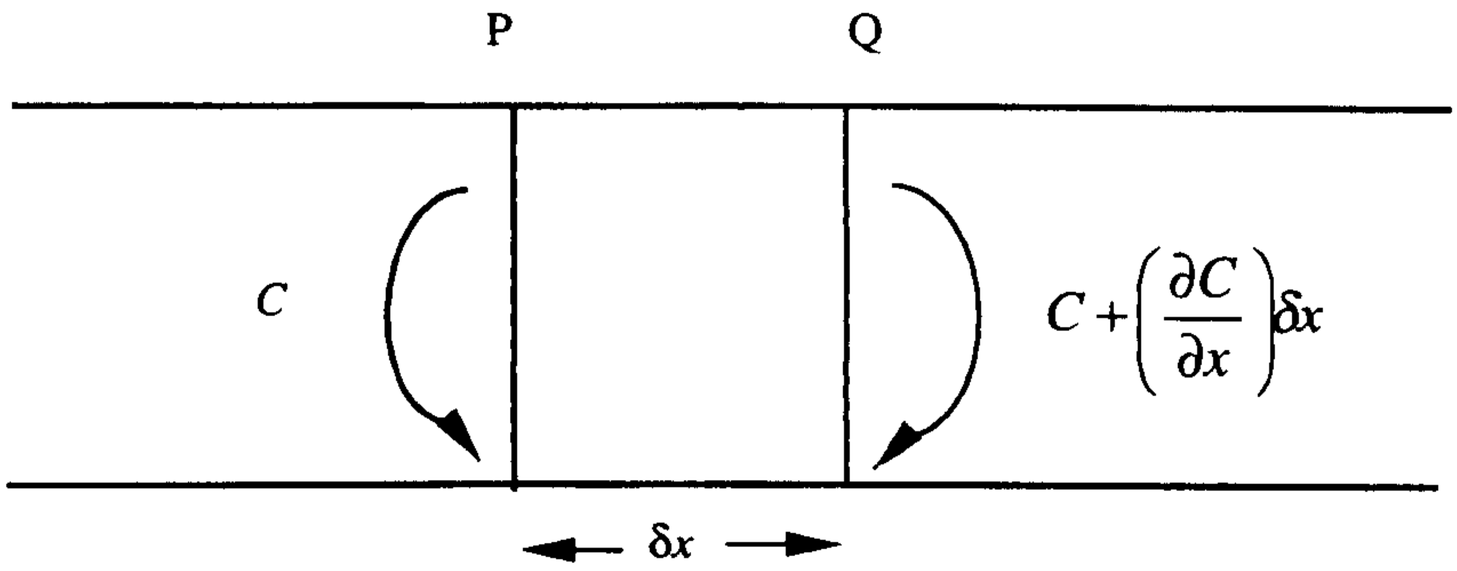

Figure 3.3: *Element of a bar in torsional motion*

With a couple (or torque), C, acting on the element through P, an opposing couple $C+(\partial C/\partial x)\delta x$ will result on the element through Q. For a solid rotating body the resultant couple is equal to the product of moment of inertia (I), and angular acceleration. Therefore, if the moment of inertia of this section is I', the mean angle through which the element rotates isθ, and the resultant couple $(\partial C/\partial x)\delta x$ then:

$$\left(\frac{\partial C}{\partial x}\right)\delta x = I'\left(\frac{\partial^2 \theta}{\partial t^2}\right) \qquad \textbf{3.16}$$

Consider two opposing couples, both of magnitude C, acting on both ends of a cylinder of length x', and of radius r. A relative angular rotation will be produced between the two end faces of value θ', where

$$C = \frac{\pi \mu r^4 \theta'}{2x'} \qquad \textbf{3.17}$$

and μ is the shear modulus. Therefore, if $\delta\theta$ is the relative rotation between the sections through P and Q then in the limit:

$$C = \left(\frac{\pi \mu r^4}{2}\right)\frac{\partial \theta}{\partial x} \qquad \textbf{3.18}$$

Now the moment of inertia, I', of the cylindrical element PQ about its axis is given by the product of mass and radius squared:

$$I' = \left(\frac{\pi \rho r^4}{2}\right)\delta x \qquad \textbf{3.19}$$

Substituting C and I' from Equations 3.18 and 3.19 into Equation 3.16 the following is obtained:

$$\mu\left(\frac{\partial^2 \theta}{\partial x^2}\right) = \rho\left(\frac{\partial^2 \theta}{\partial t^2}\right) \qquad \textbf{3.20}$$

It can be seen that Equation 3.20 is of the form of the 1D wave equation (Equation 3.10), and therefore, torsional waves propagate down a cylinder with the velocity $\sqrt{\mu/\rho}$.

3.3.3. Flexural motion in a bar

The theory for this type of wave is more complex than that of the other two. Even the elementary theory, described here, will show that the velocity is dependent on the wavelength. In this simplified analysis of flexural motion in bars of arbitrary, but uniform cross-section, it is assumed that the motion of each element of the bar is purely one of translation in a direction perpendicular to the bar.

Consider a small element of the bar, PQ, of length δx which has been bent in the xz plane (see Figure 3.4). The bending moment will vary along the length of the bar, and if the moment at P is defined as M, then the value at Q is $(M + (\partial M / \partial x)\, \delta x)$ [79].

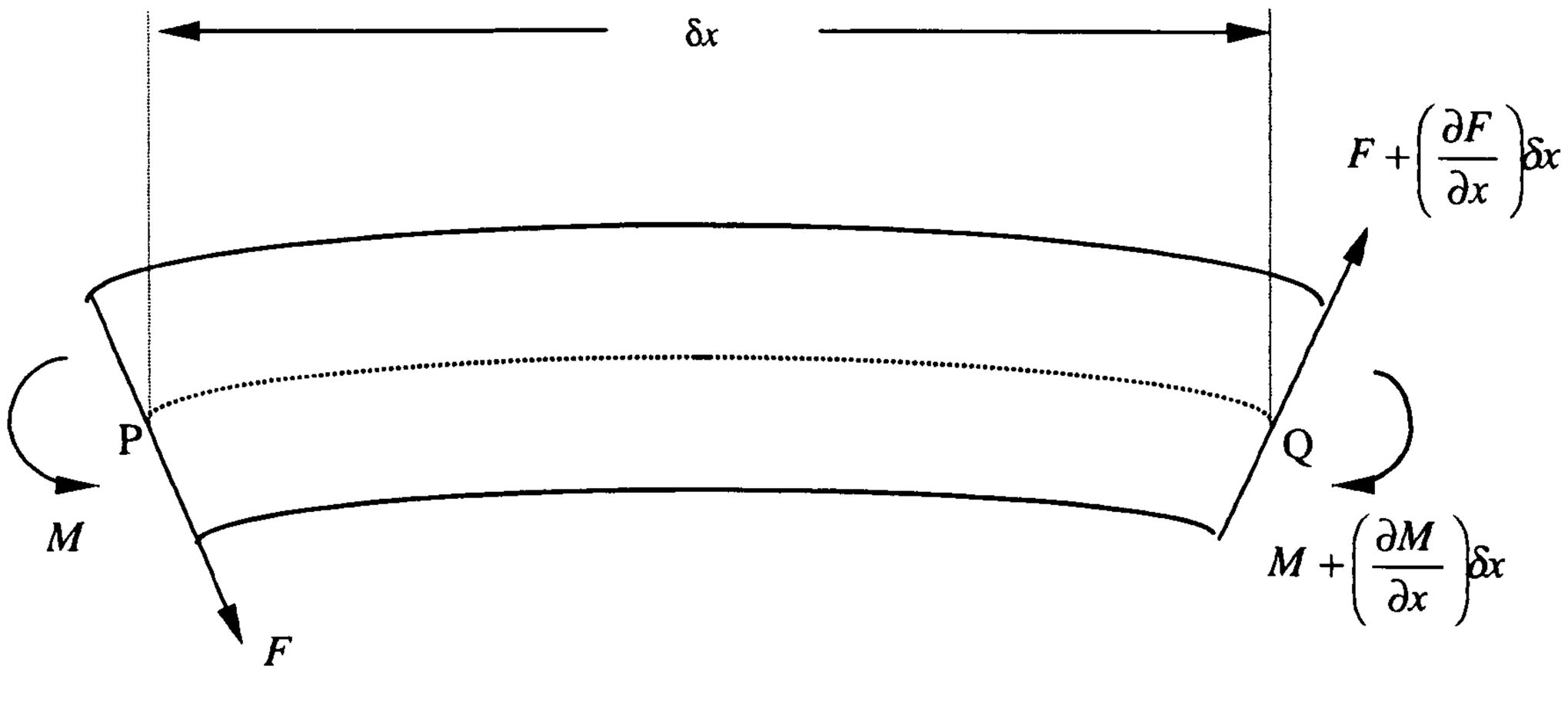

Figure 3.4: *Element of a bar in flexural vibration*

Shearing forces acting parallel to the z-axis will balance the bending moment. The shearing force on the section through P is taken to be F, and that through Q is given by $(F + \partial F / \partial x)\delta x$. Therefore, from Newton's second law, the equation of motion of the element in the z-direction is,

$$\rho A\left(\frac{\partial^2 u_z}{\partial t^2}\right)\delta x = \left(\frac{\partial F}{\partial x}\right)\delta x$$

giving,

$$\rho A\left(\frac{\partial^2 u_z}{\partial t^2}\right) = \left(\frac{\partial F}{\partial x}\right) \qquad \textbf{3.21}$$

If F is expressed in terms of u_z and the elastic constants of the material, then Equation 3.21 can be solved. Taking moments round an axis in the y-direction, through the centre of the element, Equation 3.22 is obtained.

$$\left(\frac{\partial M}{\partial x}\right)\delta x + \left(2F + \left(\frac{\partial F}{\partial x}\right)\delta x\right)\frac{\delta x}{2} = 0 \qquad \textbf{3.22}$$

In the limit as $\delta x \rightarrow 0$ this becomes:

$$F = -\frac{\partial M}{\partial x} \qquad \textbf{3.23}$$

It is necessary to obtain a relation for M in terms of u_z. Therefore, the element of the bar is considered to comprise a number of parallel filaments, some stretched and

some compressed. For a radius of curvature of the neutral surface R, and a second moment of the cross-section about a diameter in this surface I,

$$M = (EI / R). \qquad \textbf{3.24}$$

$1/R$ is given by $\partial^2 u_z / \partial x^2$ for small deformations, and so Equation 3.23 becomes:

$$F = -EI\left(\frac{\partial^3 u_z}{\partial x^3}\right) \qquad \textbf{3.25}$$

Now on the substitution of Equation 3.25 into Equation 3.21,

$$\rho A\left(\frac{\partial^2 u_z}{\partial t^2}\right) = -EI\left(\frac{\partial^4 u_z}{\partial x^4}\right) \qquad \textbf{3.26}$$

which can be written as,

$$\left(\frac{\partial^2 u_z}{\partial t^2}\right) = -C_0{}^2 K^2\left(\frac{\partial^4 u_z}{\partial x^4}\right) \qquad \textbf{3.27}$$

Here, K is the radius of gyration of the cross section about an axis in the neutral surface perpendicular to the axis of the bar. For cylindrical bars of radius a, $K = a/2$ which is related to the moment of inertial by the relationship $I = K^2 A$.

Equation 3.27 shows the wave equation for flexural vibrations. Since it is not of the familiar one 1D wave equation form, the substitution of a solution of the form $u_z = F(x - Ct)$, or $u_z = F(x + Ct)$ is not sufficient. It can, therefore, be deduced that flexural motion of arbitrary shape propagating along the rod will be frequency dependent. Consider now a flexural wave that is sinusoidal in nature propagating along the bar.

$$u_z = D\cos(pt - fx) \qquad \textbf{3.28}$$

Where D is the amplitude, $f = 2\pi/\Lambda$ (Λ being wavelength), and $p = 2\pi C/\Lambda$. Substitution of Equation 3.28 into Equation 3.27 and performance of the appropriate differentiation yields:

$$p^2 = C_o{}^2 K^2 f^4$$

Thus,

$$C = \frac{2\pi C_o K}{\Lambda} \qquad \textbf{3.29}$$

Equation 3.29 is only valid for waves with large Λ compared with a, the radius of the bar. The simplified treatment breaks down when the wavelength and radius are of the same order for two reasons: (1) for short wavelengths, rotary motion of the sections of the bar must be considered and so the assumption that the motion is

purely translation in the z-direction is not valid; (2) it is invalid to assume that longitudinal sections of elements of the bar remain uniform in shape during motion.

Equation 3.29 defines a linear relationship between C and ($1/\Lambda$), which is only valid at low frequencies where Λ is large compared with a. Rayleigh, who took rotary inertia into account obtained an improved approximation and Redwood [80] shows this to yield the following relationship.

$$C = \frac{C_0}{\sqrt{1 + \frac{\Lambda^2}{4\pi^2 K^2}}} \qquad \textbf{3.30}$$

Timoshenko further modified the elementary theory by adding a correction for shear deformations resulting in a dispersion relation that was very accurate over the entire range [1]. Equation 3.31 shows this dispersion relationship.

$$C^2 - (\gamma K)^2 \left(C^2 - C_0{}^2\right) \frac{C^2}{R' C_s{}^2} - 1 = 0 \qquad \textbf{3.31}$$

Here $\gamma = \omega / C$, which is described as the propagation constant, and R' is a constant that depends on the shape of the cross section (10/9 for a circle).

3.4 Exact Solution of Elastic Wave Propagation in Solid Cylinders

To obtain a solution for elastic wave propagation in solid cylinders it is convenient to define the relevant relations in cylindrical co-ordinates r, θ, and, z that is radial, angular, and axial components respectively, see Figure 3.5.

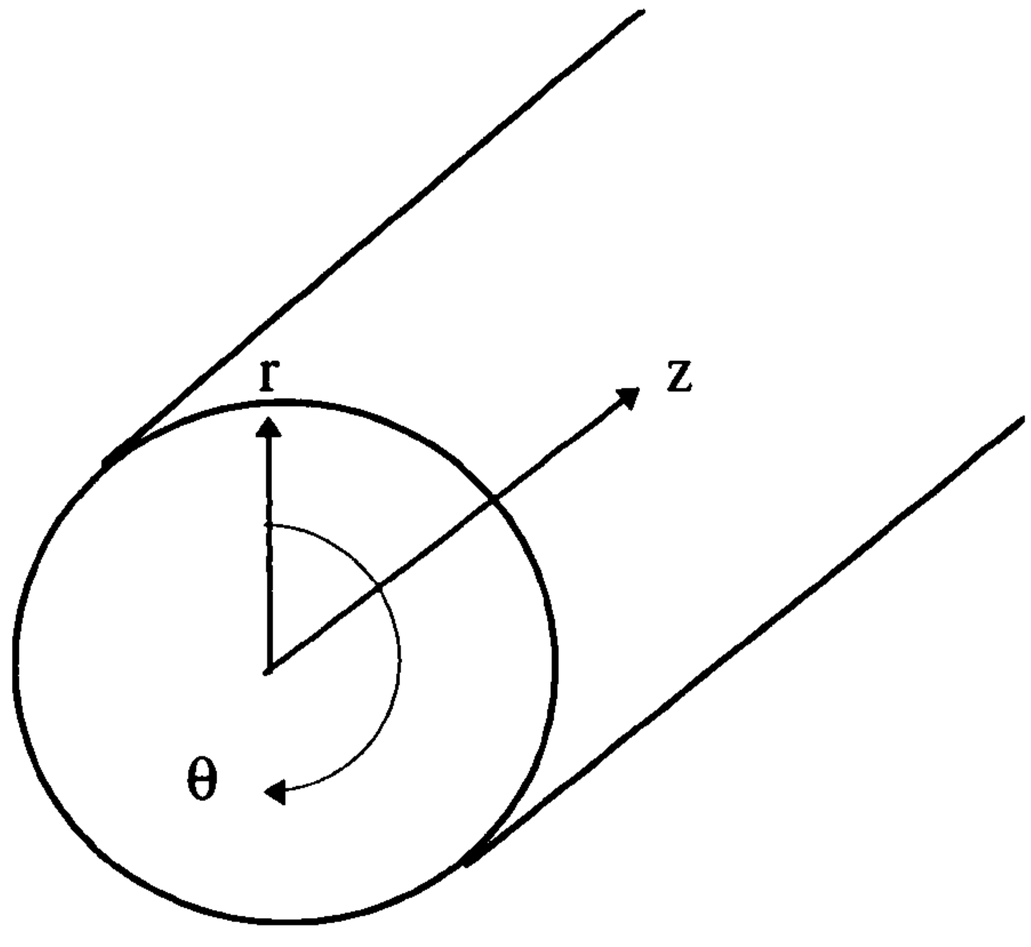

Figure 3.5: *Cylindrical Co-ordinate System*

For such a co-ordinate system Love[81] defines the relationship between strain and particle displacements.

$$\varepsilon_{rr} = \frac{\partial u_r}{\partial r} \qquad \varepsilon_{r\theta} = \frac{\partial u_\theta}{\partial r} - \frac{u_\theta}{r} + \frac{1}{r}\left(\frac{\partial u_r}{\partial \theta}\right)$$

$$\varepsilon_{zz} = \frac{\partial u_z}{\partial z} \qquad \varepsilon_{\theta z} = \frac{1}{r}\left(\frac{\partial u_z}{\partial \theta}\right) + \frac{\partial u_\theta}{\partial z} \qquad \textbf{3.32}$$

$$\varepsilon_{\theta\theta} = \frac{u_r}{r} + \frac{1}{r}\left(\frac{\partial u_\theta}{\partial \theta}\right) \qquad \varepsilon_{zr} = \frac{\partial u_r}{\partial z} + \frac{\partial u_z}{\partial r}$$

In Section 3.3.2 the relationship between stress and particle displacement for an infinite isotropic solid was derived (Equation 3.5). It would be beneficial to relate these quantities in cylindrical co-ordinates, therefore substitution of Equation 3.32 into Equation 3.5 using cylindrical co-ordinates (r, θ, z) yields that stress, and particle displacement are related thus:

$$\sigma_{rr} = \lambda\Delta + 2\mu\frac{\partial u_r}{\partial r} \qquad \sigma_{r\theta} = \frac{\mu}{r}\left(\frac{\partial u_r}{\partial \theta} - u_\theta\right) + \mu\left(\frac{\partial u_\theta}{\partial r}\right)$$

$$\sigma_{\theta\theta} = \lambda\Delta + \frac{2\mu}{r}\left(\frac{\partial u_\theta}{\partial \theta} + u_r\right) \qquad \sigma_{\theta z} = \mu\left(\frac{1}{r}\left(\frac{\partial u_z}{\partial \theta}\right) + \frac{\partial u_\theta}{\partial z}\right) \qquad \textbf{3.33}$$

$$\sigma_{zz} = \lambda\Delta + 2\mu\frac{\partial u_z}{\partial z} \qquad \sigma_{zr} = \mu\left(\frac{\partial u_r}{\partial z} + \frac{\partial u_z}{\partial r}\right)$$

Dilation in cylindrical co-ordinates is defined as $\Delta = \varepsilon_{rr} + \varepsilon_{\theta\theta} + \varepsilon_{zz}$, therefore, from Equation 3.32.

$$\Delta = \frac{\partial u_r}{\partial r} + \frac{1}{r}\left(u_r + \frac{\partial u_\theta}{\partial \theta}\right) + \frac{\partial u_z}{\partial z} \qquad \textbf{3.34}$$

The pertinent relationships in Equation 3.33 are σ_{rr}, $\sigma_{\theta\theta}$, and σ_{zz}, which, for an isotropic cylinder, must equate to zero at the cylinder's surface to satisfy the boundary condition that the surface is traction free, therefore:

$$\sigma_{rr} = \sigma_{\theta\theta} = \sigma_{zz} = 0 \quad |_{r=a} \qquad \textbf{3.35}$$

where a = radius of the cylinder.

If displacement is defined as a finite, uniform and continuous vector field which vanishes at infinity, then the Helmholtz theorem [83] allows it to be expressed as the sum of the gradient of a scalar ϕ and the curl of a zero-divergence vector ψ. Therefore, in vector notation displacement may be written as:

$$\underline{u} = \underline{\nabla}\phi + \underline{\nabla} \mathrm{x} \underline{\psi} \qquad \textbf{3.36}$$

where, $\underline{\nabla}.\underline{\psi} = 0$

Here ϕ and ψ are termed the scalar and vector potential functions respectively. Cylindrical displacements are obtained from Equation 3.36 using the relevant vector identities in cylindrical co-ordinates (see Appendix A) to provide the following components:

$$u_r = \frac{\partial \phi}{\partial r} + \frac{1}{r}\left(\frac{\partial \psi_z}{\partial \theta}\right) - \frac{\partial \psi_\theta}{\partial z}$$

$$u_\theta = \frac{1}{r}\left(\frac{\partial \phi}{\partial \theta}\right) + \frac{\partial \psi_r}{\partial z} - \frac{\partial \psi_z}{\partial r} \qquad \textbf{3.37}$$

$$u_z = \frac{\partial \phi}{\partial z} + \left(\frac{1}{r}\right)\frac{\partial (\psi_\theta r)}{\partial r} - \frac{1}{r}\left(\frac{\partial \psi_r}{\partial \theta}\right)$$

To solve for wave motions propagating in the positive axial direction of a cylinder an appropriate set of solutions of the form shown in Equation 3.38 can be assumed for the vector and scalar potential functions [85]:

$$\phi = f(hr)\cos(n\theta)e^{i(\gamma z-\omega t)}$$

$$\psi_z = g_z(kr)\sin(n\theta)e^{i(\gamma z-\omega t)}$$

$$\psi_r = g_r(kr)\sin(n\theta)e^{i(\gamma z-\omega t)} \qquad \textbf{3.38}$$

$$\psi_\theta = g_\theta(kr)\cos(n\theta)e^{i(\gamma z-\omega t)}$$

Here γ is the propagation constant ($\gamma = 2\pi/\Lambda$, where Λ denotes wavelength), ω is angular frequency, n is an integer in the range 0,1,2,...,∞, and the quantities h and k are related to γ and ω through the following identities.

$$h^2 = \frac{\omega^2}{C_l^{\,2}} - \gamma^2 \qquad k^2 = \frac{\omega^2}{C_s^{\,2}} - \gamma^2 \qquad \textbf{3.39}$$

C_s and C_l are the shear and longitudinal wave velocities respectively and are defined in Equation 3.40.

$$C_s^{\,2} = \frac{\mu}{\rho} \qquad C_l^{\,2} = \frac{\lambda + 2\mu}{\rho} \qquad \textbf{3.40}$$

The differential equation determining *f(hr)* of Equation 3.38 is defined as:

$$\frac{\partial^2 f(hr)}{\partial r^2} + \frac{1}{r}\frac{\partial f(hr)}{\partial r} + \left(h^2 - \frac{n^2}{r^2}\right) f(hr) = 0 \qquad \textbf{3.41}$$

Here, the appropriate solution to Equation 3.41 is:

$$f(hr) = AJ_n(hr) \tag{3.42}$$

Similarly the differential equation and solution for $g_z(kr)$ are:

$$\frac{\partial^2 g_z(kr)}{\partial r^2} + \frac{1}{r}\frac{\partial g_z(kr)}{\partial r} + \left(k^2 - \frac{n^2}{r^2}\right) g_z(hr) = 0 \tag{3.43}$$

$$g_z(kr) = C_3 J_n(kr) \tag{3.44}$$

The two remaining differentials $g_r(kr)$, and $g_\theta(kr)$ are coupled and of the form:

$$\left[\frac{\partial^2}{\partial r^2} + \frac{1}{r}\frac{\partial}{\partial r} + \left(k^2 - \frac{(n+1)^2}{r^2}\right)\right](g_r(kr) - g_\theta(kr)) = 0 \tag{3.45}$$

$$\left[\frac{\partial^2}{\partial r^2} + \frac{1}{r}\frac{\partial}{\partial r} + \left(k^2 - \frac{(n-1)^2}{r^2}\right)\right](g_r(kr) + g_\theta(kr)) = 0 \tag{3.46}$$

The solutions to Equations 3.45 and 3.46 are, therefore, as follows:

$$g_r(kr) - g_\theta(kr) = 2C_2 J_{n+1}(kr) \tag{3.47}$$

$$g_r(kr) + g_\theta(kr) = 2C_1 J_{n-1}(kr) \tag{3.48}$$

hence,

$$g_r(kr) = C_1 J_{n-1}(kr) + C_2 J_{n+1}(kr) \tag{3.49}$$

$$g_\theta(kr) = C_1 J_{n-1}(kr) - C_2 J_{n+1}(kr) \tag{3.50}$$

The potential function solution (Equation 3.38) therefore provides 4 arbitrary constants A, C_1, C_2, C_3. However, only 3 constants are required to specify an arbitrary displacement vector [53], and therefore, any of the C_i constants can be equated to zero without loss of generality. Therefore setting $C_1 = 0$ provides the following equality from Equations 3.49, and 3.50.

$$g_r(kr) = -g_\theta(kr) \qquad \textbf{3.51}$$

Therefore, in summary:

$$\begin{aligned} f(hr) &= AJ_n(hr) \\ g_z(kr) &= C_3 J_n(kr) \\ g_r(kr) &= C_2 J_{n+1}(kr) \\ g_\theta(kr) &= -g_r(kr) \end{aligned} \qquad \textbf{3.52}$$

It is useful to note (for the purpose of reduction in subsequent calculations) that substitution of Equation 3.51 into Equation 3.45 yields the following relationship:

$$\left[\frac{\partial^2}{\partial r^2} + \frac{1}{r}\frac{\partial}{\partial r} + \left(k^2 - \frac{(n+1)^2}{r^2}\right)\right](g_r(kr)) = 0 \qquad \textbf{3.53}$$

Now, if Equation 3.38 is substituted into Equation 3.37 then the displacement can be defined in the following format.

$$\begin{aligned} u_r &= U(r)\cos(n\theta)e^{i(\gamma z - \omega t)} \\ u_\theta &= V(r)\sin(n\theta)e^{i(\gamma z - \omega t)} \\ u_z &= W(r)\cos(n\theta)e^{i(\gamma z - \omega t)} \end{aligned} \qquad \textbf{3.54}$$

where,

$$U(r) = f'(hr) + \frac{n}{r} g_z(kr) + i\gamma g_r(kr)$$

$$V(r) = -\left(\frac{n}{r}\right) f(hr) + i\gamma g_r(kr) - g_z'(kr) \qquad \textbf{3.55}$$

$$W(r) = i\gamma f(hr) - g_r'(kr) - \left(\frac{n+1}{r}\right) g_r(kr)$$

In order to satisfy the boundary conditions at the traction-free surface, Equation 3.35 must hold true. Therefore, substitution of Equation 3.54 into the relevant relations of Equation 3.33 provides the following. (Note that Equations 3.43, 3.53 and the relation $\Delta = \nabla^2\phi = -(h^2 + \gamma^2) f(hr) cos(n\theta) e^{i(\gamma z - \omega t)}$ are utilised in the calculation for reduction, where ∇^2 is defined for cylindrical co-ordinates in Appendix A)

$$\sigma_{rr} = \left\{ \begin{array}{l} -\lambda(h^2 + \gamma^2) f(hr) \\ +2\mu\left[f''(hr) + \frac{n}{r}\left(g_z'(kr) - \frac{g_z(kr)}{r} \right) + i\gamma g_r'(kr) \right] \end{array} \right\} cos(n\theta) e^{i(\gamma z - \omega t)}$$

$$\sigma_{r\theta} = \mu \left\{ \begin{array}{l} -\frac{2n}{r}\left(f'(hr) - \frac{f(hr)}{r} \right) - \left(2g_z''(kr) + k^2 g_z(kr) \right) \\ -i\gamma\left(\frac{1+n}{r} g_r(kr) - g_r'(kr) \right) \end{array} \right\} sin(n\theta) e^{i(\gamma z - \omega t)} \qquad \textbf{3.56}$$

$$\sigma_{rz} = \mu \left\{ \begin{array}{l} 2i\gamma f'(hr) + \frac{ni\gamma}{r} g_z(kr) - \frac{n}{r} g_r'(kr) \\ -\left[\frac{n^2 + n}{r^2} + k^2 - \gamma^2 \right] g_r(kr) \end{array} \right\} cos(n\theta) e^{i(\gamma z - \omega t)}$$

Therefore, on substitution of the values of $f(hr)$, $g_r(kr)$, *and* $g_z(kr)$ from Equation 3.52 into Equation 3.56, and application of the boundary condition (Equation 3.35), the following set of simultaneous equations are obtained.

$$\left\{\begin{array}{c} A\left[\left(\frac{\lambda(h^2+\gamma^2)a^2}{2\mu}\right)J_n(ha)-a^2J_n''(ha)\right] \\ +C_3\left[nJ_n(ka)-naJ_n'(kr)\right]-C_2\left[i\gamma a^2J_{n+1}'(ka)\right] \end{array}\right\} = 0$$

$$\left\{A\left[2n(J_n(ha)-aJ_n'(ha))\right]-C_3\left[2a^2J_n''(ka)+(ka)^2J_n(ka)\right]\right\} = 0 \qquad \textbf{3.57}$$
$$-C_2\left[i\gamma a((1+n)J_{n+1}(ka)-aJ_{n+1}'(ka))\right]$$

$$\left\{\begin{array}{ccc} A[2ia\gamma J_n'(ha)] & + & C_3[ni\gamma J_n(ka)] \\ -C_2\left[nJ_{n+1}'(ka)+\frac{1}{a}\left(n^2+n+a^2\left(k^2+\gamma^2\right)\right)J_{n+1}(ka)\right] & & \end{array}\right\} = 0$$

For subsequent reductions it is convenient to express $J_n''(ha)$ and $J_n''(ka)$ in terms of J_n' and J_n, therefore, the following relationship (Equation 3.58) was deduced from first principles (see Appendix B, Part I for derivation).

$$r^2J_n''(hr)=\left[n^2-(hr)^2\right]J_n(hr)-rJ_n'(hr) \qquad \textbf{3.58}$$

Equation 3.57 can therefore be expressed as follows.

$$\begin{Bmatrix} A\left[\left(\frac{\lambda(h^2+\gamma^2)a^2}{2\mu}+(ha)^2-n^2\right)J_n(ha)+aJ_n'(ha)\right] \\ +C_3[nJ_n(ka)-naJ_n'(kr)]-C_2[i\gamma a^2 J_{n+1}'(ka)] \end{Bmatrix} = 0$$

$$\begin{Bmatrix} A[2n(J_n(ha)-aJ_n'(ha))]+C_3\left[\left((ka)^2-2n^2\right)J_n(ka)+2aJ_n'(ka)\right] \\ -C_2[i\gamma a((1+n)J_{n+1}(ka)-aJ_{n+1}'(ka))] \end{Bmatrix} = 0 \quad \textbf{3.59}$$

$$\begin{Bmatrix} A[2ia\gamma J_n'(ha)] + C_3[ni\gamma J_n(ka)] \\ -C_2\left[nJ_{n+1}'(ka)+\frac{1}{a}\left(n^2+n+a^2\left(k^2+\gamma^2\right)\right)J_{n+1}(ka)\right] \end{Bmatrix} = 0$$

The coefficients of the 3 quantities A, C_2, and C_3 of Equation 3.59 form a determinant, which when set equal to zero results in the general frequency equation describing the modes of elastic wave propagation in a cylinder [53]. Hudson [86] reduces this frequency equation into the following format.

$$\begin{vmatrix} n^2-1-(ka)^2\left[\frac{b-1}{2b-1}\right] & n^2-1-(ka)^2 & 2(n^2-1)\varphi_n(ka)-(ka)^2 \\ -1 & b\varphi_n(ka)-1 & n^2-2\varphi_n(ka)-(ka)^2 \\ \varphi_n(ha) & (1-b)\varphi_n(ka) & n^2 \end{vmatrix} = 0 \quad \textbf{3.60}$$

Where,

$$b=\frac{1}{2}\left(\frac{\omega^2}{\gamma^2 C_s^{\,2}}\right) \qquad \text{and,} \qquad \varphi_n(ka)=(ka)\frac{J_n'(ka)}{J_n(ka)}$$

Equation 3.60 relates three variables, any one of which may be determined from the other two. In dimensionless form, these three variables are Poisson's ratio (ν), dimensionless angular frequency ($\Omega = \omega a / C_s$), and dimensionless propagation constant (γa).

3.5. Modes of Propagation

The following discussion involves the consideration of a number of different modes of propagation, and therefore a standard shorthand notation is adopted [51]. Longitudinal and torsional modes have n = 0 and subsequently L(0,q) is used to denote longitudinal modes and T(0,q) torsional modes, where q is the branch number of the given family. F(n,q) will be used to denote flexural modes (where $n \geq 1$); and again q represents the branch number of the given family. For example L(0,1) defines the lowest longitudinal mode, and F(1,1) defines the lowest flexural mode.

3.5.1. Dispersion Characteristics

In the context of elastic wave propagation, the phenomenon of dispersion refers to the distortion of a sound pulse as it propagates through a medium. Consider a wideband pulse propagating in a dispersive medium. The various frequency components of the signal will propagate at different velocities and be subject to various degrees of attenuation. This results in a distortion of the original pulse shape.

The velocity at which a pulse as a whole propagates is termed the *group velocity*, C_g, while points of equal phase propagate at the *phase velocity*, $C = \omega / \gamma$. A system is said to be dispersive when these two velocities are unequal. *Normal* dispersion refers to a system where the phase velocity is greater than the group velocity while, the contrary is termed *anomalous* dispersion. The group velocity is related to phase velocity by the following relationship [79].

$$C_g = C - \Lambda \frac{\partial C}{\partial \Lambda} \qquad \textbf{3.61}$$

3.5.2. Longitudinal Modes

The condition for purely longitudinal modes is that $n = 0$, and $u_\theta = 0$. Application of this condition results in a reduced frequency equation describing longitudinal modes only. The solution to this problem was first solved by Pochhammer [87] and independently by Chree [88]. The relevant displacement equalities are obtained from Equation 3.37 with $u_\theta = 0$.

$$u_r = \frac{\partial \phi}{\partial r} - \frac{\partial \psi_\theta}{\partial z}$$

$$u_z = \frac{\partial \phi}{\partial z} + \left(\frac{1}{r}\right)\frac{\partial (\psi_\theta r)}{\partial r} \qquad \textbf{3.62}$$

Equation 3.38 provides the following where $n = 0$.

$$\phi = AJ_0(hr)e^{i(\gamma z - \omega t)} \qquad \textbf{3.63}$$

$$\psi_\theta = C_2 J_1(kr)e^{i(\gamma z - \omega t)}$$

Therefore, substitution of Equation 3.63 into Equation 3.62, and utilisation of the relations $J_0'(hr) = -hJ_1(hr)$ (Equation B11, derived in Appendix B, Part II), and $J_1'(kr) = kJ_0(kr) - r^{-1}J_1(kr)$ (Equation B13, derived in Appendix B, Part III) yields the following.

$$u_r = \left[-AhJ_1(hr) - Ci\gamma J_1(kr)\right]e^{i(\gamma z - \omega t)}$$

$$u_z = \left[Ai\gamma J_0(hr) + CkJ_0(kr)\right]e^{i(\gamma z - \omega t)} \qquad \textbf{3.64}$$

The boundary condition states that at the cylindrical surface ($r = a$) the stresses must be zero. Therefore, substitution of Equation 3.64 into the values of σ_{rr} and σ_{rz} of Equation 3.33 and application of the boundary condition provides the following two simultaneous equations (note that the identity, $\frac{\lambda}{2\mu}(h^2+\gamma^2)+h^2=\frac{1}{2}(k^2-\gamma^2)$ can be deduced from Equations 3.39 and 3.40, and is utilised in this calculation).

$$A\left[-\frac{1}{2}(h^2-\gamma^2)J_0(ha)+\frac{h}{a}J_1(ha)\right] + C_2\left[-i\gamma kJ_0(ka)+\frac{i\gamma}{a}J_1(ka)\right] = 0$$

$$A[2i\gamma hJ_1(ha)] - C_2\left[(k^2-\gamma^2)J_1(ka)\right] = 0 \qquad \textbf{3.65}$$

The coefficients of the 2 quantities, A and C_2 form a determinant, which when set equal to zero yields the Pochhammer frequency equation describing longitudinal modes of elastic wave propagation in a cylinder.

$$\frac{2h}{a}(k^2+\gamma^2)J_1(ha)J_1(ka) - (k^2-\gamma^2)J_0(ha)J_1(ka) - 4\gamma^2khJ_1(ha)J_0(ka) = 0 \qquad \textbf{3.66}$$

Equation 3.66 was coded and solved using the maths package MATLAB [90] to yield dispersion curves in terms of phase velocity (C) versus dimensionless frequency ($\Omega = \omega a/C_s$). Curves of group velocity, C_g, versus Ω were also calculated from the phase velocity curves using Equation 3.61. Examples of the first four longitudinal dispersion curves for phase and group velocities are shown in Figure 3.6 for $\nu = 0.34$ (Copper). There are slight distortions in the group velocity curves, because of the

error introduced by differentiating the phase velocity data, which is a set of discrete points.

The lowest branch of the longitudinal family extends to zero frequency (see Figure 3.6). This is the familiar longitudinal mode whose propagation velocity in the low-frequency limit is governed by Young's modulus. As the frequency is increased, the phase velocity drops to a minimum value that is slightly below the Rayleigh velocity, then approaches the Rayleigh velocity asymptotically from below [1]. The displacement distribution changes with increased frequency, and at very high frequencies the disturbance is concentrated near the surface, like a Rayleigh wave [91].

The dispersion curves for longitudinal modes are dependent not only on Young's modulus, but also on Poisson's ratio. Bancroft [91], and Hudson [86] both give data for the fundamental longitudinal mode L(0,1) for various values of ν, and show that it has a significant effect. The lowest longitudinal mode which is often called "Young's modulus mode" extends to zero frequency. All other longitudinal modes have a finite cut-off point, that is a frequency at which the motion is independent of z, and so only at frequencies above this point will there be propagation of that mode in the z-direction. The form of motion at cut-off can be split into two types, in the first case the z-independent motion is axial shear of concentric cylinders, and in the second case it is purely radial [1]. Note that all cut-off frequency equations and values shown in this Chapter were presented by Thurston [1], however, a selection of them has been verified using MATLAB.

The cut-off values for the axial shear modes are given by Equation 3.67.

$$-J_1(\Omega)=0 \qquad \textbf{3.67}$$

The first three values of Ω are therefore 3.832, 7.016, and 10.173.

For the modes whose motion is purely radial at cut-off, the cut-off frequencies are obtained from Equation 3.68 [1].

$$\Phi\frac{J_0(\Phi)}{J_1(\Phi)}=2\frac{{C_s}^2}{{C_l}^2}=\frac{1-2\nu}{1-\nu} \qquad \textbf{3.68}$$

Where

$$\Phi=\frac{\omega a}{C_l}=\Omega\frac{C_s}{C_l}$$

These cut-offs are, therefore, dependent on Poisson's ratio. The first two cut-offs have been calculated for $\nu=0.34$ using MATLAB, Ω = 4.413, 7.773. From Equations 3.67 and 3.68 it can be seen that the first 3 cut-off values for $\nu=0.34$, are 3.832, 4.413, and 7.016. These correspond to the cut-offs of modes L(0,2), L(0,3) and L(0,4) of Figure 3.6.

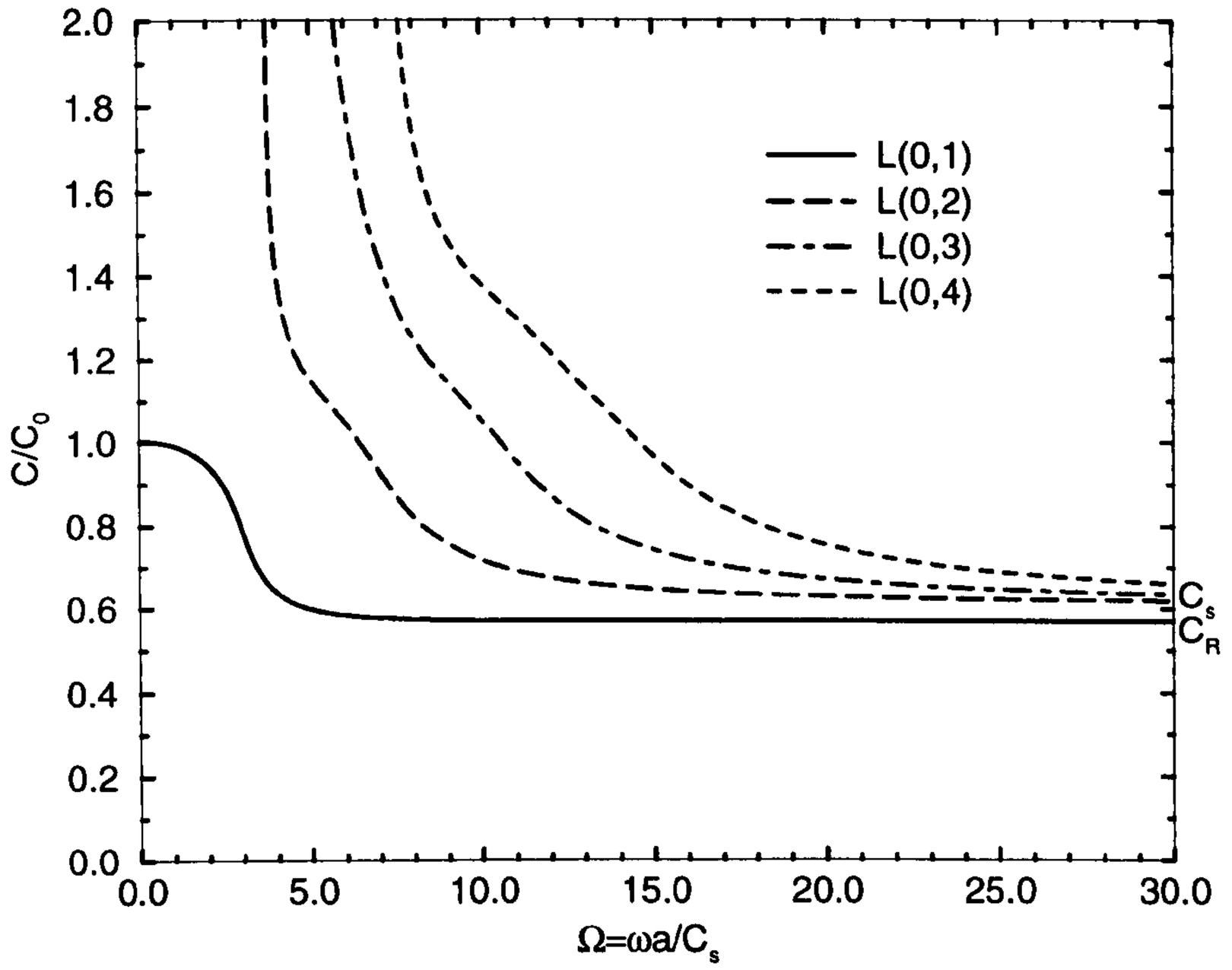

Figure 3.6(a): *Phase velocity dispersion curves of the first four longitudinal modes*

($\nu = 0.34$)

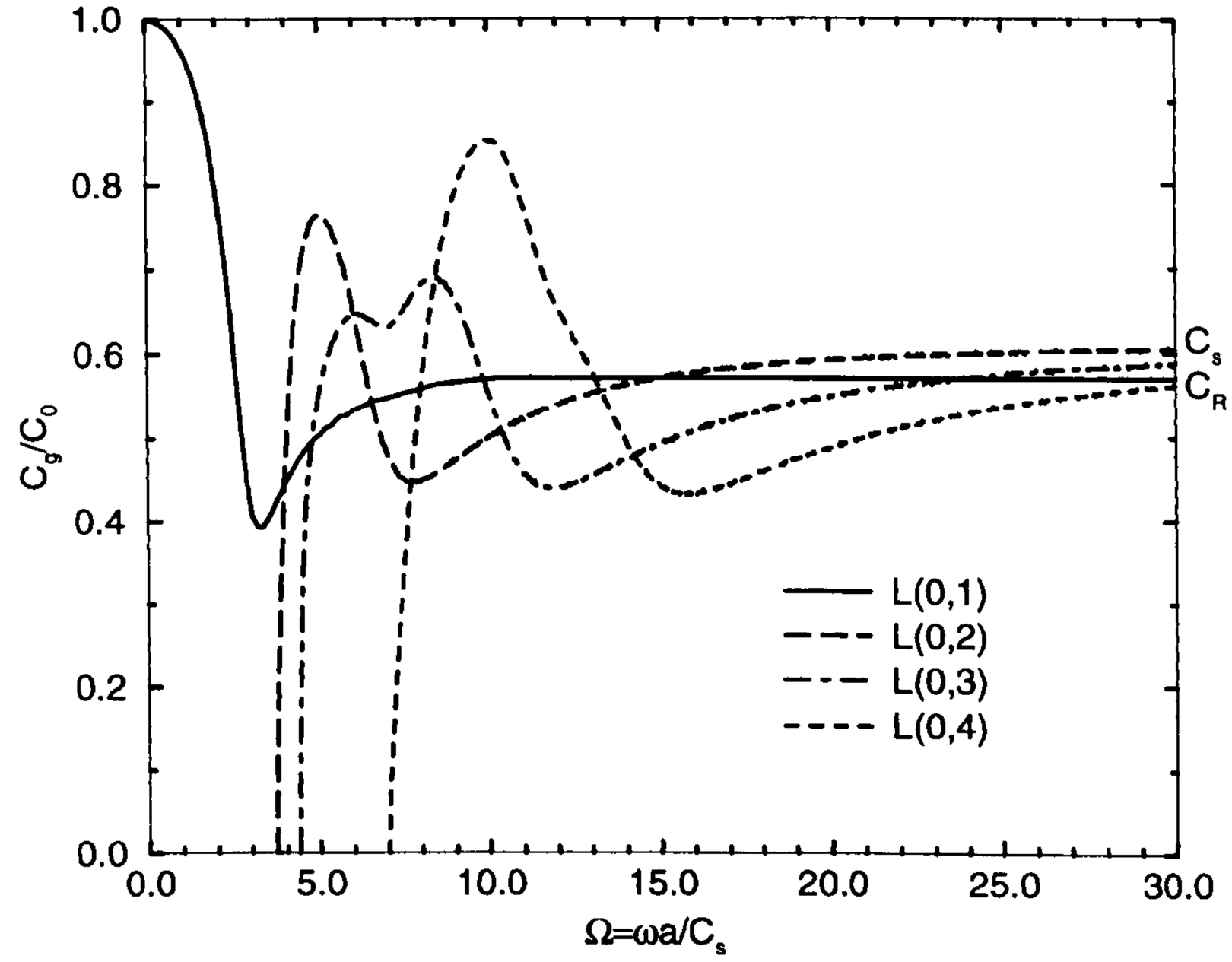

Figure 3.6(b): *Group velocity dispersion curves of the first four longitudinal modes*

($\nu = 0.34$)

3.5.3. Torsional Modes

The equations of motion for time-harmonic waves propagating in the axial direction along a cylinder may be written as [92]

$$\nabla^2 u_r - \frac{u_r}{r^2} - \frac{2}{r^2}\left(\frac{\partial u_\theta}{\partial \theta}\right) + \frac{1}{1-2\nu}\frac{\partial \Delta}{\partial r} = \frac{1}{C_s^{\,2}}\frac{\partial^2 u_r}{\partial t^2}$$

$$\nabla^2 u_\theta - \frac{u_\theta}{r^2} + \frac{2}{r^2}\left(\frac{\partial u_r}{\partial \theta}\right) + \frac{1}{1-2\nu}\frac{1}{r}\frac{\partial \Delta}{\partial \theta} = \frac{1}{C_s^{\,2}}\frac{\partial^2 u_\theta}{\partial t^2} \qquad \textbf{3.69}$$

$$\nabla^2 u_z + \frac{1}{1-2\nu}\frac{\partial \Delta}{\partial z} = \frac{1}{C_s^{\,2}}\frac{\partial^2 u_z}{\partial t^2}$$

The condition for torsional modes is that $n = 0$, $u_z = u_r = 0$, and that u_θ is finite and independent of θ. Therefore, only one equation of motion remains.

$$\frac{\partial^2 u_\theta}{\partial r^2} + \frac{1}{r}\left(\frac{\partial u_\theta}{\partial r}\right) - \frac{u_\theta}{r^2} + \frac{\partial^2 u_\theta}{\partial z^2} = \frac{1}{C_s^{\,2}}\frac{\partial^2 u_\theta}{\partial t^2} \qquad \textbf{3.70}$$

An appropriate solution to this is [53],

$$u_\theta = BJ_1(ka)e^{i(\gamma z - \omega t)} \qquad \textbf{3.71}$$

The only non-trivial boundary condition (Equation 3.35) is that, $\sigma_{r\theta} = 0$ at $r = a$.

Therefore, from Equation 3.33,

$$\frac{\partial u_\theta}{\partial r} - \frac{1}{a} u_\theta = 0 \qquad \textbf{3.72}$$

Substitution of Equation 3.71 into Equation 3.72, and application of the identity given by Equation B13 (Appendix B, Part III) delivers the following frequency relationship,

$$(ka) J_0(ka) - 2 J_1(ka) = 0 \qquad \textbf{3.72}$$

Note that $ka = 0$, is a solution to Equation 3.72. Therefore, if Equation 3.39 is recalled $(k^2 = (\omega^2 / C_s^{\,2}) - (\omega^2 / C^2))$, it can be seen that $ka = 0$ when $C = C_s$. Therefore, the fundamental torsional mode T(0,1) propagates with a phase and group velocity of C_s regardless of frequency. The non-dispersive nature of this mode is extremely useful and has been exploited for delay lines where undistorted pulse propagation is required [80]. Equation 3.72 also permits the deduction that all torsional modes are dependent only on the shear modulus μ.

Equation 3.72 was solved using MATLAB and phase velocity dispersion curves for the first three torsional modes are presented in Figure 3.7(a). Group velocity information is calculated from these curves using Equation 3.61 and is shown in Figure 3.7(b). The fundamental T(0,1) mode extends to zero frequency while all higher order modes have finite cut-off points where C goes to infinity and C_g to zero.

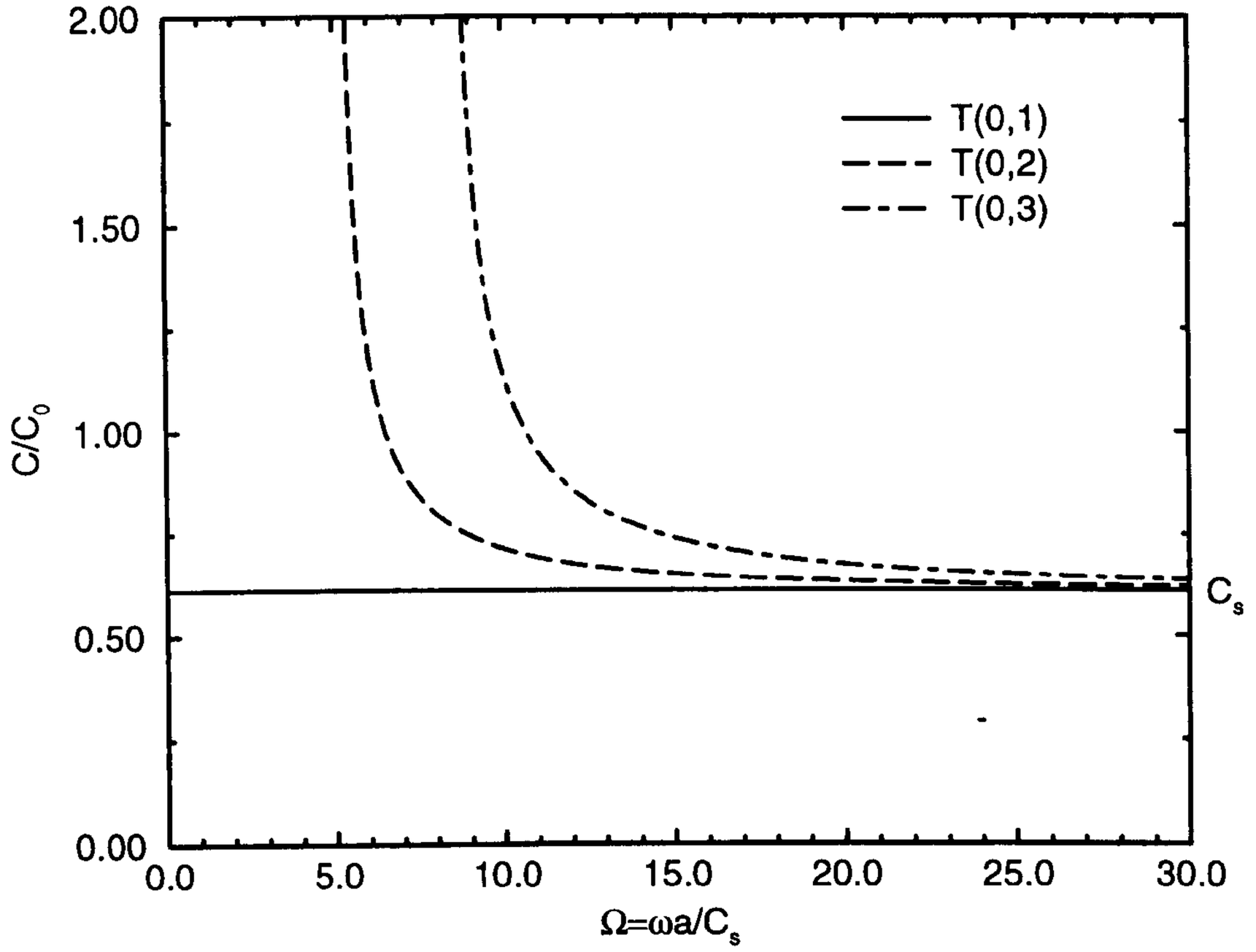

Figure 3.7(a): *Phase velocity dispersion curves for the first three torsional modes*

($\nu = 0.34$)

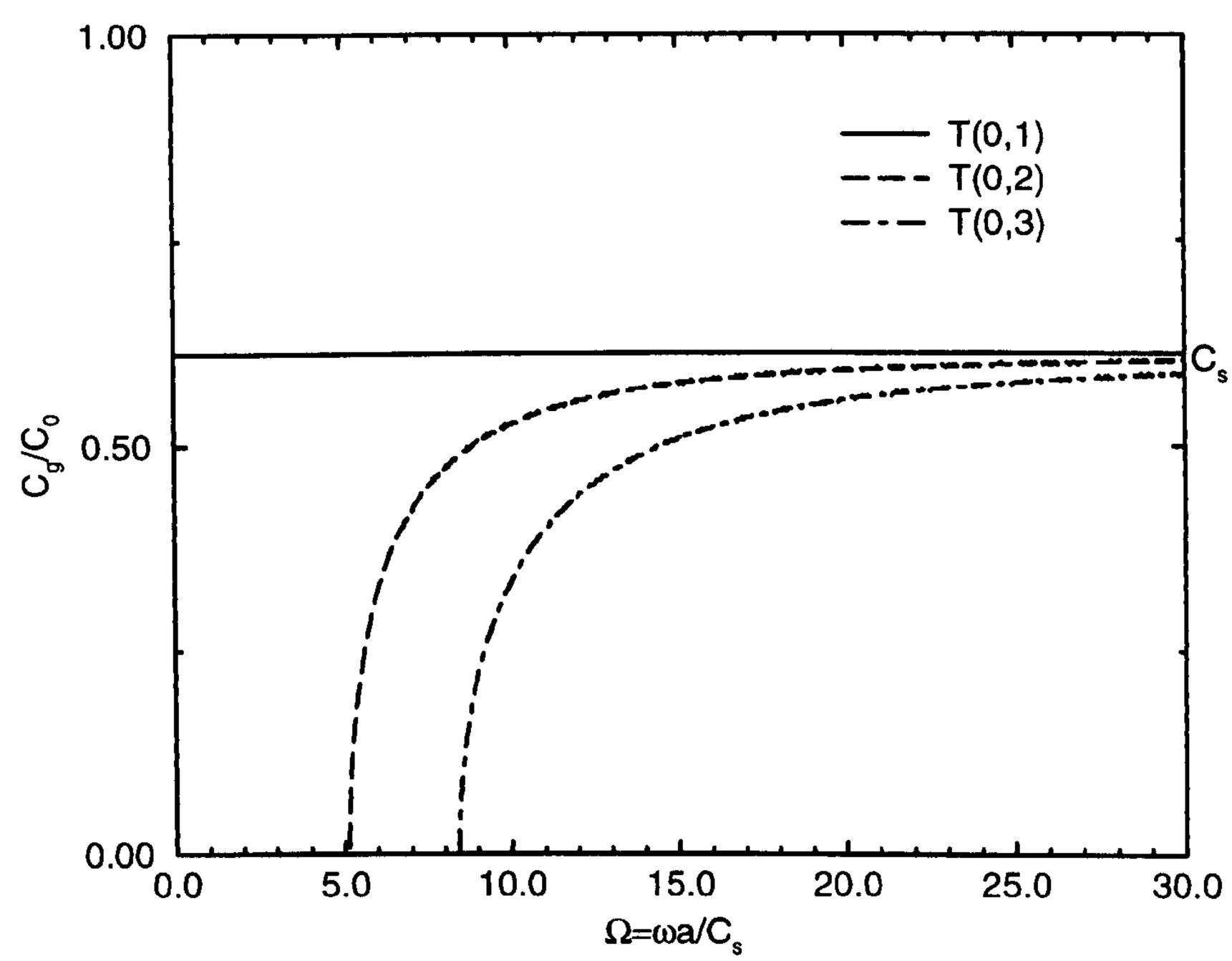

Figure 3.7(b): *Group velocity dispersion curves for the first three torsional modes*

($\nu = 0.34$)

3.5.4. Flexural Modes

Flexural modes are described for values of $n \geq 1$. Here the motion occurs in the θ, r, and z directions. The lowest branch of the family of modes given by $n = 1$, that is F(1,1), extends to zero frequency. It is this mode whose motion at low frequency displays bending or flexing properties. For higher frequencies the wavelength is much smaller than the diameter of the bar, and so higher branches for values of $n = 1$ may be described as shear waves that are nearly linearly polarised [1]. Here the motion is not really flexural, but the name is used to describe all these modes. Modes for values of $n > 1$ are often called "screw modes" or "flexural modes of higher circumferential order", again clearly being tagged as flexural.

Dispersion curves for flexural modes have been calculated from the general frequency equation (Equation 3.60) using MATLAB. Figure 3.8 shows the first four flexural modes with $n = 1$ and a Poisson's ratio $\nu = 0.34$. Figure 3.9 shows a selection of flexural modes of higher circumferential order, again with $\nu = 0.34$.

The fundamental mode with $n = 1$, i.e. F(1,1), is characterised at low frequency by a flexing motion, where one side of the rod is stretched in the axial direction while the other side is compressed. It can be shown, from the general frequency equation (Equation 3.60), that at the low frequency limit this mode is correctly described by the elementary theory of flexure (Equation 3.29) previously outlined [79]. From Figure 3.8(a) it can be seen that the velocity is zero at $\omega = 0$, and increases monotonically with increasing frequency, tending asymptotically to the Rayleigh velocity. Like the longitudinal modes, flexural mode dispersion curves vary with

Poisson's ratio, and Hudson [86] has plotted F(1,1) for various values of ν to show its effect.

In the low frequency limit, when the theory of flexure applies, the axial component of displacement varies linearly with perpendicular distance from the neutral plane and the cross section oscillates essentially rigidly [1]. As the frequency increases the displacement distribution associated with this mode becomes increasingly concentrated near the surface, and the velocity tends to the Rayleigh velocity, C_R.

All other flexural modes with $n = 1$ have cut-offs where C goes to infinity and C_g goes to zero. At cut-off the motion is either axial-shear or plane strain with no axial component. The modes with axial-shear motion at cut-off have cut-off frequencies given by Equation 3.73.

$$\frac{\Omega J_0(\Omega)}{J_1(\Omega)} = 1 \qquad \textbf{3.73}$$

The first 3 values of Ω are: 1.84118, 5.33144, and 8.53632.

The modes whose motion has no axial component at cut-off, have cut-offs given by Equation 3.74.

$$2(\Phi) + 2(\Omega) + \Omega^2 - 8 = 0 \qquad \textbf{3.74}$$

Typically there are one or two modes with this type of cut-off between those with axial-shear cut-offs. With increasing frequency, the phase and group velocities of these higher modes tend to C_s.

The flexural modes with $n > 1$ have no real branches that extend to zero frequency, therefore all the branches have cut-offs. Again, the motion at cut off is either axial-shear or plain strain with no axial component. The cut-off for axial-shear modes satisfies Equation 3.75.

$$\vartheta_n(\Omega) = \frac{\Omega J_{n-1}(\Omega)}{J_n(\Omega)} = n \qquad \textbf{3.75}$$

The cut-off frequencies of the modes for which the motion at cut-off has no axial component is given by Equation 3.76.

$$\begin{vmatrix} n^2 - 1 - \frac{\Omega^2}{2} & 2(n^2-1)(\vartheta_n(\Omega) - n) - \Omega^2 \\ \vartheta_n(\Phi) - n - 1 & 2n^2 - 2(\vartheta_n(\Omega) - n) - \Omega^2 \end{vmatrix} = 0 \qquad \textbf{3.76}$$

For any n, the lowest branch of the dispersion relation has a high frequency asymptote that corresponds to propagation at the Rayleigh velocity C_R, and all other branches tend asymptotically to the shear velocity C_s. This is seen in Figure 3.9 where F(2,1) and F(3,1) tend to C_R, while F(2,2) and F(3,2) tend to C_s.

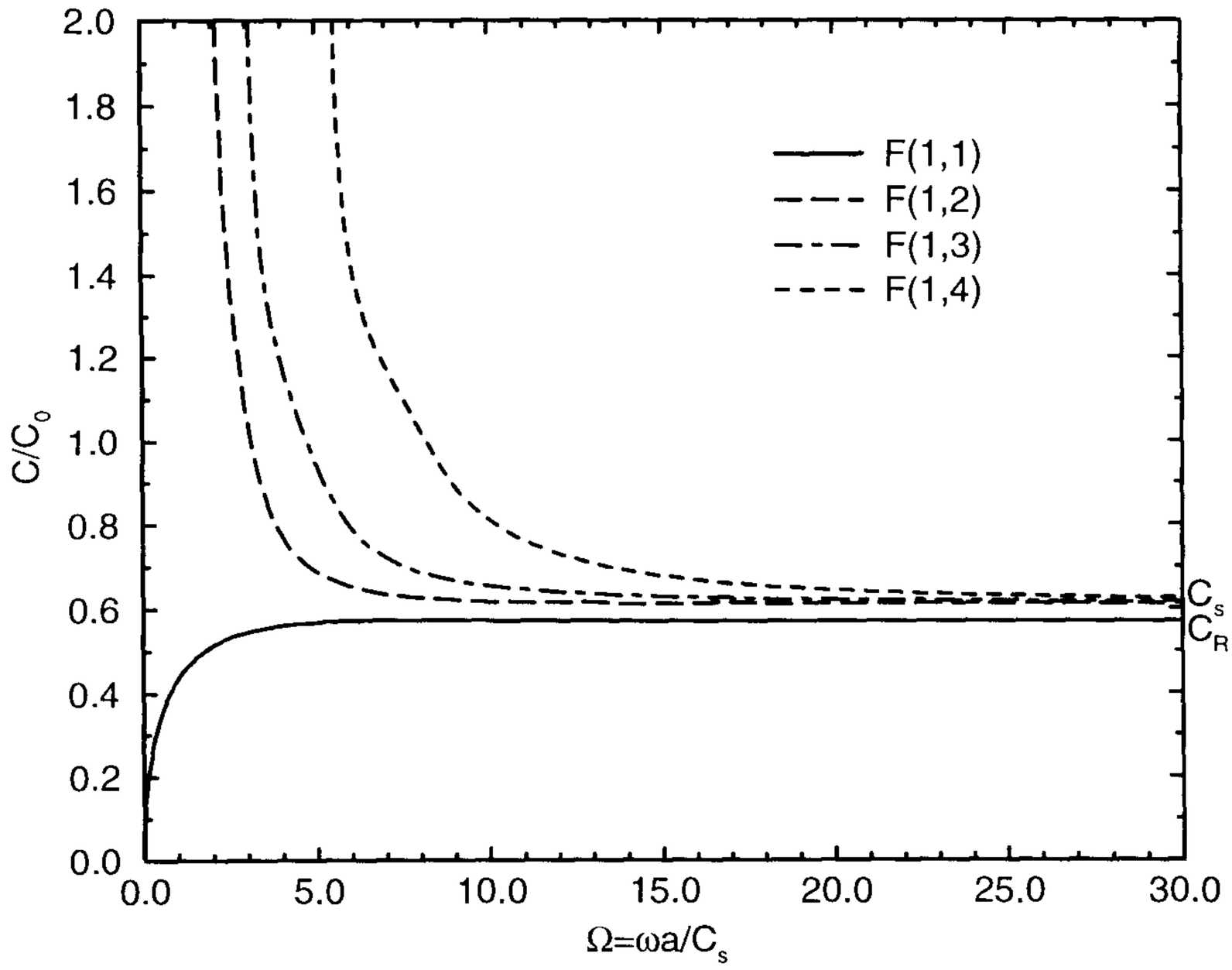

Figure 3.8(a): *Phase velocity dispersion curves of the first four flexural modes with n=1 (ν=0.34)*

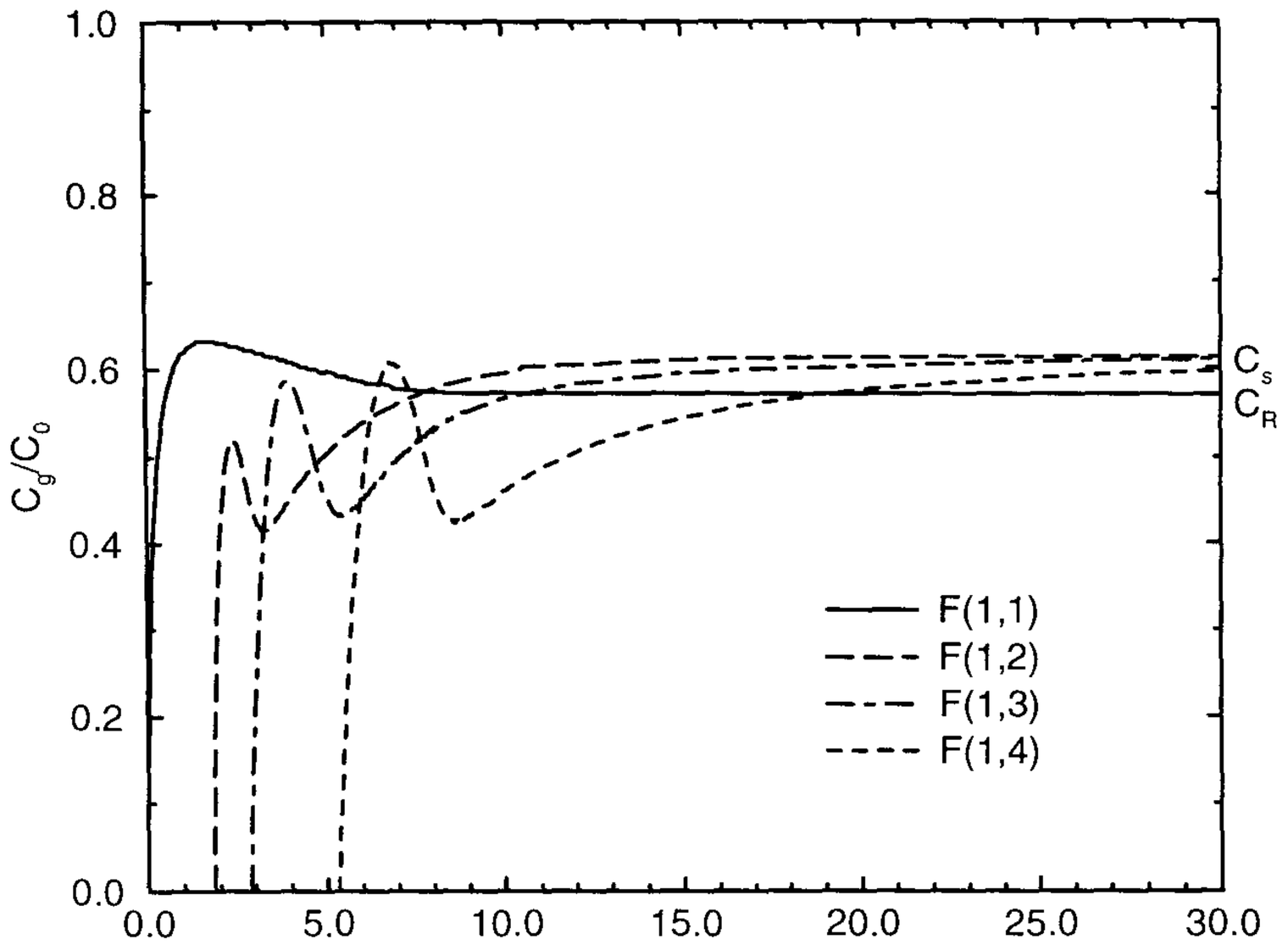

Figure 3.8(b): *Group velocity dispersion curves of the first four flexural modes with n = 1 (ν = 0.34)*

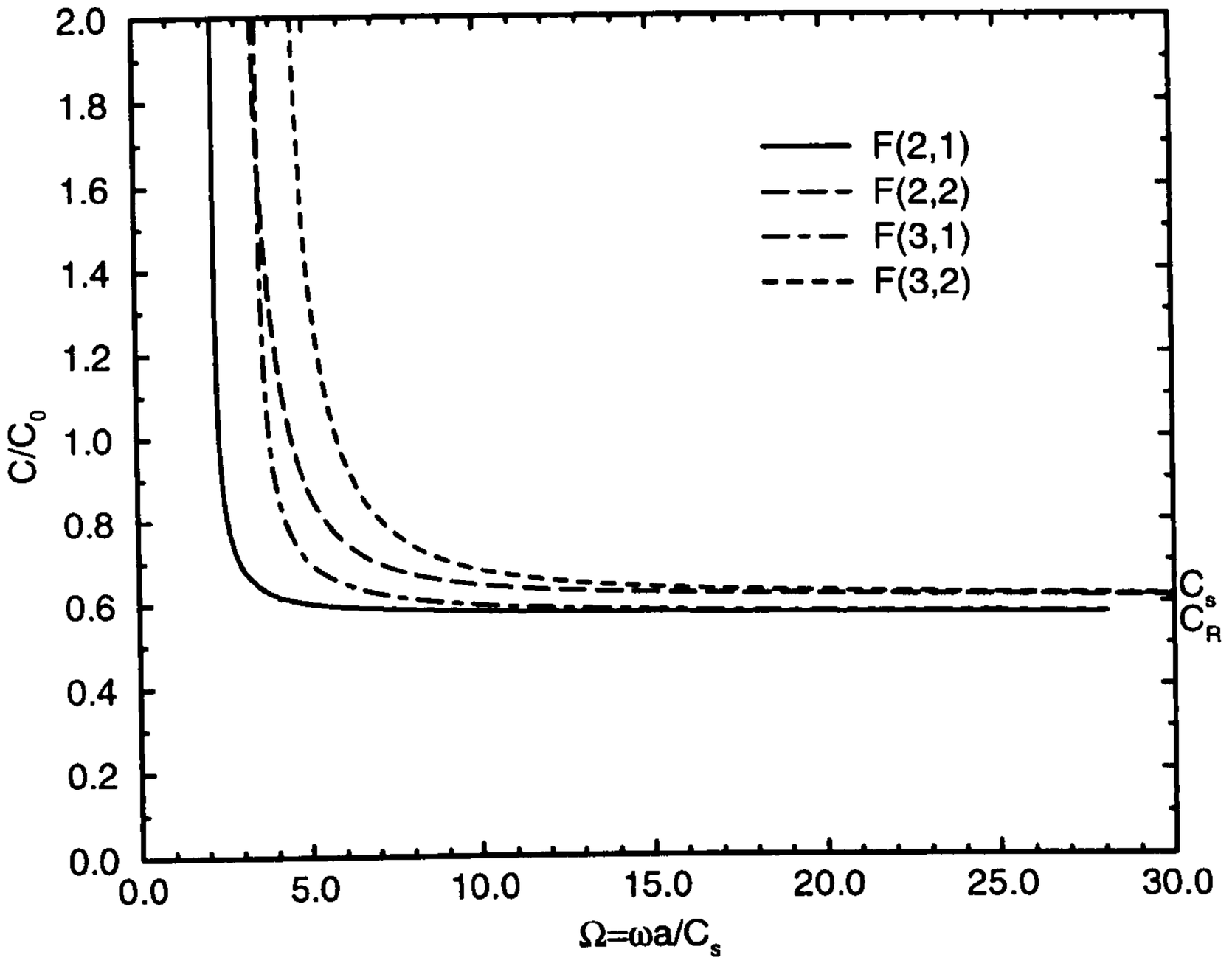

Figure 3.9(a): *Phase velocity dispersion curves of flexural modes with n > 1 (ν = 0.34)*

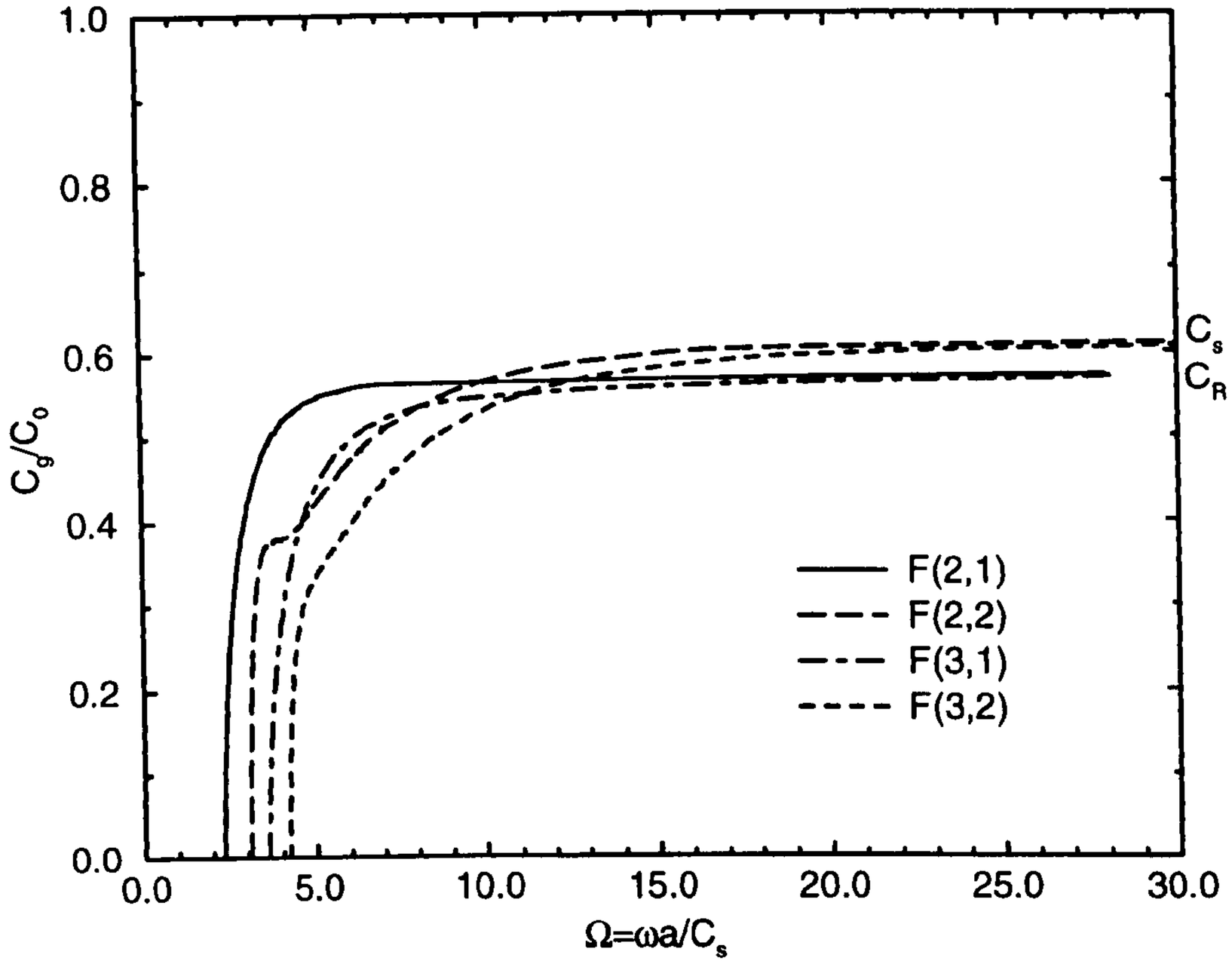

Figure 3.9(b): *Group velocity dispersion curves of flexural modes with n > 1 (ν = 0.34)*

3.6. Anomalous Interference Effects

3.6.1. End Resonance

When calculating dispersion curves it is assumed that the rod is infinitely long. That is, the boundary conditions at the end faces are ignored. Therefore, there is not necessarily a direct relationship between the dispersion curves that have been presented and the frequencies of resonance of a rod of finite length. However it has been shown elsewhere that end effects are relatively small when $\Omega < 2.6$ [91, 93]. Since the work described here is concerned only with this region, end effects can be safely ignored.

3.6.2. Mode Coupling

The phenomenon of mode coupling occurs in numerous areas of physics, and the general theory indicates that independent to the coupling mechanism, a combination of the following conditions will cause modes of propagation to couple most strongly: (1) that the two modes have equal phase velocities; (2) the medium has low attenuation per wavelength; (3) the coupling is uniform, that is independent of position.

Meeker and Meitzler [51, 53] discuss the case of mode coupling in cylindrical acoustic waveguides. Here they suggest that since ideal elastic waveguide modes of propagation are independent, coupling is a result of wave scattering by imperfections in the interior, or at the surface of the guide. An experimental example of mode coupling is discussed for the case of a 365.8 cm long, 0.178 cm diameter aluminium

wire. Here the L(0,1) mode was generated via a piezoelectric transducer excited by a Gaussian enveloped tone burst, and received via a similar transducer. Initially the L(0,1) mode was generated at a frequency where no mode coupling would occur resulting in a clean unimodal signal being received. The L(0,1) mode was then excited at a frequency for which the wave motion in the mode had an identical phase velocity to that of the F(2,1) mode. At this frequency mode coupling occurred resulting in the following effects:

- A reduction in the peak amplitude,
- Significant lengthening of the duration of the pulse,
- A pronounced *beat pattern* distortion in the trailing edge. That is, an interference pattern similar to that displayed by two sound waves of slightly different frequency, which results in a signal with periodic variations in amplitude, or *beats*.

The critical frequency for mode coupling between these two modes was just above the cut-off frequency of the F(2,1) mode, where its phase velocity is in an area of rapid change, while its group velocity is relatively low. This is considered to play an important role in the extension of the pulse duration and the trailing edge beat pattern interference.

A useful way to determine the critical frequencies of a waveguide is to plot frequency against propagation constant. Figure 3.10 shows such a graph for ν =0.34, calculated from the frequency equations previously discussed. Critical frequencies exist where

modes cross, that is at point of equal phase velocity. It can be seen that modes of the same family and order do not couple, for example coupling can occur between L(0,q) and F(n,q) modes, and between F(n,q) and F(m,q) modes, where m≠n. It can be seen that the two lowest critical frequencies are a result of coupling to the F(2,1) mode. Therefore, mode coupling effects can safely be ignored when operating at frequencies below which this mode exists. Figure 3.10 shows this value to be approximately $\Omega = 2.3$.

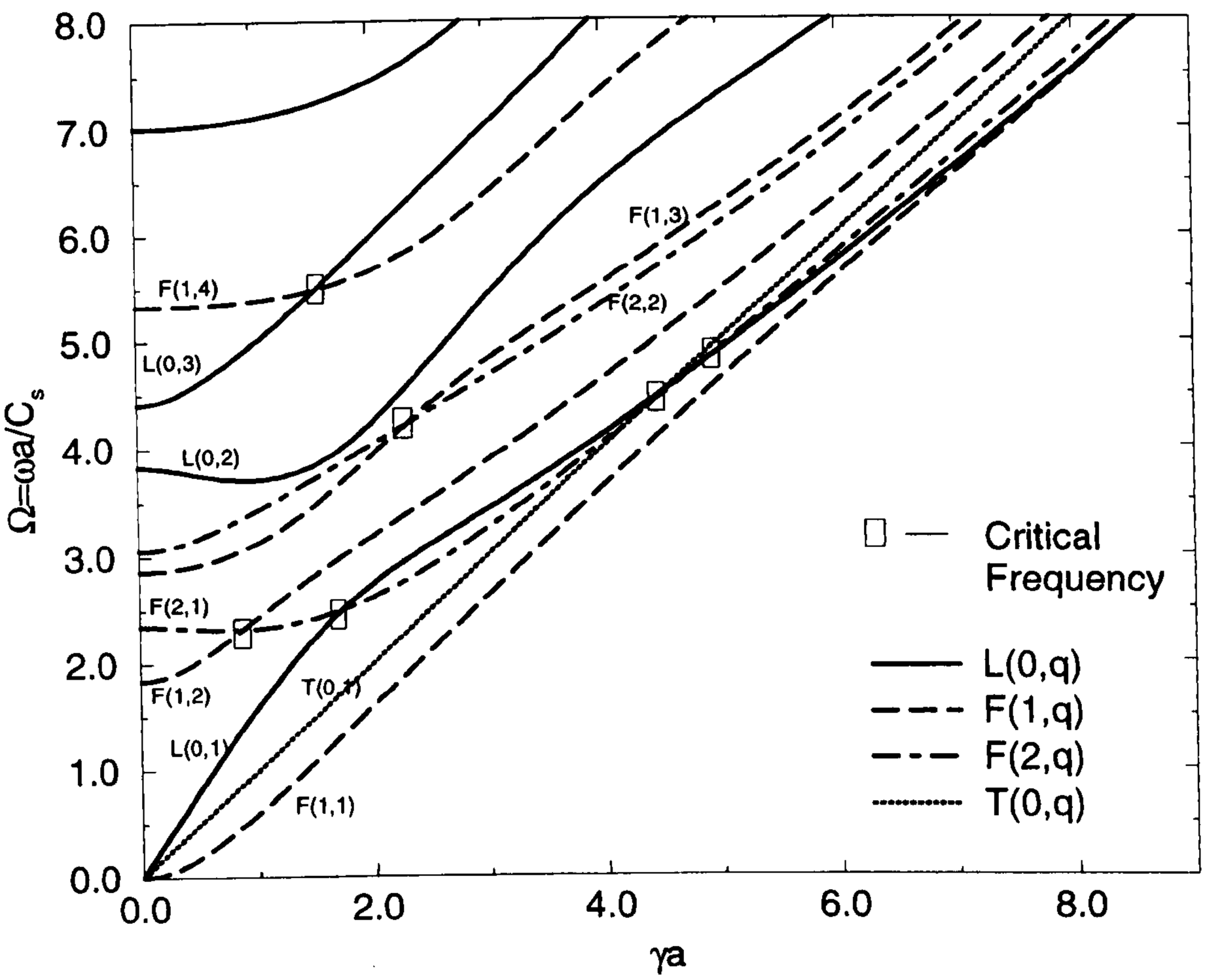

Figure 3.10. *Frequency Spectrum of the Propagation Constant of Various Cylindrical Waveguide Modes with ν=0.34*

3.7. Requirements of Mode for Proposed Monitoring System

With regards to the application proposed in this Thesis, the envisaged monitoring system employs an array of embedded fibre waveguides to deliver ultrasonic energy to plate-type structures for Lamb wave excitation. As such, the embedded fibre waveguide array introduces a series of periodic stresses to the load plate to generate a desired Lamb wave mode. With this in mind, single mode propagation along each waveguide is desired, since additional modes will complicate the nature of the loading mechanism into the plate. Moreover, control of the phase of the ultrasonic signal released into the load structure by each waveguide is critical to ensure the selective generation of the desired Lamb wave mode. This acoustic energy will be transferred into the surrounding plate media via the circumference of the waveguide, and so knowledge of the phase of the waveguide mode at the waveguide's circumference is paramount. Consequently, the L(0,1) mode is of particular interest because of its axisymmetric nature, which demonstrates equal phase around the circumference of the waveguide at any given axial position. This quality ensures that the phase of the ultrasonic signal at the desired release point is purely a function of propagation distance along the waveguide, thereby eliminating the need to quantify the rotational alignment of each individual fibre in the array. This significantly simplifies the embedding process, and increases confidence in the ability deliver an ultrasonic signal of quantifiable phase. The generation of a single L(0,1) mode in the waveguides is, therefore, proposed to best match the requirements of the system.

3.8. Conclusions

This Chapter introduced relationships between stress, strain and displacement for an isotropic solid. An elementary and exact analysis of elastic wave propagation in cylindrical bars was then discussed. Dispersion curves were presented and various modal features highlighted. It was shown that an isotropic cylinder can support three families of elastic wave propagation namely, longitudinal, torsional, and flexural and that only the fundamental mode of each of these families will extend to zero frequency. Two anomalous interference effects namely end resonance and mode coupling, were investigated and reported to have no effect when operating below a specified value of Ω. For the frequency range of interest these effects can therefore be ignored. Furthermore, it was highlighted that the properties of the axisymmetrical L(0,1) mode are particularly well suited to the proposed fibre waveguide monitoring system. The next Chapter will therefore go on to describe experimental, and finite element analysis performed to investigate the coupling of energy into this fibre waveguide mode from a piezoelectric transducer via an epoxy bond.

CHAPTER 4

The Fibre-Transducer Interface

4.1. Introduction to Chapter

The previous Chapter presented the theory of elastic wave propagation in cylinders and discussed the various acoustic modes that propagate in this geometry. It was noted that the fundamental longitudinal mode, L(0,1), is particularly well suited to the requirements of the proposed fibre based monitoring system. In an attempt to couple into this mode, initial experiments involved the bonding of waveguides normal to the surface of thickness-mode piezoceramic transducers using hard setting epoxy. Ultrasonic energy is generated by electric stimulation of the piezoelectric transducer across its thickness, and is subsequently coupled into the fibre waveguide via the epoxy bond, which was roughly conical in shape. It was anticipated that the thickness mode resonance of the transducer would couple strongly into the waveguide to induce longitudinal propagation. Surprisingly, by far the strongest signals were detected at lower frequencies, corresponding to lateral resonances in the transducers. Since it was unclear if this was due to 'cut off' in the guides or the geometry and nature of the bond, this interesting result provoked the development of a theoretical model for prediction of the interface behaviour. The model was established utilising a symmetric, two-dimensional (2D) Finite Element Method (FEM), and consequently a brief introduction to FEM is presented. This is followed by a description of how the Finite Element Analysis (FEA) code PZFlex [96] was utilised to interrogate the transducer-fibre interface and simulate the generation and detection of longitudinal ultrasonic wave propagating along the fibre waveguide. An extended 2D axisymmetrical model is also demonstrated for improved geometrical accuracy and to permit the simulation of disc transducers. Experimental verification

of the coupling hypothesis resulting from the model is reported. In addition, the geometry of the epoxy bond is theoretically investigated for improved coupling efficiency into the waveguide. The Chapter then goes on to experimentally investigate and quantify this coupling technique in terms of uni-modal L(0,1) propagation along fibre waveguides. Finally, design guidelines are detailed and conclusions are drawn.

4.2. Introduction to FEM

The FEM is a numerical procedure used for solving the differential equations encountered in a variety of engineering applications [95]. It was first applied in the aerospace industry in the early 1950's to permit vital analysis of complex structures. However, when it was shown to be a variation of the Rayleigh-Ritz procedure of minimising the potential energy of a system, it came to be used in other application areas. FEM increased in popularity after the demonstration that the equations could be derived by using a weighted residual procedure such as Galerkin's method and hence could be applied to any system of differential equations. The other major factor in the development of FEM was the microcomputer revolution which enabled such a complex modelling technique to be carried out far more cheaply and quickly than in its early development stages.

The need for and popularity of FEM can be appreciated when we consider the problem of calculating the stresses and strains in structures in almost every branch of engineering, including aeronautical, mechanical, nuclear, and marine, where the

structures are complex [95]. The main structural problem is essentially one of geometrical shape in the first instance. After description and manipulation of the complex geometry via a computer, the laws of equilibrium, motion, strain compatibility, and stress-strain can be invoked and the process of analysis can begin.

The fundamental concept of FEA is that any continuous quantity such as temperature, pressure, or displacement for a domain can be approximated by a discrete model composed of a set of piece-wise continuous functions defined over a finite number of sub domains. The discrete model is constructed using the following procedure [94]:

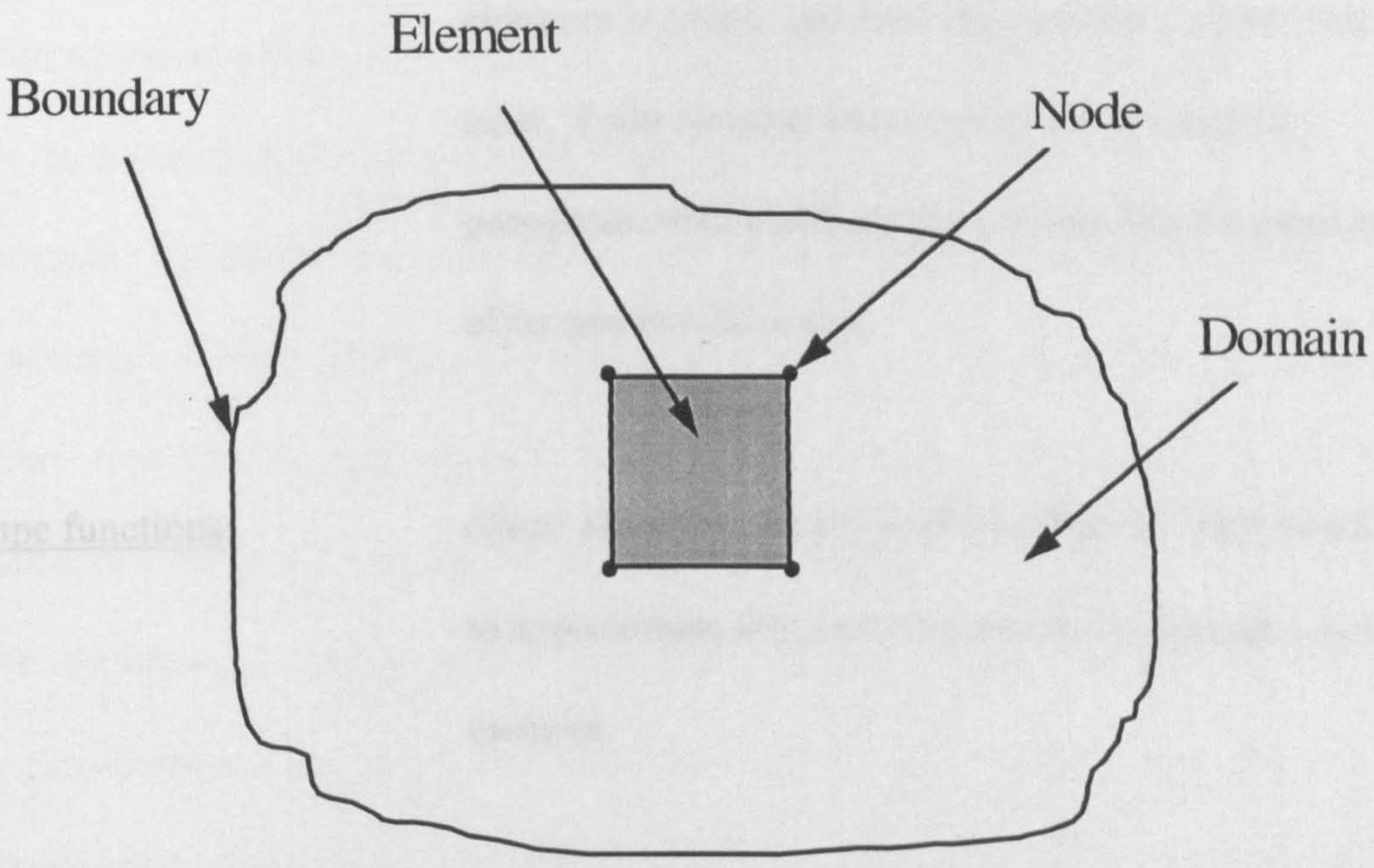

Figure 4.1: *FEM closed system*

Nodes: Within the domain of the problem a finite number of discrete points called *nodes* are chosen.

Degree of freedom (DOF): At each node the value of a continuous quantity is denoted as a *DOF* and is either set before or determined by the analysis process as an unknown. More than one quantity can be incorporated in the analysis as is the case of piezoelectric elements where both displacement and voltage are *DOFs* at the nodes.

Elements: A partitioning process called *meshing* is used to divide the domain into a finite set of sub-domains called *elements.* At each vertex of the element a node must exist. Each *element* has a unique set of material properties, which defines the relationship between each of its constituent nodes.

Shape functions: *Shape functions* are polynomials that are interpolated to approximate the continuous quantity through each element.

FEA is carried out by generating, and then solving a matrix equation, which describes the relationships between constituent nodes to produce the conduct of the nodes around each element. Using this information the element's complete behaviour is computed with respect to the parameters of interest.

FEM is an extremely useful tool in the field of ultrasonics since it can be applied to model piezoelectric transducer behaviour and elastic wave propagation. In the work described here the finite element analysis code PZFlex supplied by Weidlinger Associates of Los Altos, CA, USA was utilised. This is a time domain code for linear piezoelectric applications.

4.3. 2D FEA on the Coupling Technique

The finite element analysis code PZFlex was employed to simulate in 2D space the coupling of energy from a piezoceramic transducer, via a conical polymer bond, into a thin cylindrical bar. The structural system that was modelled is shown in Figure 4.2. In addition to the symmetrical boundary condition, illustrated in the Figure, an absorbing boundary was defined at the unbonded end of the waveguide (to approximate infinite length) and the other boundaries were unconstrained. The entire system was meshed with equally sized square elements, whose dimensions were chosen to establish 15 nodes per minimum wavelength. The degrees of freedom were displacement, and pressure throughout the system, and voltage and charge over the piezoceramic electrodes. This input to the model was a voltage applied across the piezoceramic electrodes. The voltage signal utilised was one cycle of an 8MHz sinusoid, which had a DC offset to make the entire signal positive going, and a 90° phase shift so that its magnitude is zero at zero time, as illustrated in Figure 4.2. The resultant signal is a wideband pulse with an upper 3dB-corner frequency of approximately 5MHz, which amply covers the frequency range of interest.

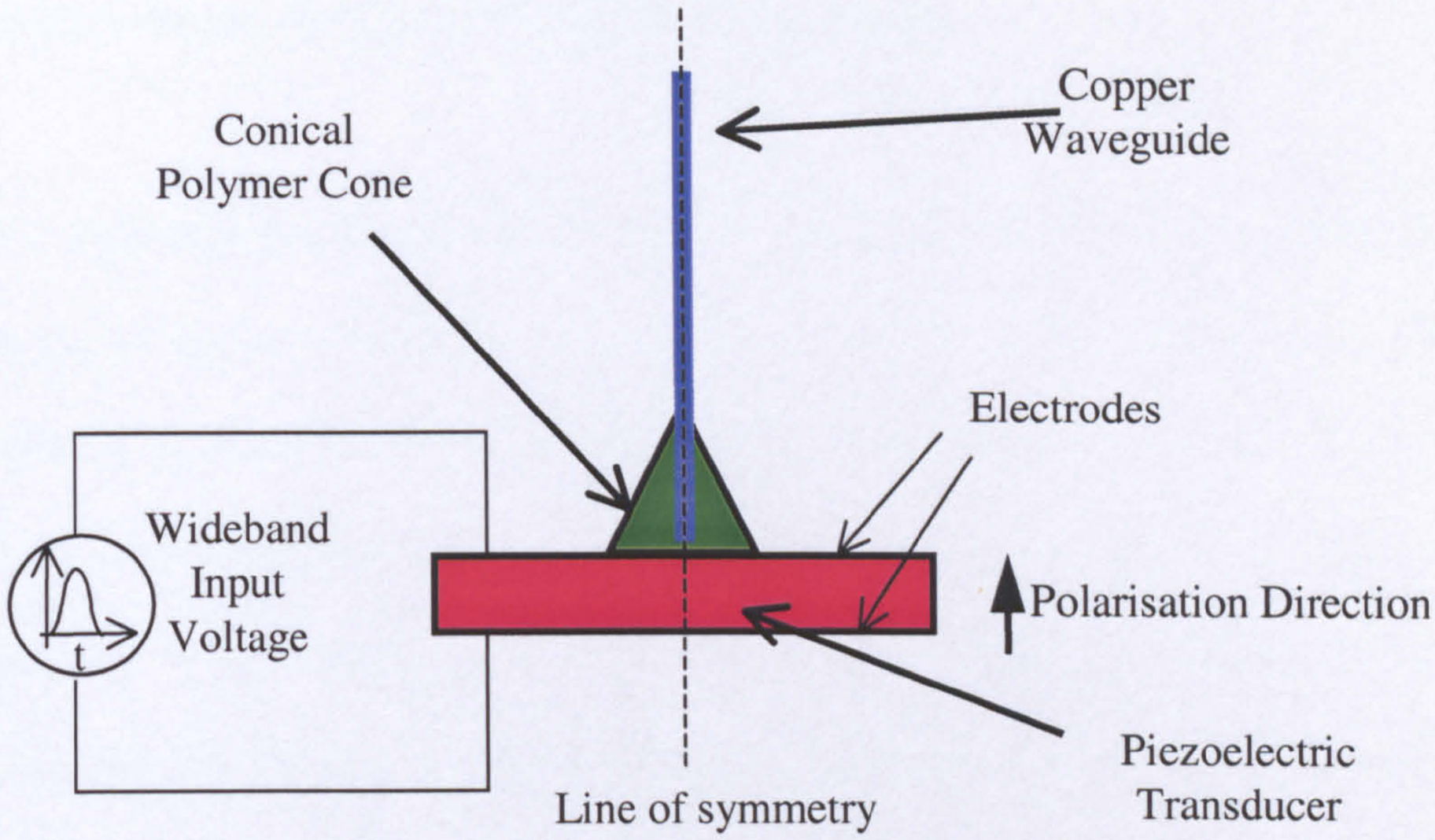

Figure 4.2: *The structural system to be modelled*

The actual piezoceramic transducer material employed in the initial experiments was a uniformly electroded thickness mode piezoceramic plate (PZT5A) of dimensions 30mm x 30mm x 1.96mm, corresponding to a 1MHz centre frequency. Therefore, for 2D simulation purposes the plate was approximated as a 30mm by 1.96mm section, as indicated in Figure 4.2, which was excited with the wideband impulse voltage of bandwidth 5MHz previously described. For this specific transducer material and geometry, two principal vibrational modes are of interest. Firstly, the thickness mode of the plate transducer is excited in the polarisation axis and corresponds to maximum displacements in the transducer height. The second type of mode is excited at right angles to the polarisation direction. These modes and

overtones correspond to the lateral dimensions (width/length) and represent maximum displacements of these transducer boundaries.

The copper waveguide was of diameter 0.25mm, length 40mm, and the polymer used was the hardsetting (Shore 80) epoxy CY1301/HY1300 (described in Appendix C), preformed to a conical bond of base diameter 4mm and height 3.5mm. The model was run with symmetry through its centre in the axial direction of the waveguide, see Figure 4.2. Consequently the model will only predict longitudinal propagation along the waveguide, and for the frequency range of interest only the L(0,1) mode will be supported.

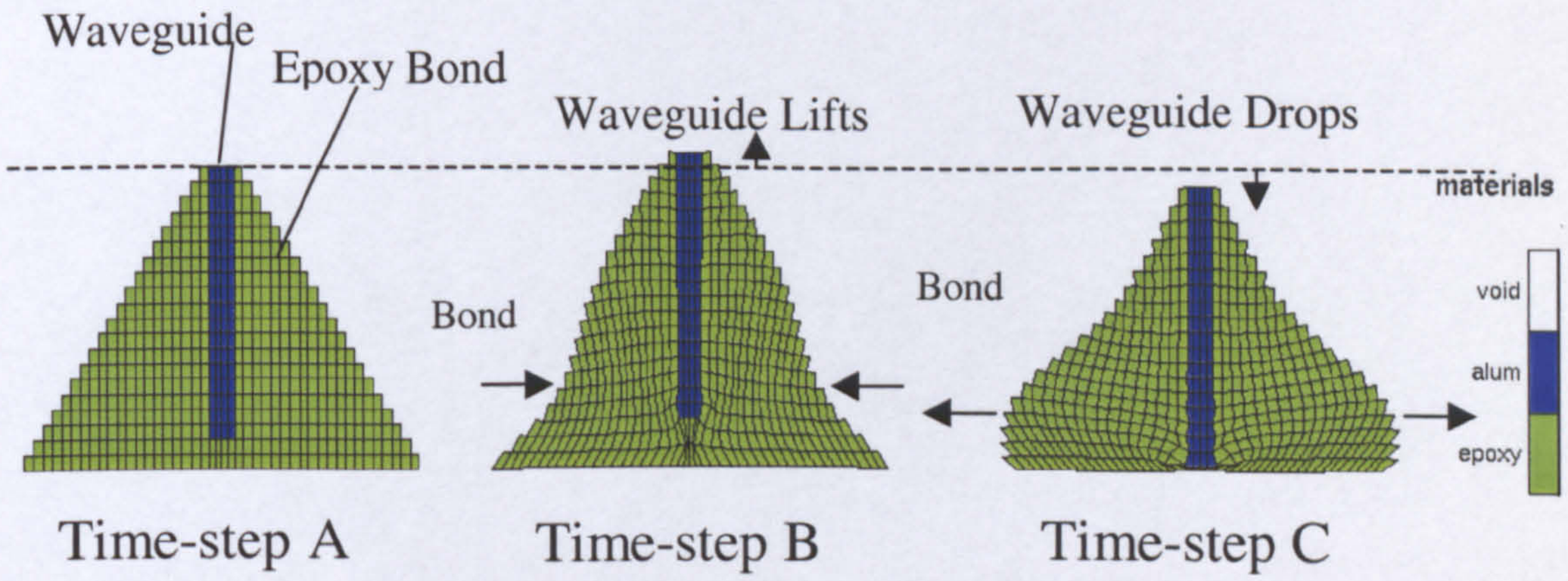

Figure 4.3: *Coupling motion of the fibre-bond-transducer structure*

Figure 4.3 shows the bond and the section of the waveguide held within the bond at three different time-steps during the model operation, where time-step A shows the initial structure position. The displacements indicate that as the bond is pinched inwards the waveguide is forced upward (time-step B) and then as the bond is

stretched the waveguide drops (time-step C). Thus it would appear that the lateral action in the transducer is being converted into longitudinal motion in the waveguide by the epoxy bond. To investigate this hypothesis, time histories of the longitudinal displacements of individual nodes within the waveguide were examined to obtain the spectral content of the propagating energy, and how this related to the various lateral and thickness modes of the transducer. First, the transducer was modelled alone to obtain its electrical impedance characteristics (frequency against impedance magnitude), which provides information on the resonant frequencies and overtones of the device. Typically, an isolated mode will exhibit a pair of resonant frequencies corresponding to a minimum in impedance magnitude (often termed the electrical resonant frequency) and a slightly higher frequency, demonstrating an impedance maximum (the mechanical resonant frequency). Each appearance represents a particular mode or harmonic, all of which can be related to device geometry and constituent material parameters. For the present situation, two types of mode and the corresponding overtones are of interest: the thickness modes which occur in the polarisation direction, and the lateral or width modes which depend on transducer width and length and are at right angles to the direction of polarisation.

After obtaining a theoretical impedance plot of the transducer, a simulation of the entire system shown in Figure 4.2 was performed. Information on the frequency content of the ultrasonic signal propagating along the waveguide was obtained by performing a Fast Fourier Transform (FFT) on the predicted displacement time history, monitored at a row of nodes half way along the waveguide length. This data

and the impedance plot of the transducer were compared for resonant activity and the results are shown in Figure 4.4.

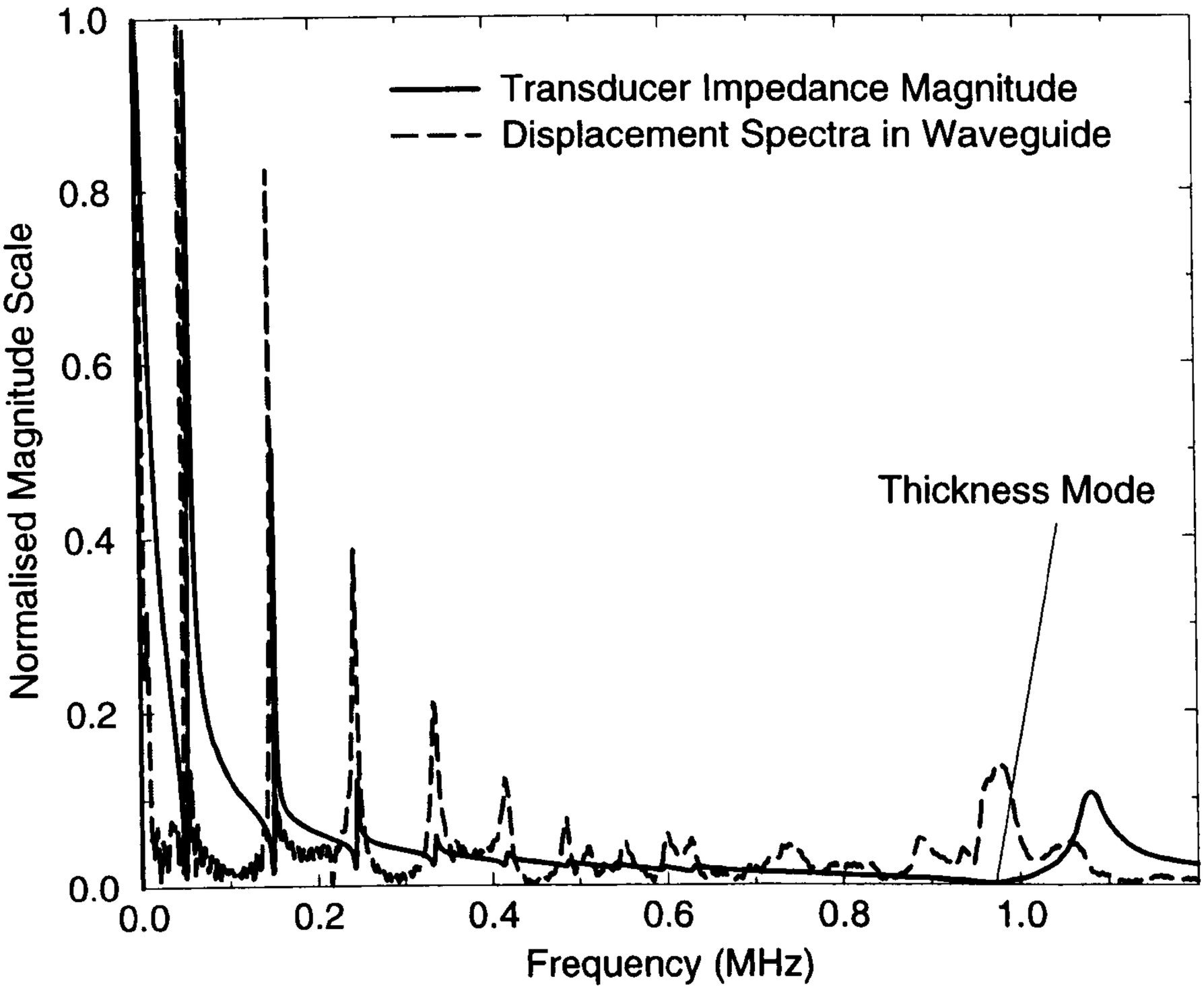

Figure 4.4: *PZFlex results: frequency content of signal in waveguide and impedance plot of transducer*

It can be seen that the frequency content of the displacement induced in the waveguide is in good agreement with the resonant activity of the transducer. Moreover, the peaks in the displacement spectra coincide with the transducer's impedance minima. In general, such impedance minima (electrical resonant frequencies) are associated with the maximum displacements of the transducer and consequently the optimum frequencies for transmission purposes. Significantly, the lateral modes in the transducer, which are those lower in frequency than the highlighted thickness mode, are converted more efficiently into longitudinal wave

propagation in the copper waveguide, than the thickness mode. Therefore, it appears that the epoxy bond acts as a mechanical transformer, with the base of the cone moving in sympathy with expansion and contraction of the piezoelectric plate in the lateral direction. As a result, the apex of the cone undergoes corresponding compression and expansion, resulting in longitudinal motion in the waveguide. The overall effect is not unlike that observed in some forms of flextensional transducers, such as the well-known *moonie*, and *cymbal* devices [97, 98] developed for underwater hydrophone applications. Both operate on the same principle and are pictorially illustrated in Figure 4.5, where it can be seen that metal endcaps are attached to the top and back surfaces of piezoceramic discs. In both cases the small radial displacements of the piezoceramic discs are converted and amplified into much larger axial displacements normal to the surface of the caps. The cymbal transducer configuration has several advantages over the moonie devices, including a more readily tailored performance, reduced cost, and easier fabrication [98]. In addition, cymbals have been demonstrated to out-perform moonies, in terms of axial displacement, and generated force [97].

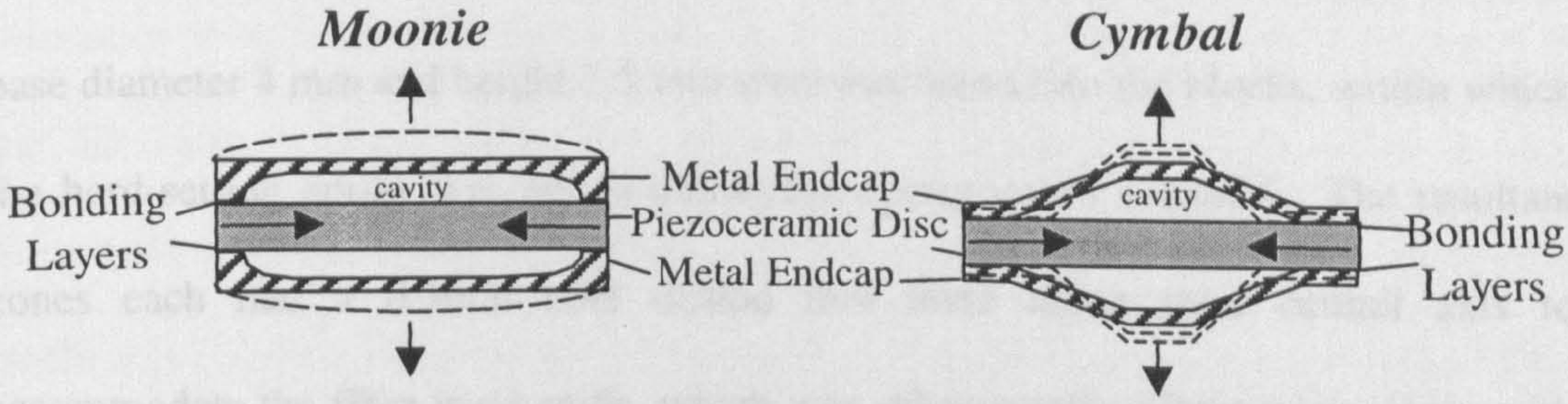

Figure 4.5: *Flextensional Devices: Moonie and Cymbal Transducers*

4.4. Comparison between PZFlex and Experiment

To establish that the 2D model of the system used was yielding reliable results it was necessary to make a direct comparison between data from the FEA and the experimental system. To do this, an experiment was carried out to transmit and receive ultrasound along a length of 0.25mm diameter copper wire, as illustrated in Figure 4.6, and PZFlex was then used to simulate this experiment. Ultrasonic energy was introduced to, and detected from the waveguide by means of two equally sized 1MHz thickness mode PZT5A piezoceramic transducers of dimensions, 20mm x 15mm x 1.96mm, which were approximated by 20mm x 1.96mm plates for 2D simulation purposes. The waveguide was interfaced each of these transducers via a conical (triangular in 2D) hardsetting polymer bond of base diameter 4mm and height 3.5mm. The transmitter was excited by a voltage spike of duration 30ns, delivered by a Panametrics 5052PR unit, which also functioned as the receiving amplifier, with a bandwidth of 1kHz to 35 MHz. To ensure that all the simulation parameters could be replicated for the model, moulds were required to obtain accurate epoxy bond sizes. The moulds were made out of Polytetrafluoroethylene (PTFE), because of its non-adhesive properties. Two blocks of PTFE were obtained and conical holes of base diameter 4 mm and height 3.5 mm were machined into the blocks, within which the hard-setting epoxy was set to obtain the epoxy cones required. The resultant cones each had a 0.3mm hole drilled into them along their central axis to accommodate the fibre waveguide, which was subsequently adhered into place with additional hard-setting epoxy.

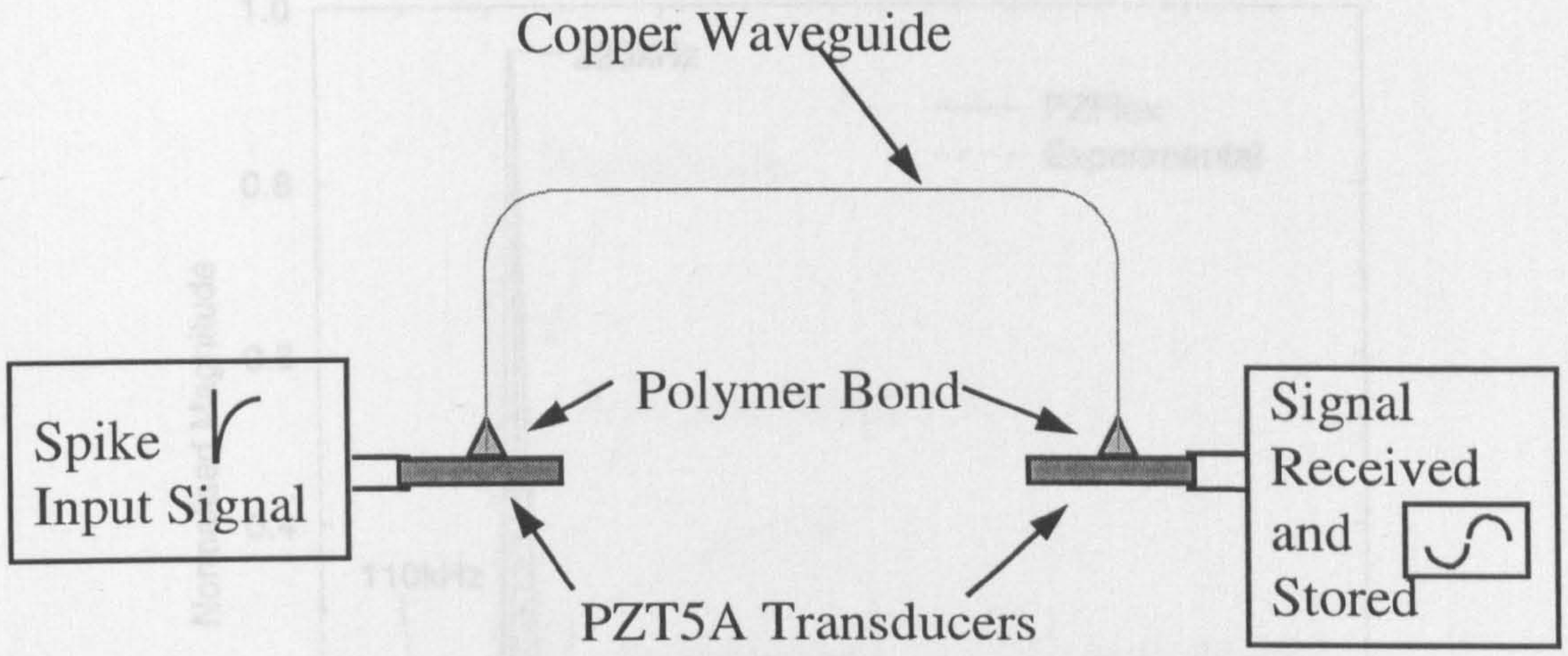

Figure 4.6: *Experimental Arrangement for comparison*

The input voltage applied to the model was obtained by recording the input voltage signal from the Panametrics pulser/receiver unit on a digital oscilloscope and applying this digitised signal to the model as an input parameter. Fourier transforms were performed on the received data from both the model and experiment and comparisons made. Figure 4.7 displays the results and there is clearly good agreement, with maximum coupling achieved at 226kHz, which is a lateral harmonic of the transducers (measured with the HP 4194A impedance analyser). The additional peak in the experimental data, at about 110kHz, corresponds to a lateral resonance in the 15mm dimension of the transducer, which was not represented in the 2D FEA model. Again both theory and experimental results show a poor magnitude response around the 1MHz thickness mode resonance as a consequence of inefficient coupling between the thickness displacements and the conical bond. This result confirms the earlier hypothesis that the cone is behaving as a mechanical transformer converting lateral displacements at its base into longitudinal displacements at its apex.

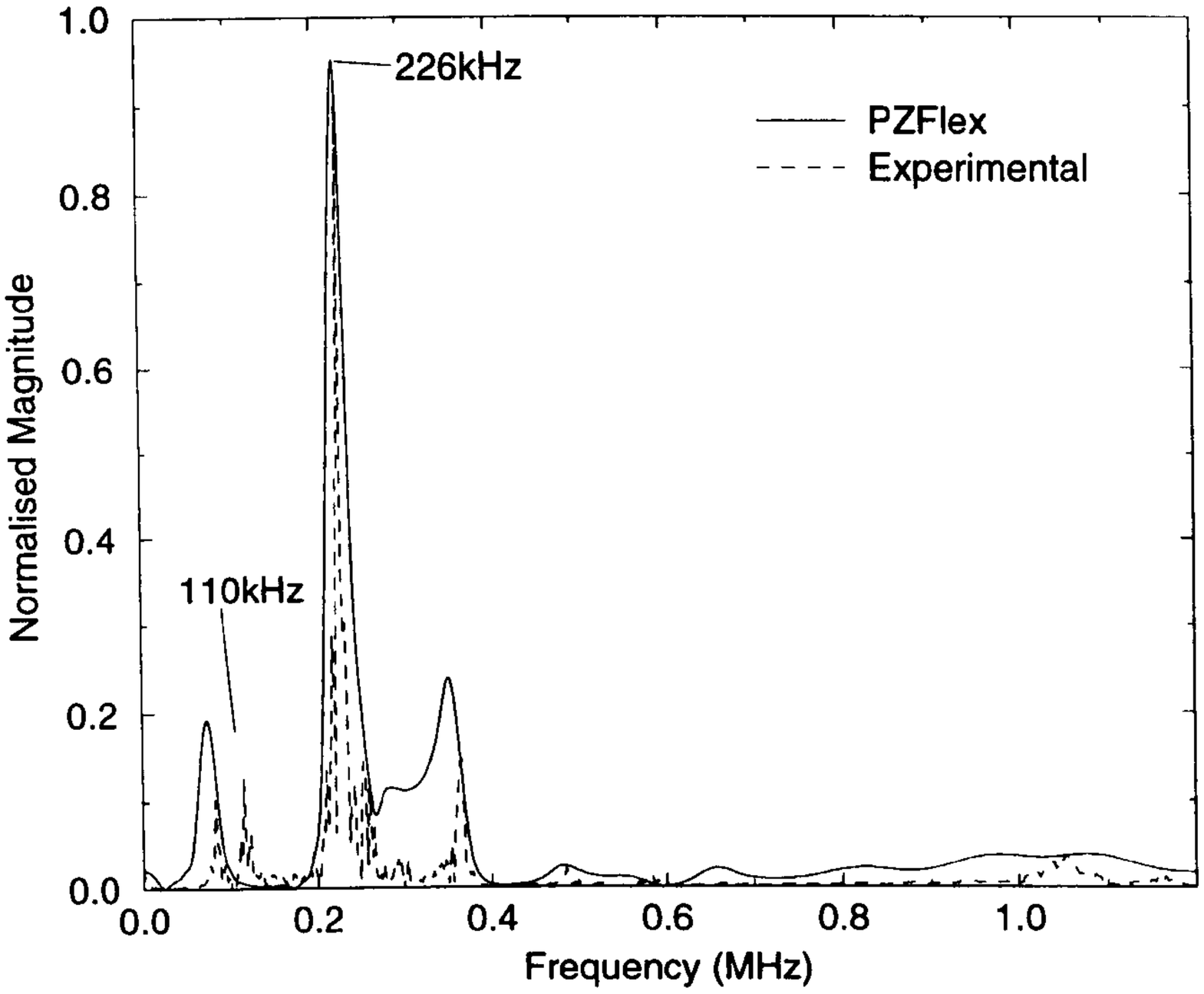

Figure 4.7: *PZFlex and Experimental Comparison Result*

4.5. 2D Axisymmetrical FEA on the Coupling Technique

The previous FEA utilised a 2D model, with a line of symmetry about its centre, to approximate the coupling of ultrasound from a piezoceramic plate into a waveguide interfaced with a polymer bond (see Figure 4.2). However, to improve the geometrical accuracy of the model, and permit actual piezoceramic disc transducers to be modelled, a 2D axisymmetric approach was adopted, as shown in Figure 4.8. Here the structure is rotated about a defined axis through 360°, which permits cylindrical geometries to be modelled in 2D space. Consequently, the cylindrical waveguide and conical bond are more accurately represented and the piezoceramic transducer is considered to be a disc, corresponding to subsequent practical implementations.

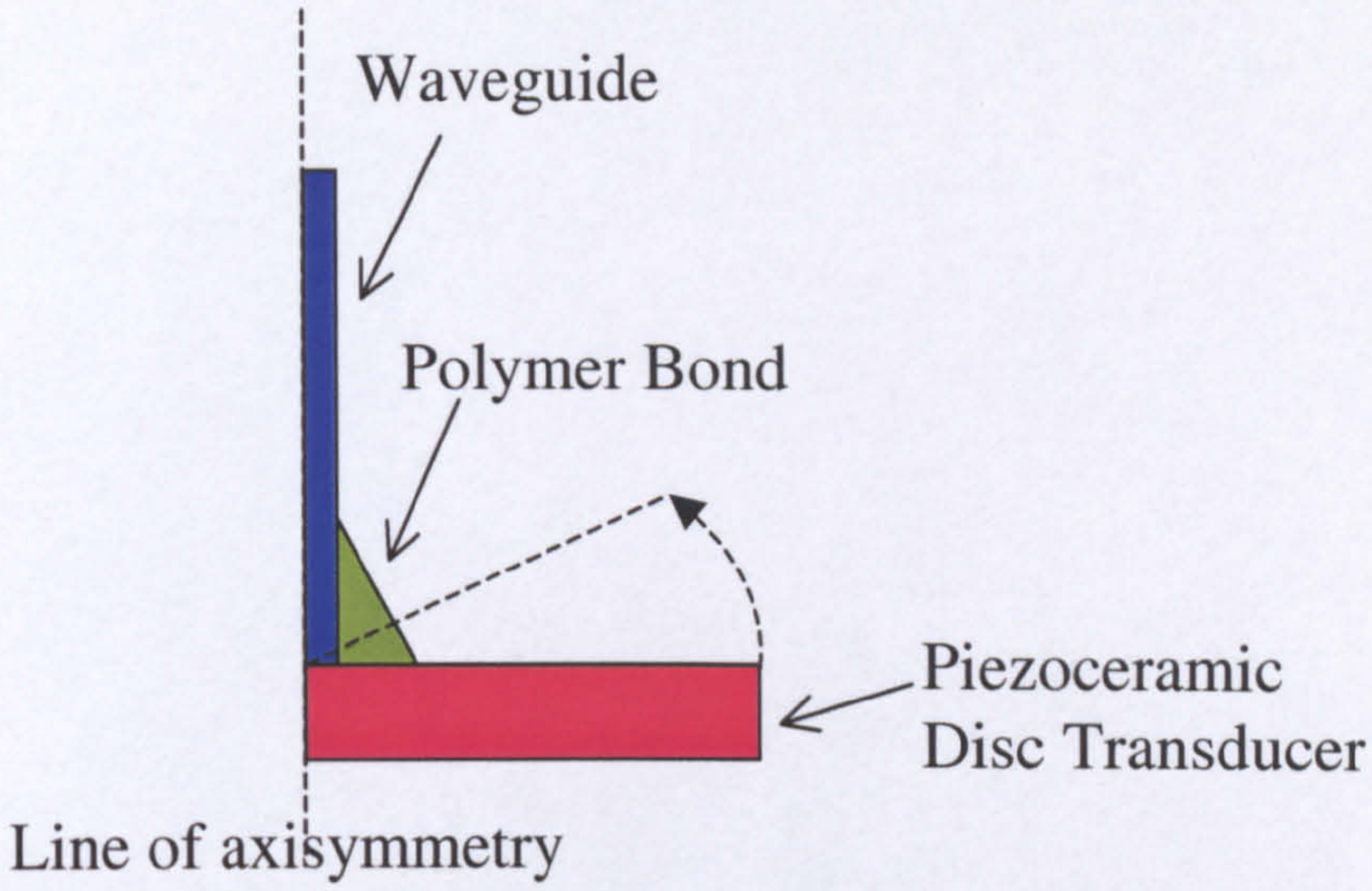

Figure 4.8: *Axisymmetric model of system*

The analysis described in Section 4.3 was repeated with axisymmetry applied to the model and all other parameters kept the same. That is, the piezoceramic was initially modelled alone to obtain a theoretical impedance plot of the disc transducer, followed by a simulation of the entire system to compare the spectral content of the ultrasonic propagation along the waveguide with the resonant activity of the transducer. The results of the model are presented in Figure 4.9, where once more it can be seen that the frequency content of the propagating ultrasound is in good agreement with the electrical resonances of the transducer, and that the most efficient coupling occurs at lateral (or radial for a disc) modes of the transducer rather than the 1MHz thickness mode.

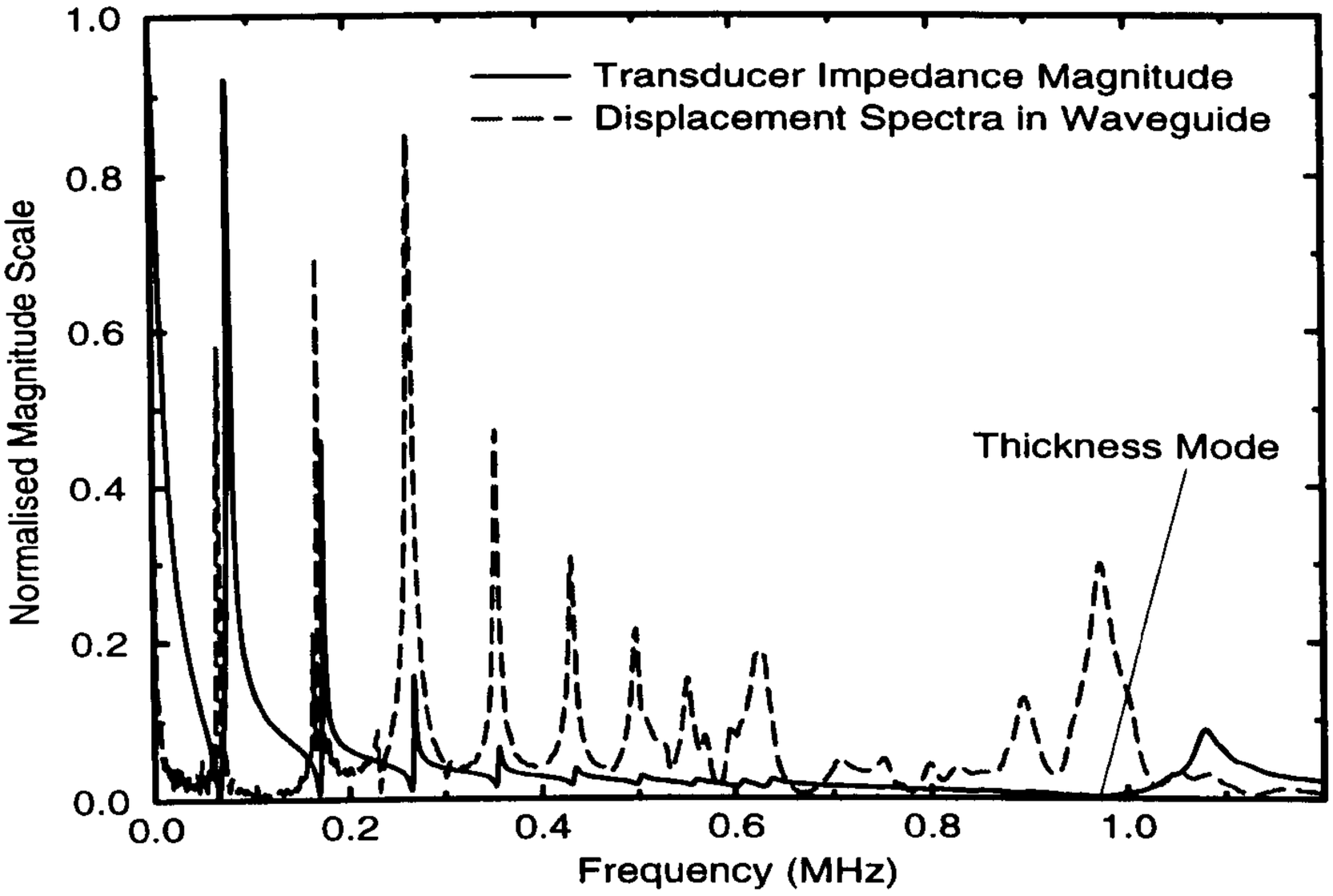

Figure 4.9: *PZFlex axisymmetric model results: frequency content of signal in waveguide and impedance plot of disc transducer*

4.6. An Experimental Verification of the Lateral Mode Coupling Hypothesis using MPT Disc Transducers

The piezoelectric strain constant, d_{31}, provides an indication of the energy coupling between the voltage across the thickness of the transducer and mechanical strain in the lateral directions of the transducer under transmit conditions, and has the units mV^{-1}, or CN^{-1}. The previous analysis used the piezoceramic material PZT5A, which has relatively strong lateral coupling ($d_{31} = -171e^{-12}$), to induce ultrasonic propagation along the waveguide. To further verify the theory that the lateral modes of the transducer would best couple into the guide, an experiment was carried out using modified lead titanate (MPT) transducers. This material has very low lateral coupling efficiency ($d_{31} = -21e^{-12}$), almost an order of magnitude weaker than PZT5A. Therefore, MPT transducers are beneficial for this investigation since the low d_{31} value reveals that there is weak lateral mode activity in the device when a

voltage is applied across its thickness. Consequently, if the polymer cone technique is fundamentally a mechanism which favours the coupling of lateral displacements, then even the weak lateral modes of the MPT transducer would be expected to couple into the waveguide. In the next experiment, two 1MHz thickness mode MPT disc transducers with a diameter of 30mm were used for the generation and reception of ultrasound along a copper wire of length 1m and diameter 0.25mm. The polymer bond used was the hard setting epoxy described previously. Figure 4.10 shows the experimental arrangement. The Panametrics 5052PR unit was again used to excite the transmitter with a voltage spike and to function as the receiving amplifier. The received signal was stored and a Fourier transform was performed on the data to provide frequency information. An impedance plot of the transducers was also recorded using a HP 4194A impedance analyser.

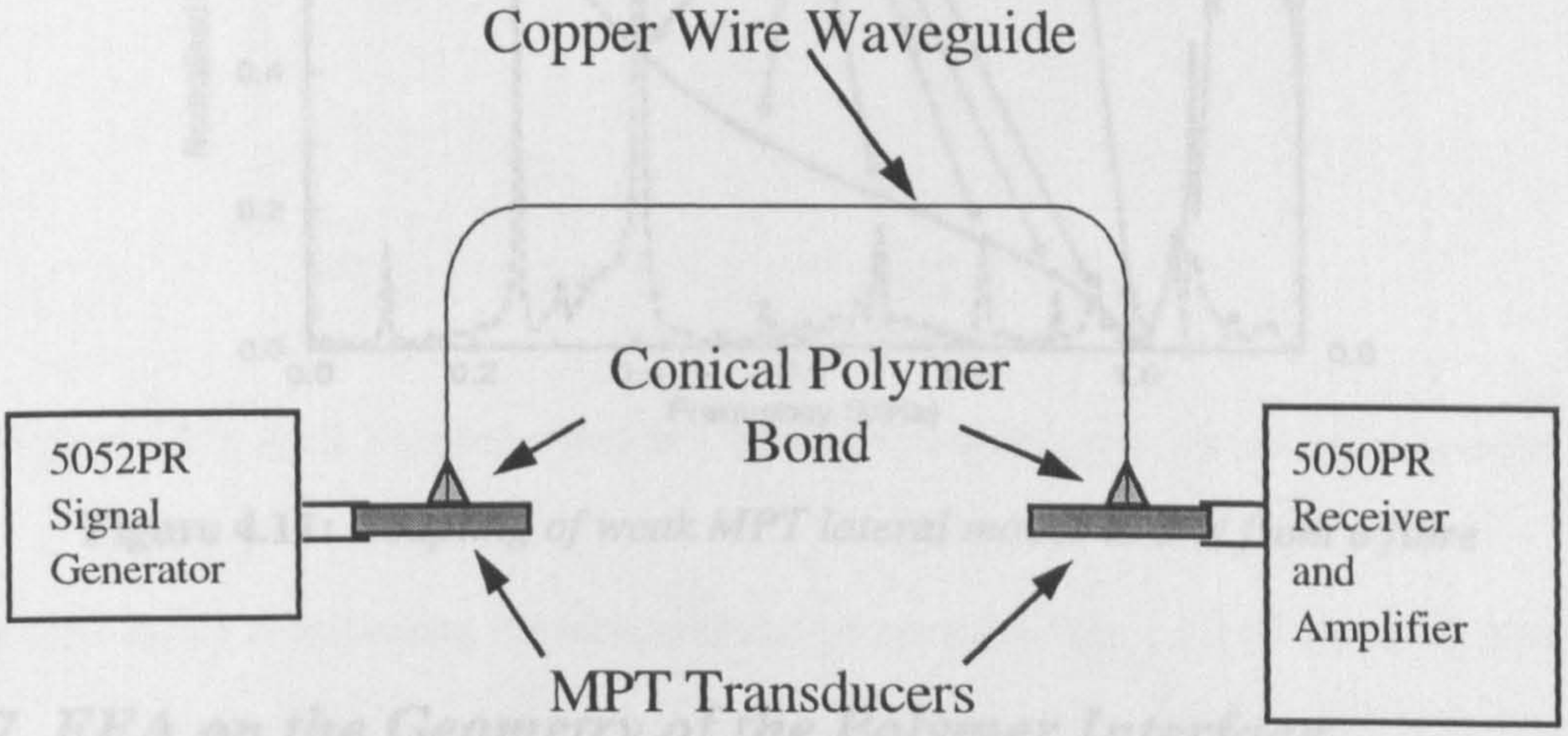

Figure 4.10: *Experimental arrangement of generation and detection of ultrasound through a fibre using MPT transducers*

Figure 4.11 shows the recorded impedance plot superimposed onto the FFT of the received ultrasonic signal. As may be observed, even the weak lateral modes of the

MPT transducer have been successfully transmitted and received along the wire waveguide more efficiently than that of the 1 MHz thickness mode, the response to which is relatively small. Furthermore, it can be seen that there is maximum coupling at the 5^{th} radial harmonic of the transducer, which occurs at approximately 400kHz. It should be noted that there are several additional modes superimposed onto the thickness resonance, which have coupled a small degree of acoustic energy to and from the waveguide. The nature of these modes has not been investigated in this work, but it is thought that they are either due to mode coupling occurring between radial harmonics and the thickness mode, or due to anisotropy in the sample.

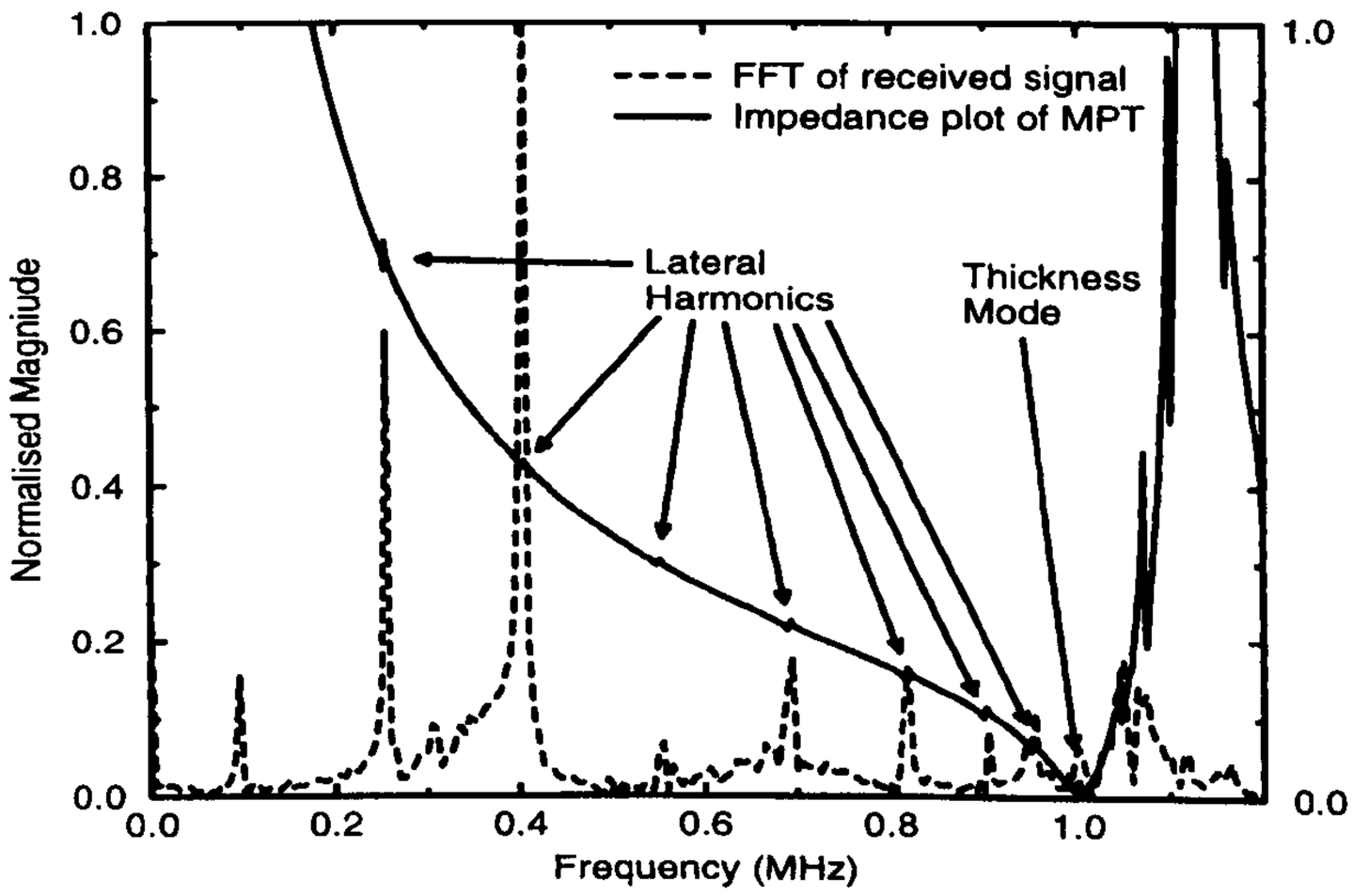

Figure 4.11: *Coupling of weak MPT lateral modes to and from a fibre*

4.7. FEA on the Geometry of the Polymer Interface

It is clear that the lateral resonant frequencies of a thickness mode piezoceramic transducer can be coupled into a cylindrical waveguide, and are preferred to the thickness mode resonance. However, the FEA and experimental results of this Chapter have so far shown that for each case a single lateral mode frequency is

favoured, resulting in a higher peak in the spectral data for that particular mode. In order to ascertain the reason for this, a systematic approach was adopted, whereby a series of simulations were performed to investigate the effects of various model parameters. The 2D axisymmetrical model described in Section 4.5 was utilised for this analysis, but with narrowband excitation being adopted. Specifically, for each simulation the transducer was excited with a 20 cycle 'Hanning windowed' toneburst at a frequency corresponding to one of the disc transducer's lateral (radial) resonant harmonics, which were identified from the impedance plot depicted in Figure 4.9.

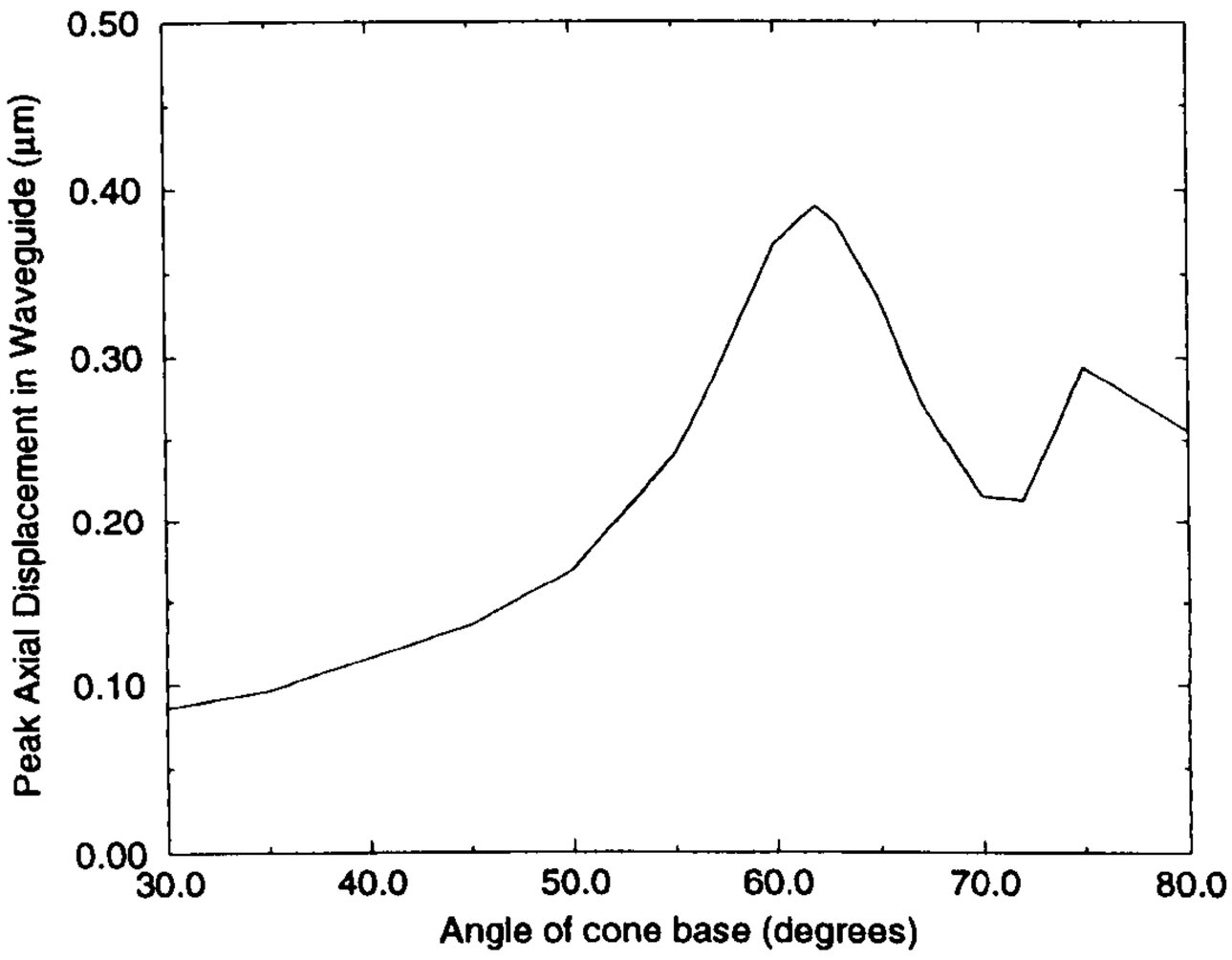

Figure 4.12: *Peak Displacement in Copper Waveguide for Various Cone Angles*

The first set of simulations investigated the geometry of the conical bond by altering the angle of the cone for each run of the model, while maintaining a constant base diameter of 4mm. The input voltage applied across the piezoceramic disc was a 265kHz toneburst, to excite the 5th lateral harmonic of the transducer. For each simulation the axial displacement of the signal propagating in the waveguide was monitored along a diameter of nodes at half the waveguide's length. Subsequently,

the average peak displacement was plotted against the angle of the cone, as depicted in Figure 4.12. This result shows that the geometry of the bond significantly affects the response, and is critical for efficient coupling into the waveguide. For this case the optimum coupling was achieved with a cone angle of 62°, although there is a second peak in the response at 75°.

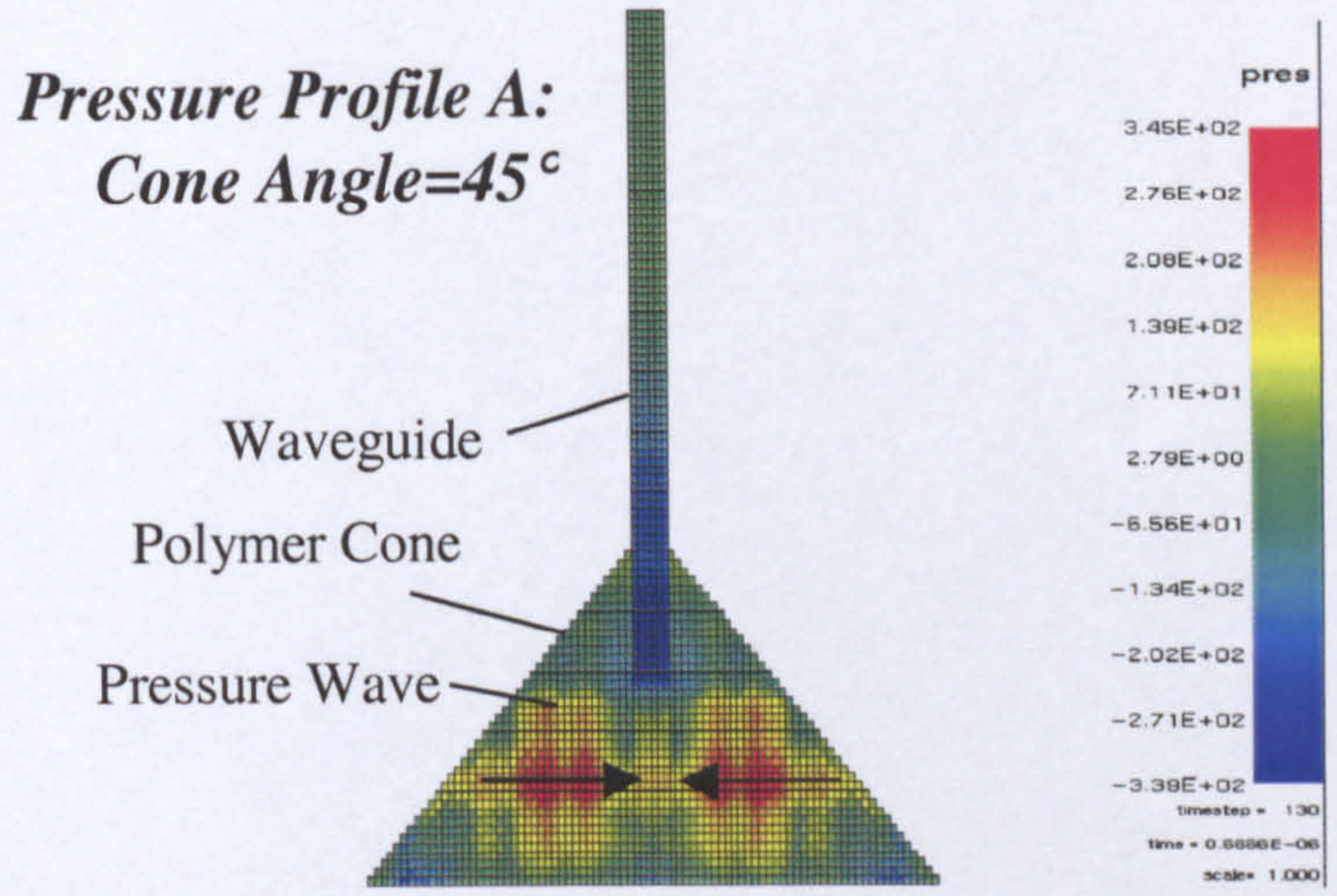

Figure 4.13: *Pressure Profiles of Ultrasound Coupling into Waveguide*

In addition to storing the axial displacement in the waveguide, pressure profiles of the entire system were recorded. Figure 4.13 demonstrates two such profiles during

the first microsecond of the simulations. Profile A depicts the pressure distribution for a 45° cone, where it can be seen that the pressure wave induced in the cone by the transducer has normal incidence to the waveguide. Furthermore, profile B reveals the pressure distribution for a 60° cone, where it can be seen that the pressure wave induced in the cone by the transducer has an incident angle of θ to the normal of the waveguide. Consequently, it can be seen that varying the bond angle affects the pressure wave's angle of incidence on the waveguide load. A well-documented concept utilised to couple ultrasound into Lamb waves (guided acoustic waves propagating in plate geometries) is that of the wedge transducer [99, 100]. Here the wedge is utilised as a coupling block to control the angle of incidence of an ultrasonic source. For a given wedge and load material an optimum angle can be deduced for maximum coupling into a desired Lamb wave mode. The relationship that determines this angle is known as the coincidence principle and is given by $sin\theta = C_w / C$, where θ is the angle of incidence, C_w is the acoustic velocity in the wedge material, and C is phase velocity of the desired Lamb wave mode [99]. Consequently, for a given wedge material the optimum coupling angle is determined by the phase velocity of the desired mode in the load plate. It was considered that for the discussed fibre waveguide coupling technique the optimum cone angle could be the result of a coincidence angle being established, thus maximising the coupling of the incident pressure wave into the L(0,1) waveguide mode. To determine if this was feasible, the simulations were repeated for a different load material, in this case aluminium. As discussed in the previous Chapter, the phase velocity of the L(0,1) mode at low frequency-radius can be approximated to the bar velocity of the

propagation medium, i.e. for copper 3700ms^{-1}, and aluminium 5000ms^{-1}. These phase velocities would determine the optimum angle of incidence and therefore the optimum angle of the cone for a response that was related to the coincidence principle. Consequently the two load materials would be expected to yield significantly different responses. The predicted peak displacement response for varying angles of the cone is displayed in Figure 4.13 for both the copper and aluminium load waveguides. It can be seen that while the load material changes the efficiency of the coupling, it has little affect on the optimum angle of the cone. Subsequently, it can be deduced that the optimum cone angle is not related to the coincidence principle. This result is in good agreement with the proposed coupling hypothesis, which describes the cone as a mechanical transformer. That is, the geometry of the bond determines the optimum coupling irrespective of the load material.

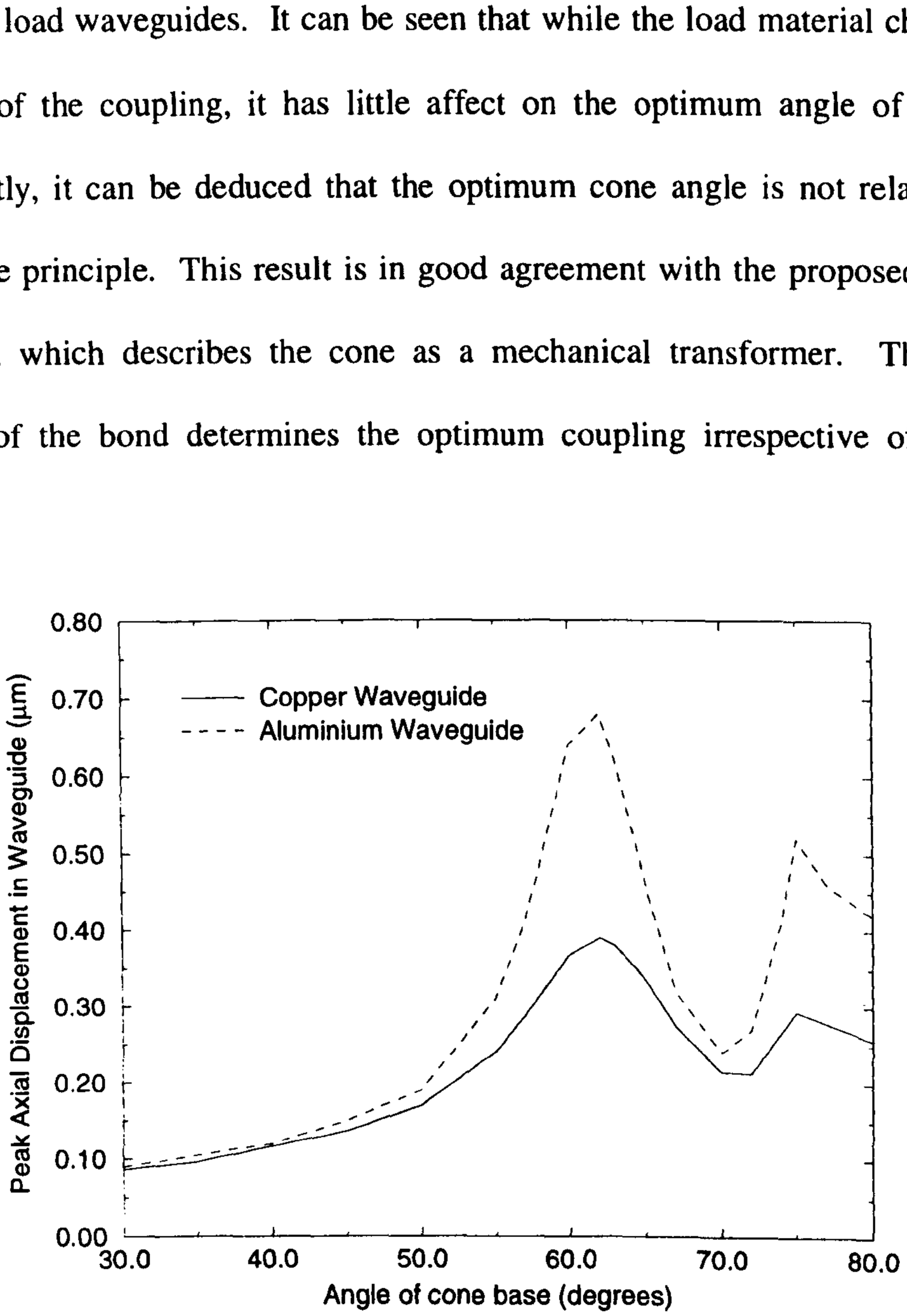

Figure 4.14: *Optimum Cone Angle for Copper and Aluminium Loads*

The next set of simulations investigated the cone angle response for other frequencies of operation, continuing with the aluminium waveguide. The procedure was carried out for 170kHz and then 354kHz, which are also lateral resonant frequencies of the disc transducer. These responses along with the 265kHz results are displayed in Figure 4.15, where it can be seen that the optimum angle changes for different frequencies of operation. Therefore, while it has been shown in the previous Sections that the resonant modes of the transducer determine the frequencies that can be coupled into the waveguide, the geometry of the conical bond interface is critical for optimised efficiency at a particular frequency.

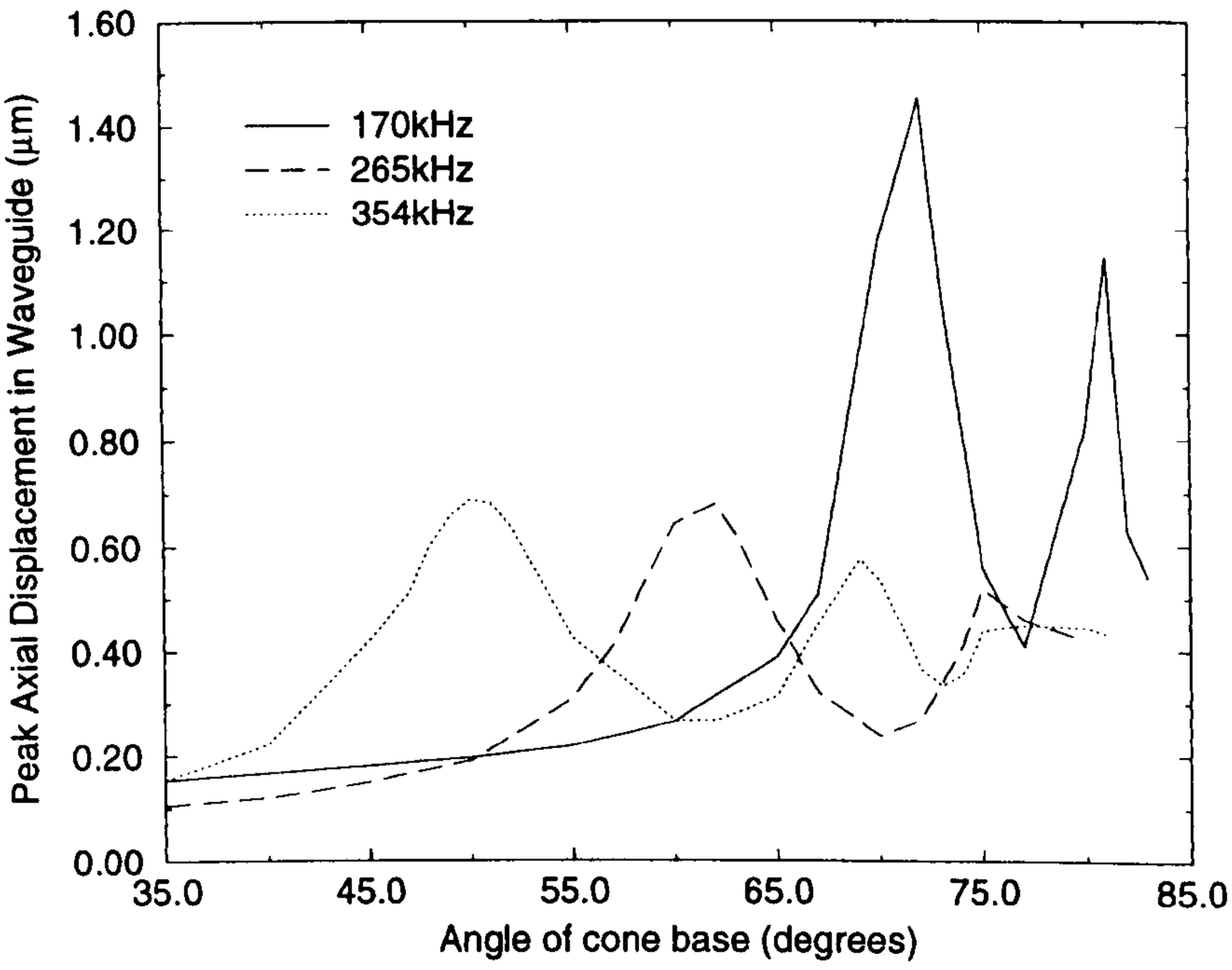

Figure 4.15: *Peak Displacement against Cone Angle for Various Frequencies*

The next set of simulations investigated the cone angle response for various fibre waveguide diameters. The analysis was performed at 265kHz, and the waveguide material was aluminium. The simulations were performed for diameters of

0.125mm, 0.25mm, 0.375mm, and 0.5mm, and the results are displayed in Figure 4.16. Firstly, it can be seen that the diameter of the waveguide does influence the optimum coupling angle of the cone. Moreover, the results display that the peak displacement increases with a reduction in diameter. This seems logical for a coupling mechanism that behaves as a mechanical transformer. That is, as the waveguide diameter is reduced the cone has a lighter load to mechanically drive and subsequently imparts larger displacements.

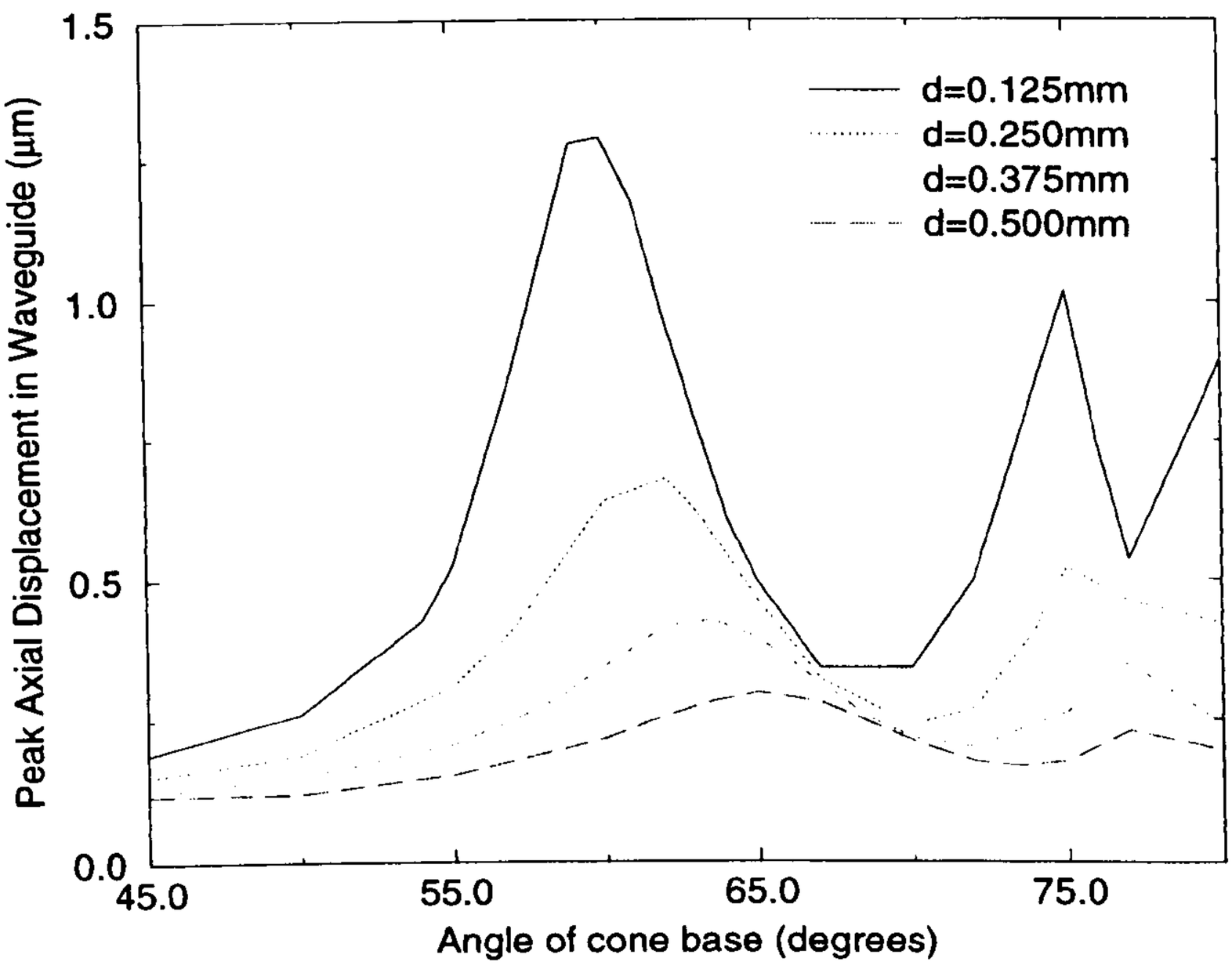

Figure 4.16: *Peak Displacement against Cone Angle for Various Diameters*

The analysis thus far has considered a polymer cone of constant base diameter equal to 4mm. Since the product of the base radius and the tangent of the cone angle determine the height of the cone, the previous peak displacement results could be plotted against cone height instead of cone angle. Consequently to determine which

parameter (angle or height) has the most significant influence on the coupling response the simulations were run for various cone base sizes and the peak displacement data was plotted against both cone angle and cone height. The simulations were performed at an operating frequency of 265kHz and with an aluminium load waveguide, of diameter 0.25mm. Figure 4.17(a) reveals the responses plotted against cone angle, where it can be seen that the optimum angle varies considerably for the differing base diameters. However, Figure 4.17(b) displays the same responses plotted against cone height, where it is revealed that the optimum heights for each bond size are closely matched. This result indicates that the height of the cone is a more significant geometrical parameter than the angle of the cone with respect to optimised coupling. Furthermore it can be clearly seen that an increase in base diameter induces an increase in peak displacement over the entire range of cone heights.

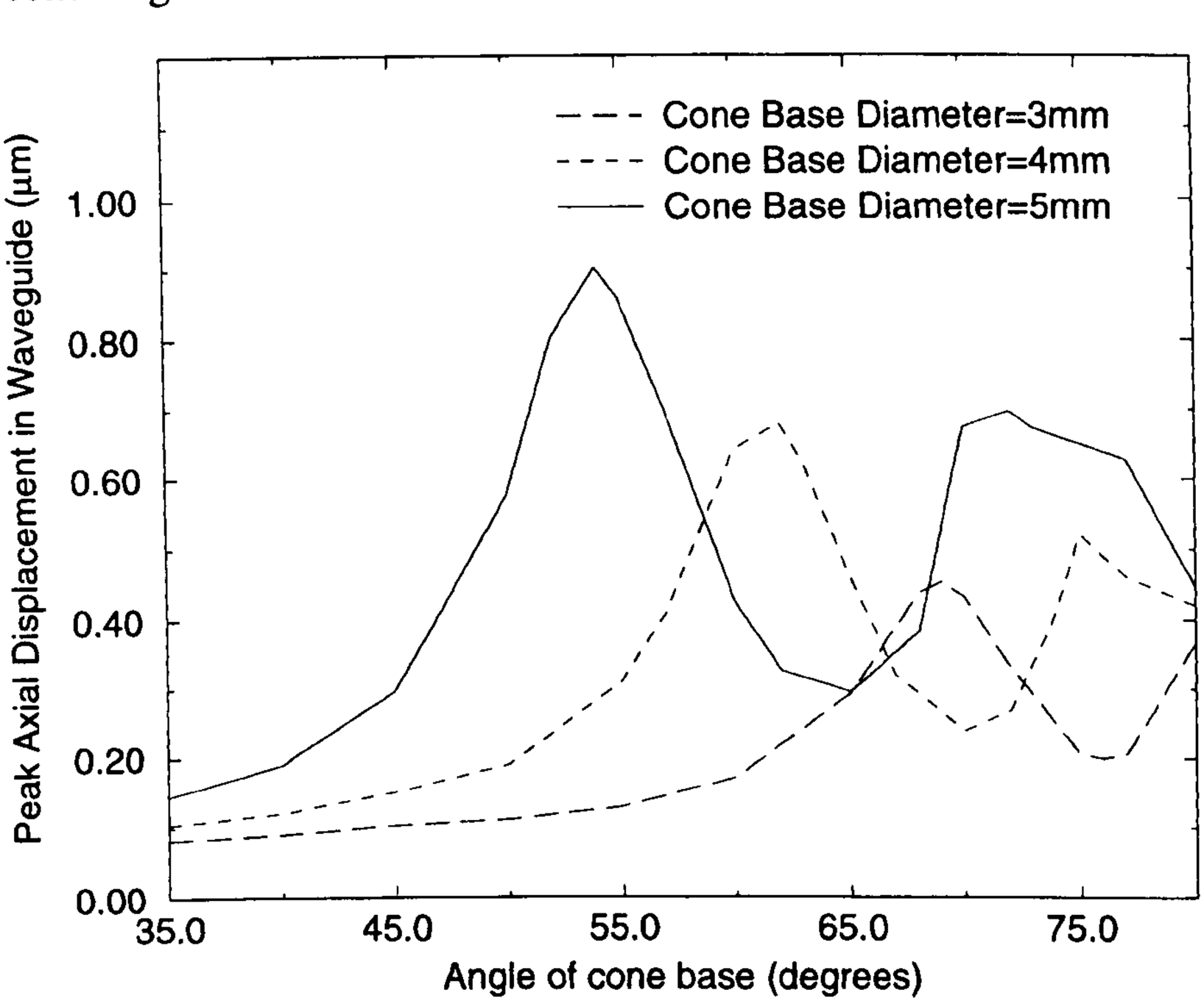

Figure 4.17(a): *Peak Displacement versus Cone Angle for Various Base Diameters*

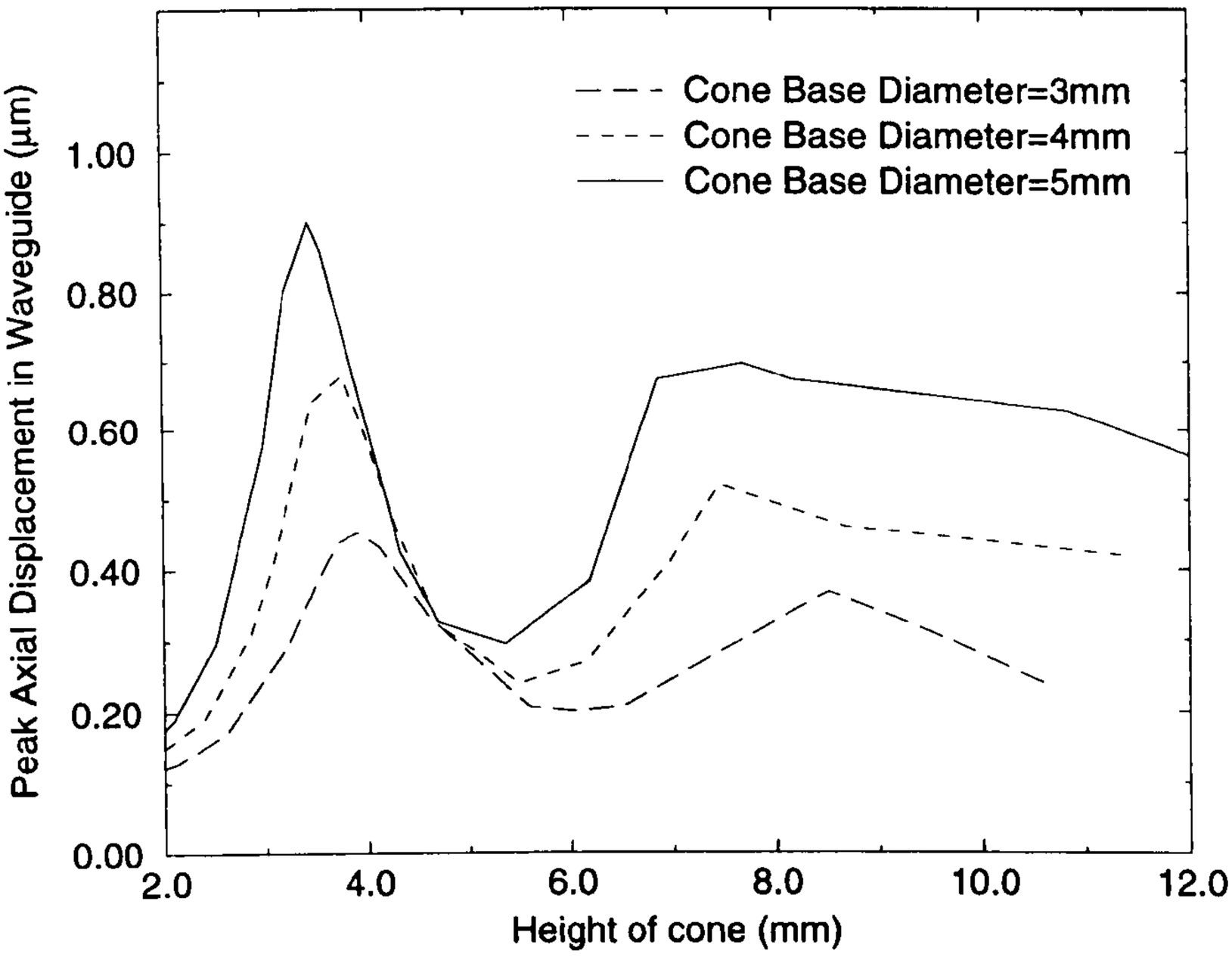

Figure 4.17(b): *Peak Displacement versus Cone Height for Various Base Diameters*

The velocities of the various types of acoustic wave that can propagate in a solid material can be calculated from the elastic constants of the material concerned, namely: Young's modulus of elasticity, E (Nm^{-2}), density, ρ (kgm^{-3}), and Poisson Ratio, ν (dimensionless) [101]. The Poisson ratio (ν) of a material defines the ratio between the lateral compressional strain induced by longitudinal extensional strain [102], and for all solids, $|\nu|$ lies between 0 and 0.5. Given the nature of the polymer cone coupling mechanism, which transforms lateral displacements at the base of the cone, into longitudinal displacements at its apex, it is logical to assume that the Poisson ratio of the cone material will be of significance, and that furthermore a high Poisson ratio would be preferable. To confirm this assumption a final set of simulations was performed to obtain cone angle responses for polymer cones of

varying ν. The polymer utilised for this procedure was a modified version of the previously utilised hard-set epoxy, that is E, and ρ were kept constant while ν was assigned the following values for each set of simulations: ν=0.3, ν=0.35, ν=0.4, ν=0.45. The frequency was 265kHz, and the waveguide was aluminium of diameter 0.25mm. The results are presented in Figure 4.18, where it can be seen that, as expected, an increase in ν results in an improved coupling response. Again, this result corroborates the hypothesis that the polymer cone is acting as a mechanical transformer converting lateral displacements at the base of the cone into longitudinal displacements at its apex.

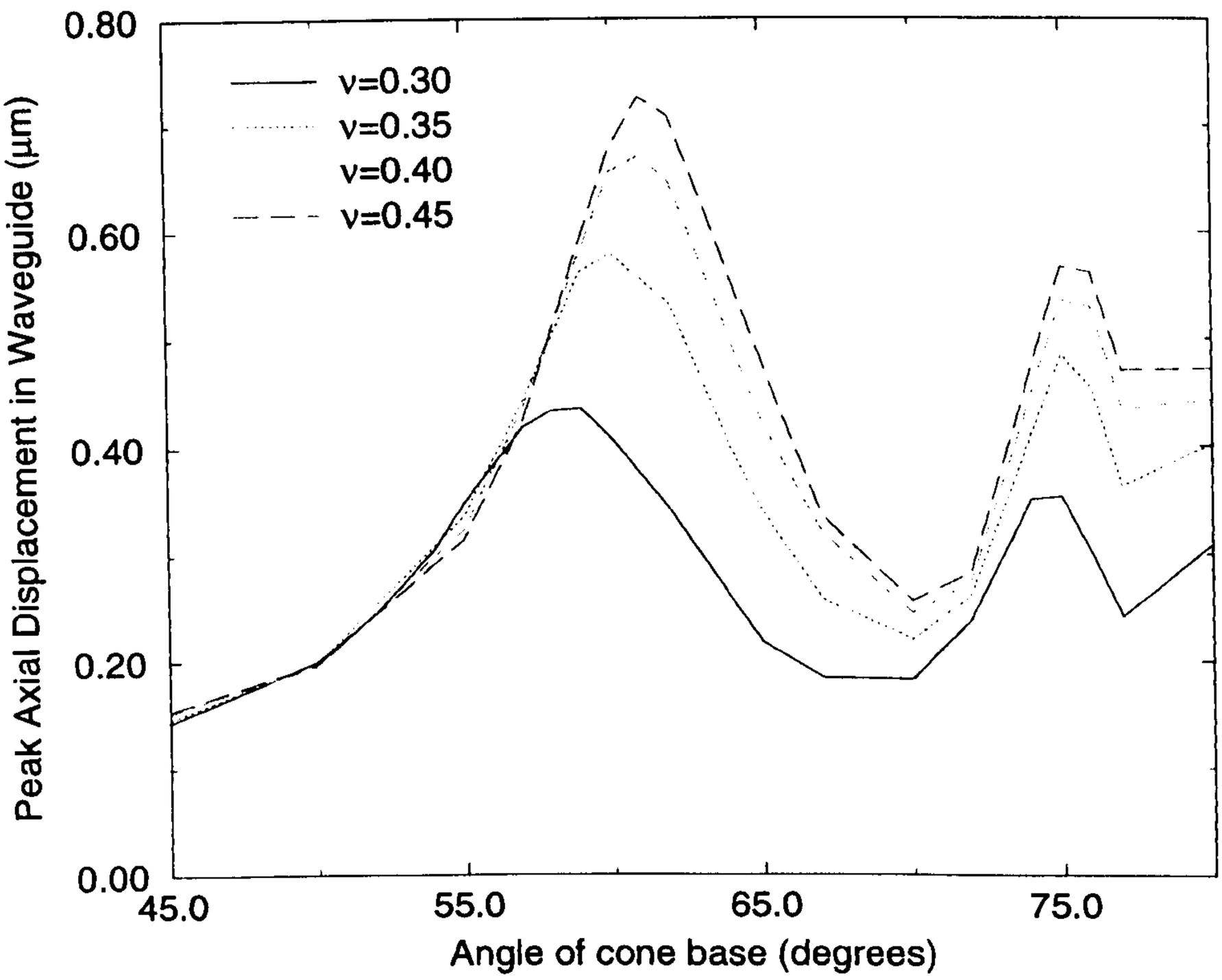

Figure 4.18: *Peak Displacement versus cone angle for various Poisson Ratios*

Section 4.7 has highlighted the importance of the bond geometry to maximise efficient coupling. It was shown that the frequency of operation, diameter of waveguide, and diameter of the cone all have an influence on the efficiency of the coupling and the optimum angle (height) of the cone geometry. Furthermore, it was shown that the fibre waveguide load material does not largely affect the optimum bond geometry, and consequently the coupling mechanism is not related to the coincidence principle. Moreover, these results have all corroborated the hypothesis that the cone is behaving as a mechanical transformer.

4.8. Single L(0,1) Waveguide Mode Considerations for practical Narrowband Experimental Operation

This Chapter so far has discussed the polymer cone coupling mechanism utilised to induce L(0,1) mode propagation in fibre waveguides. The models described were either symmetric, or axisymmetric about the fibre axis, and therefore capable only of predicting the axisymmetric longitudinal modes. In reality, the fundamental flexural mode F(1,1) is also excited albeit to a lesser extent. Figure 4.20 illustrates a typical signal that would be received, adopting the experimental arrangement of Figure 4.19. The transducers utilised for transmission and reception in this experiment were 500kHz, thickness mode PZT5A discs with a strong lateral harmonic at 256kHz. Consequently, a 256kHz, 20 cycle 'Hanning windowed' voltage toneburst of magnitude 20Vp-p was employed to stimulate the transmitting transducer. The waveguide utilised was a copper wire of length 0.7m and diameter 0.5mm, and the receiving amplifier had a gain of 20dB.

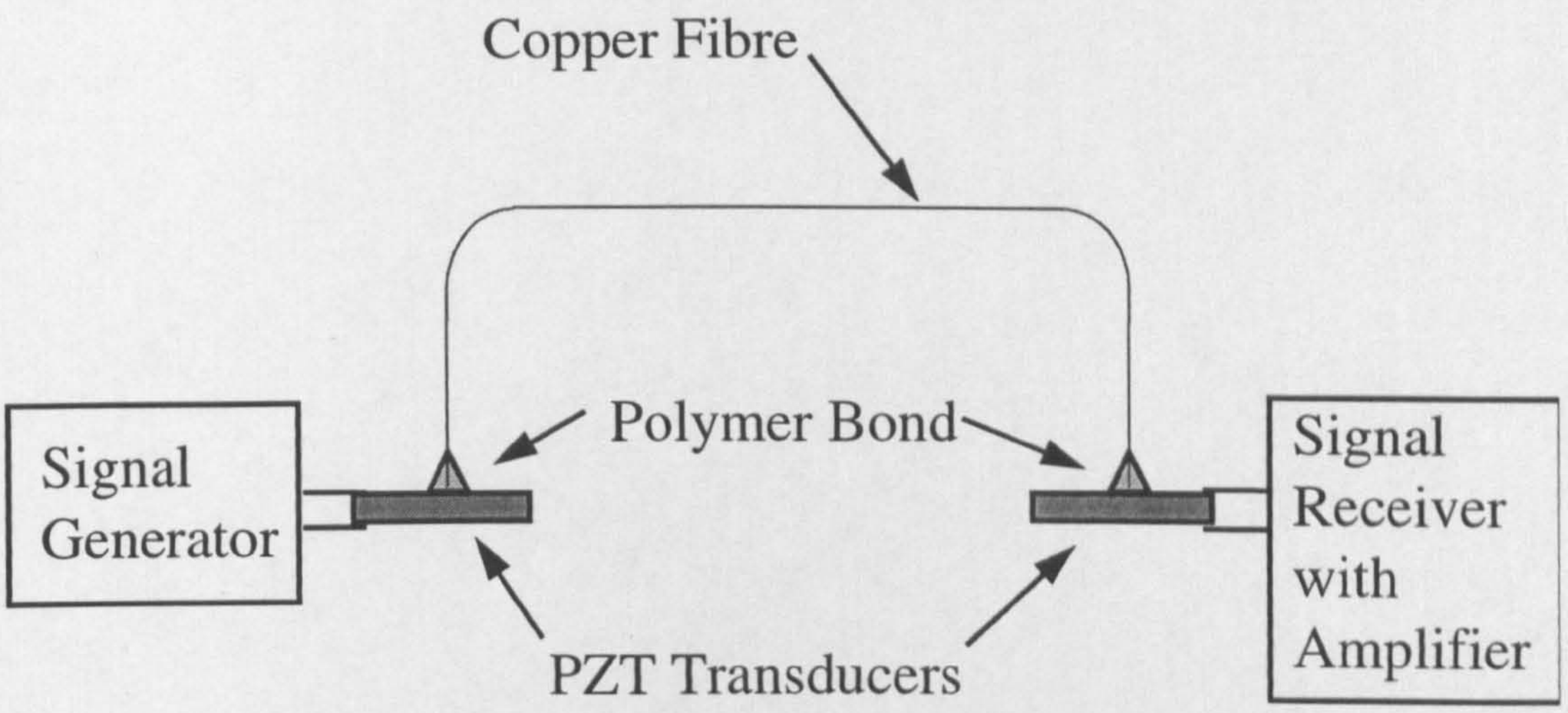

Figure 4.19: Typical Experimental Arrangement

Figure 4.20 shows the efficient generation of the L(0,1) using this coupling technique and represents a typical signal for such an experiment. The Signal to Noise Ratio (SNR) of the excited L(0,1) mode is in excess of **40dB,** however, the F(1,1) mode has also been generated and received. As discussed in Chapter 3, the propagation of non-axisymmetric modes in the waveguides is undesirable for the proposed fibre waveguide monitoring system. Consequently, the F(1,1) may be termed *coherent noise*, and as such the signal to coherent noise ratio (SCNR) of the received signal is much lower, at **17.4dB**.

As highlighted in Chapter 3, the Lamb wave monitoring system proposed in this Thesis requires a transduction technique for robust, efficient uni-modal L(0,1) generation in cylindrical fibre waveguides. As such, a very attractive level of SCNR

would be 40dB to ensure that the L(0,1) is generated as efficiently as depicted in Figure 4.20, while reducing the F(1,1) mode to the random noise level.

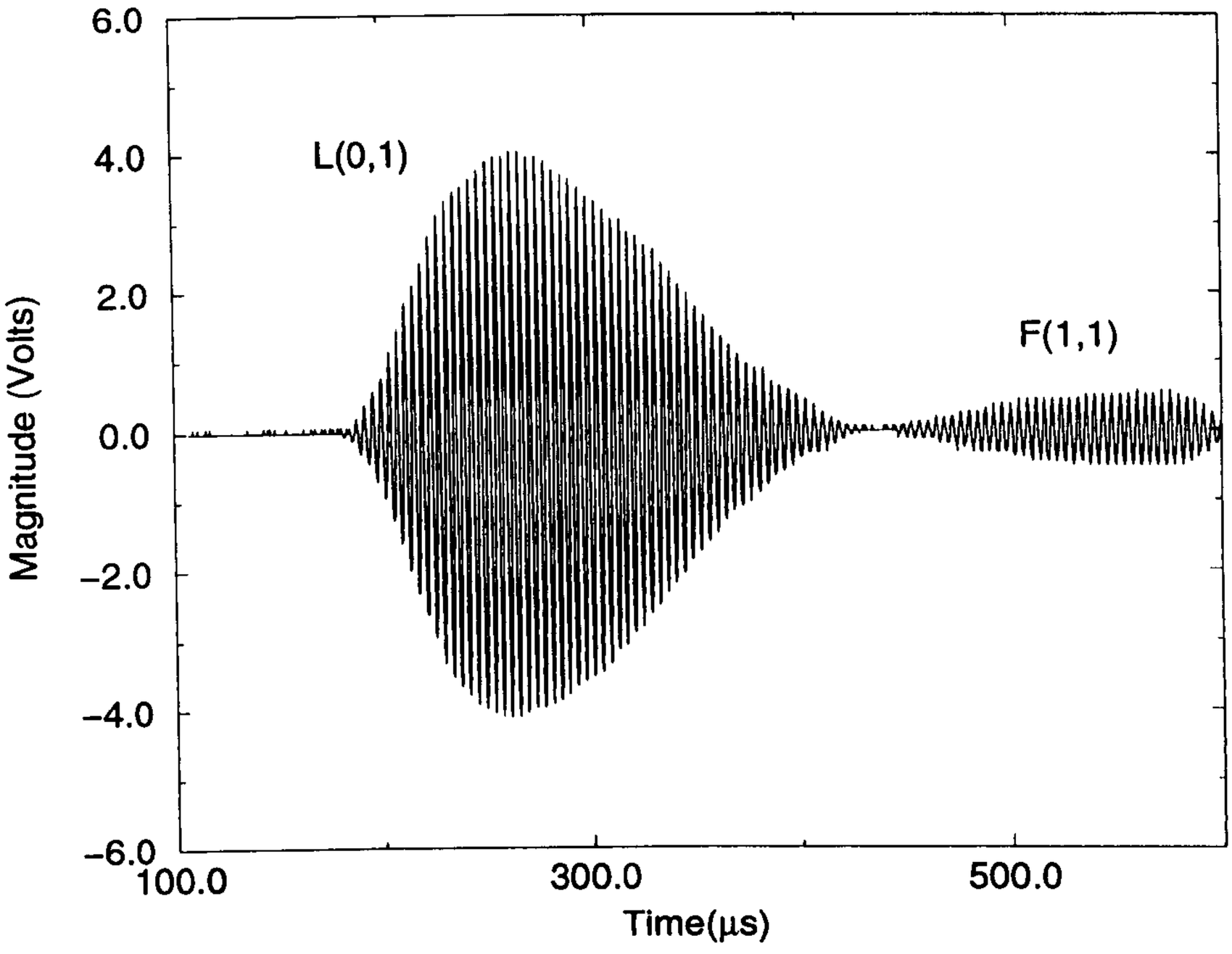

Figure 4.20: Signal Received Using Typical Experimental Arrangement

4.9. Uni-modal Propagation in a Steel Rod

The small diameters associated with fibre waveguides can make absolute control of the displacements imparted on them by the transducer difficult to quantify. Consequently, the generation of single mode propagation in fibre waveguides is non-trivial. However, for larger diameter cylinders (of comparable lateral dimensions to the excitation transducer) uni-modal propagation is more readily achieved. Therefore, this Section will investigate single mode propagation in a steel rod, in an attempt to highlight any critical factors that may be applicable to uni-modal operation

in fibres. The modes of particular interest are L(0,1) and F(1,1) since these are readily excited in fibres. The steel rod utilised in the following experiments has a diameter of 3.2mm, a length of 1050mm. In addition, its ends were machined square with the rod held in a collet. The group velocity dispersion curves for the rod are presented in Figure 4.21, calculated from the relevant theory presented in Chapter 3.

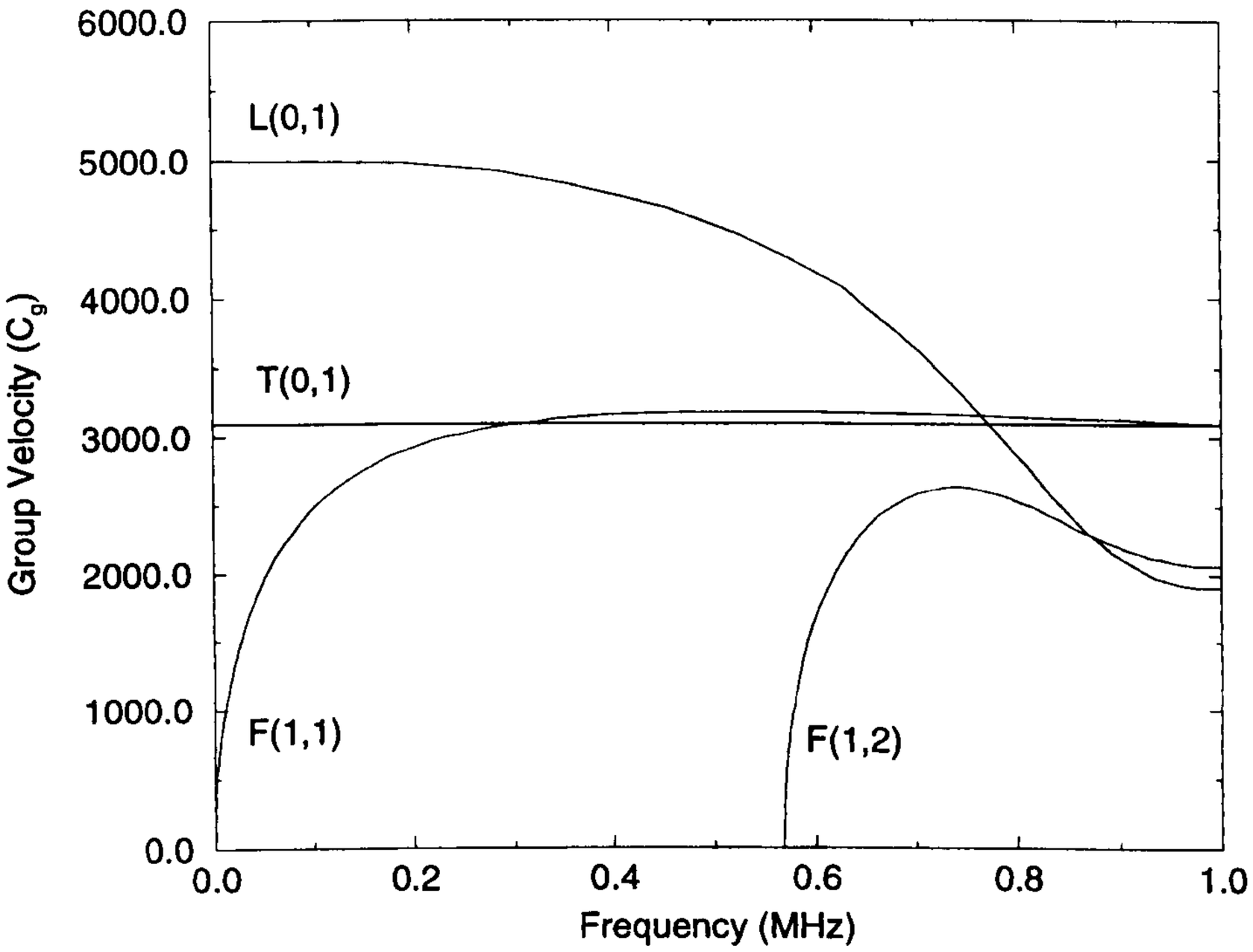

Figure 4.21: *Dispersion Curves for a 3.2 mm Steel Rod*

4.9.1. L(0,1) Generation in a Steel Rod

This Section describes an experiment to generate and receive the L(0,1) mode in the steel rod described previously. The transducers utilised to generate and receive the ultrasonic energy were 270kHz thickness-mode rectangular PZT5A pillars of thickness 5.04mm and lateral dimensions 3.2mm x 3.2mm. As illustrated in Figure

4.22, these were adhered to each end of the rod, with the transducer's thickness mode vibration in-line with the rod's axis. The input signal applied to the transmitting pillar transducer was a 270kHz, 15Vp-p, 'Hanning windowed' toneburst of 20 cycles, and the receiver amplifier had a gain of 20dB.

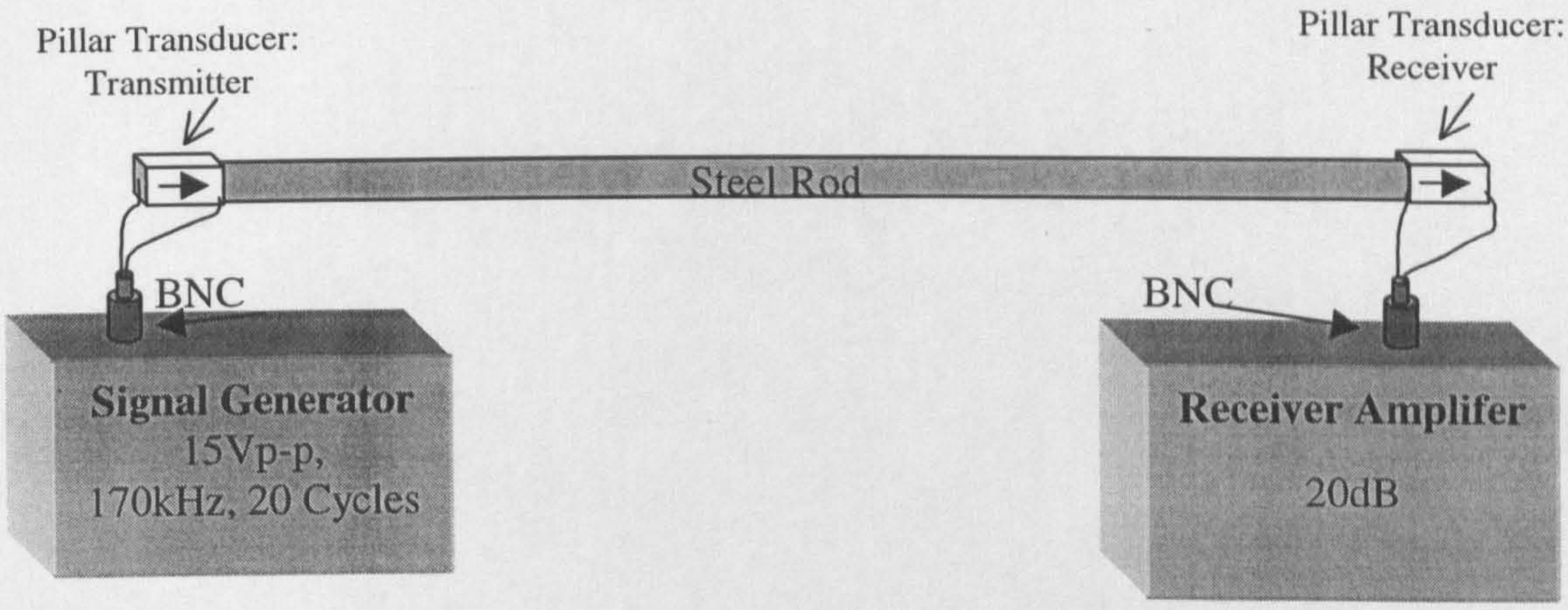

Figure 4.22: *Experimental Arrangement for L(0,1) Excitation in a Steel Rod*

From the dispersion curves shown in Figure 4.21 it can be established that for a frequency of 270kHz, the group velocities of the L(0,1) and F(1,1) modes are $4895ms^{-1}$ and $3055ms^{-1}$ respectively, and consequently the propagation times along the rod are 215μs and 344μs respectively. The received signal is shown in Figure 4.23, where it can be seen that the L(0,1) mode has been singly excited and received with a SNR of 34dB.

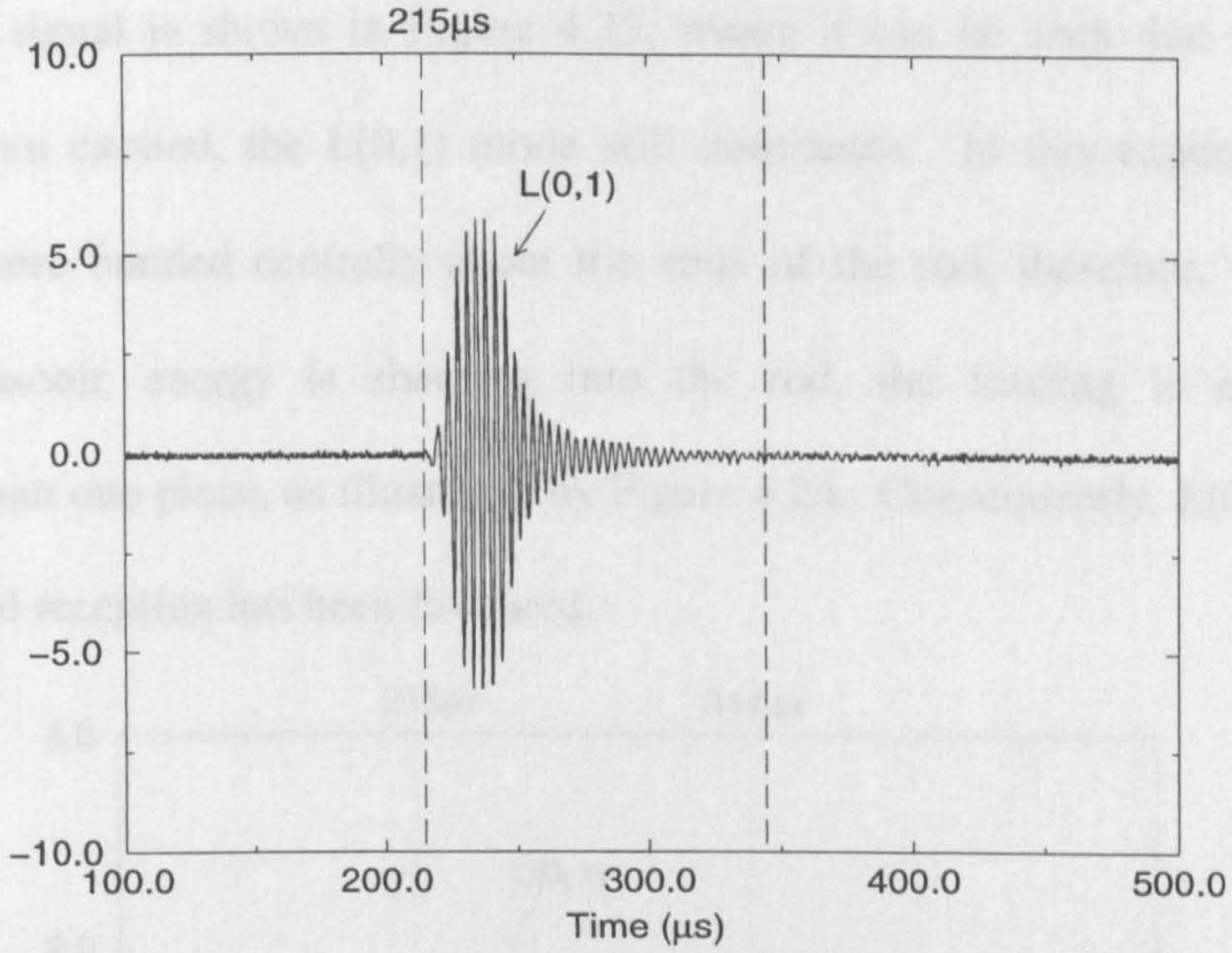

Figure 4.23: *Signal Received for L(0,1) mode Excitation in a Steel Rod*

4.9.2. F(1,1) Generation in a Steel Rod

In an attempt to stimulate F(1,1) mode propagation, the previous experiment was repeated with the pillar transducers adhered normally (with respect to their thickness mode vibration) to the ends of the rod, as depicted in Figure 4.24. It was considered that this form of acoustic coupling would be more conducive to flexural mode excitation, since the transmitter would impart shear stresses to the end of the rod.

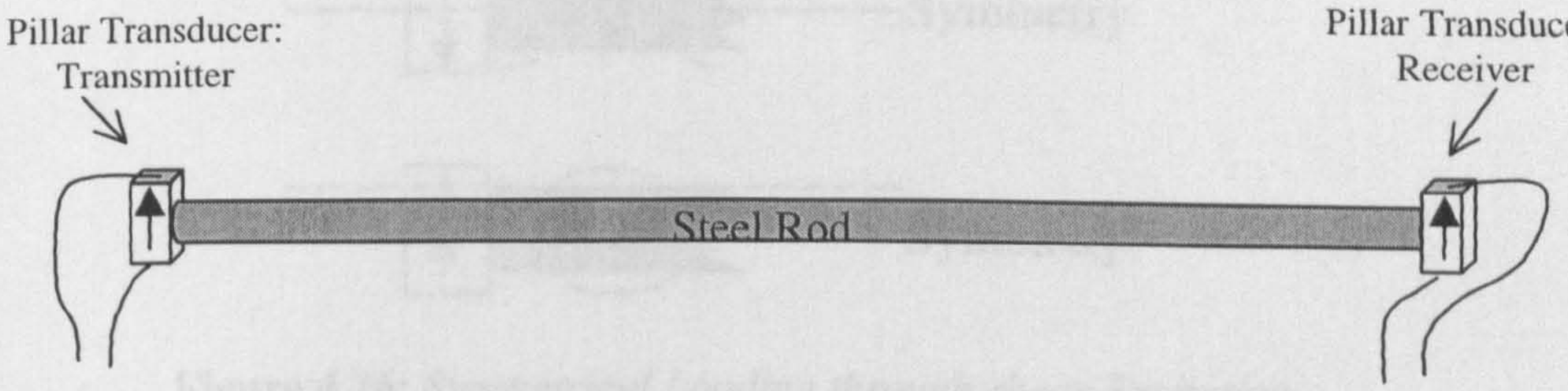

Figure 4.24: *Experimental Arrangement for F(1,1) Excitation in a Steel Rod*

The received signal is shown in Figure 4.25, where it can be seen that while the F(1,1) has been excited, the L(0,1) mode still dominates. In this experiment the transducers were bonded centrally about the ends of the rod, therefore, while the incident ultrasonic energy is shearing into the rod, the loading is essentially symmetric about one plane, as illustrated by Figure 4.26. Consequently, L(0,1) mode generation and reception has been favoured.

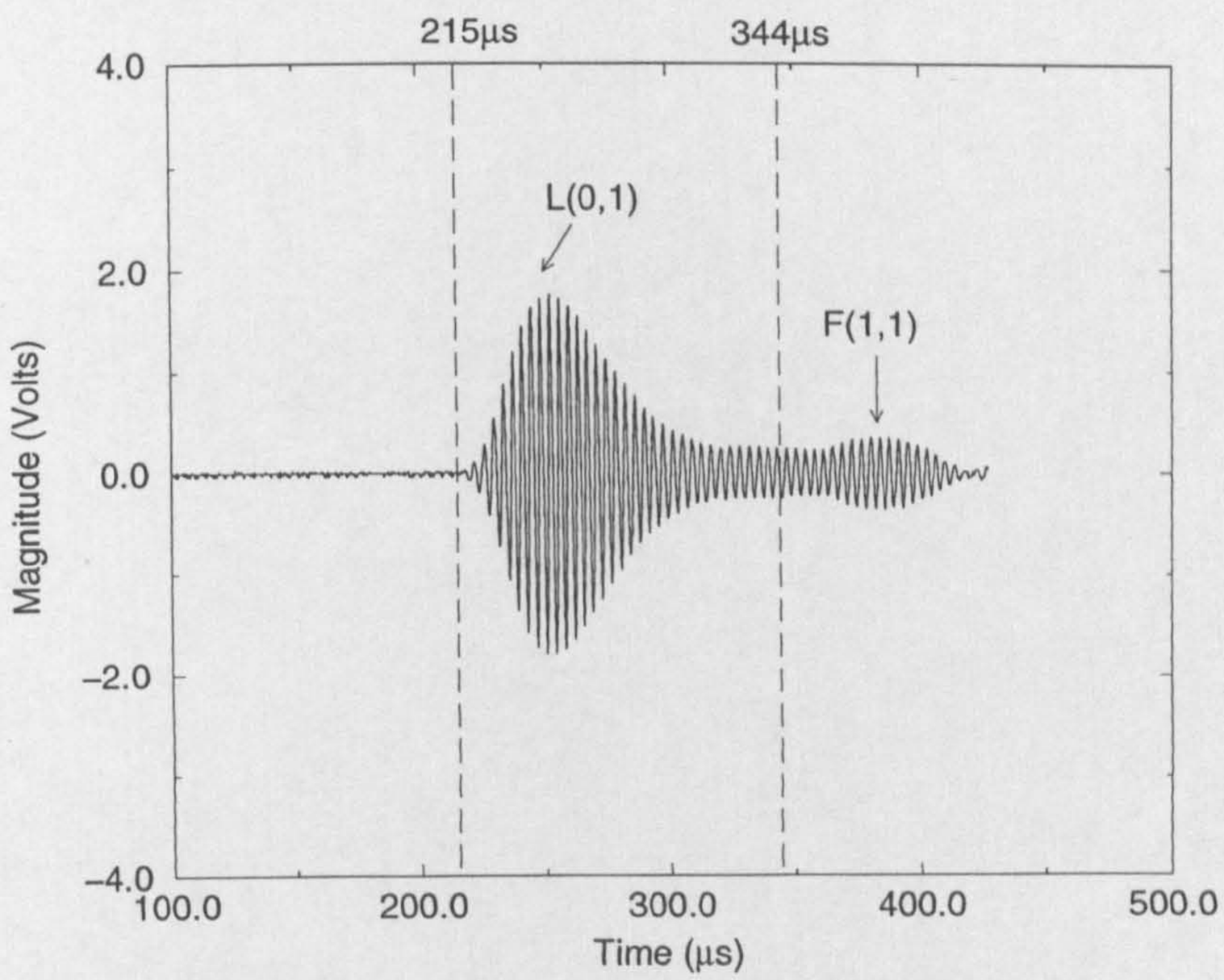

Figure 4.25: *Signal Received for F(1,1) Mode Excitation in a Steel Rod*

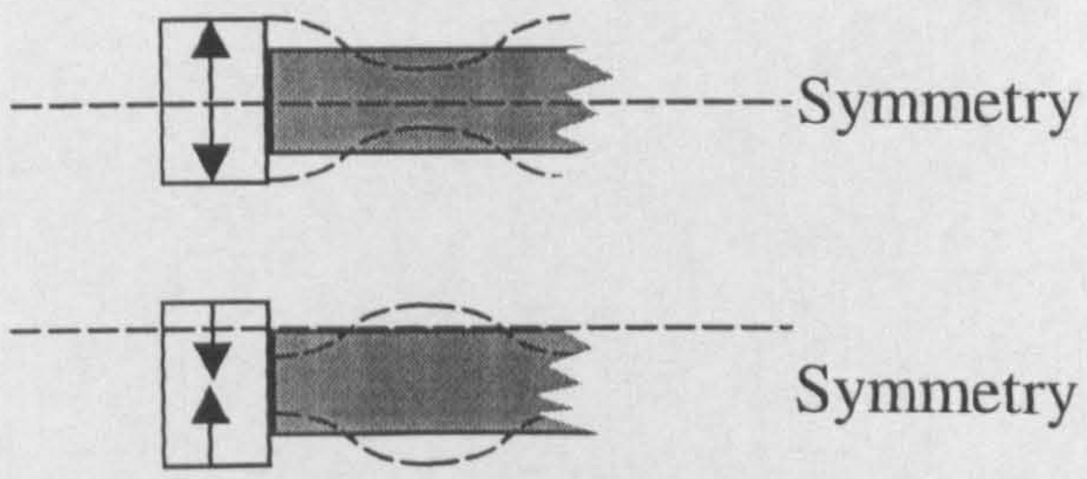

Figure 4.26: *Symmetrical Loading through shear Excitation*

In order to reduce the symmetry, the experiment was repeated with the transducers adhered off-centre. Two configurations were adopted and are shown in Figure 4.27. For configuration 1, the top edge of the transmitting and receiving pillar transducers are aligned to the centre of the rod, while in configuration 2 the transducers were adhered to the rod as near the circumference as possible. The received signals for both configurations are displayed in Figure 4.28.

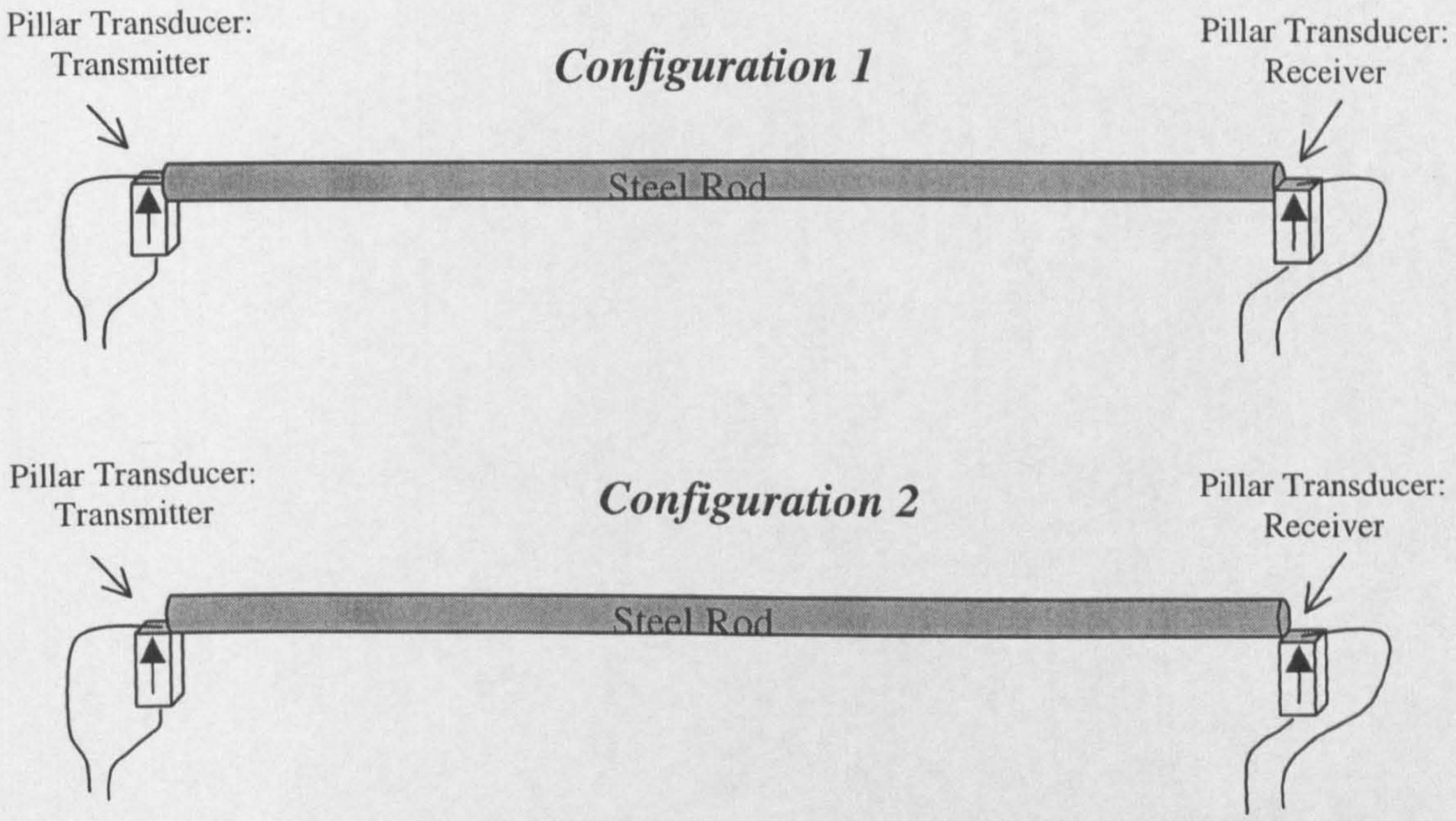

Figure 4.27: *Asymmetric Loading For F(1,1) Mode Generation in a Steel Rod*

Since the F(1,1) mode is of interest in this Section the L(0,1) mode can be considered as coherent noise, consequently, the SCNR for configuration 1 is 3.8dB. While this value is rather low it is a marked improvement on the previous experiment where the centrally adhered transducer preferentially generated the L(0,1) mode. Moreover, it can be seen that as the asymmetry of the loading increases the SCNR of the F(1,1)

mode increases, with configuration 2 providing a SCNR of 22.2dB. It should be noted that configuration 2 actually generates a weaker F(1,1) mode than configuration 1. This is because less of the active area of the transducer is in contact with the rod, however the SCNR is the parameter of merit for this discussion.

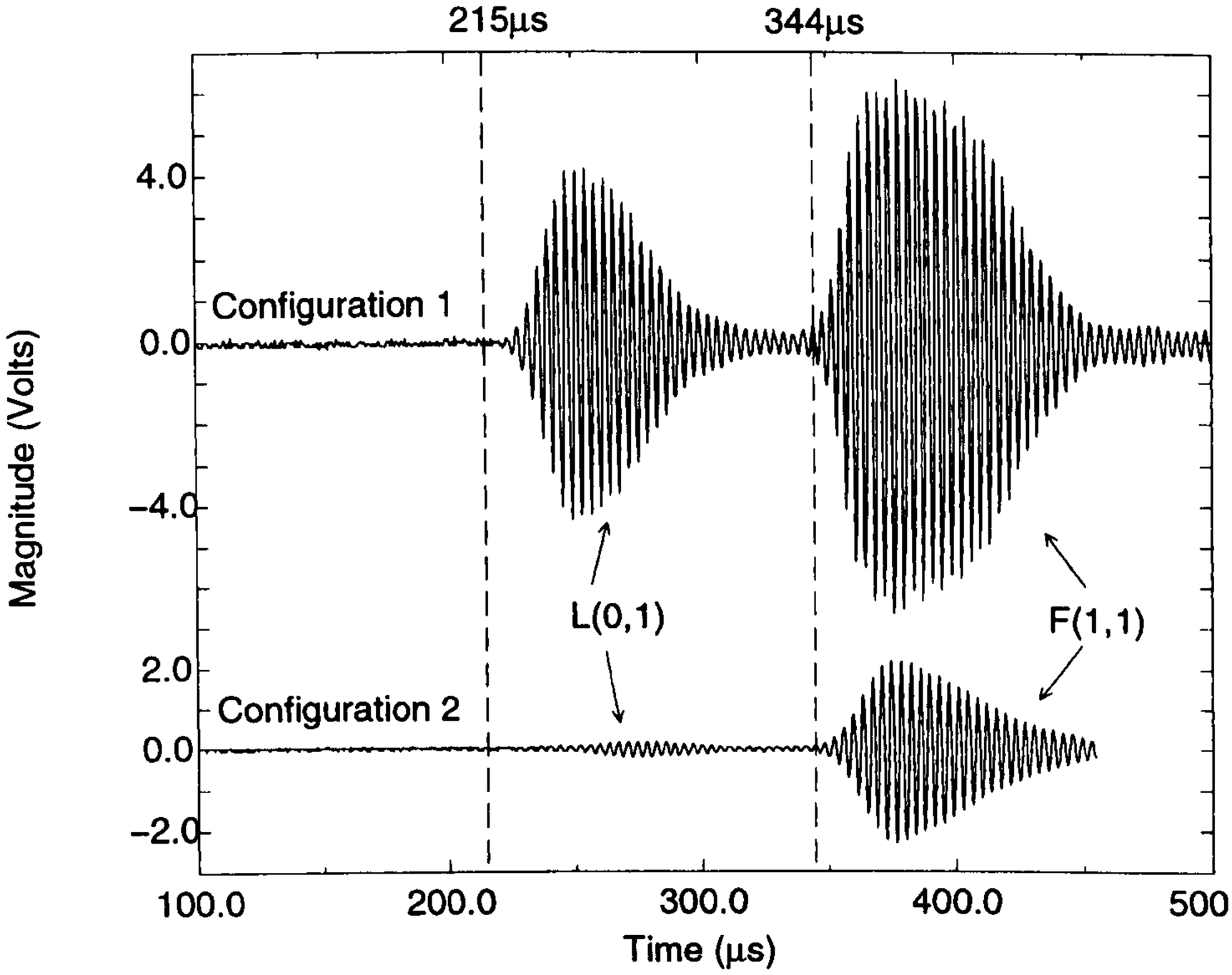

Figure 4.28: *Signals Received with Asymmetrical Configurations for F(1,1) Excitation*

When a driving voltage is applied across the electrodes of a piece of shear poled ceramic it deforms in a manner depicted by Figure 4.29, generating shear stresses perpendicular to the applied voltage [103]. Consequently, a 400kHz shear poled MPT ceramic pillar was cut with lateral dimensions 3.2mm x 3.2mm, to impart an

asymmetrical load onto the end of the steel rod, with a similar transducer used in reception. The experimental arrangement is similar to that of Figure 4.22, except that the driving voltage frequency is 400kHz, to excite the shear poled ceramic pillar described.

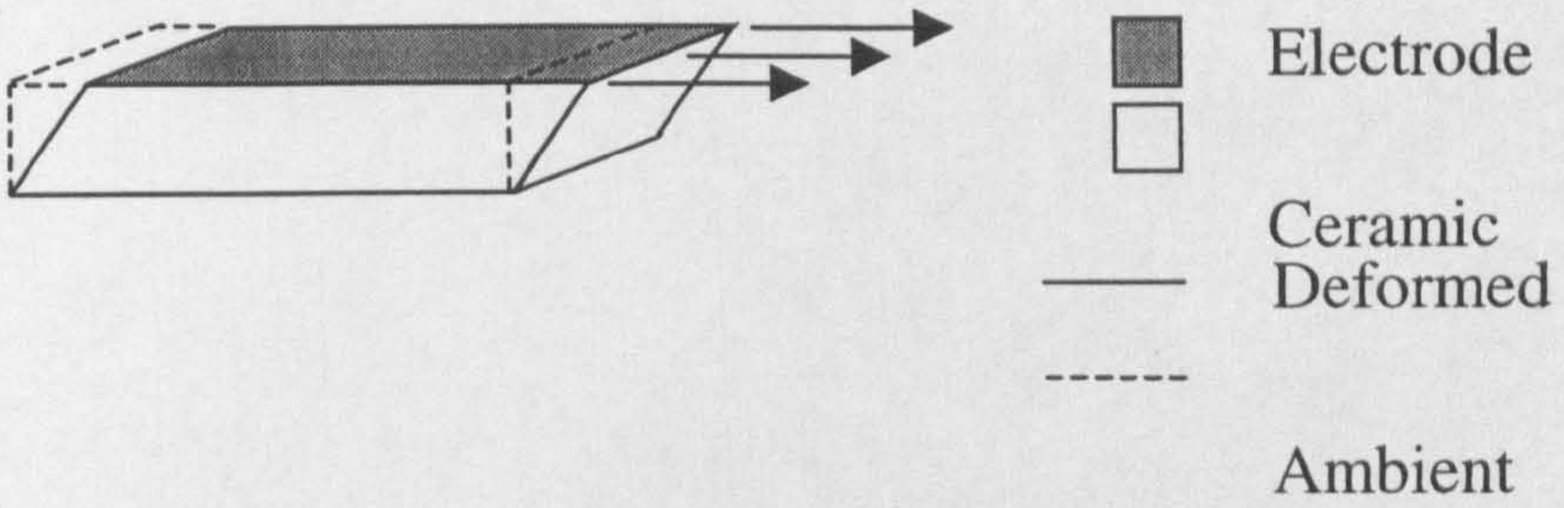

Figure 4.29: *Shear Poled Ceramic*

From the dispersion curves shown in Figure 4.21 it can be deduced that for a frequency of 400kHz the group velocities of the L(0,1) and F(1,1) modes are $4735ms^{-1}$ and $3160ms^{-1}$ respectively, and consequently the propagation times along the rod are 222μs and 332μs respectively. The received signal is shown in Figure 4.30, where it can be seen that the F(1,1) mode has been singly excited and received with a SNR in excess of 28dB.

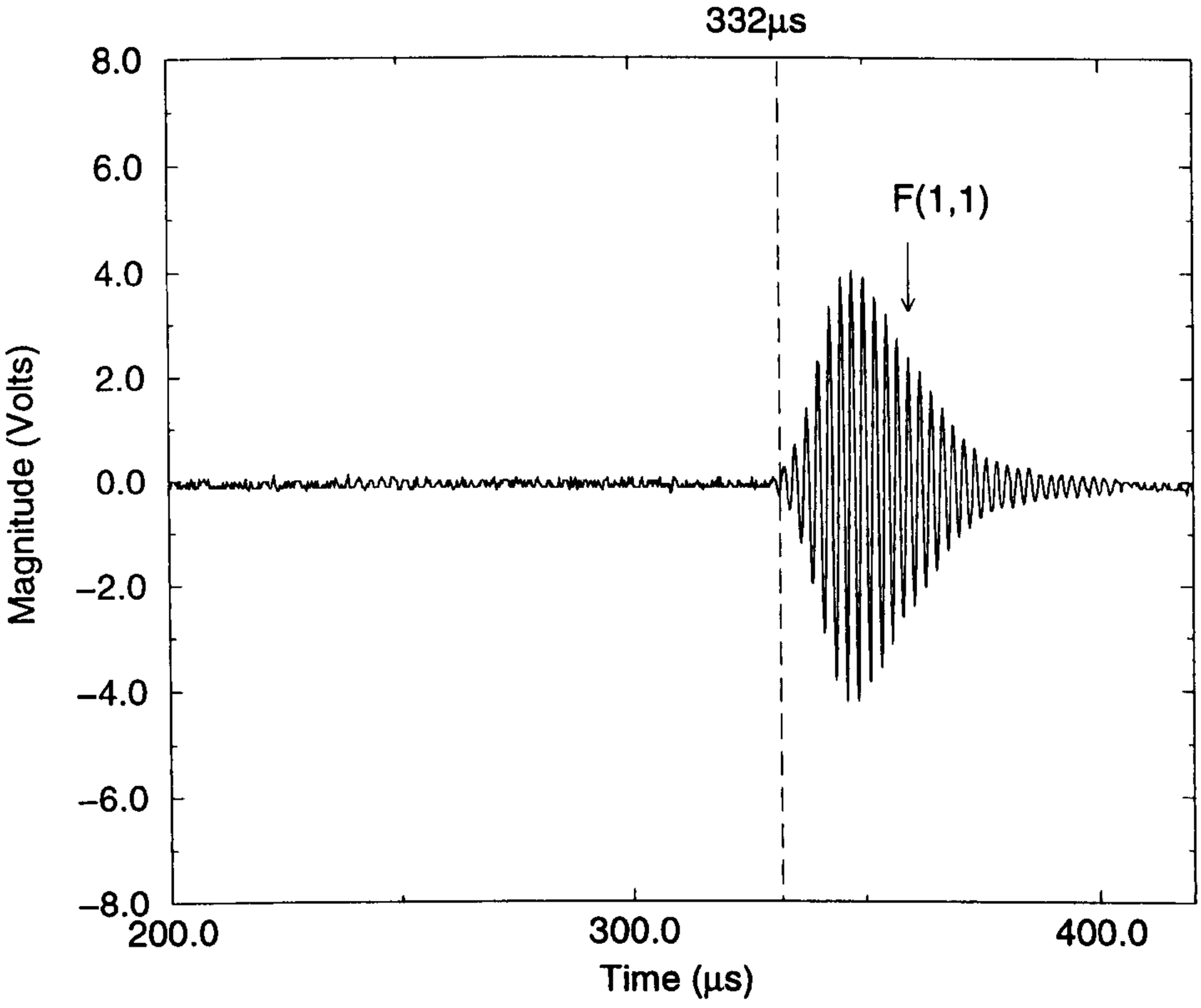

Figure 4.30: *Signal Received with Shear Poled Ceramic Excitation of mode F(1,1)*

4.9.3. Discussion on Uni-modal Propagation in a Rod

Uni-modal L(0,1) excitation in a steel rod was shown to be easily achieved in Section 4.9.1. Here axial stresses were imposed on the end of a rod by simply attaching a piezoceramic pillar transducer (of comparable lateral dimensions to that of the rod's diameter) to an end of the rod. Section 4.9.2 provided the interesting result that when coupling normal to the axis of the rod, the greater the asymmetry of the loading the better the SCNR of the received F(1,1) signal. Section 4.9.3 then went on to show that using shear polled ceramic to impart an asymmetrical loading to the end of the rod, resulted in uni-modal F(1,1) excitation.

Therefore, it can be seen that that minimising asymmetry in the loading will minimise flexural generation. Consequently, for longitudinal operation in fibre waveguides, the coupling arrangement should be configured as axisymmetrically as possible to suppress flexural excitation. This task, while easily achievable in rods where the ends can be machined flat and the transducers are of comparable size to the rod's diameter, becomes increasingly more difficult as the diameter is reduced.

4.10. Polymer Cone Revisited

Section 4.8 included a description of an experiment carried out using the polymer cone coupling technique to generate and receive ultrasound along a 0.7m length of 0.5mm copper wire waveguide at 256kHz. It was shown that a typical response for L(0,1) mode operation using this technique yielded a SNR of 40dB and a SCNR of 17dB. However, in reaction to the findings of the previous Section, the experiment was repeated with the intention of improving on the axisymmetry of the interface. That is, extra attention was taken to centralising the polymer cone on the piezoceramic disc transducer, in both generation and reception, and in ensuring that the waveguide was located centrally within the bond. Figure 4.31 reveals the signal that was received when this procedure was adopted. It can be seen that a superior response has been achieved with a SCNR of **25dB** and a SNR of **41dB**.

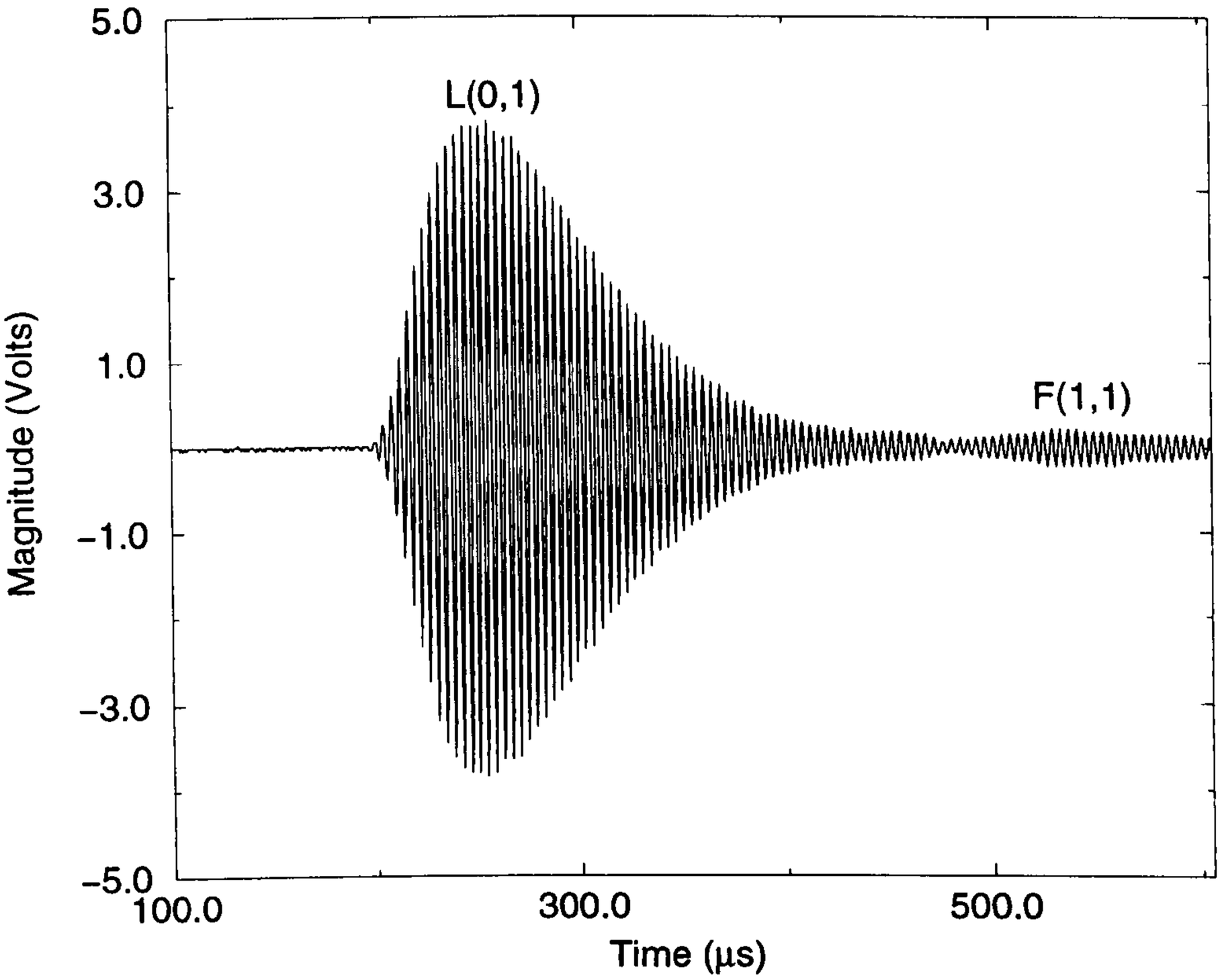

Figure 4.31: *Polymer Cone Revised with Improved Axisymmetrical Layout*

4.11. Design Guidelines

When designing a waveguide system utilising this form of coupling for efficient L(0,1) mode generation the following design parameters should be considered:

- A piezoceramic material with strong lateral activity (high d_{31}) such as PZT5A should be utilised and excited at one of its lateral harmonics.

- A polymer bond with a high Poisson Ratio is favoured since the bond behaves as a mechanical transformer converting lateral displacements at its base into longitudinal displacements at its apex.

- For a given frequency, diameter of waveguide, and bond material an optimum cone geometry will exist to maximise the coupling efficiency. This can be established utilising FEA, where a systematic approach is adopted to sweep through various cone geometries.

- The coupling arrangement should be configured as axisymmetrically as possible. That is, the fibre should be held centrally within the polymer cone, and the cone should be attached centrally on the surface of the piezoceramic disc.

4.12. Conclusions

This Chapter has presented FEA results on the coupling of mechanical energy from a piezoceramic transducer into ultrasonic propagation along a cylindrical waveguide via a conical polymer bond. As such, early visual analysis on the displacement of the polymer interface indicated that it acts as a mechanical transformer, with its base moving in sympathy with expansion and contraction of the piezoelectric plate in the lateral direction, resulting in the apex of the cone undergoing corresponding compression and expansion to induce longitudinal motion in the waveguide. This hypothesis was strengthened with the revelation that the lateral harmonics of the piezoceramic transducer were more efficiently coupled into the waveguide than its thickness mode when excited with a wideband voltage signal. The FEA was then modified to an axisymmetric model to simulate piezoceramic disc transducers and improve the geometrical accuracy. Again the lateral (in this case radial), harmonics

of the disc were shown to couple more efficiently into the waveguide than the thickness mode. These theoretical results were confirmed experimentally where even the weak lateral modes of an MPT disc transducers where preferentially coupled into the waveguide.

Furthermore, narrowband analysis on the polymer interface demonstrated that the geometry of the bond is critical for optimised coupling efficiency. It was shown that the frequency of operation significantly influences the optimum bond angle. Additionally, for conical bonds of various base diameters, it was shown that the optimum cone angle was not constant, however the optimum height of the cone is similar. Importantly, it was shown that the load medium does not largely affect the optimum bond geometry, which eliminated the possibility of the response being related to the coincidence principle. Significantly, it was revealed that the thinner the fibre waveguide, the larger the axial displacements induced within it, which corroborates the mechanical transformer hypothesis since the polymer cone would generate larger displacements in a lighter load.

The Chapter then went on to experimentally quantify the generation of undesirable non-axisymmetric modes in fibre waveguides when utilising the polymer cone technique and narrowband excitation. Initial experiments indicated a SNR of 40dB, and a SCNR of 17.4dB for L(0,1) mode operation. In an attempt to improve on this the Chapter went on to investigate uni-modal longitudinal and flexural propagation along a steel rod of diameter 3.2mm. Significantly, it was established that reducing

the asymmetry of the loading reduced the relative coupling into the flexural mode. Consequently the polymer cone technique was revisited to improve upon the axisymmetrical nature of the layout, resulting in an enhancement of the SCNR from 17.4dB to 25dB.

In Section 4.8 it was proposed that an attractive SCNR value would be 40dB to reduce erroneous modes down to the random noise level. It is evident that this has not been achieved and that further investigation into uni-modal coupling techniques for acoustic fibre waveguides is required. However, the polymer cone coupling technique, whose mechanism is well understood from the FEA of this Chapter does provide a cheap, simple, robust coupling strategy with a high SNR and reasonable SCNR, and shall therefore be utilised in the subsequent Chapters.

CHAPTER 5

Proof of Concept: Surface Mounted Fibre Lamb Wave System

5.1. Introduction to Chapter

This Thesis is concerned with the realisation of an embedded ultrasonic monitoring system for operation in a smart structure environment. As such, permanently attached or embedded sensors may be required to inspect large areas. Since Lamb waves are capable of propagating over large distances, the integration of Lamb wave sensors into a host material has recognised potential for smart structure technology [5]. However, it is essential that any embedded instrumentation does not detract from the integrity of the structure and therefore should be minimal in size. Consequently, this Chapter describes and demonstrates a novel system exploiting the use of thin cylindrical ultrasonic fibre waveguides for Lamb wave generation and detection.

To outline the relevance of the work carried out in this Chapter an introduction to Lamb wave technology will be provided to discuss relevant theory and current Lamb wave excitation methodology. The Chapter then goes on to describe the realisation of a fibre based monitoring system, whereby fibre waveguides are bonded to aluminium plates for the generation and detection of Lamb waves with experimental and modelling results presented. These preliminary surface mount results provide a 'proof of concept' to show that fibre waveguides can be utilised to generate and detect suitable ultrasonic signals for a smart structure environment. As such these results provide the first logical step to establishing a fully embedded ultrasonic fibre waveguide monitoring system.

5.2. Introduction To Lamb Wave Technology

5.2.1. Lamb Wave Overview

Lamb waves, also known as plate waves, are guided waves that propagate in a direction parallel to the surface of the plate at velocities that depend on the elastic properties of the plate, its thickness, and the frequency of the wave. An excellent description of Lamb wave propagation and relevant theory is provided by Viktorov [99]. There are two types of Lamb wave, the asymmetrical (or bending) wave, and the symmetrical (or stress) wave. All Lamb waves produce both in-plane and out-of-plane displacements. The asymmetrical Lamb wave modes are flexural waves, producing primarily out-of-plane displacements, whereas the symmetric Lamb wave modes are predominantly in-plane displaying longitudinal particle motion along their central plane. The out-of-plane surface displacement largely governs the excitability of the mode when generated via surface loading [104] resulting in asymmetrical Lamb wave modes often being more readily produced. Figure 5.1 provides a graphical description of the two fundamental wave types.

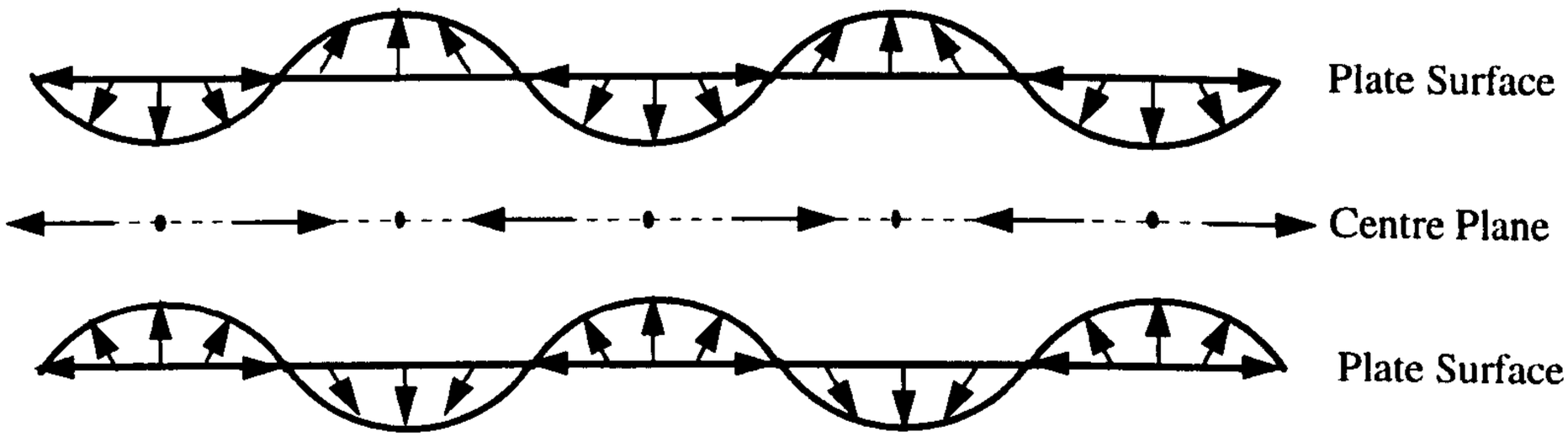

Fundamental Symmetric Lamb Wave

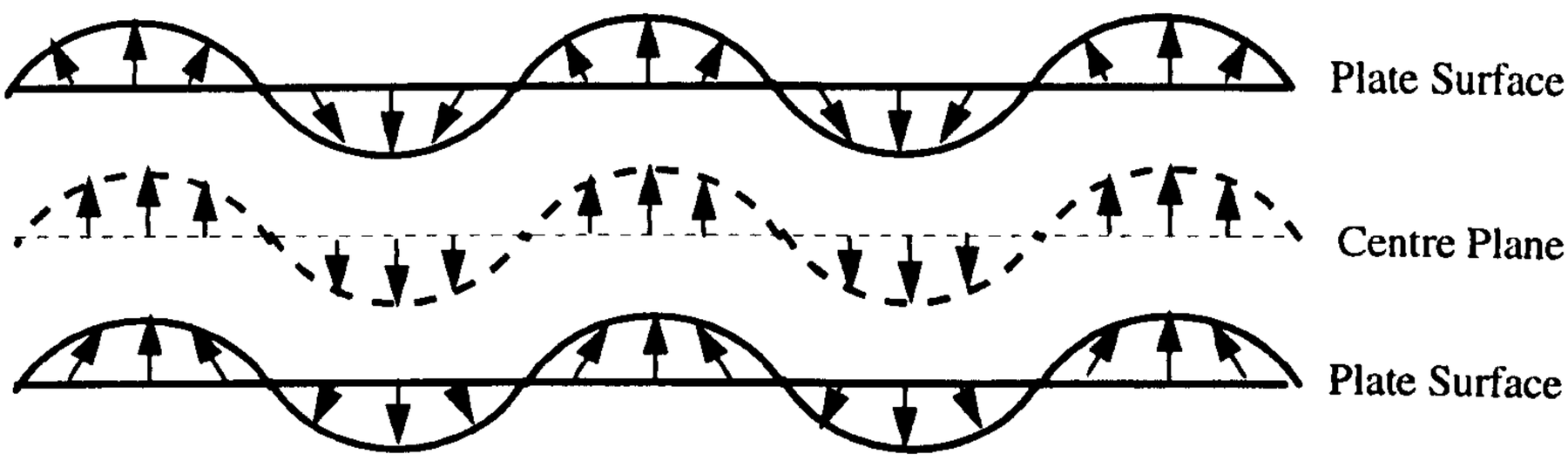

Fundamental Asymmetric Lamb Wave

Figure 5.1: *Fundamental Lamb Wave Mode Shapes*

As with acoustic guided waves in cylinders, which were discussed at length in Chapter 3, Lamb waves are dispersive, and thus have dispersion curves associated with them providing phase and group velocity information on the possible modes of propagation. The frequency equation utilised to yield Lamb wave dispersion curves is given by Equation 5.1, and is commonly known as the Rayleigh-Lamb wave Equation [99].

$$\frac{\tanh\left(\frac{\beta h}{2}\right)}{\tanh\left(\frac{\alpha h}{2}\right)} = \left[\frac{4k^2\alpha\beta}{\left(k^2+\beta^2\right)^2}\right]^{N=\pm 1} \qquad \textbf{5.1}$$

Where:

$$\alpha = 2\pi f\sqrt{\frac{C_l^{\,2}-C^2}{C_l^{\,2}C^2}} \qquad \textbf{5.2}$$

and

$$\beta = 2\pi f\sqrt{\frac{C_s^{\,2}-C^2}{C_s^{\,2}C^2}} \qquad \textbf{5.3}$$

In these Equations C_l, C_s, and C are longitudinal, shear, and Lamb wave phase velocities respectively, and k ($2\pi/\Lambda$) is the wavenumber. When $N = 1$ Equation 5.1 is solved for symmetrical modes, while for N = -1, the solution is for asymmetrical modes. As an example the phase velocity Lamb wave dispersion curves for aluminium are provided in Figure 5.2. With the exception of the two fundamental modes, A_0 and S_0, all Lamb wave modes have finite cut-off frequencies that are dependent upon, the material properties, and the thickness of the plate sample. Therefore, the frequency of operation limits the number of possible modes available in a given system.

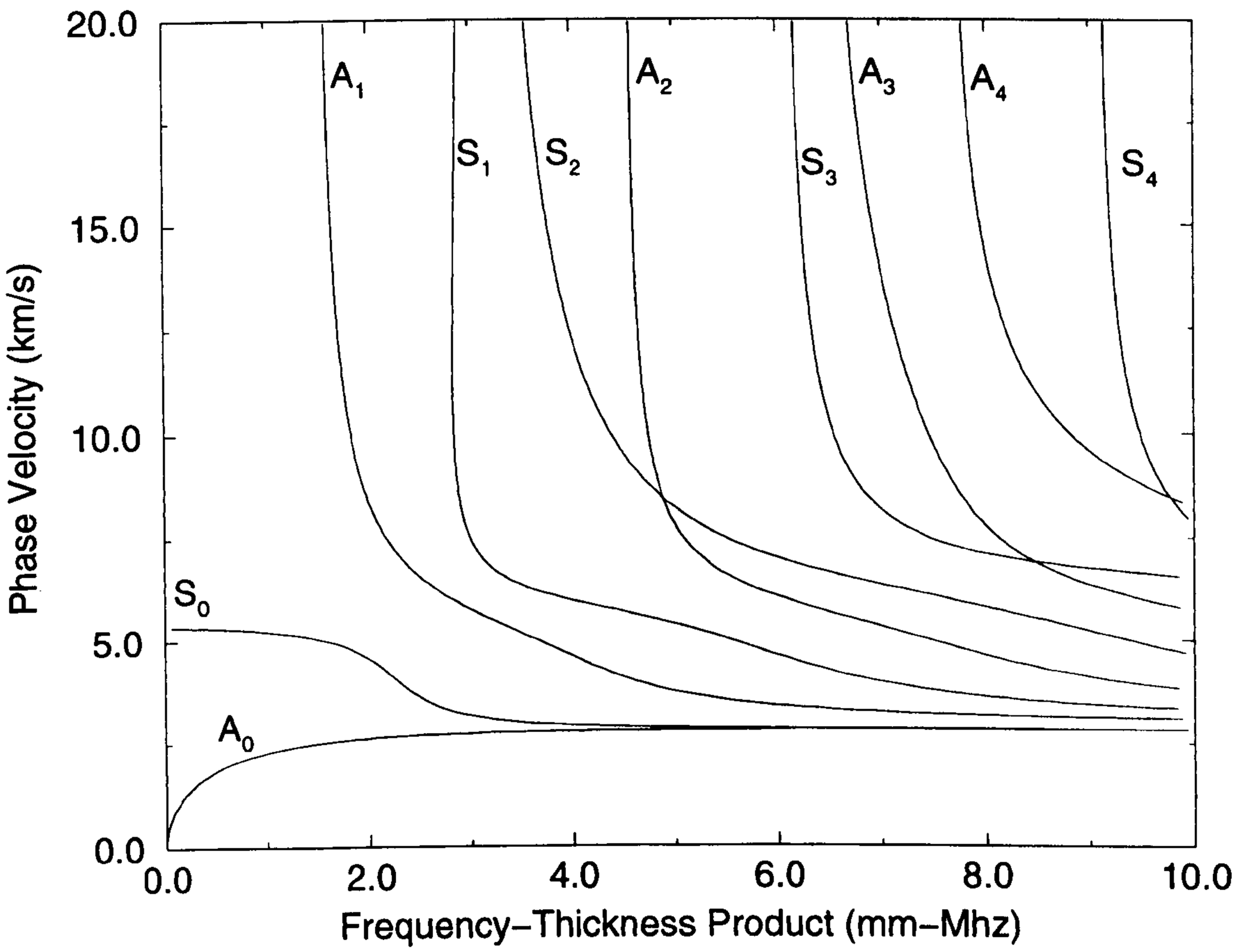

Figure 5.2: *Phase Velocity Lamb Wave Dispersion Curves in Aluminium*

5.2.2. Lamb Wave Excitation Methods

There are several recognised techniques for the generation and detection of Lamb waves, with all methods having their own advantages associated with them depending upon the application. Therefore, various Lamb wave technologies will be presented in this Section with their merits discussed.

5.2.2.1. Wedge Transducers

A problem often associated with Lamb waves generation is the coexistence of many undesired modes in the plate, resulting in difficulties in data interpretation. To introduce a degree of mode selectivity wedge transducers can be utilised where the angle of the wedge is chosen to optimise the excitation of one specified mode, see Figure 5.3.

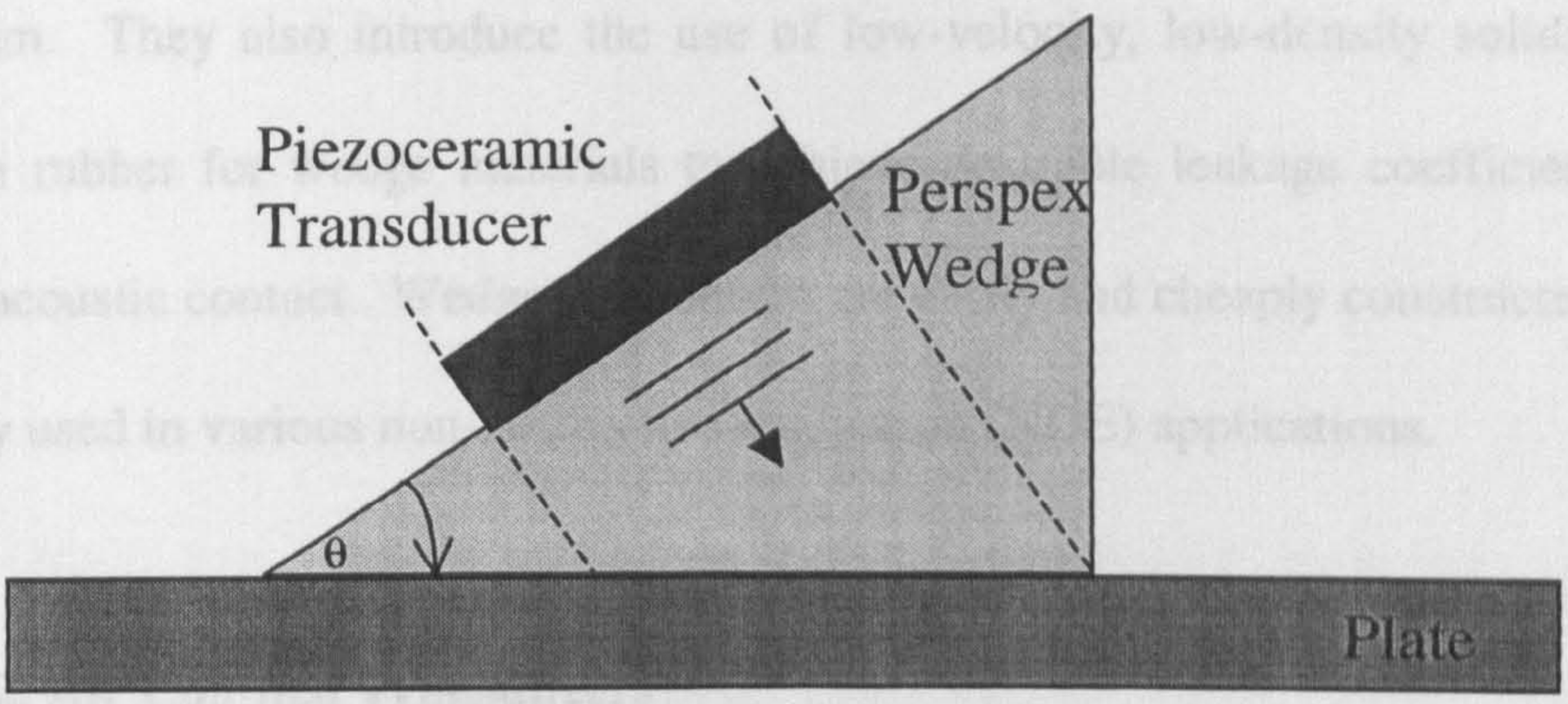

Figure 5.3: *Lamb Wave Wedge transducer*

Maximum excitation of the Lamb wave mode of interest is achieved by setting θ, the angle of the wedge, to satisfy Equation 5.4 [99]. Here C is the phase velocity of the desired Lamb wave mode, and C_{wl} is the longitudinal velocity in the wedge material.

$$\sin\theta = \frac{C_{wl}}{C} \qquad \textbf{5.4}$$

For Equation 5.4 to hold true the longitudinal velocity in the wedge material must be less than that of the phase velocity of interest. Thus, excitation of Lamb waves in plate materials with low velocities can be complicated using this technique since a suitable wedge material needs to be found. Immersing the plate in a liquid is one solution where the liquid acts as the wedge medium, however, this is impractical for many industrial applications. Fraser et al [100] discuss normal mode theory for the design of efficient broadband wedge transducers and suggest that the wedge medium should be chosen to have a much lower shear-wave impedance than that of the load medium. They also introduce the use of low-velocity, low-density solids such as silicon rubber for wedge materials to achieve desirable leakage coefficients and a good acoustic contact. Wedge transducers are easily and cheaply constructed and are widely used in various non-destructive evaluation (NDE) applications.

5.2.2.2. Air Coupled Transducers

In many NDE applications attaching transducers to the test material under investigation is impractical due to say, the requirement for a clean environment, or operation at elevated temperatures. Therefore, an attractive option for the interrogation of plate-type structures under such conditions is a non-contact, air-coupled ultrasonic Lamb wave system. Here the excitation concept is similar to that of the wedge transducer and the incident angle is again determined by Equation 5.4, however, the medium being used to couple the ultrasound into the test sample is air. This introduces a significant implementation problem since any air-coupled ultrasonic system is fraught with difficulties, principally due to the enormous attenuation in the ultrasonic signal at each air/solid boundary [105]. This large signal

attenuation tends to demand the use of a high driving power for transmission, and signal processing, i.e. averaging, at reception. However, an industrial setting may demand both: rapid real-time scanning, where signal averaging is inappropriate; and immunity to changing environmental influences, i.e. humidity, temperature, and air currents, requiring high SNR [105]. Therefore, for an effective air-coupled ultrasonic Lamb wave system, robust, well tailored, and sensitive transducers are essential. There are two transducer technologies with the potential to suit the requirements for such a system:

1. *Electrostatic*
2. *Piezocomposite*

Electrostatic devices consist of an electrically conductive backplate with a thin dielectric membrane stretched across it. The backplate, which forms an electrode, is machined, chemically etched, or even micro machined to give a quantifiable surface finish. The dielectric material is coated on one side to create a second electrode, forming a capacitor between it and the backplate. The application of a high electric field (D.C. bias voltage) across the electrodes pulls the membrane onto the backplate where small compressed air pockets are formed. Therefore, when an alternating signal is applied to the electrodes an oscillation in the membrane is produced, exciting an acoustic wave. These devices display wide bandwidth characteristics, and good electro-mechanical coupling to air. However, they may suffer in harsh environments due to the fragile nature of the membrane (less than 10μm). An example of a non-contact, air coupled Lamb wave system incorporating electrostatic

transducers is provided by Luukala and Merilainen [106]. Here flaw detection in metallic plates using the fundamental asymmetrical Lamb wave at frequencies below 100kHz is discussed. This low frequency range reduces attenuation, however, the resulting wavelengths in the metal plates are long reducing defect resolution. A more recent example is provided by Wright *et al.* [107] who utilise an ultrasonic tomographic imaging technique to generate images of machined flaws in aluminium, perspex and carbon fibre reinforced polymer plates. Varying degrees of success were presented depending on the plate material and, size, shape, and position of the flaw.

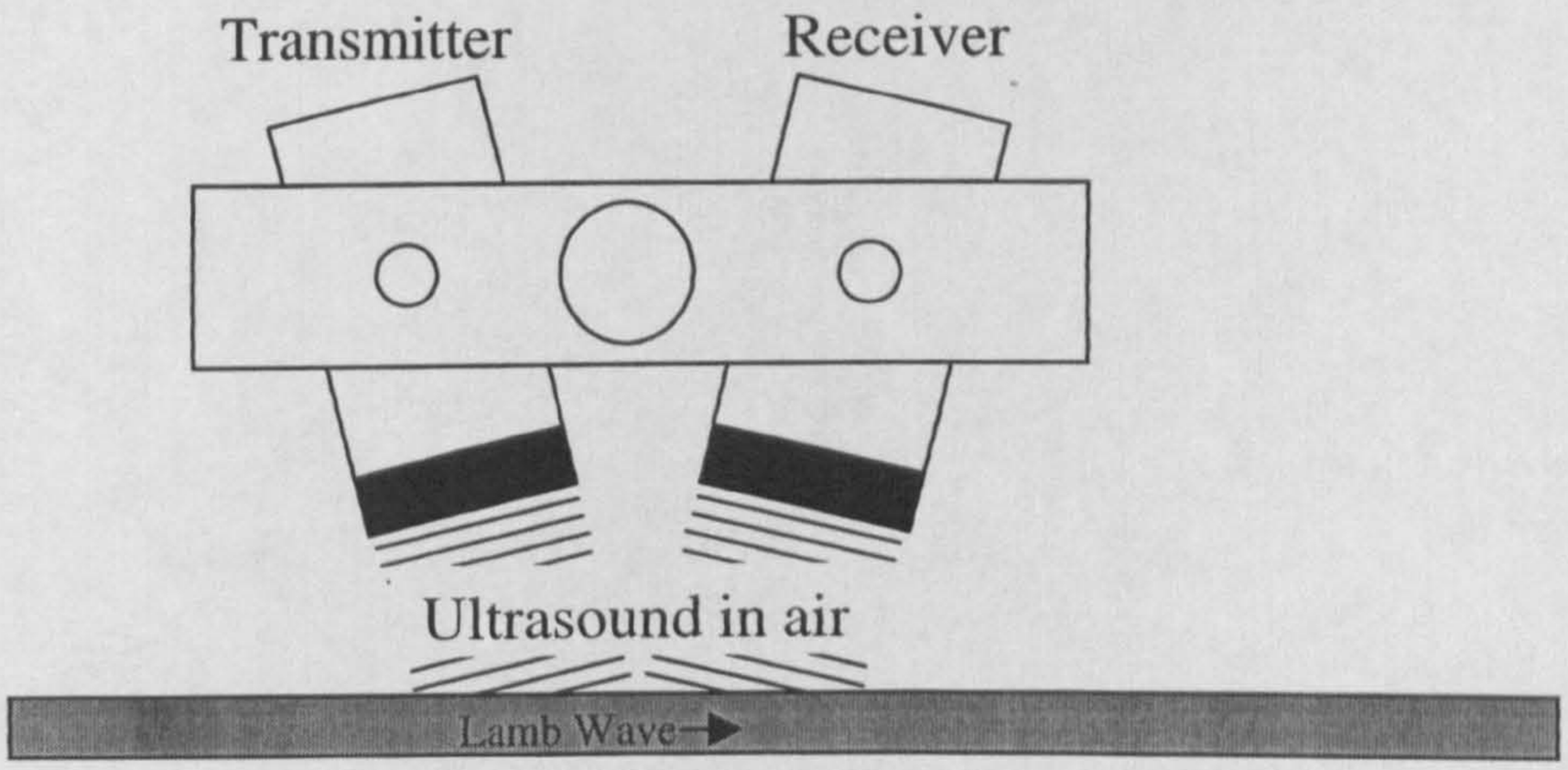

Figure 5.4: *Air-Coupled Lamb Wave System*

A more robust choice of transducer is the 1-3 connectivity piezocomposite, which consists of a matrix of piezoceramic pillars embedded within a passive polymer phase. Compared to conventional piezoceramic, such devices display high electro-

mechanical coupling coefficients and low acoustic impedances allowing them to couple into air more efficiently than solid ceramic devices. Furthermore the application of a novel matching layer system has been reported to increase such devices' sensitivity by up to 23 dB [108]. An example of an automated real-time piezocomposite Lamb wave scanner system is reported by Farlow and Hayward [105]. Here, high resolution images of internal defects are presented for both metallic and composite plates facilitated by the design of sensitive transducers and low-noise analogue electronics.

5.2.2.3. Laser Techniques

Another technique available for non-contact generation and detection of Lamb waves is that of pulsed laser technology. These are wideband sources and in general there are three mechanisms available for ultrasonic generation [109, 110]:

- The first mechanism is known as *thermoelastic generation*, where the optical power density is less than that required to melt the irradiated solid surface. The laser radiation is absorbed within a small volume element at the surface, which initiates a rapid step-like thermal expansion in the load medium. Such excitation generates elastic waves in the solid with a predominantly in-plane motion.
- The second method operates in the *plasma regime* utilising an increased power density sufficient to cause vaporisation of surface material. This can either be the evaporation of a previously applied coating, or ablation of the substrate surface itself. The rapid removal of surface material produces a strong pulse like force predominantly normal to the sample.

- Another option is *air breakdown sources,* which prevent direct interaction with the laser energy and sample surface. Here far infra-red sources produce a spark close to the sample surface launching a shock wave to the sample.

These laser sources can be utilised for Lamb wave excitation, with thermoelastic sources and their dominant in-plane motion coupling most efficiently into symmetrical Lamb wave modes, while plasma sources with their out-of-plane motion couple more effectively into asymmetrical modes [110]. An example of pulsed laser generation of Lamb waves is provided by Hutchins *et al.* [109] who present tomographic images of synthetic flaws in thin metallic sheets.

Nevertheless, there is a significant problem associated with high power laser sources, which is their ability to cause surface damage thus jeopardising their credibility as an NDE tool. Recent work addressing this problem includes the demonstration of a low-power pseudorandom noise modulation approach to continuous wave (CW) laser-ultrasound generation [111]. Here broadband Lamb wave excitation is demonstrated with no surface damage to the sample.

5.2.2.4. Electromagnetic Acoustic Transducers

A further non-contact ultrasonic transduction method is that of the electromagnetic acoustic transducer (EMAT) whose operation is constrained to electrically conducting test samples [112]. Ultrasonic energy is realised by passing a current transient through the EMAT's inductive coil. This induces an eddy current in the sample's surface establishing the presence of a static magnetic field, which in turn

produces a Lorentz force causing ultrasonic waves to be radiated. In reception mode, ultrasonic waves produce mechanical displacement of the conducting sample within the magnetic field. This permits eddy current generation which is detected by the coil. The coil and magnetic field geometry can be varied to optimise the EMAT for detection of a particular ultrasonic wave.

The EMATs is a simple robust transducer making it a good candidate for operation at elevated temperatures; however, disadvantages include the need for the test sample to be conductive, in conjunction with poor device sensitivity and low bandwidth in generation. An example of two EMAT devices each optimised for the reception of a particular Lamb wave mode is described by Hutchins *et al.* [109]. Here the magnetic field and coil are arranged for maximum sensitivity, one for normal motion (i.e. asymmetrical lamb wave mode detection), and one for in-plane motion (i.e. symmetrical lamb wave mode detection).

5.2.2.5. Hertzian Contact Transducers

A Hertzian contact is realised when two solid bodies brought in contact deform elastically under a small applied force [113]. Such a contact does not deform the solids permanently, and can be used for ultrasonic energy transmission without any coupling medium. A Hertzian transducer design has been developed at Stanford University for single mode Lamb wave excitation with NDE applications [78, 114]. The transducer concept is depicted in Figure 5.5. Here extensional waves are generated within the metal rod by a small piezoelectric element bonded to one end. The other end of the rod, which is tapered, is brought into contact with a plate under

force to couple ultrasound and generate the Lamb wave mode. Spring loading provides the downward force and allows contoured samples to be interrogated. This form of asymmetrical loading can efficiently provide single A_0 mode excitation.

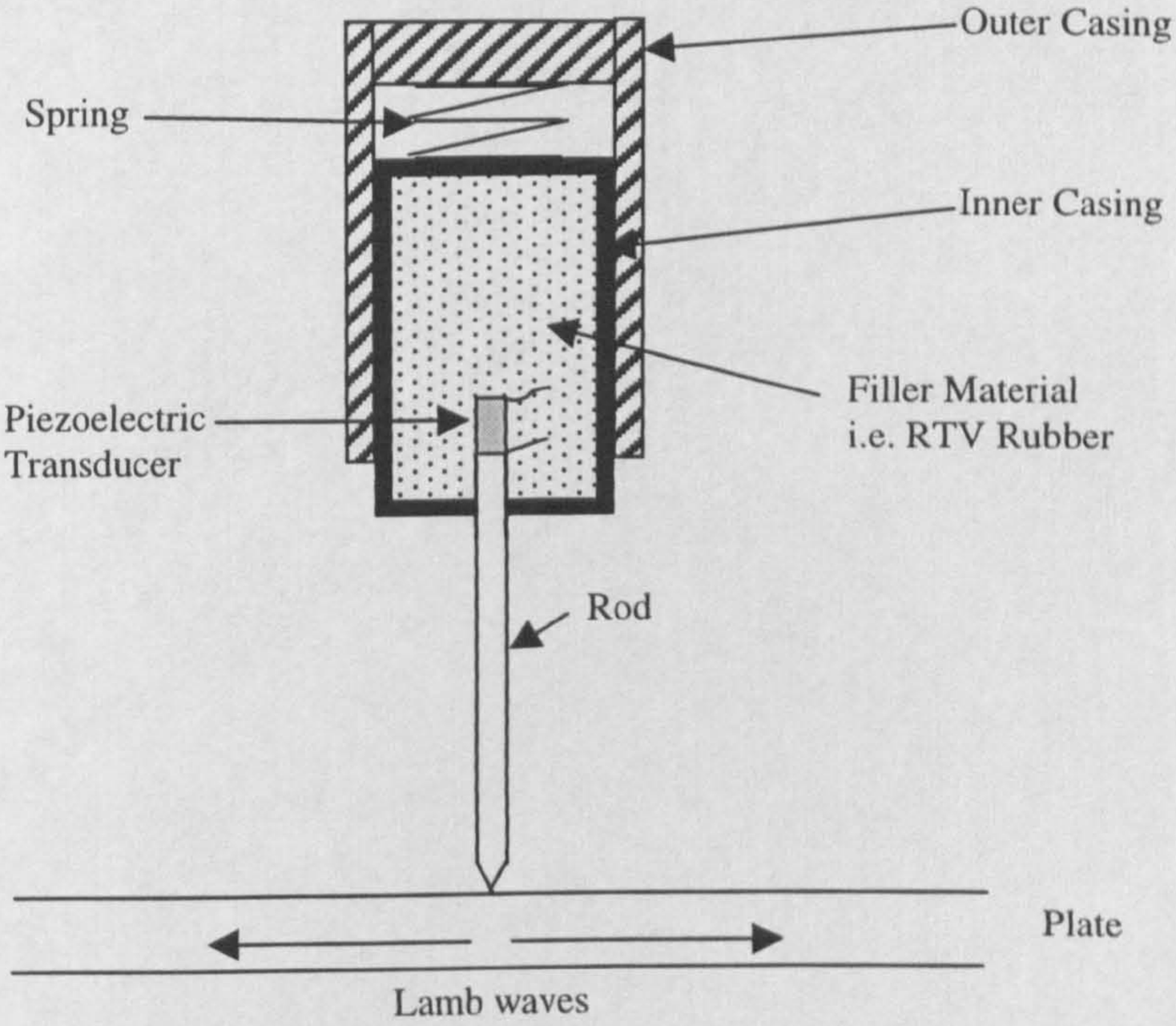

Figure 5.5: *Hertzian Transducer Arrangement*

The contact size depends on the geometry of the of the rod tip, the material properties of the rod and sample, and the downward force generated by the spring. For two spherical isotropic solids of radii R_1 and R_2, the contact is circular and of radius a, given by Equation 5.5 [113].

$$a = F^{1/3}\left[\frac{DR_1R_2}{R_1 + R_2}\right]^{1/3} \qquad \textbf{5.5}$$

Where

$$D = \frac{3}{4}\left(\frac{1-\nu_1^2}{E_1} + \frac{1-\nu_2^2}{E_2}\right), \qquad \textbf{5.6}$$

E_1 and E_2 are Young's moduli of the two media, ν_1 and ν_2 are Poisson's ratio of the two media, and F is the applied force. For the transducer configuration described in Figure 6.5, R_2 can be assumed to be infinite. Typically, when working in the kHz region, the contact radius will be orders of magnitude smaller than the Lamb wave wavelengths being generated, therefore, a point contact source can be assumed.

A significant advantage of these transducers is there ability to generate Lamb wave modes without the need for coupling gels while, unlike air coupled Lamb wave systems, generating large signals thus removing the need for specialised amplifiers and/or signal processing. This provides significant promise for clean environment NDE applications. High temperature measurements are also possible since the piezoelectric element is separated from the test piece by a buffer rod, therefore, the correct choice of rod with respect to acoustic and thermal characteristics should be determined for optimisation of the application.

5.2.2.6. Interdigital Transducers

Interdigital transducers (IDTs) are designed to introduce a series of periodic stresses to a plate-type structure to generate a desired Lamb wave mode, see Figure 5.6.

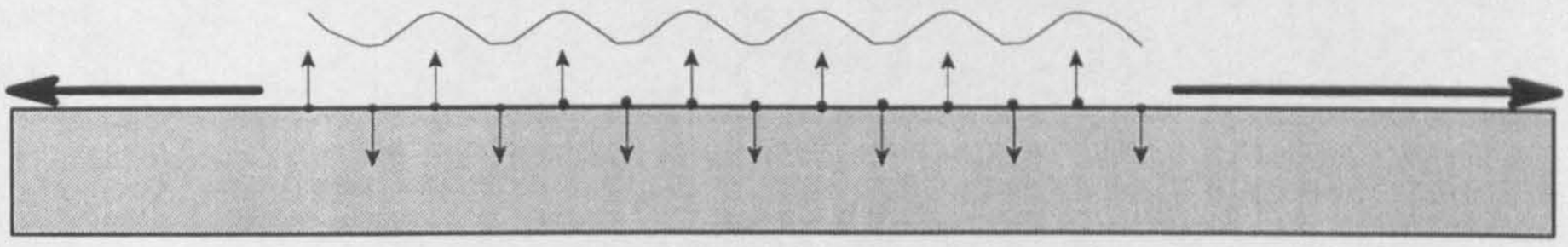

Figure 5.6: *Interdigital Excitation of Lamb waves*

By choosing the spatial period of a transducer array to match the wavelength of the Lamb mode of interest, in conjunction with appropriate apodisation, it is possible to be highly selective, both in terms of spatial response and isolation of the required mode. Figure 5.7 shows typical IDT electrode patterns.

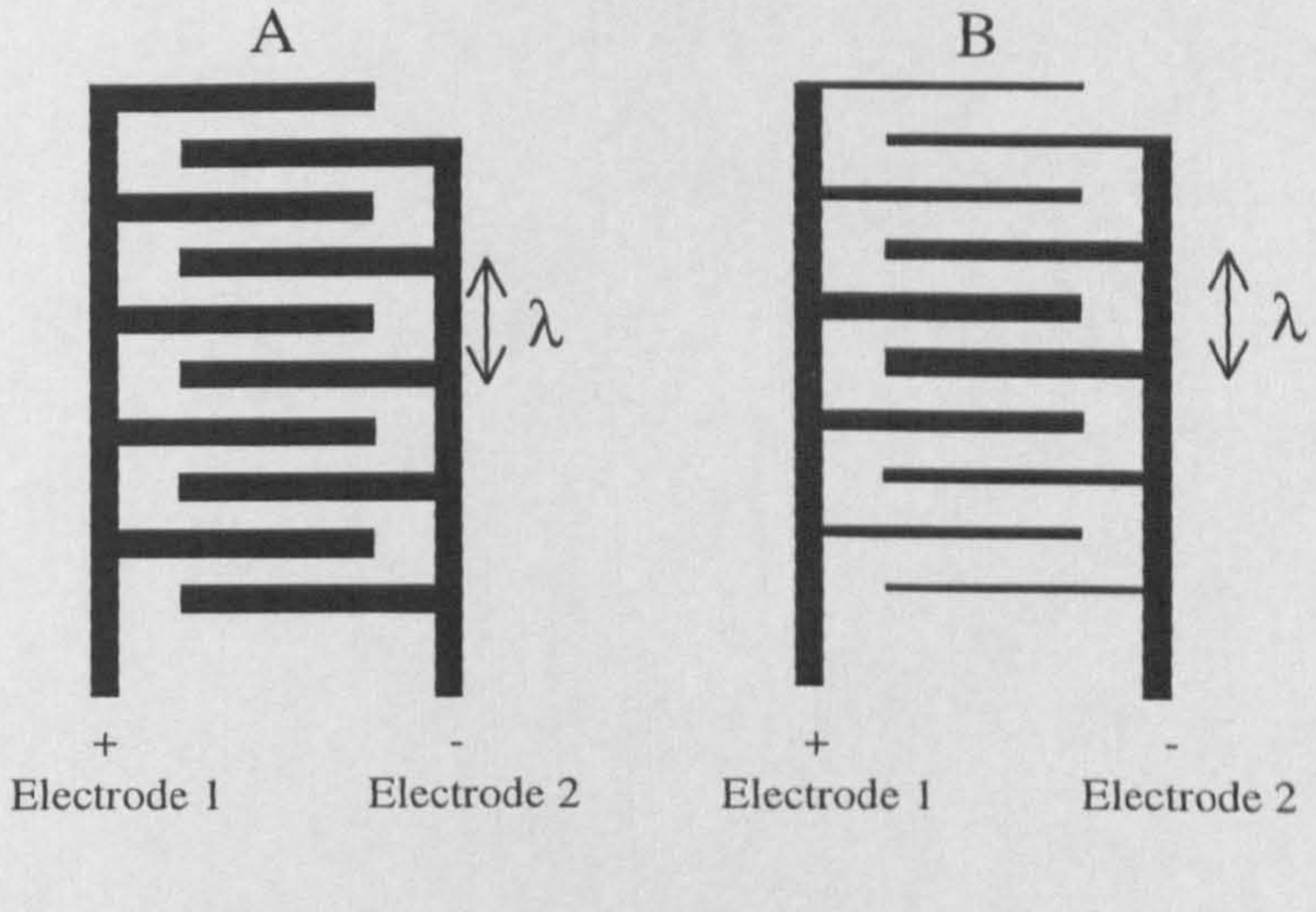

Figure 5.7: *IDT Electrode Patterns: A-Standard, B-Apodised*

IDTs provide the potential for in-situ condition monitoring for application in ultrasonic NDE where the ideal transducer is required to be both flexible and unobtrusive with respect to the thickness of the host material under evaluation [40]. There are two available IDT technologies that meet these requirements namely piezopolymer devices [5], and flexible low profile piezoceramic devices [40]. Piezopolymer materials have the advantage that they are extremely light and flexible, exerting minimal impact on the test material, although they display relatively low electro-mechanical coupling efficiency when compared with alternative, piezoceramic methods of generation and detection [40]. Leading work on piezopolymer IDTs is provided by Monkhouse and co-workers at Imperial College, London [5].

Conventional piezoceramic transducers are unsuitable for low-profile IDT designs due to their inherent stiffness. However, the development of a novel flexible low profile device comprising of active piezoceramic platelets embedded within a softsetting passive polymer phase has addressed this problem [40]. A hybrid system has been developed by researchers at The University of Strathclyde [115] utilising such piezoceramic interdigital transducer to generate Lamb waves, with detection provided by an embedded optical fibre in carbon fibre plates. Although spatial discrimination was not as good as the complete ultrasonic systems described in [40], detection of delamination due to impact damage was shown to be feasible.

5.3. Overview of Proposed Surface Mount Lamb Wave System

The previous section described current Lamb wave excitation methodology. Out of the technologies discussed, only the low profile piezopolymer and piezoplatelet IDTs provided the potential for operation in a smart structure environment. However, the integration of such devices into structures is still to be realised. This Chapter aims to show that fibre waveguides can be configured as a pseudo IDT, delivering ultrasound to specific points on a structure, thus introducing periodic stress to generate Lamb waves. An aim of the Thesis is to develop an embedded monitoring system utilising this concept. This Chapter, therefore, presents preliminary surface bonded experiments as a proof of concept.

Using the information obtained in Chapter 4 on the nature of the coupling to and from waveguides, various demonstration NDE systems were established utilising thin cylindrical waveguides to transport acoustic energy, in the L(0,1) mode, to and from an aluminium plate. The waveguides were bonded to the plate's surface, to generate and detect the fundamental asymmetric (A_0), and fundamental symmetric (S_0) Lamb wave modes using interdigital techniques. For maximised acoustic coupling into the L(0,1) waveguide mode the frequency of operation of such a system is constrained by the available lateral resonances of the piezoceramic (PZT5A) sample. In each case, the operational frequency chosen for the system corresponds to the lateral mode frequency that couples the maximum amount of energy into the waveguides under narrowband operating conditions. This frequency and the thickness of the aluminium load plate provide the system frequency thickness product (FTP). When designing a

system to generate and detect Lamb waves dispersion information of the load material is required. Consequently, Figure 5.8 shows the dispersion curves for the S_0 and A_0 lamb wave modes in aluminium. The phase velocity (C) associated with a mode, at a given FTP, provides information on the wavelength (Λ) spacing required to generate that mode (Equation 5.7). The group velocity (C_g) provides information on how fast energy will propagate in the plate for a particular mode.

$$\Lambda = \frac{C}{f} \qquad \textbf{5.7}$$

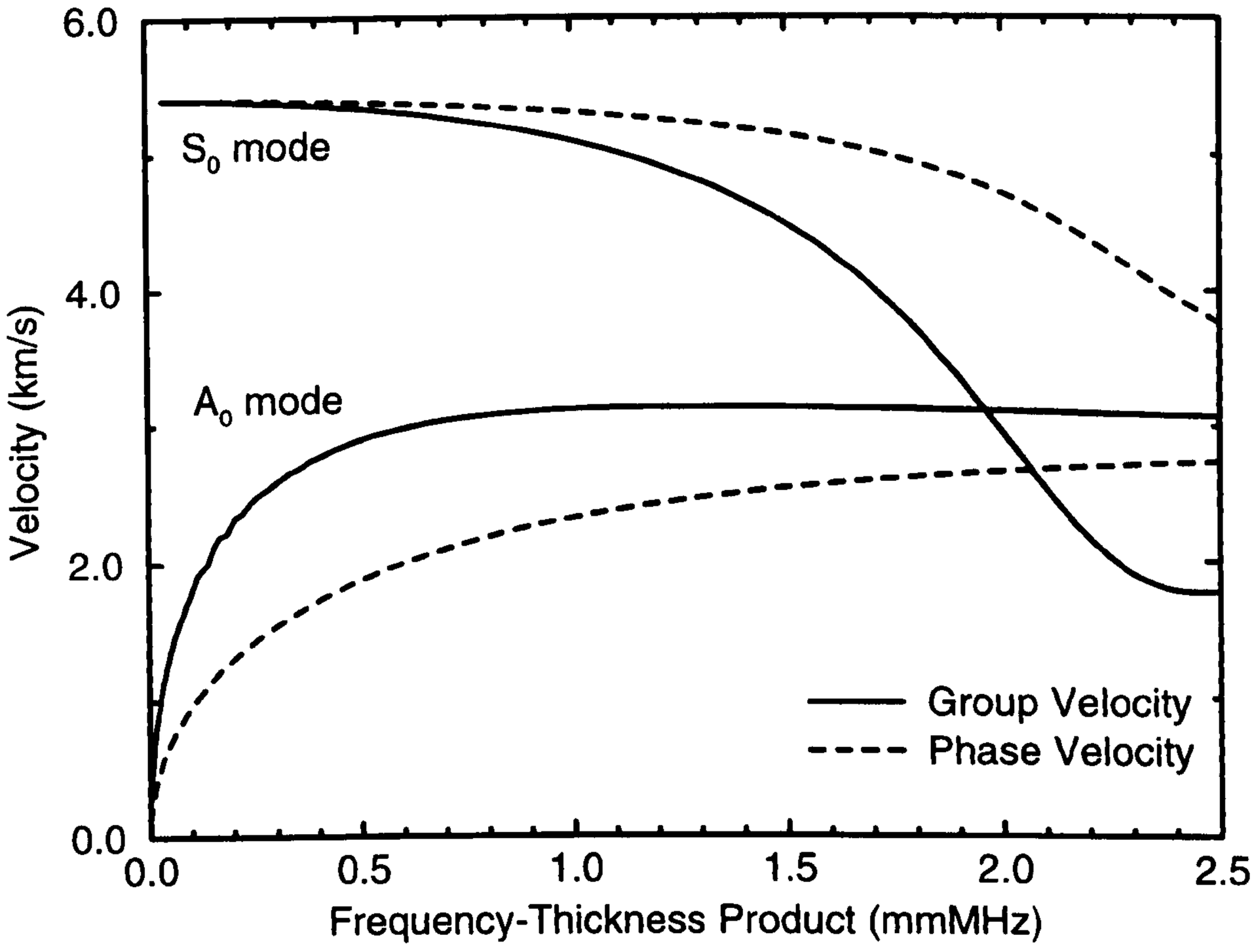

Figure 5.8: *Fundamental Lamb Wave Dispersion Curves in Aluminium*

Once the wavelength has been established the desired Lamb wave was generated by bonding a number of waveguides to the top surface of the aluminium load plate to act as point sources, as shown in Figure 5.9. As such the waveguides deliver a series of

periodic stresses to the surface of the load plate for interdigital excitation. Adjacent point sources are separated by half the wavelength ($\Lambda/2$) of the Lamb wave being generated. This configuration requires that adjacent sources are 180° out of phase, achieved by using two PZT5A transmitting transducers (of equal geometry) driven 180° out of phase by a transformer stage, with adjacent waveguides bonded to alternate transducers.

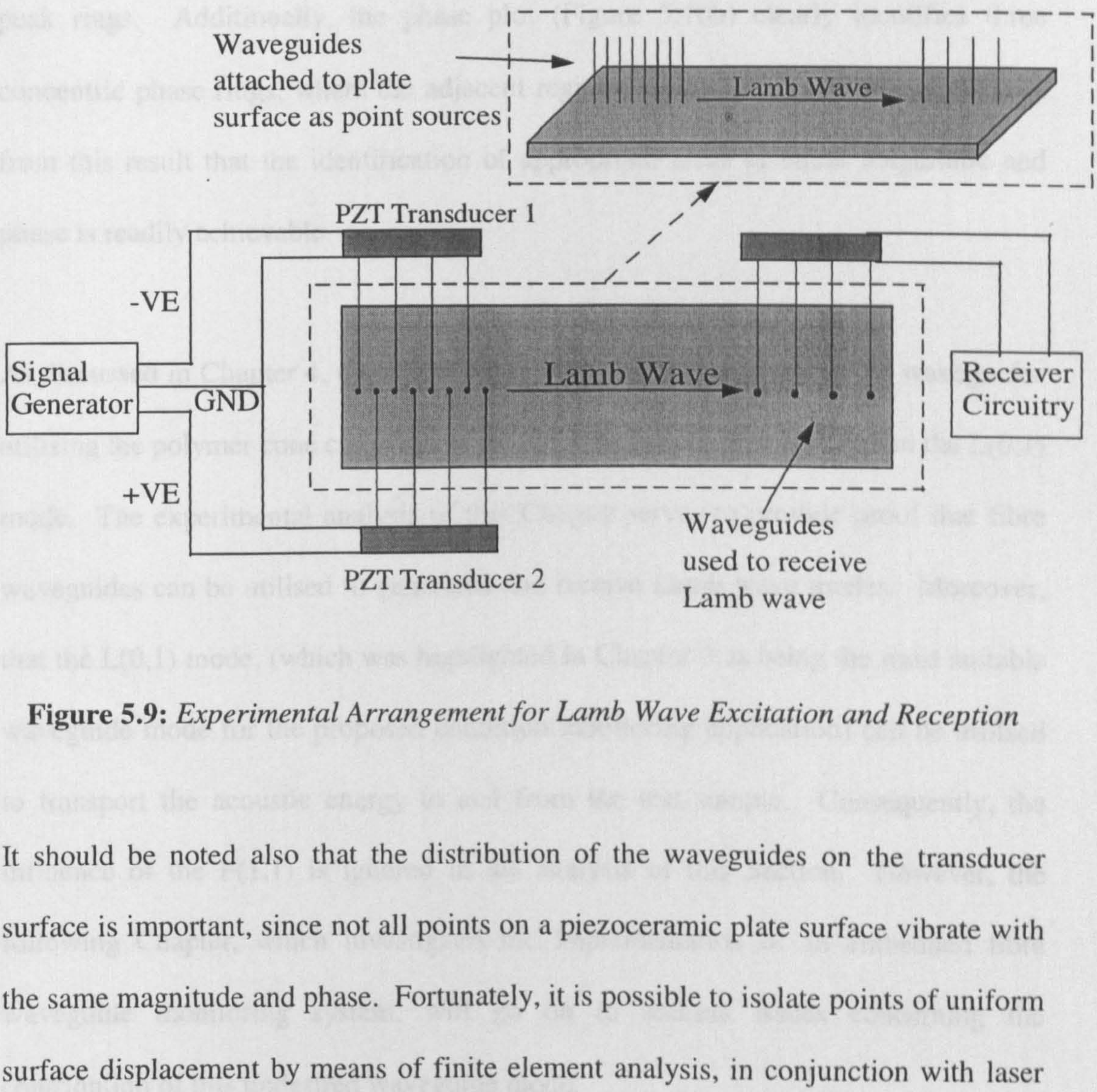

Figure 5.9: *Experimental Arrangement for Lamb Wave Excitation and Reception*

It should be noted also that the distribution of the waveguides on the transducer surface is important, since not all points on a piezoceramic plate surface vibrate with the same magnitude and phase. Fortunately, it is possible to isolate points of uniform surface displacement by means of finite element analysis, in conjunction with laser scanning of the surface profile [116]. This procedure was adopted for the transducers

in question and as far as possible, the waveguides were attached to regions of uniform displacement and phase at the operating frequency. As an example, a laser vibrometer scan of a 500kHz, thickness mode, PZT5A, piezoceramic disc transducer of diameter 30mm is provided (see Figure 5.10). This device has a radial harmonic at 250kHz and the surface displacement profile was recorded when driven at this frequency. The magnitude plot (Figure 5.10a) reveals a region of maximum displacement at the centre of the device surrounded by alternating concentric null and peak rings. Additionally, the phase plot (Figure 5.10b) clearly identifies three concentric phase rings, where the adjacent regions are out-of-phase. It can be seen from this result that the identification of appropriate areas of equal magnitude and phase is readily achievable.

As discussed in Chapter 4, the F(1,1) mode will also be generated in the waveguides utilising the polymer cone coupling technique, albeit to a lesser extent than the L(0,1) mode. The experimental analysis of this Chapter serves to provide proof that fibre waveguides can be utilised to generated and receive Lamb wave modes. Moreover, that the L(0,1) mode, (which was highlighted in Chapter 3 as being the most suitable waveguide mode for the proposed condition monitoring application) can be utilised to transport the acoustic energy to and from the test sample. Consequently, the influence of the F(1,1) is ignored in the analysis of this Section. However, the following Chapter, which investigates the implementation of an embedded fibre waveguide monitoring system, will go on to address issues concerning the contribution of this undesired waveguide mode.

Surface Displacement Profile

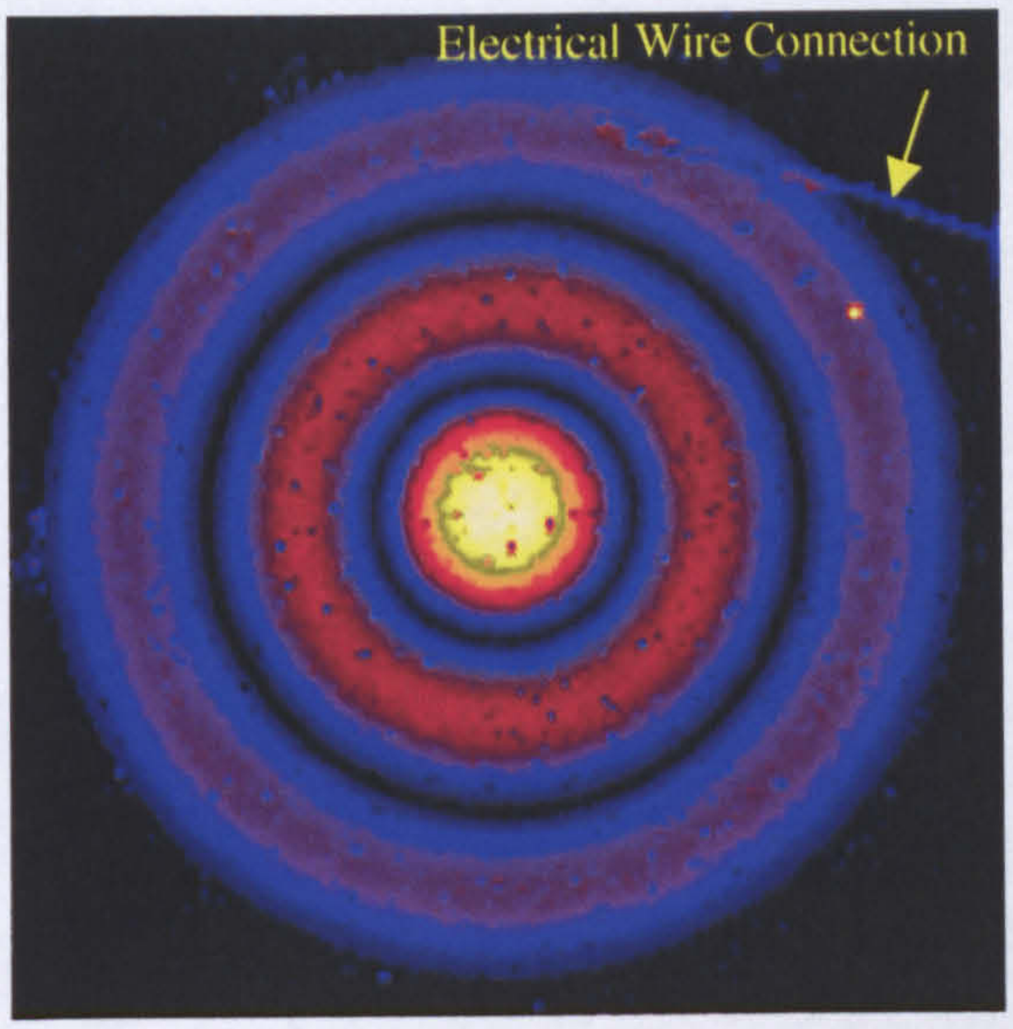

Cross-Section Through Central Axis

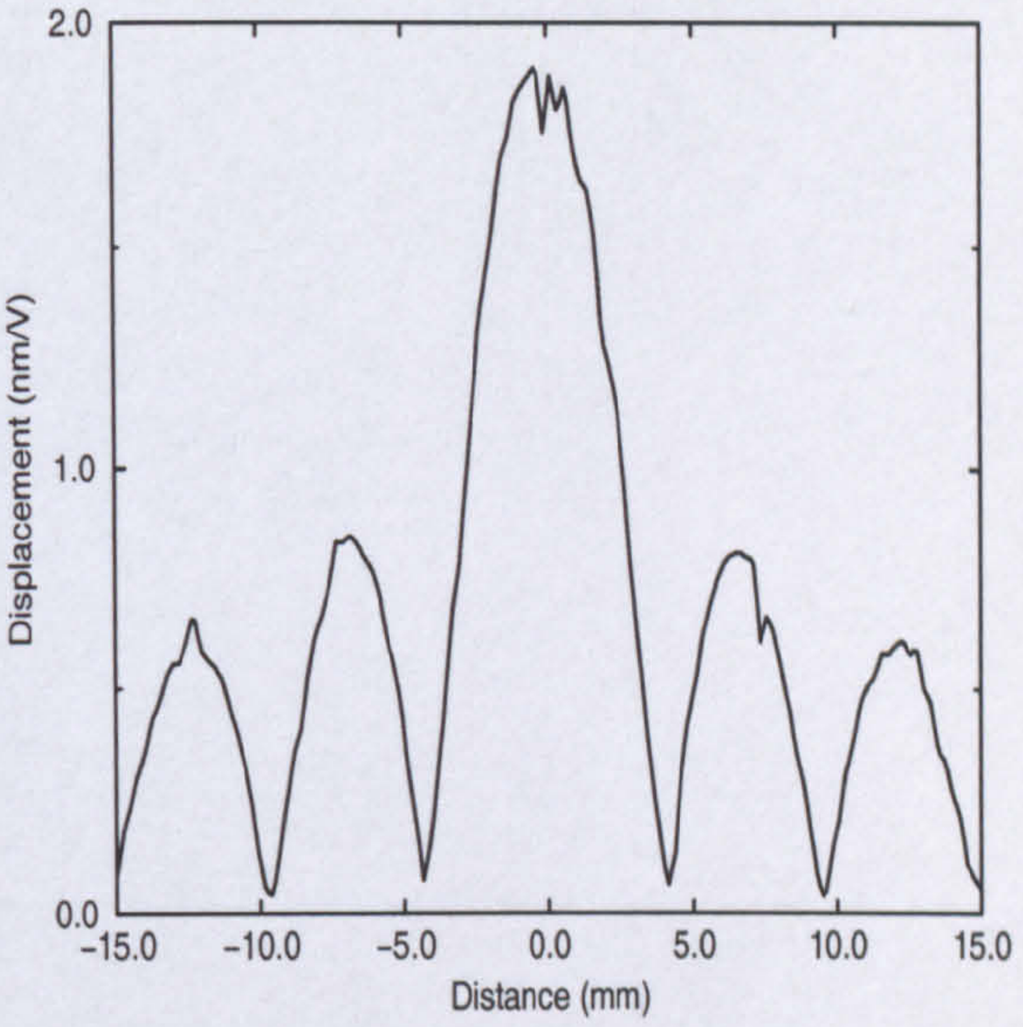

Figure 5.10(a): *Magnitude Response: Laser Scan of Disk Transducer at 250 kHz*

Surface Displacement Profile

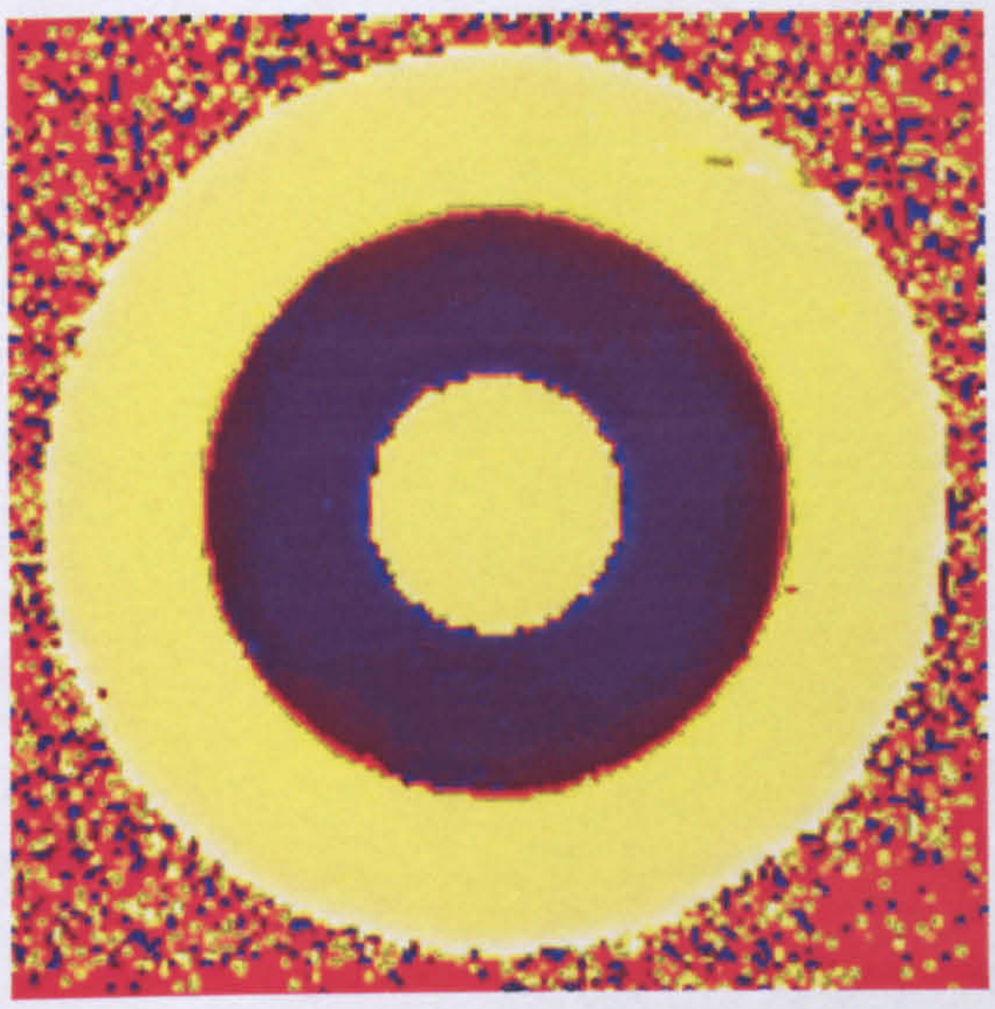

Cross-Section Through Central Axis

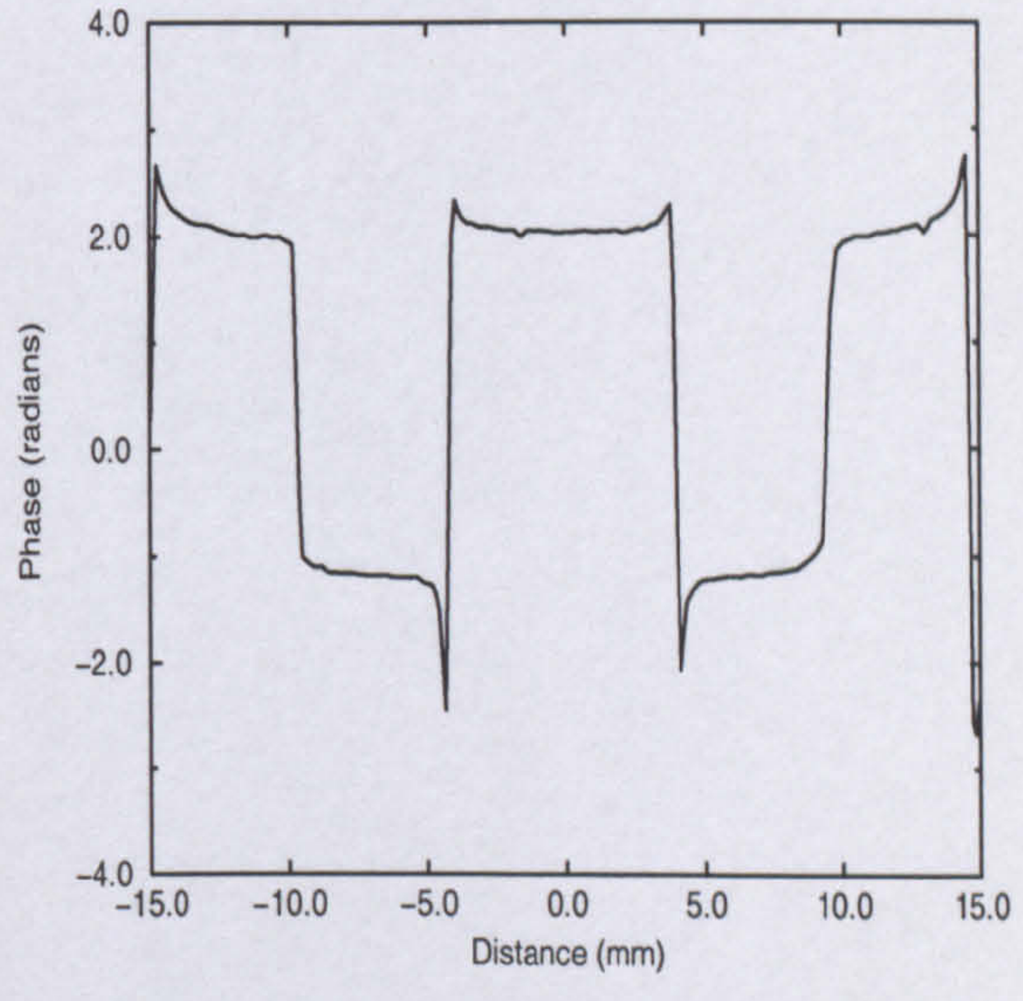

Figure 5.10(b): *Phase Response: Laser Scan of Disk Transducer at 250kHz*

In the following Lamb wave experiments all the waveguides were copper wire of diameter 0.25mm. The narrowband voltage signal utilised to excite the transmitting piezoceramic transducers, and the Lamb wave detection technique is described in each experiment. Predicted propagation times are calculated from the summation of the time it takes the ultrasound to propagate along the waveguides in the L(0,1) mode and the time taken for the ultrasound to propagate along the plate at the Lamb wave mode group velocity.

5.4. S_0 Lamb Wave Mode Generation and Detection in an Aluminium Plate using Copper Waveguides

In this first experiment the S_0 mode was designed for since it displays minimal dispersion in the low FTP regime of interest (see Figure 5.8), and it is documented that the symmetrical modes are, in general, better suited to long range monitoring applications [5]. The frequency of operation for this system was 250kHz, and the aluminium load plate was of thickness 1.15mm yielding an FTP of 0.36MHz.mm. Consequently, from the data depicted in Figure 5.8, it can be deduced that the S_0 mode has a group velocity of 5353ms^{-1}, a phase velocity of 5381ms^{-1}, and therefore a wavelength of 20.2mm. The transmitting piezoceramic transducers were excited with a 250kHz, 200Vp-p, 10 cycle toneburst, modulated by a Gaussian envelope for narrowband operation. This voltage signal was achieved using a programmed HP33120A signal generator followed by an ENI 2100L RF power amplifier. For reception of the induced Lamb wave mode four waveguides of equal length were bonded to the surface of the plate, each separated by a wavelength spacing in an

attempt to 'tune' to the desired S_0 mode. The generating waveguides were 300mm in length, the receiving waveguides 280mm, and the distance between the generating and receiving waveguides was 473mm. Therefore, the expected arrival time of the Lamb wave is **246μs**. Figure 5.12 illustrates the signal received, where it can be seen that the S_0 mode has indeed been generated and received using waveguides. However, there is a major A_0 component, which is expected at **333μs** for this system FTP. The result is in agreement with data provided by other workers see for example [114], who indicate that for surface point source excitation of plate structures, the fundamental antisymmetric mode is generated preferentially due to the asymmetrical nature of the loading.

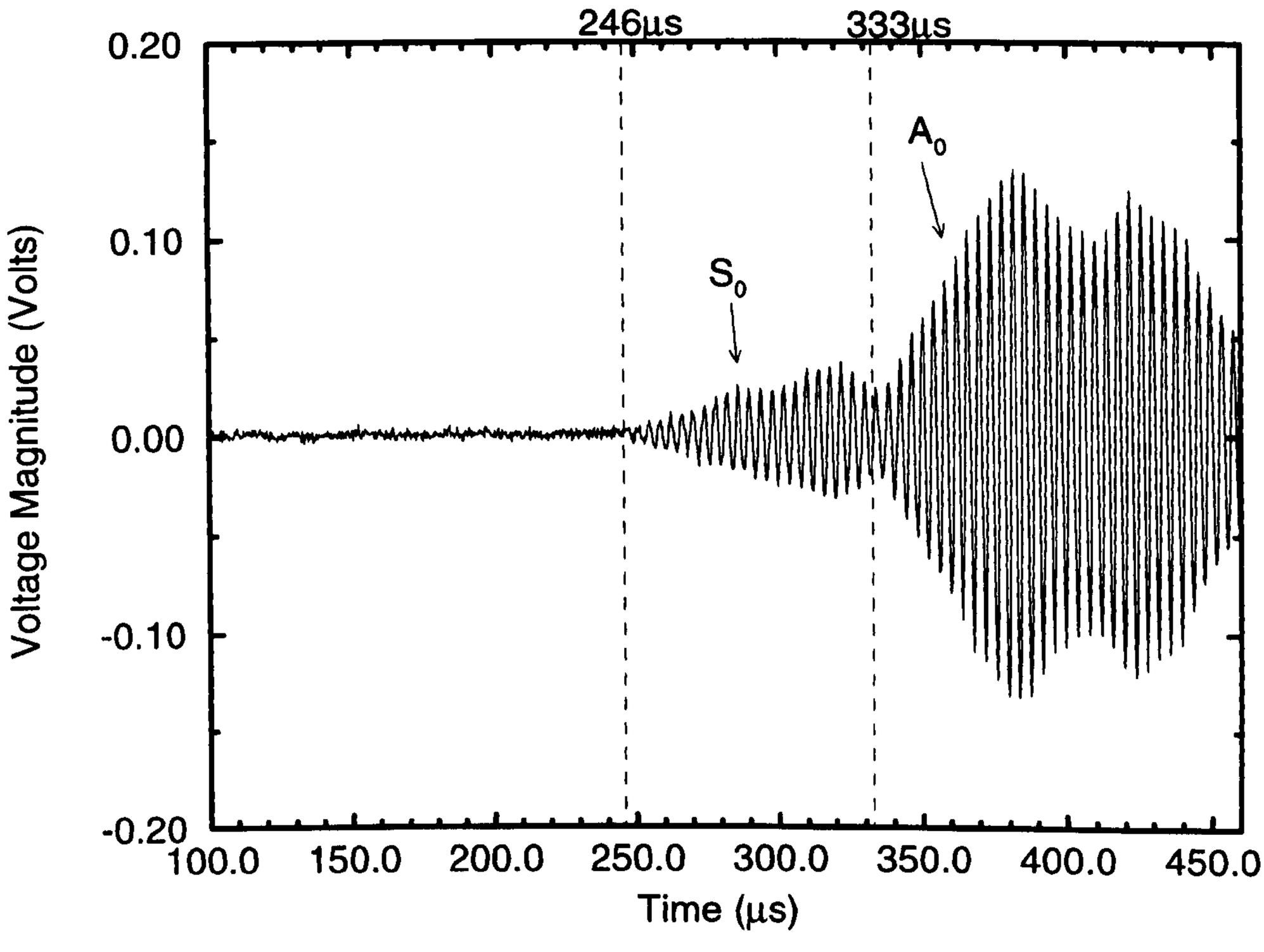

Figure 5.12: *A_0 and S_0 mode generated and received using waveguides*

5.5. Modelling the Lamb Wave System

5.5.1. Finite Element Analysis of Lamb Wave Propagation

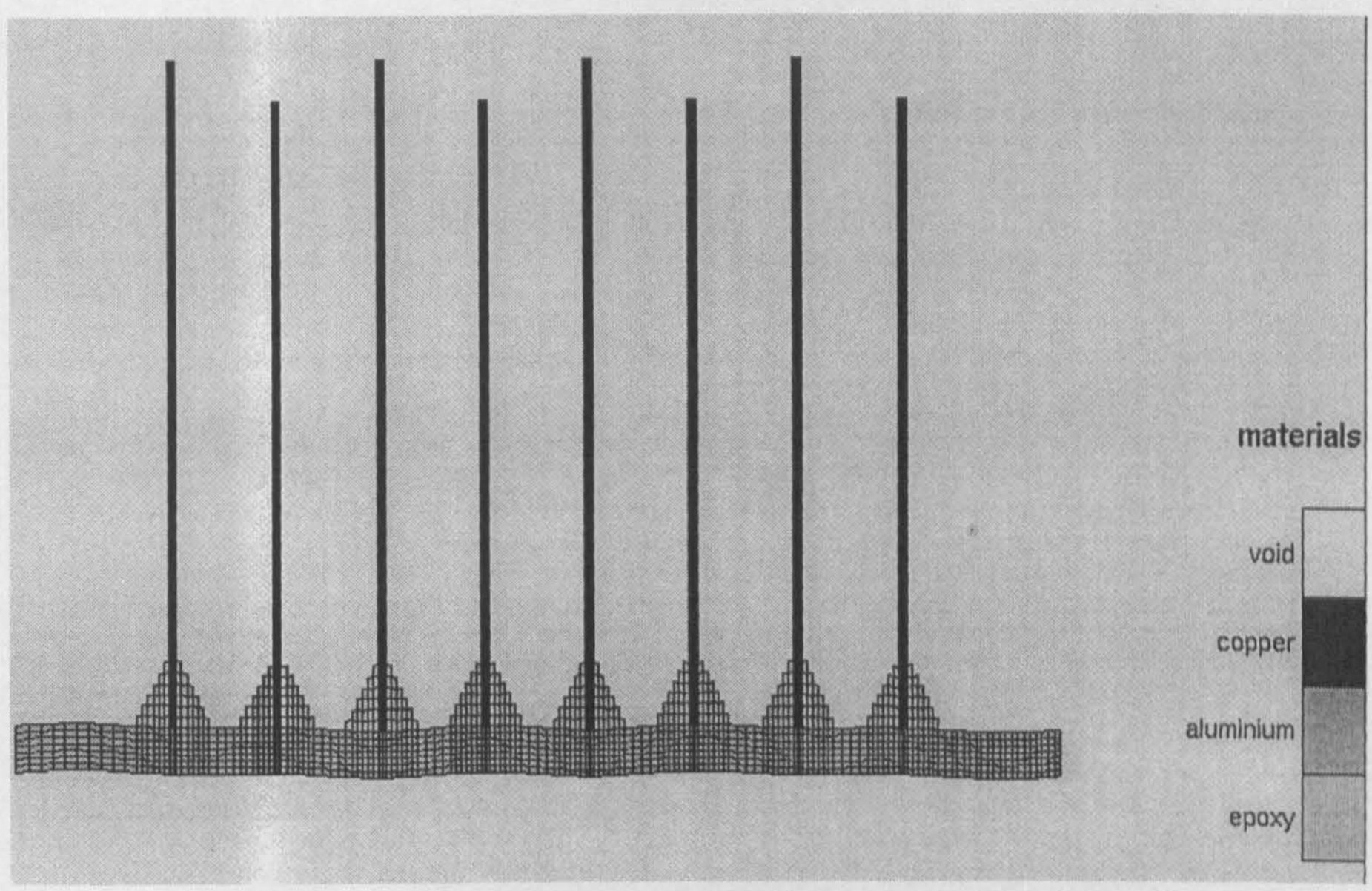

Figure 5.13: *FEA of waveguides exciting Lamb waves in an Aluminium Plate*

In reaction to the previous experiment, a PZFlex FEA Lamb wave propagation model was developed to further investigate the application of thin cylindrical waveguides delivering periodic stress to the surface of a plate. The model was run to investigate both A_0 and S_0 mode operation at 250kHz. Furthermore, experimental verification of the model was performed, and the subsequent results are presented in this Section.

Figure 5.13 shows the waveguides coupled to a section of the aluminium plate via conical polymer bonds. Here the plate thickness was 1.45mm, the waveguide diameter 0.25mm, and the polymer bonds were of base size 2mm and height 2mm.

Longitudinal propagation in the waveguides was induced by applying a 10 cycle, 'Hanning windowed', pressure load toneburst to the ends of the waveguides, with adjacent waveguides being loaded 180° out-of-phase. This input signal was obtained by taking a digitised recording of the signal to be utilised in the experimental comparison. Displacement was monitored on the plate surface 300mm from the waveguides and the model was run for both A_0 (Λ = 6.7mm) and S_0 (Λ = 21.5mm) operation at 250kHz.

Experimental verification of the results was carried out with all parameters replicated as accurately as possible. The experimental procedure of the previous Section was followed except the Macro Design Ltd. Wavemaker-Duet signal generator was utilised to provide a 10 cycle Hanning windowed toneburst. Surface displacement was experimentally monitored using a 250kHz, PZT5A thickness mode, piezoceramic plank transducer bonded to the plate. Figures 5.14 and 5.15 present the FEA and experimental results for A_0, and S_0 operation respectively. As can be seen there is good agreement between the experimental and theoretical results. Again A_0 mode generation is shown to be dominant for this form of excitation even when configured for the S_0 mode corroborating the previously discussed experimental result.

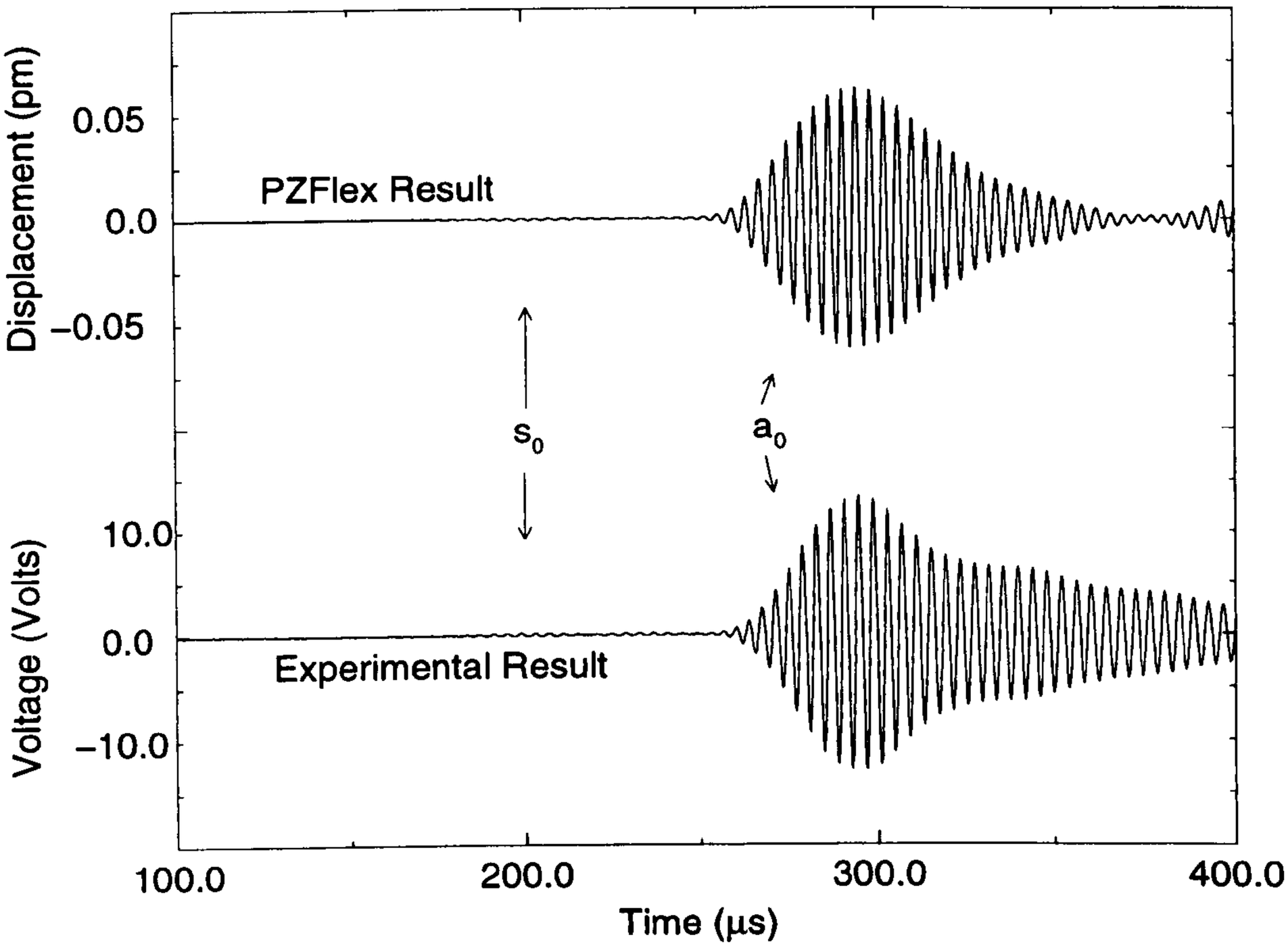

Figure 5.14: *FEA and Experimental Results for A_0 Operation*

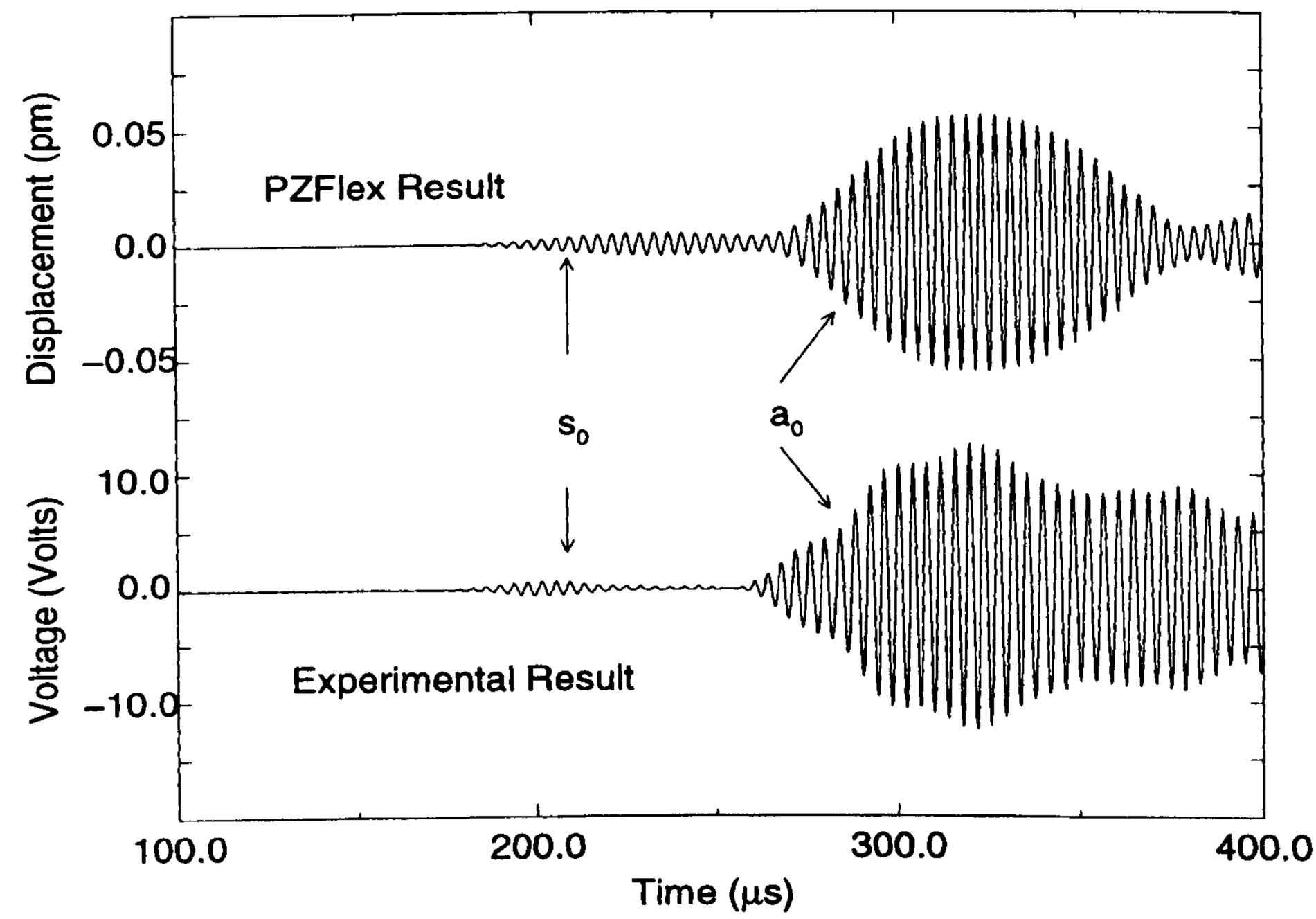

Figure 5.15: *FEA and Experimental Results for S_0 Operation*

5.5.2. Huygens' Model for Acoustic Beam Profiles

A Huygens' Model has been developed at Imperial College, London [104] to predict the acoustic fields of piezopolymer IDTs. Here, a number of axisymmetric point sources are utilised to represent an IDT operating on an isotropic homogenous load plate. At each position on the plate, the acoustic field is calculated by summing the surface displacement contribution from each point source that serve to comprise the IDT. In the model, the IDT is excited with a Hanning windowed toneburst to represent narrowband operation. The resultant acoustic field represents the ultrasonic energy packet propagating from the source at a specific moment in time. A version of the Huygens' model described in reference [104] was obtained by courtesy of Imperial College London. This model was utilised to represent a line array of eight point sources at half wavelength spacing to approximate the experimental arrangement of this Chapter. Adopting the wavelength spacing for the A_0 mode operation of Section 5.5.1. ($\Lambda = 6.7$mm) an acoustic surface displacement profile was obtained, as illustrated in Figure 5.16. The profile was mapped at the time required for the wave packet to propagate a distance of 50mm from the source. It should be noted that Figure 5.16 displays half of the entire profile, which is symmetrical about the y-axis.

To verify the predicted field the following experiment was carried out. A similar Hertzian transducer to those developed at Stanford University (described in section 5.2.2.5.) was manufactured with the following characteristics: the rod used was

stainless steel of diameter 3.17mm, and length 140mm; the piezoelectric element was a PZT5H pillar of thickness 5mm and cross section 3.2mm by 3.2mm; the filler material was a soft setting epoxy (CY208/HY956, described in Appendix C); and the outer casing was made of aluminium and the inner casing of brass. The transducer described has a centre frequency of 200kHz and a -3dB bandwidth of 500kHz. The Hertzian transducer was held in a clamp and used to manually scan the surface of the plate. The scan was taken to the right of the centre of the fibre line array and the area scanned was of length 200mm and width 120mm to match the Huygens' model plate geometry. In the Huygens' model the profile was stored at the time it takes the wave packet to propagate 50mm. Therefore, the time taken for the wave packet to propagate 50mm in the experimental arrangement was noted and all values stored correspond to the signal magnitude at this moment in time. The resulting acoustic surface displacement profile is show in Figure 5.17, where measurements were taken every 5mm along both axes. Note that an example A_0 mode signal detected by the Hertzian transducer, 50mm from the source, is shown in Figure 5.18.

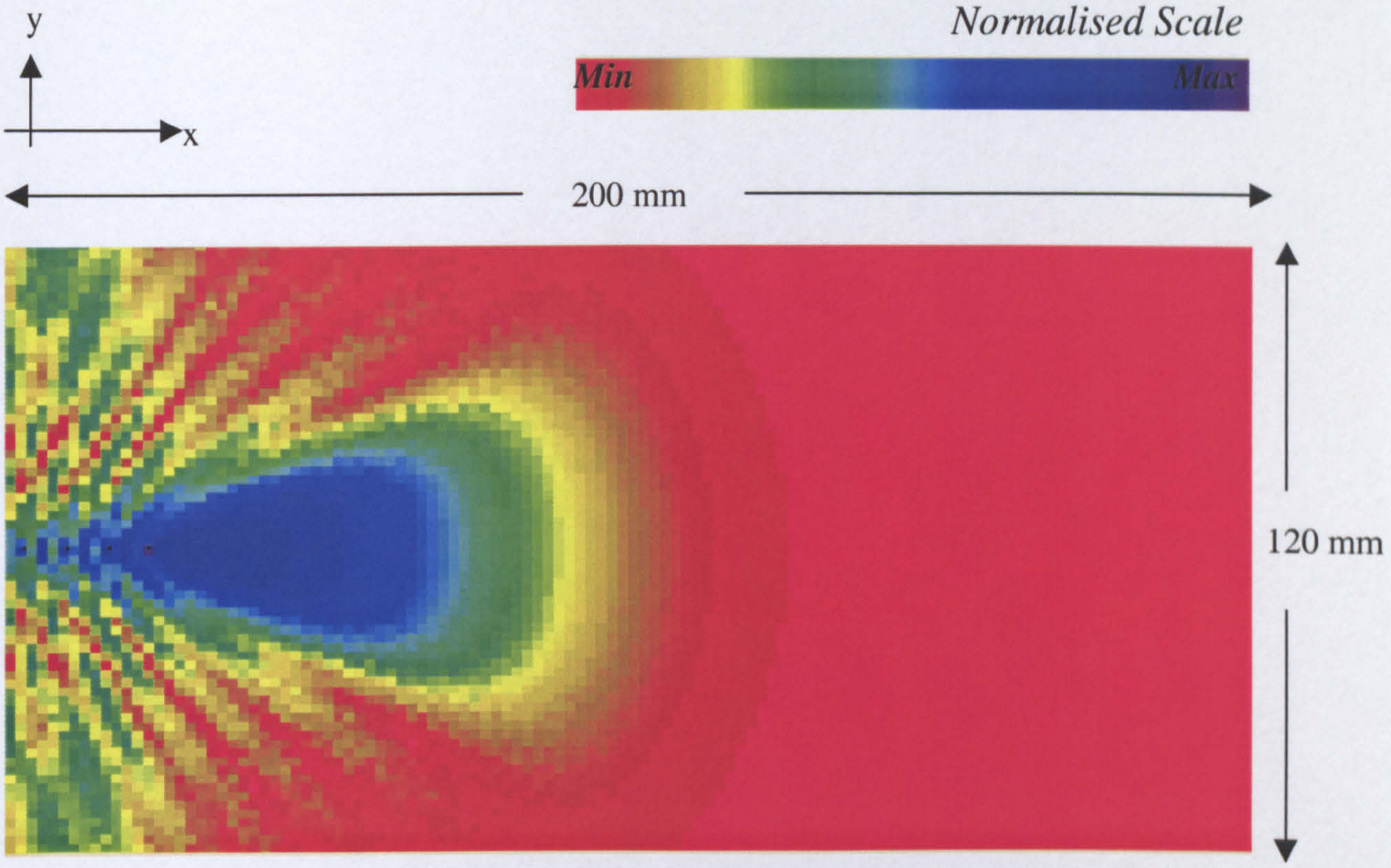

Figure 5.16: *Predicted Acoustic Profile of Fibre Line Array Using Huygens' Model*

Figure 5.17: *Measured Acoustic Profile of Fibre Line Array Using Hertzian Transducer*

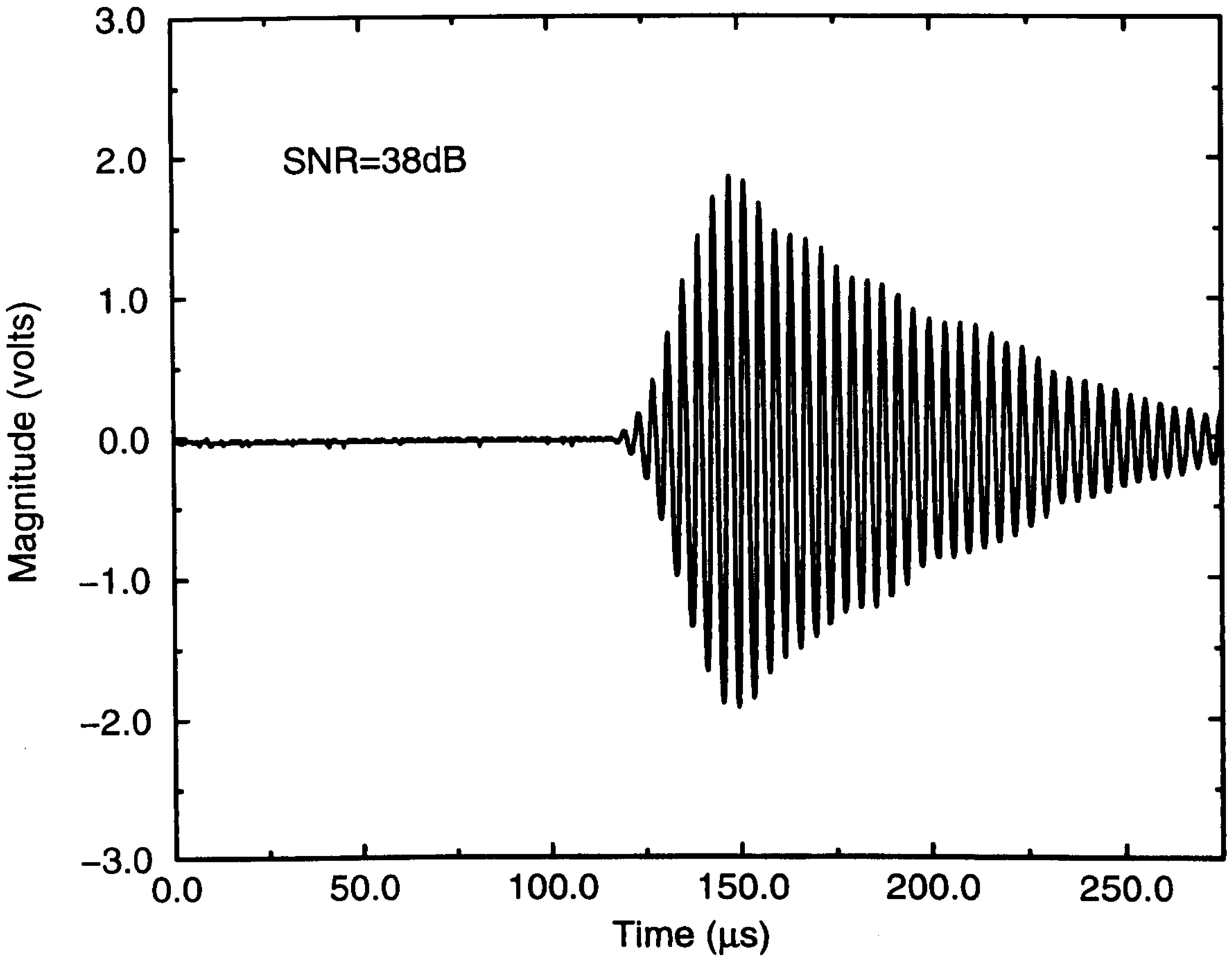

Figure 5.18: *Signal Detected with Hertzian Transducer 50mm From Source*

Considering each fibre source is simply represented by a point source and that the method of reception is unaccounted for by the model, then it is fair to say that the general trends of the predicted (Figure 5.16), and the measured (Figure 5.17) acoustic profiles are in good agreement. The model is intrinsically symmetric, which is evident in the predicted profile, however, the measured profile also yields a relatively symmetrical response. Both display a divergent acoustic beam propagating centrally away from the source, and significant side activity in the form of an interference pattern. The measured profile does however indicate greater side activity and the

presence of these signals is undesirable since spurious reflections can complicate signal identification for NDE. With confidence in the model's ability to predict the acoustic field of a fibre line array it was utilised to obtain a suitable configuration to eliminate side activity. By employing a second line array, aligned and in parallel with the first and separated by half a wavelength, it was envisaged that destructive interference would be induced thus suppressing signals propagating laterally from the source. The model predicted that for this configuration the side activity would be negligible, as illustrated in Figure 5.19.

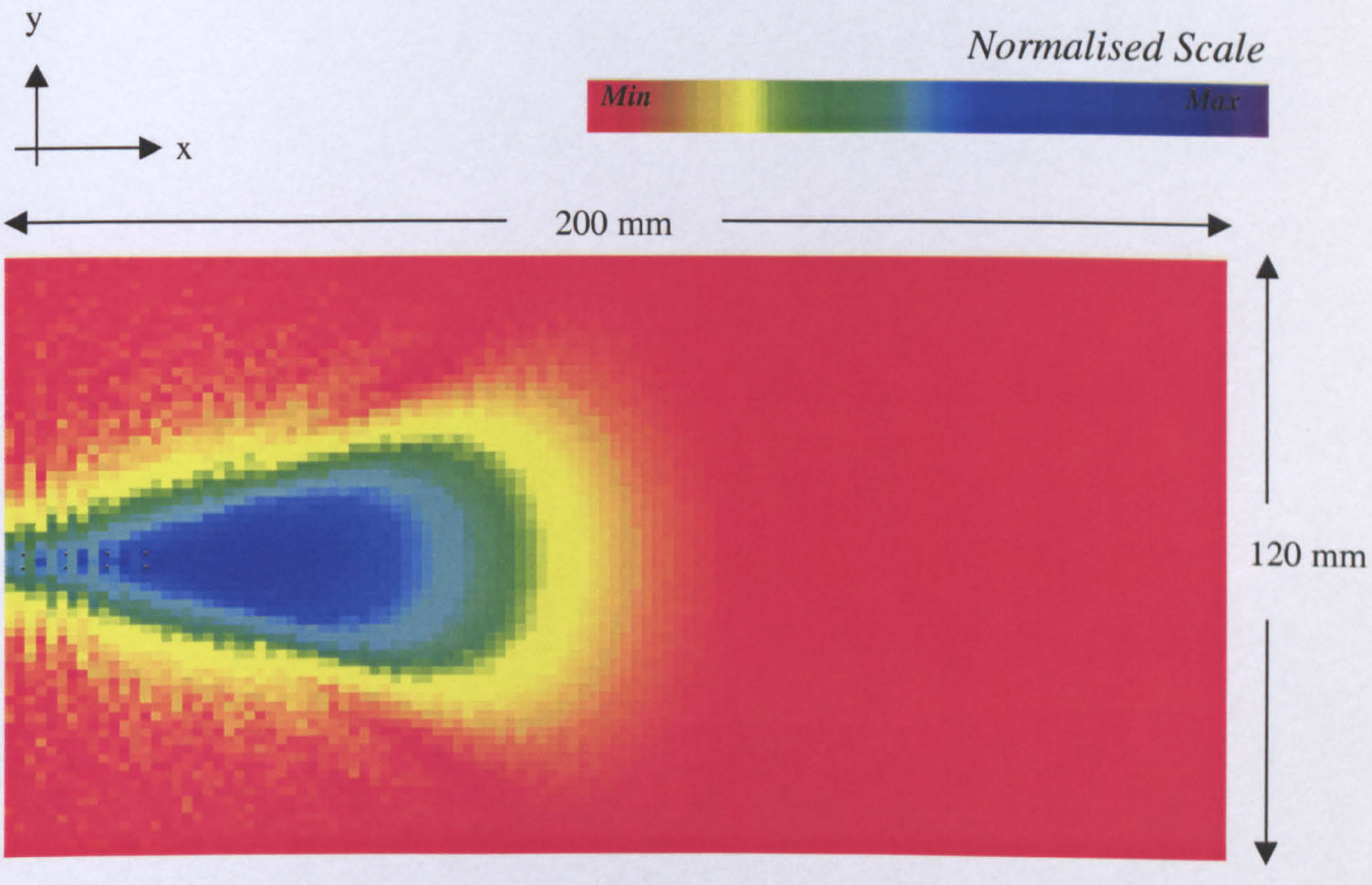

Figure 5.19: *Predicted Acoustic Profile for Dual Line Array (Λ/2 separation) Using Huygens' Model*

Experimental verification of this result was not performed due to the time consuming nature of this experiment, and since a degree of confidence in the model's ability to predict the projected beam profile was obtained from the previous comparison. It therefore seemed more prudent to forge ahead investigating other areas. However, it is proposed that further experimental work in this area should be performed to evaluate the possibility of steering and focusing the projected beam profile through selective phasing of the waveguide array.

5.6. Example Transducer Arrangement for NDE

It has been shown that Lamb waves can be generated and received successfully using thin cylindrical waveguides. The fact that individual point sources can be attached to the surface of a structure for subsequent interrogation is an attractive property for curved plates such as pipes or indeed objects with unusual shapes. Although this technology is proposed for embedded structural monitoring, an example portable transducer arrangement is presented for surface mount Lamb wave NDE. This is provided to demonstrate the ability of Lamb waves to detect defects in plates and is not meant to represent a practical transducer arrangement.

The portable transducer arrangement was realised by attaching a waveguide line array to a 75μm copper membrane. The membrane in turn was coupled to the aluminium test plate via a thin layer of ultrasonic coupling gel to allow mobility and efficient energy transfer into the load medium. This system was designed for A_0 mode operation since it is the most efficiently generated mode. Narrowband excitation was

again used (for better mode selectivity) with identical characteristics to that of Section 5.5. A portable waveguide transducer is also used for the detection of the Lamb wave to tune to the desired mode and enhance the performance. A diagram of the experimental arrangement is given in Figure 5.20.

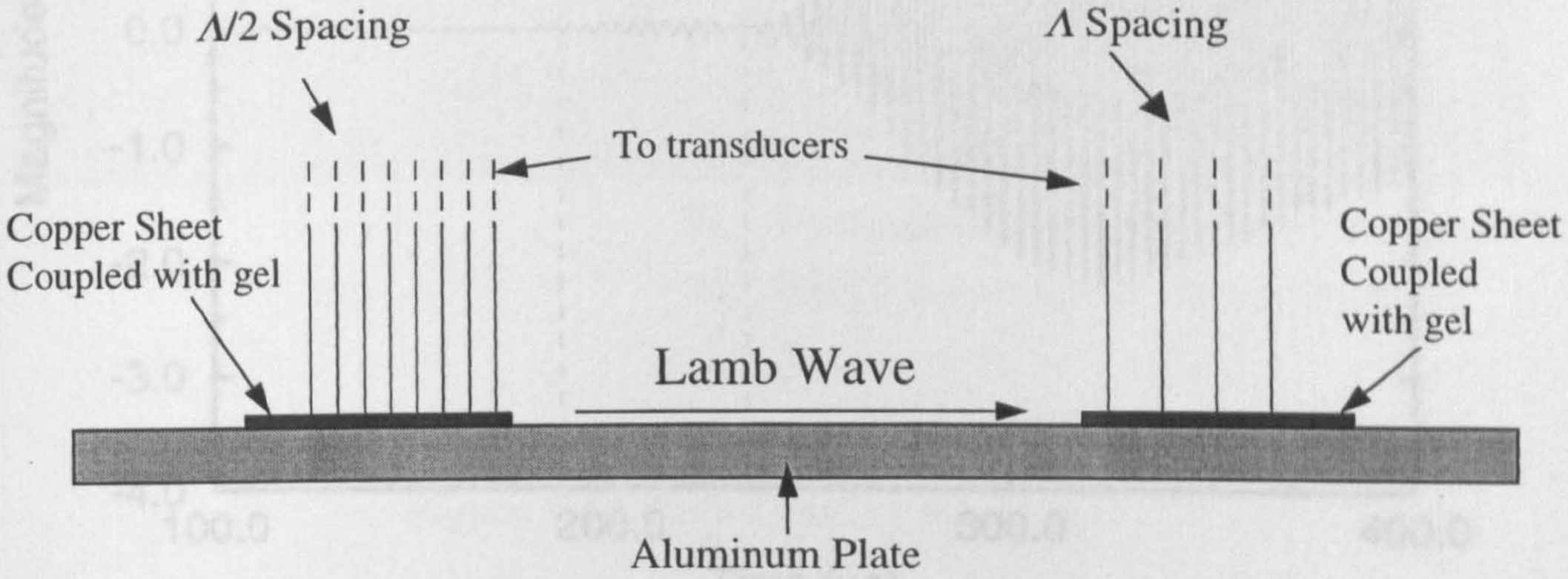

Figure 5.20: *Experimental Arrangement for portable waveguide transducers*

As previously stated the FTP of this system is 0.36MHz.mm which gives a group velocity of 2707ms^{-1}, a phase velocity of 1656ms^{-1}, and therefore a wavelength of 6.7mm. The generating waveguides were of length 344mm, while the receiving waveguides were of length 176mm, with the receiving and generating set of waveguides separated by 250mm. The expected arrival time of the signal is, therefore, calculated to be **234μs.** Figure 5.21 shows the signal received, and it can be seen that the flexible portable transducers have successfully transmitted and received a strong A_0 Lamb wave mode. A small amount of S_0 mode can also be identified, which is expected at **189μs** for this system FTP.

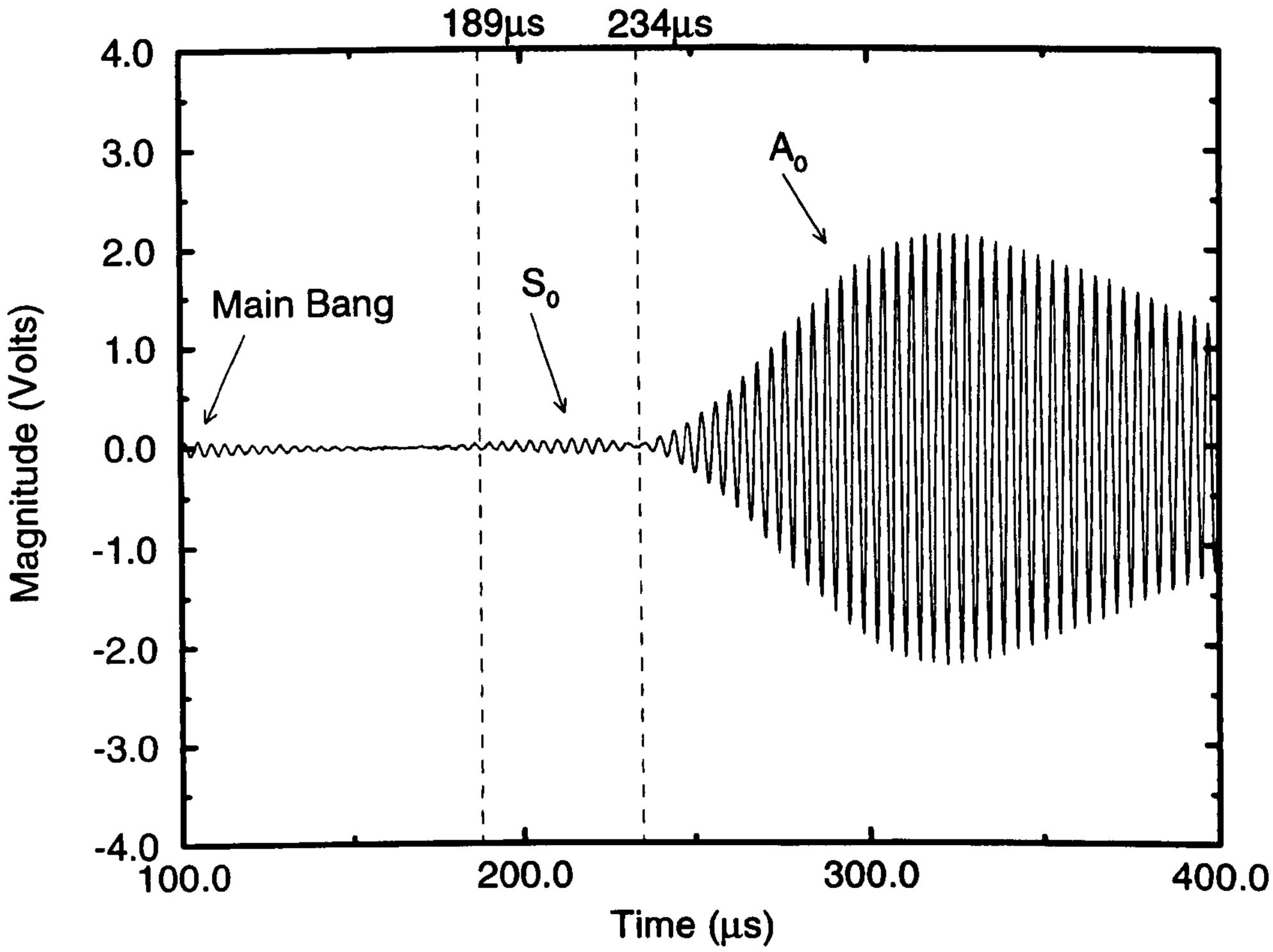

Figure 5.21: *Signal Received Utilising Portable Waveguide Transducers*

These transducers were then used to establish if a hole in the plate could be detected, by scanning an area of the plate and recording the magnitude of the received A_0 signals. Drops in magnitude correspond to transmit/receive paths that include the flaw. Scans were taken in two perpendicular directions (X and Y) to obtain position and size data of the flaw. A circular hole (diameter 16mm) was cut into the plate as a test flaw to be detected. Figure 5.22 shows an example of scanning in the Y-plane to detect the circular hole.

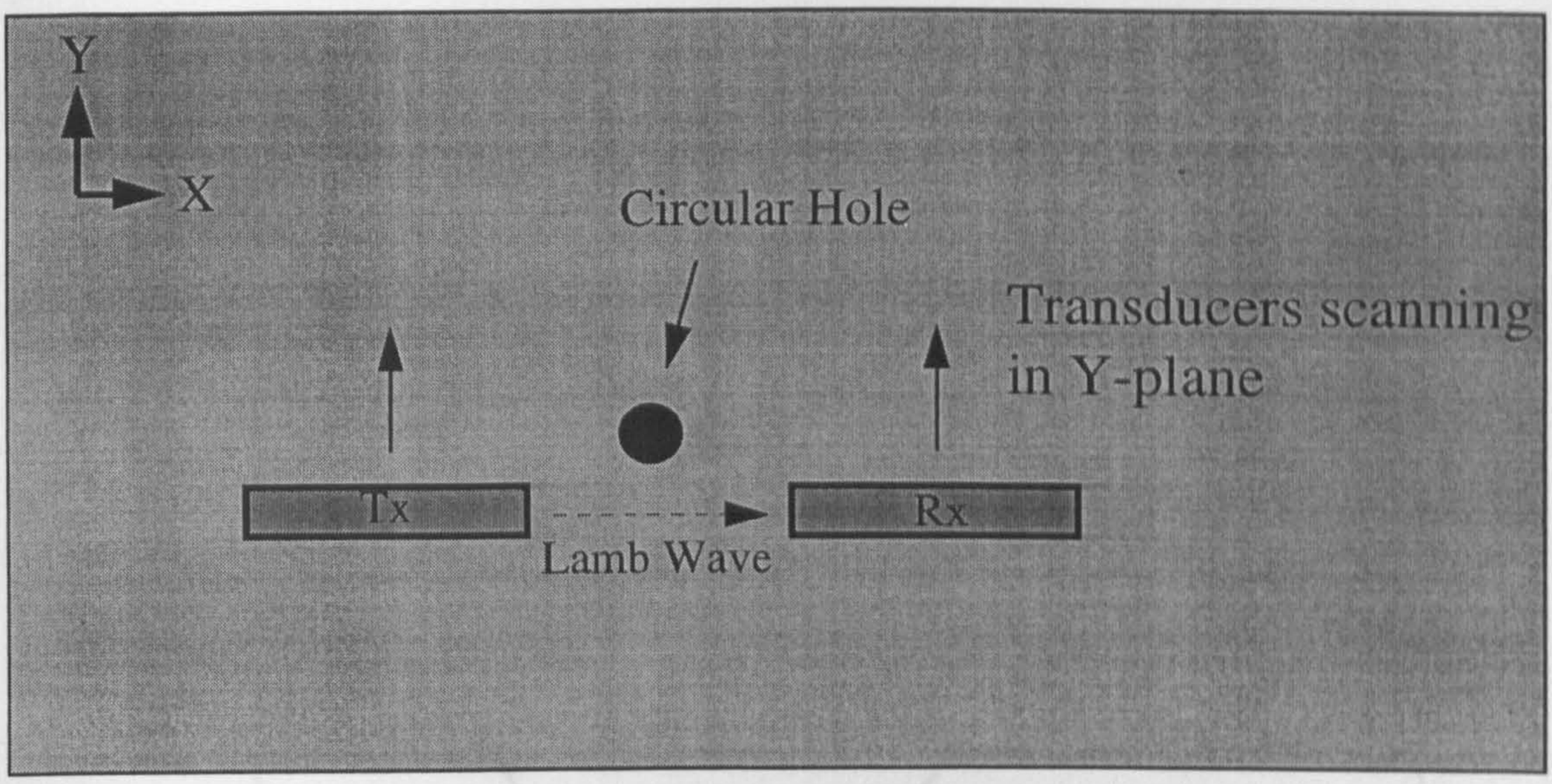

Figure 5.22: *Plate Scanning Example*

The circular hole was centred at a position X = 40mm, Y = 40mm from the origin of the scans. Figure 5.23 shows a plot of the X and Y magnitude information. The magnitude clearly drops when scanning in the defective region. The plotted information does not directly indicate a hole diameter of 16mm, because the magnitude of the received signal begins to drop as soon as the edge of the devices comes into line with the defect. The received signal further reduces as the devices become fully in the line with the defect. Therefore, selecting a suitable threshold level would allow size information to be deduced. For example a threshold level of 50% of the offset swing would yield approximately correct information for this case, i.e. there is a swing of 4 Volts and an offset of 1 Volt giving a threshold level of 3 Volts.

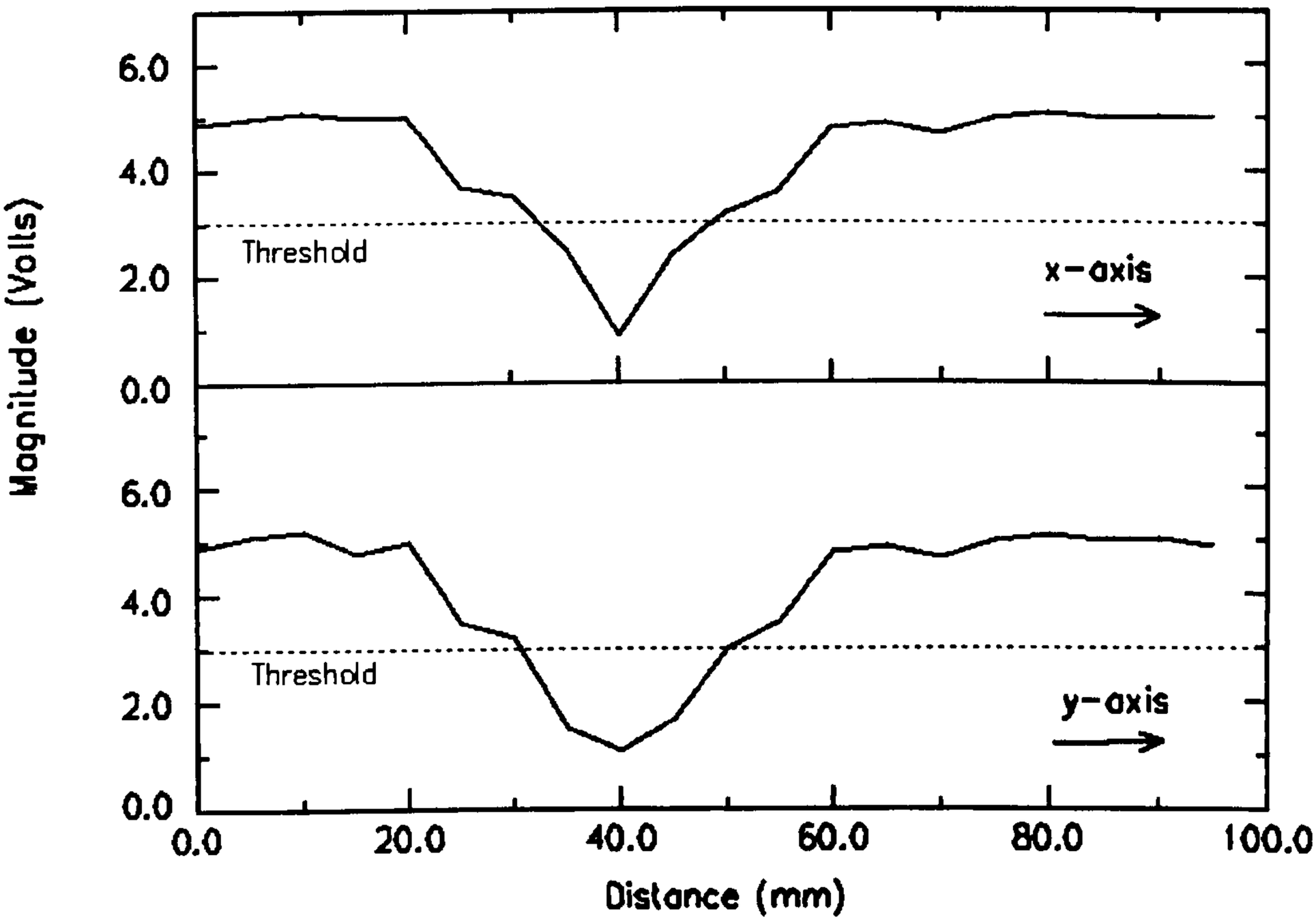

Figure 5.23: *Scan Results: Magnitude Response*

5.7. Conclusions

This Chapter has reported the development of a new Lamb wave generation and detection system. Experiment and FEA have shown that fibres may be used as mechanical waveguides to deliver ultrasound to specific points on a plate's surface. Furthermore, with the waveguides configured as a line array, using ID techniques, efficient generation and detection of ultrasonic Lamb waves was demonstrated. It is evident from the results presented that this form of surface excitation strongly favours A_0 Lamb wave mode operation, even when configured for the S_0 mode. This can be attributed to the inherent asymmetrical nature of the loading. Flexible and

movable fibre waveguide transducers were also presented and shown to successfully generate and receive Lamb waves. An example of flaw detection was provided utilising these transducers with a circular hole of 16mm being clearly identified.

The acoustic beam profile, of the fibre waveguide line array, was investigated using a theoretical model based on Huygens' Theorem. Good correlation was demonstrated between the theoretical predication and the experimentally measured response. Both model and experiment showed that in addition to the main energy lobe, significant side activity was present. The model has predicted that the employment of a second line array could eradicate this undesirable effect.

This Chapter has shown that fibre waveguides have the capability to be used as a Lamb wave sensor technology. Importantly, their small size relative to conventional transducers will enable this technology to be minimally invasive, and therefore, have significant potential as a smart structure tool. Consequently the following Chapter describes an investigation into the feasibility of a fully embedded fibre waveguide monitoring system.

CHAPTER 6

Embedded Fibre Waveguides For Lamb Wave Condition Monitoring

6.1 – Overview of Chapter

The results presented in the previous Chapter have shown that fibre waveguides provide a viable means of transporting acoustic energy for remote Lamb wave generation and detection. Furthermore, their non-invasive nature provides significant potential for an embedded system capable of operating in a smart structure environment. The envisaged monitoring system employs an array of embedded fibre waveguides to deliver ultrasonic energy to plate-type structures for Lamb wave excitation. As such, the fibre waveguide array behaves as a pseudo interdigital (ID) transducer, introducing a series of periodic stresses to the load plate to generate a particular Lamb wave mode. Similarly, an embedded waveguide receiver array can be utilised to detect the induced ultrasonic propagation. This Chapter investigates the realisation of such a system. Firstly the requirements of the waveguide geometry are considered and various configurations are evaluated through theoretical, modelling, and experimental analysis. Subsequently, an embedded tube-fibre waveguide Lamb wave system will be demonstrated in polymer and carbon fibre reinforced composite (CFRC) plates. Various design parameters are discussed and finally conclusions are drawn on the presented results.

6.2. The Fibre Waveguide Geometry

In order to utilise an embedded fibre waveguide to deliver ultrasound to a desired release location within a structure it must fulfil various criteria. This Section begins by stating the waveguide requirements, then goes on to evaluate the suitability of various possible geometric configurations.

Waveguide Requirements

Ideally, the waveguide configuration should fulfil the following criteria:

- Provide total elastic isolation for the ultrasound propagating along the waveguide from the surrounding structure.

- Be able to 'leak' the ultrasonic energy from the waveguide into the structure at a desired release location.

- Be capable of delivering a unimodal longitudinal (axisymmetric) acoustic mode. As outlined in Chapter 3, this eliminates the need to quantify the rotational alignment of the fibres since longitudinal modes have equal phase around the circumference of the waveguide at given any axial position.

- Operate within a practical frequency range for Lamb wave propagation in non-metallic plates i.e. < 1MHz

- Be non-invasive so that the structural integrity of the host is maintained.

Possible Waveguide Configurations

Three waveguide configurations shall be considered, in terms of their ability to meet these requirements. These are the homogeneous fibre, the clad fibre, and the tube-sleeved fibre, as shown in Figure 6.1.

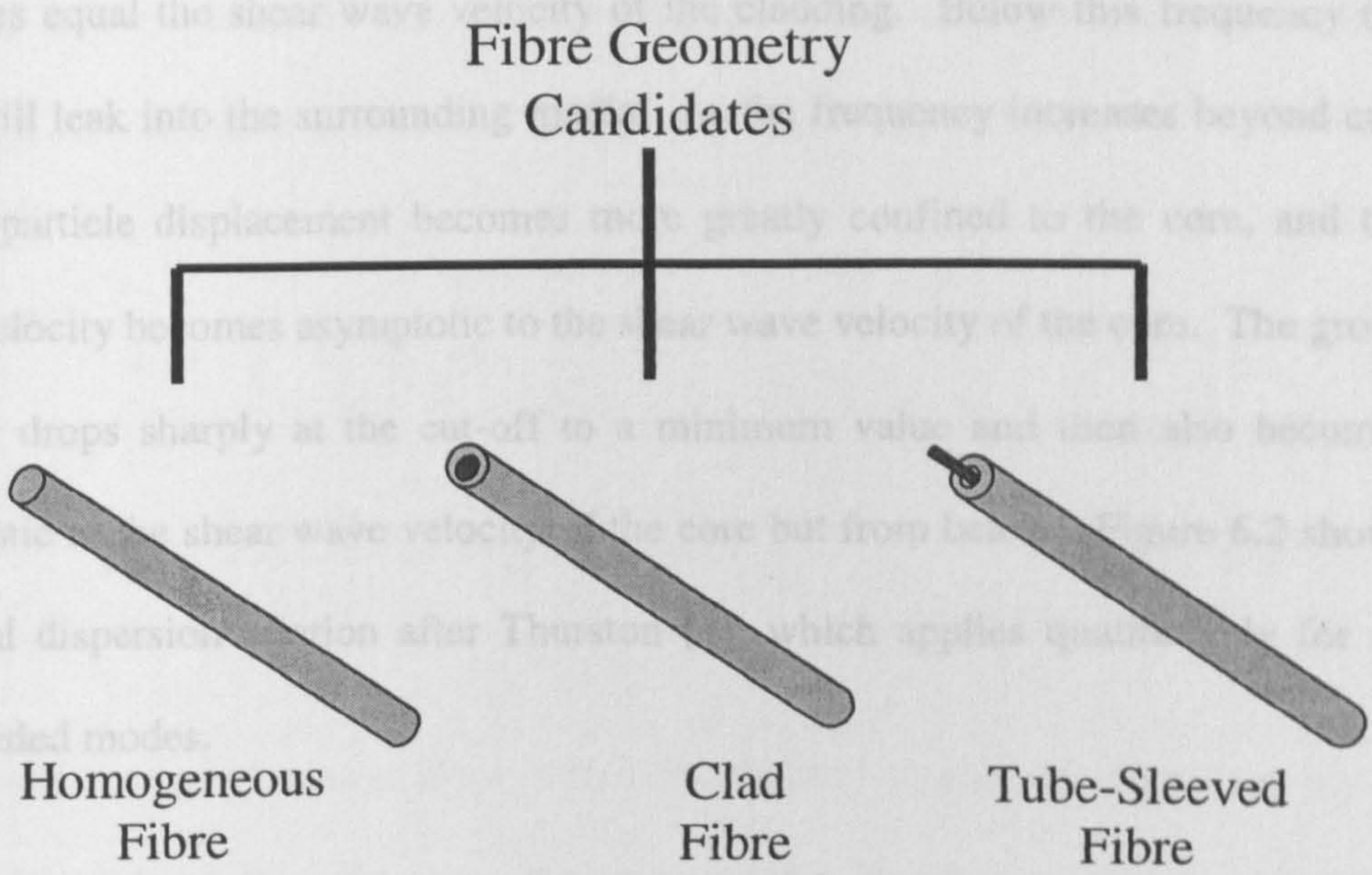

Figure 6.1: *Potential Fibre Configurations*

6.2.1. The Homogeneous Fibre

6.2.1.1. Discussion

In order to embed a homogeneous fibre into a material, and propagate ultrasound along it without leakage, confinement of the particle motion to the fibre core is required. Such a fibre embedded within a material of infinite size, is analogous to a cylindrical bar clad in an infinite medium. For this case Thurston [1] shows that guided mode propagation can only be supported when the shear wave velocity of the

cladding (C_{s2}) exceeds that of the shear wave velocity of the core (C_{s1}). Furthermore, guided mode propagation can only exist for waves that propagate with a slower phase velocity (C) than the shear wave velocity in the cladding. Therefore, a longitudinal mode with $C < C_{s2}$ is required to meet the requirements of the system. Each guided mode of propagation has a cut-off frequency where the phase and group velocities equal the shear wave velocity of the cladding. Below this frequency the mode will leak into the surrounding media. As the frequency increases beyond cut-off the particle displacement becomes more greatly confined to the core, and the phase velocity becomes asymptotic to the shear wave velocity of the core. The group velocity drops sharply at the cut-off to a minimum value and then also becomes asymptotic to the shear wave velocity of the core but from below. Figure 6.2 shows a typical dispersion relation after Thurston [1], which applies qualitatively for all core-guided modes.

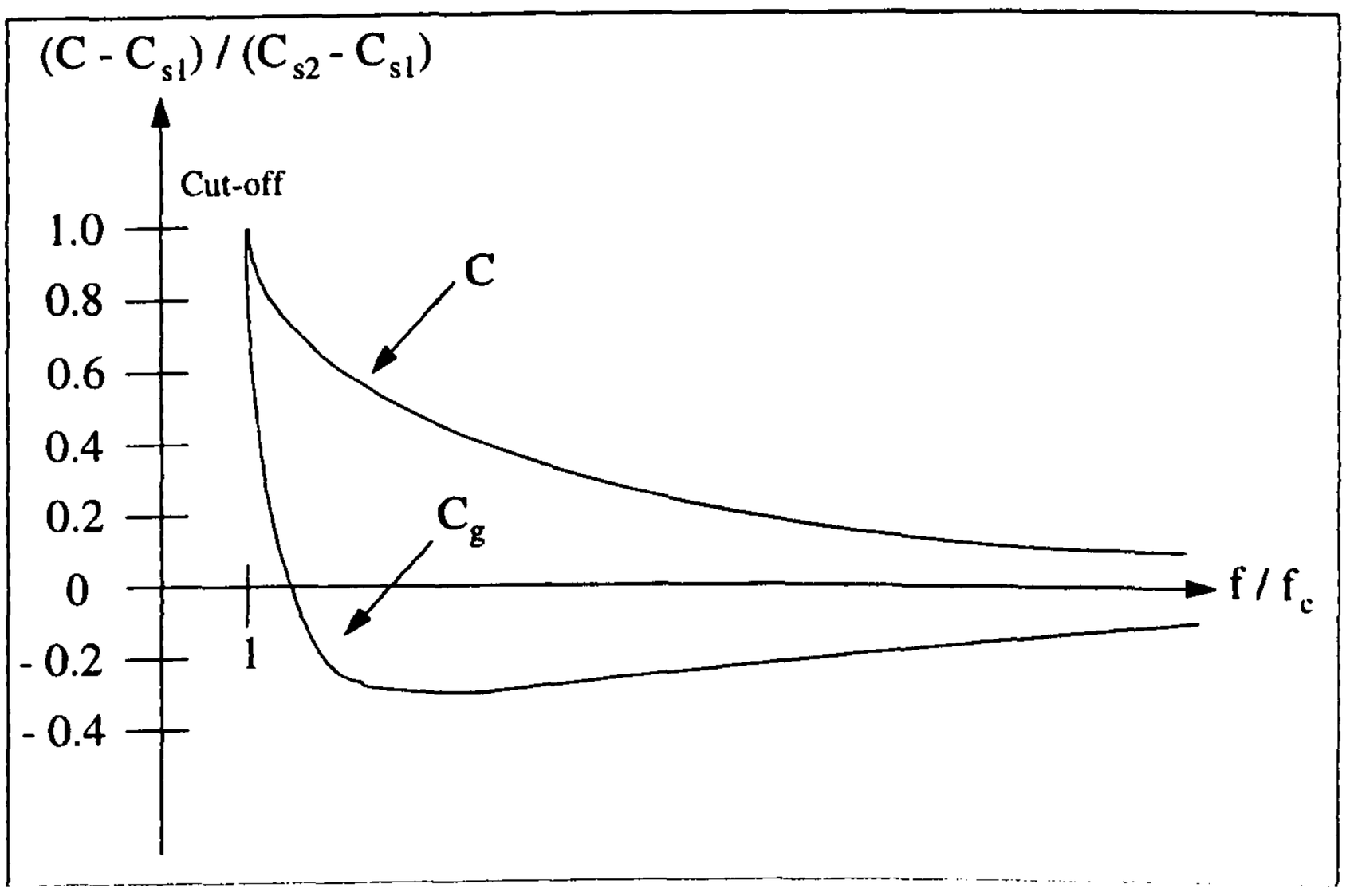

Figure 6.2: *Typical guided mode dispersion characteristics*

As illustrated in the Figure, the cut-off frequencies of core-guided modes in an infinite cladding where $C_{s2} > C_{s1}$ occur when $C = C_{s2}$. Such cut-off values are necessary to establish the operating frequency range of any given system. For the case of torsional modes the cut-off frequencies depend on the values of the core radius a, and the material properties of the core (subscript 1) and the cladding (subscript 2), and can be established from Equations 6.1 and 6.2 [1].

$$k_1 a = \frac{2\pi a f_c}{C_{s1}} \sqrt{1 - \left(\frac{C_{s1}}{C_{s2}}\right)^2} \qquad \textbf{6.1}$$

$$k_1 a \frac{J_0(k_1 a)}{J_1(k_1 a)} = -2\left[\frac{\mu_2}{\mu_1} - 1\right] \qquad \textbf{6.2}$$

The cut-off frequencies associated with non-torsional modes are described by far more complex formulae. However, the axisymmetric longitudinal modes, which are of interest, have cut-off frequencies very near to those of torsional modes [54]. Boyd *et al* [55] report on the cut-off frequencies of lower order modes for the case where the core material shear wave velocity is 3.8% lower than the cladding. Interestingly, for this material combination it was reported that no cut-off for the F(1,1) mode was found, however the wave penetrates a large distance into the cladding in the low frequency limit rendering it useless in this regime for core confined guidance.

This Section has highlighted that no guided mode propagation is possible for a waveguide with a shear wave velocity in excess of the surrounding media. Consequently, choice of waveguide material is severely restricted for operation in

non-metallic plates, such as CFRC whose shear wave velocities are typically very low. Therefore, the waveguide would be limited to a very low velocity material, which would typically display high attenuation. With this huge limitation in mind, utilising a homogeneous fibre waveguide to deliver ultrasonic energy to a structure for the present application is considered impractical.

6.2.1.2. Experiment: Embedded Homogeneous Fibre as a Lamb Wave Receiver

The previous Section has suggested that an embedded homogeneous fibre waveguide is impractical for ultrasonic delivery in the proposed system. However, the following experiment was carried out to investigate its ability to detect Lamb wave activity. A 0.5mm copper waveguide was embedded within a hard-setting shore 80 CY1300/HY1301 epoxy plate, which was cured within a PTFE frame. The copper waveguide was held in place under tension as the epoxy set, resulting in a 4mm thick hard set epoxy plate with the waveguide embedded at half its thickness. Lamb waves were generated in the epoxy plate using a Lamb wave Interdigital Transducer (IDT) as described by Gachagan *et al.* [41], surface bonded to the plate. The embedded fibre waveguide (which extends out of the plate) was attached, via a conical epoxy bond, to a thickness mode PZT5A piezoceramic disc transducer with a lateral harmonic at 400kHz to receive any signals detected. The length of fibre between the edge of the plate and the transducer was 300mm. Figure 6.3 shows the experimental arrangement.

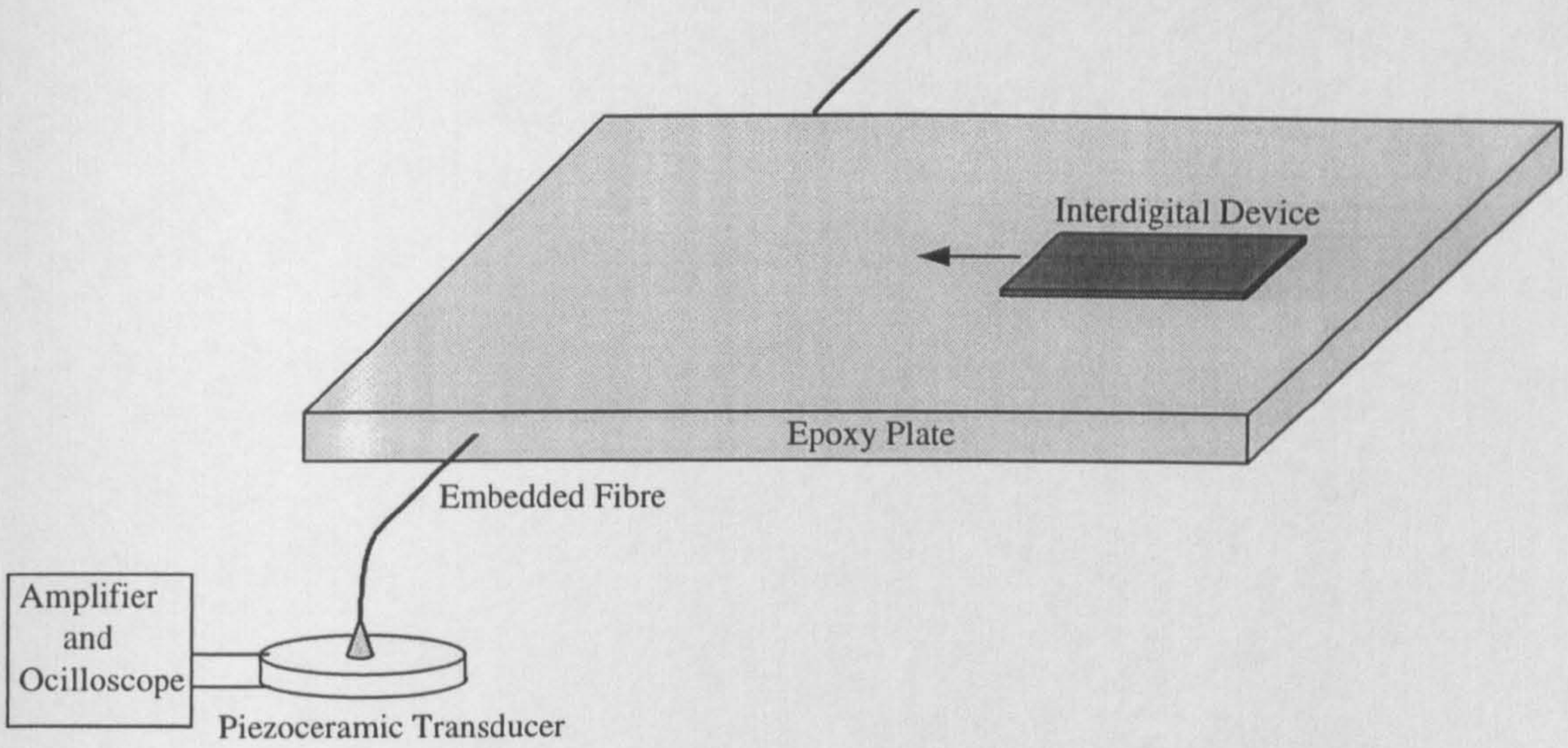

Figure 6.3: *Embedded Fibre as Lamb Wave Sensor Experimental Arrangement*

The waveguide did indeed detect Lamb wave activity, however, the received signal was by far the greatest when the IDT was angled towards the edge of the plate where the waveguide emerged. This is because any acoustic energy coupling into the embedded waveguide will not be guided out of the plate, but will leak into the surrounding epoxy. However, energy coupling into the waveguide at its exit will be guided to the piezoceramic transducer. Consequently, the IDT was directed to the waveguide's point of exit from a distance of 105mm. The IDT was driven at 400kHz yielding an FTP of 1.6. Figure 6.4 displays the Lamb wave group velocity dispersion curves for the hard-set epoxy. At a frequency thickness product (FTP) of 1.6, there are four modes that can propagate in the plate namely A_0, S_0, A_1, and S_1.

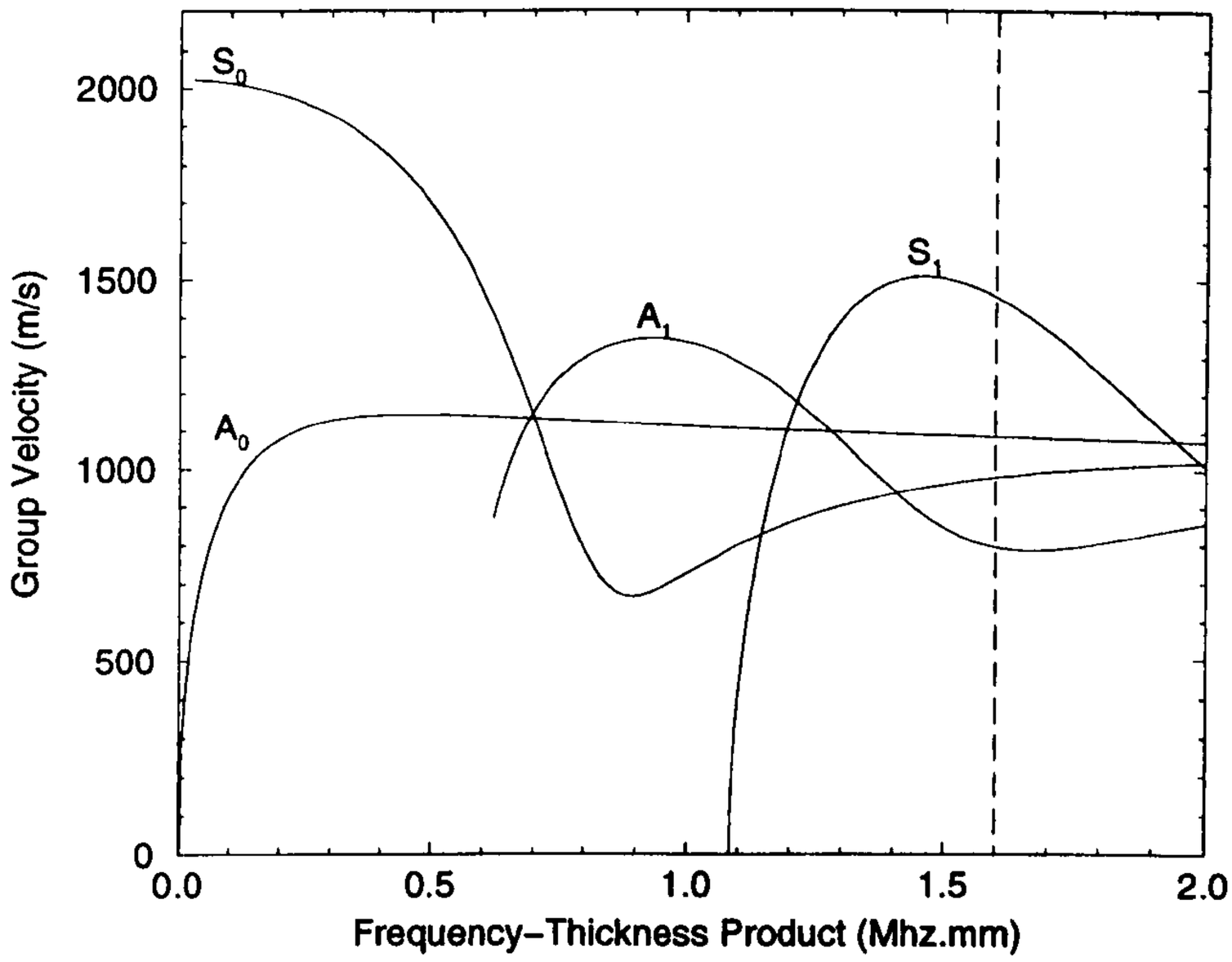

Figure 6.4: *Group Velocity Lamb Wave Dispersion Curves for Hardset Epoxy*

The group velocities and thus propagation times along 105mm of hardset epoxy at an FTP of 1.6MHz.mm are presented in Table 6.1. The total propagation time is also given, which includes the time it takes the ultrasonic signals to propagate the 300mm length of copper waveguide as the L(0,1) mode (82μs).

Mode	C_g (ms^{-1})	ΔT_{plate} (μs)	ΔT_{total} (μs)
A_0	1080	97	179
S_0	975	108	190
A_1	785	134	216
S_1	1450	72.5	154.5

Table 6.1: *Velocities and Propagation Times*

Figure 6.5 shows the signal received by the waveguide, which arrives at approximately 154.5μs as expected for S_1 propagation. There are visible phase shifts present where the A_0 and S_0 modes are expected, and the A_1 mode appears to arrive slightly earlier than predicted. The later signals are a result of reflections in the plate.

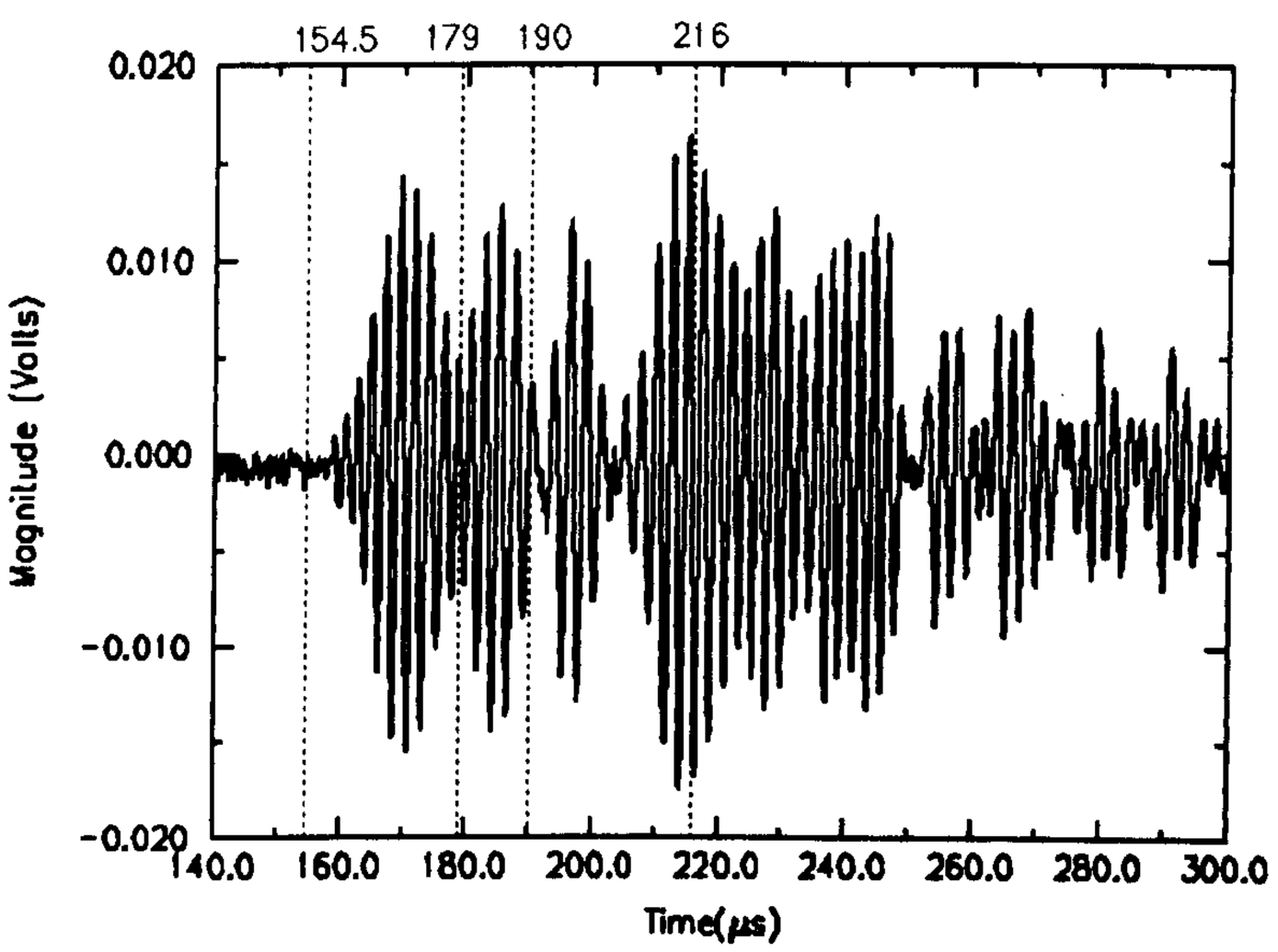

Figure 6.5: *Signal detected by embedded fibre*

It can be concluded that the embedded fibre waveguide did indeed detect Lamb waves propagating in the plate. However, the received signal corresponds to energy present at the edge of the plate where the waveguide emerges, and in that respect eliminates the significance of embedding.

6.2.1.3. Critical Analysis of the Homogenous Fibre

It has been discussed that no guided mode propagation is possible along an embedded homogeneous fibre waveguide with a shear wave velocity less than that of

the surrounding media. This severely limits the choice of waveguide material for a practical system in non-metallic plates, and therefore, eliminates this waveguide configuration. However, the described experiment did reiterate the fibre waveguide's ability to detect Lamb waves.

6.2.2. The Clad Fibre

6.2.2.1. Discussion

As discussed in Chapter 2, interest in clad rod waveguides developed due to their capacity to provide a non-lossy support, thereby permitting the coiling of long delay lines. This is possible since the correct choice of material, radius of core and cladding, and mode generation allows the propagating acoustic energy to be largely confined to the core of the waveguide. Therefore, with the correct choice of materials, could an embedded clad fibre waveguide be utilised to deliver ultrasonic energy to a structure, and meet the requirements outlined at the beginning of Section 6.2?

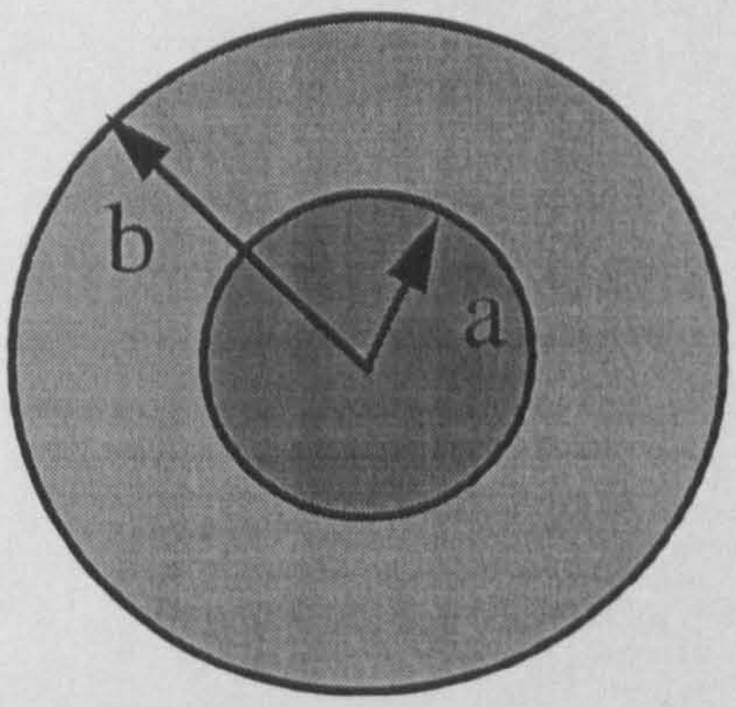

Figure 6.6: *The Clad Rod*

A clad rod, such as that shown in Figure 6.6 contains a core of one material where r<a, and a cladding of a second material for the region a<r<b. Modes guided within this geometry can only exhibit non-leaky properties when the velocity of plane shear waves in the cladding material exceeds that of the core material [1]. For such a material combination, a typical mode will exhibit core-confined propagation beyond a cut-off frequency, and become increasingly restricted to the core with frequency. Below cut-off, the motion of a mode is similar to that in an unclad rod. That is, the mode behaves as if it were propagating in a homogeneous medium and, therefore, sufficient energy is present at the surface of the rod [55].

The dispersionless T(0,1) mode of a uniform cylindrical rod cannot exist in the clad waveguide geometry, and in fact all torsional modes are dispersive [54]. The axisymmetric longitudinal modes, which are often referred to as radial modes because their primary particle displacement is radial, display similar dispersion characteristics to the torsional modes. Figure 6.7 shows the particle behaviour for the first four guided modes in a clad rod, that is F(1,1), L(0,1), T(0,1), and F(2,1), after Boyd *et al.* [55].

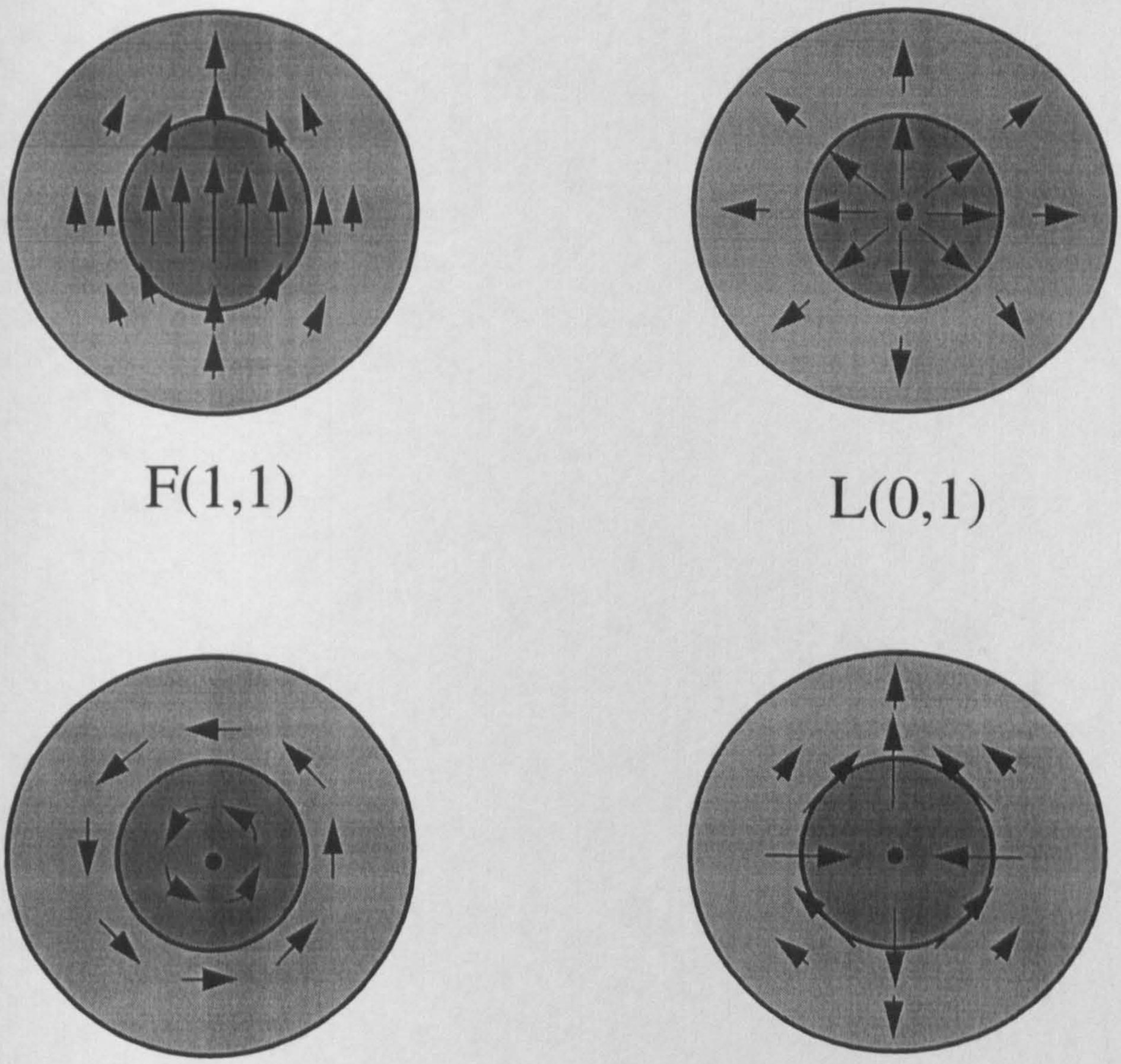

Figure 6.7: *Particle Displacement associated with the first four clad fibre modes*

6.2.2.2. Modelling: Dispersion Analysis

The NDE laboratory at Imperial College London have developed a commercial package called 'DISPERSE', which evaluates the ultrasonic dispersion characteristics of multi-layered plate and cylinder geometries [117]. This package was utilised to perform dispersion analysis on clad fibre waveguides that have material properties permitting core-guided propagation. As an example, a steel clad

copper waveguide with a core to total radius ratio of 1:4 is presented. The phase and group velocities of the first two modes, namely L(0,1) and F(1,1), against Frequency-Radius Product (FRP) are presented in Figures 6.8 and 6.9, along with the mode shapes for both *leaky* and *core-guided* regimes.

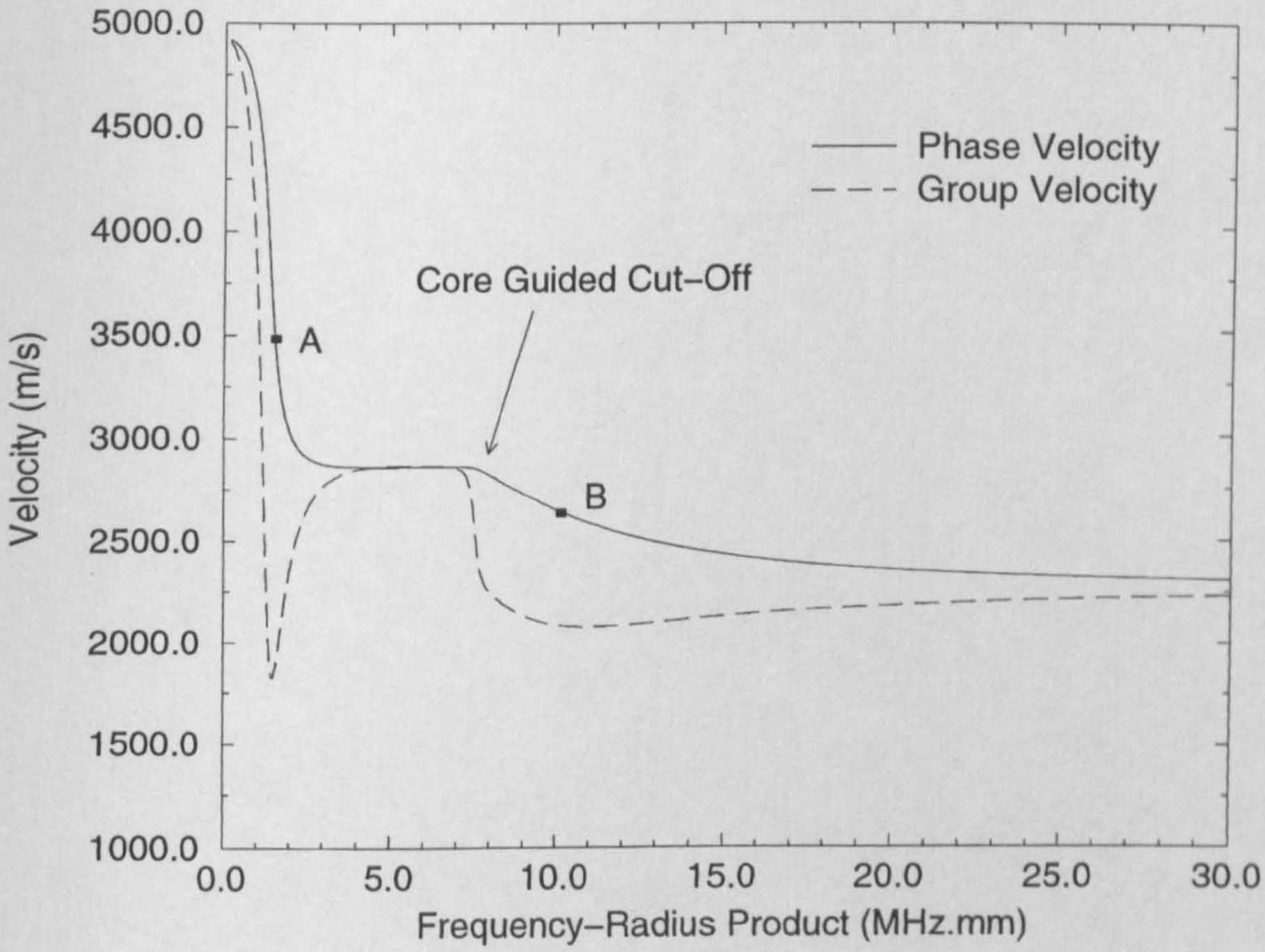

Mode Shape at A
Leaky

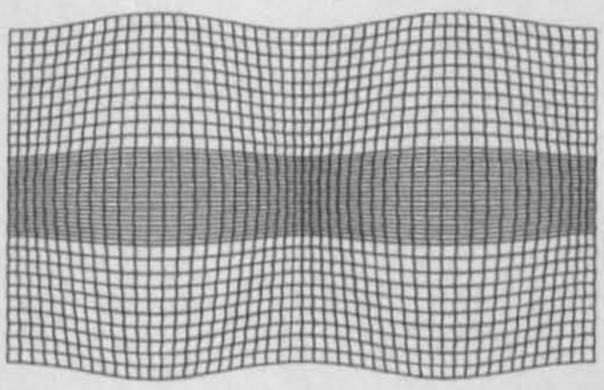

Mode Shape at B
Core-guided

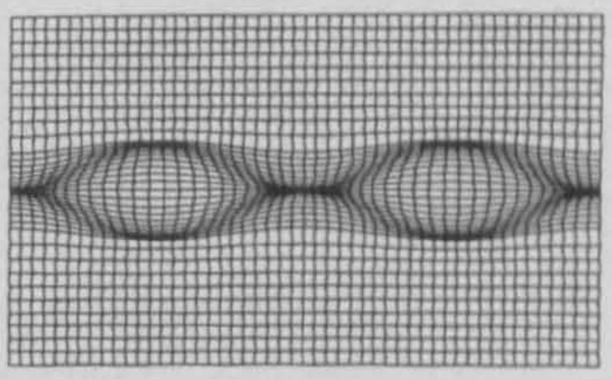

Figure 6.8: *L(0,1) Dispersion Curves in a Steel Clad Copper Core Waveguide (core radius to total radius ratio = 1:4), and Mode Shapes at Two Locations on Curves*

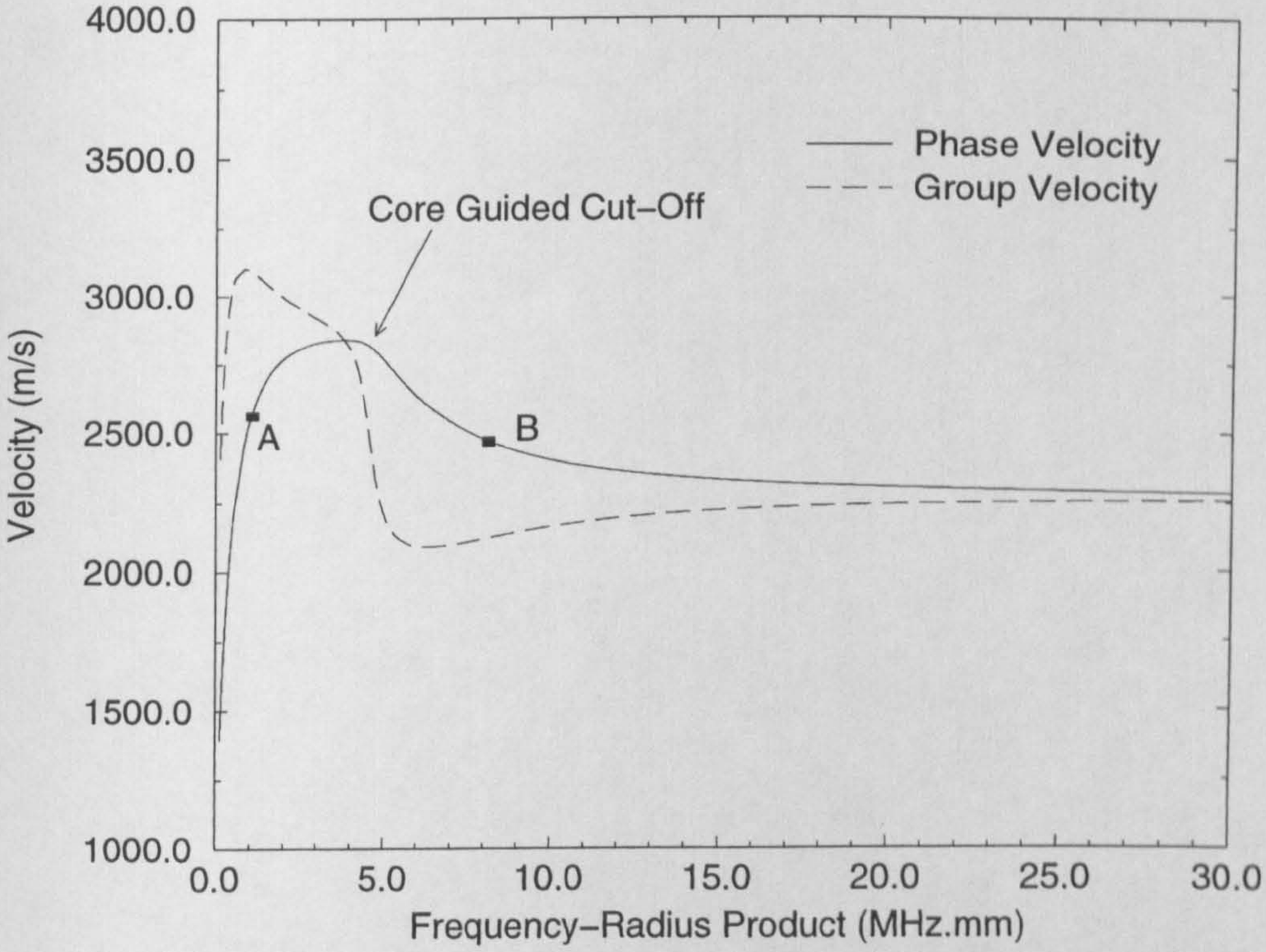

Figure 6.9: *F(1,1) Dispersion Curves in a Steel Clad, Copper Core Waveguide (core radius to total radius ratio = 1:4), and Mode Shapes at Two Locations on Curves*

For this clad waveguide configuration it can be seen that the lowest FRP at which core-guided propagation can be realised occurs with the F(1,1) mode at approximately 4MHz.mm. In addition, the first axisymmetrical mode is not core-guided until an FRP of around 7.5MHz.mm is established. Consider the requirements of the waveguide previously outlined, which included the potential to

be integrated into CFRC materials with minimal structural degradation, and an operating frequency below 1MHz. As discussed in the optical fibre sensor review of Chapter 2, the need to keep the overall diameter of optical fibre sensors to a minimum is crucial for unobtrusive integration into composite structures. A maximum diameter of 0.125mm is usually adopted since it is the typical thickness of a CFRC single ply. Therefore, with the obvious geometric similarities of acoustic, and optical fibre waveguides, an overall diameter in this region should be the desired goal. Therefore, revisiting the dispersion analysis of the steel clad copper waveguide, an overall diameter of 0.125mm (radius 0.0625mm) would ensure that core-guided propagation could only be realised above a frequency of 64MHz, while axisymmetric core-guided propagation could only be achieved above 120MHz. This is clearly well in excess of the required frequency range. Although many other material combinations were investigated, no core-guided propagation could be established within (or even near to) the required frequency range for the small fibre diameters of interest. Subsequently, this eliminates the clad waveguide configuration from the current application.

6.2.2.3. Critical Analysis of the Clad Fibre

At first consideration the clad fibre waveguide appeared to provide a likely solution to the outlined requirements. That is, with a suitable choice of materials guided acoustic energy could be confined to the core, and therefore the cladding would provide elastic isolation from the surrounding media. In addition, the trapped energy could be released by simply removing the cladding at a desired location. However, dispersion analysis proved that obtaining core-guided propagation within a practical

frequency range would not be feasible for the small fibre diameters of interest. An additional complication would have arisen utilising this configuration at the required FRP for core-guided propagation. Namely, that numerous leaky modes would also be supported by the waveguide making uni-modal generation of the desired core-guided mode problematic to achieve. Consequently, the clad fibre waveguide will not be considered any further.

6.2.3. Tube-Sleeved Fibre

6.2.3.1. Discussion

The concept of embedding a homogeneous fibre housed within a thin tube is an attractive option since it has the potential to fulfil all the requirements outlined in Section 6.2. That is, the tube-sleeve will provide elastic isolation from the surrounding structure for the ultrasound propagating along the homogenous fibre. Furthermore, removal of a section of the tube-sleeve at a desired location will enable the release of the confined ultrasonic energy into the surrounding media. Uni-modal longitudinal propagation within a practical frequency range should be achievable since the propagating medium is essentially a homogeneous fibre in free space. Therefore, as discussed in Chapter 3, at the very low FRP of interest only the three fundamental modes of propagation will be possible, i.e. L(0,1), F(1,1) and T(0,1). Therefore, the polymer cone technique discussed in Chapter 4 can be utilised to establish L(0,1) propagation in the waveguide with a SNR of 40dB and a SCNR of 25dB.

6.2.3.2. Experimental Evaluation of Mechanical Isolation Property

In this Section the tube-fibre configuration will be experimentally examined in terms of the tube's ability to mechanically isolate the ultrasound propagating along the fibre waveguide from the surrounding media. This will be investigated utilising an aluminium tube, of outer diameter 0.86mm, and inner diameter 0.76mm, housing a copper waveguide of diameter 0.25mm.

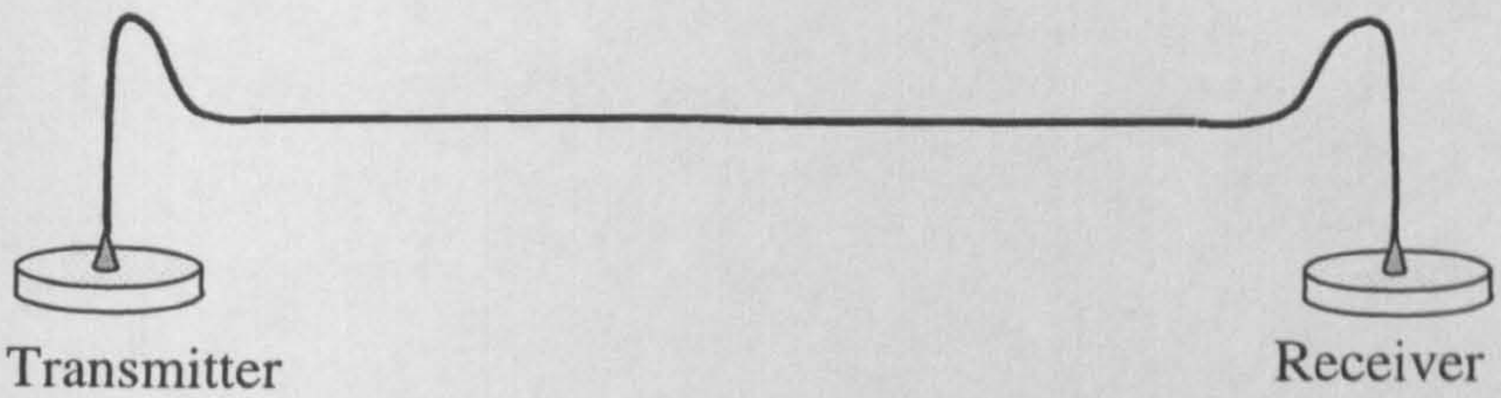

Figure 6.10(a): *0.25mm Copper Guide*

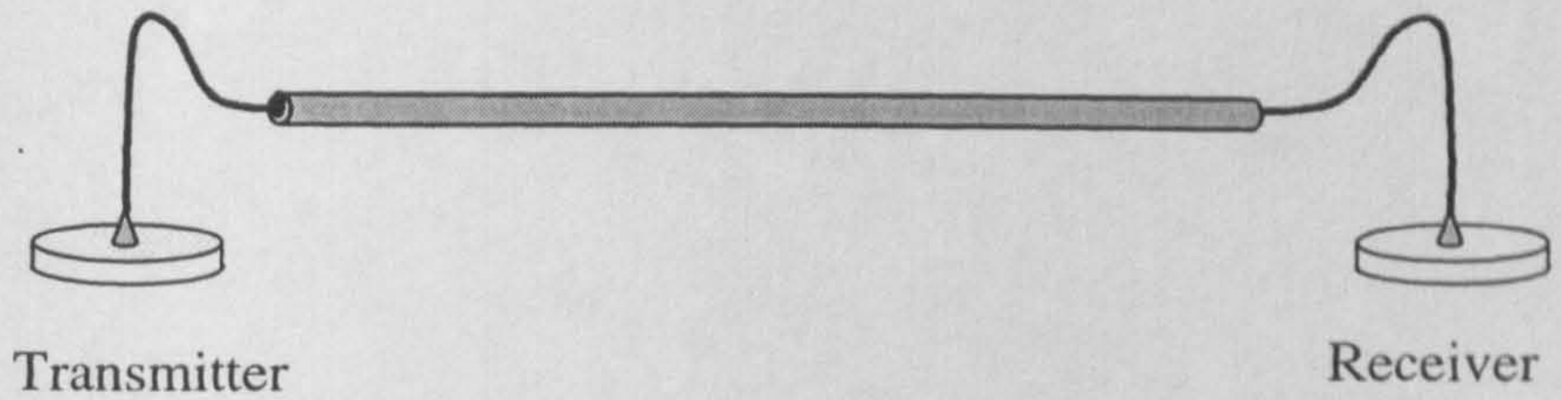

Figure 6.10(b): *0.25mm Copper Guide Inside an Aluminium Sleeve*

Firstly consider a 0.25mm copper guide of length 700mm with no aluminium sleeve. The L(0,1) mode is generated and received at 250kHz using the polymer cone technique, as illustrated in Figure 6.10(a), and the received signal is presented in Figure 6.11, trace A1. Following this, a 20mm section half way along the length of the waveguide was adhered with fast setting epoxy resin to a 1mm thick aluminium

plate. After the epoxy had fully cured the received signal was stored and is shown on Figure 6.11, trace A2. As can be seen, the received signal has been severely attenuated with the majority of propagating ultrasound leaking into the plate via the epoxy bond. This experiment was then repeated, with a 600mm length of the aluminium tubing providing a sleeve for the copper waveguide, see Figure 6.10(b). The signals received before and after a 20mm section of the tubing was adhered to the aluminium plate are shown in Figure 6.11, traces B1, and B2 respectively. It is clear that this tube-sleeve configuration has provided significant mechanical isolation for the ultrasound propagating in the copper guide with traces B1 and B2 appearing almost identical.

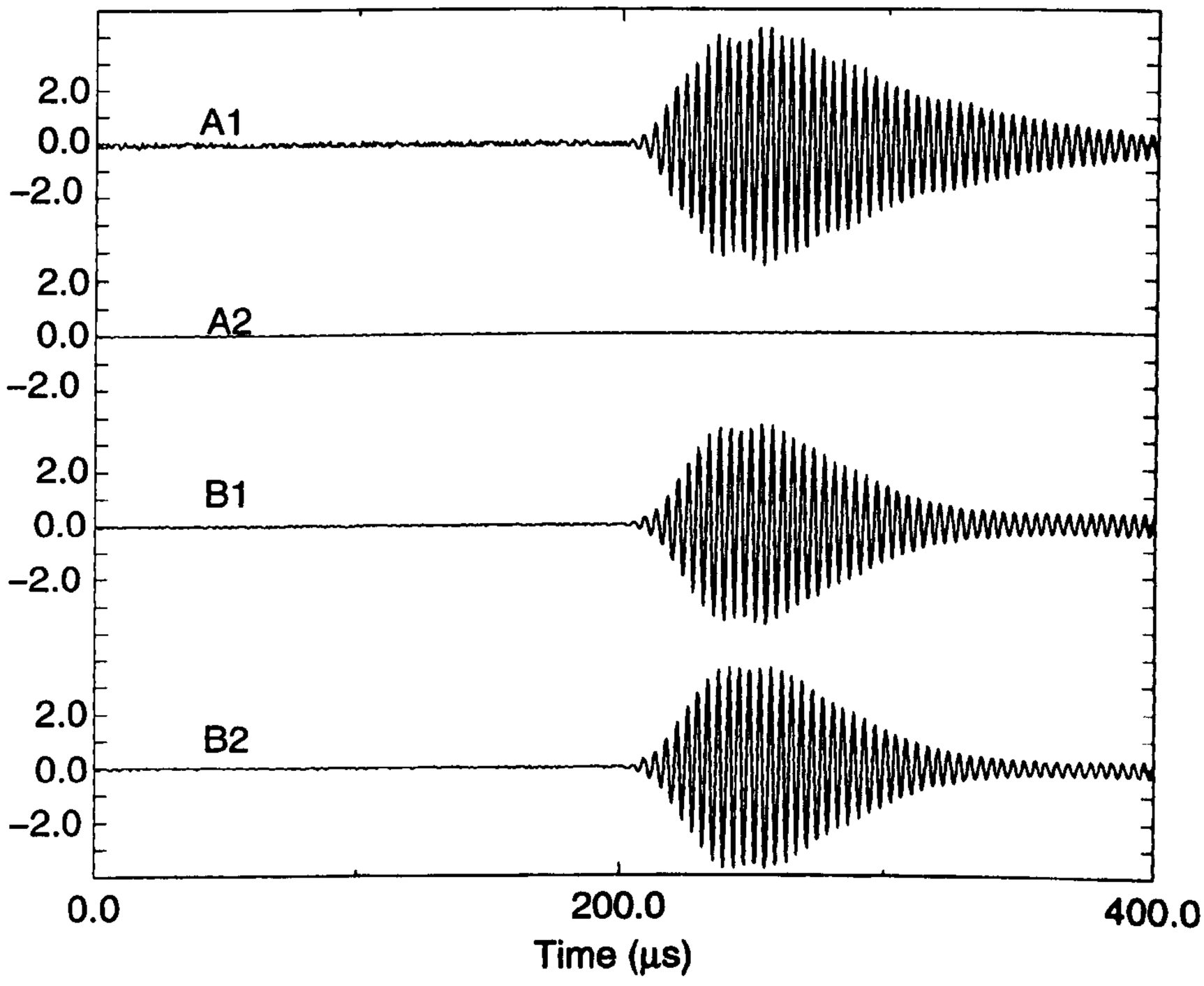

Figure 6.11: *Signals Received to Evaluate the Mechanical Isolation Provided by the Tube–Fibre Configuration*

6.2.3.3. Experimental Evaluation of Delivery Capability

In this Section the tube-fibre configuration will be experimentally examined in terms of its ability to deliver ultrasound to a desired release location within a plate-type structure. A hard-set epoxy plate of dimensions 300mm x 250mm x 5mm was cured with a tube-fibre embedded within it. The tube-fibre configuration was again an aluminium sleeve with an outer diameter, 0.86mm and inner diameter, 0.76mm housing a 0.25mm copper waveguide. A 10mm section of the sleeve was removed prior to embedding to create a release area. Fast setting epoxy was used to seal the resulting open area and provide a mechanical bond to the waveguide, see Figure 6.12. This procedure ensures that no hard setting epoxy will leak into the tube during the initial stages of its cure, which would result in undesirable mechanical bonding of the waveguide to the tubing.

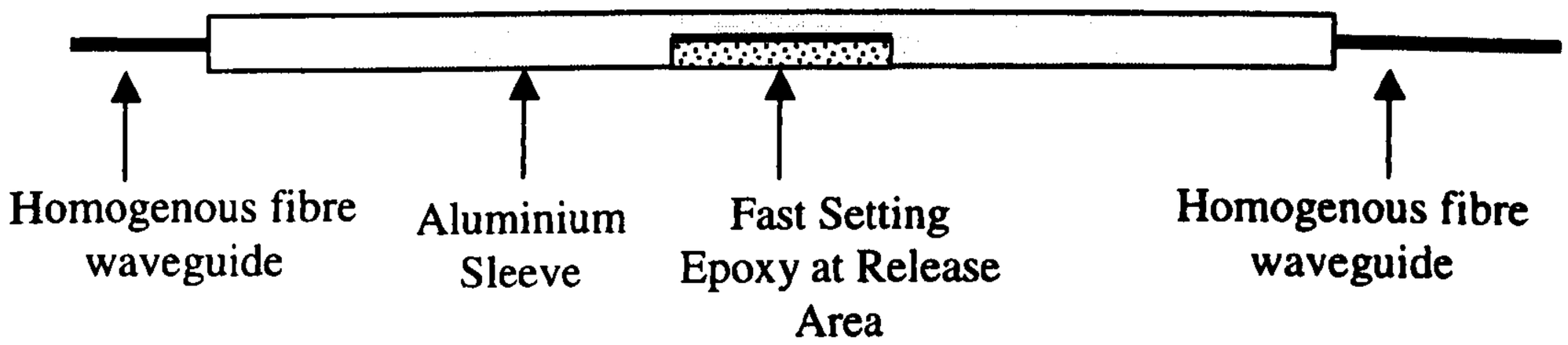

Figure 6.12: *Tube-Fibre Configuration to be embedded (not to scale)*

With the tube-fibre embedded within the epoxy plate, as depicted in Figure 6.13, ultrasonic propagation was induced within the waveguide utilising the polymer cone technique. The transducer utilised was a piezoceramic PZT5H disc with a lateral harmonic at 250kHz, consequently it was excited with a 250kHz, 200Vp-p, 'Hanning

windowed', 10 cycle toneburst. It should be noted that the waveguide is 250mm long from the excitation transducer to the centre of the release section.

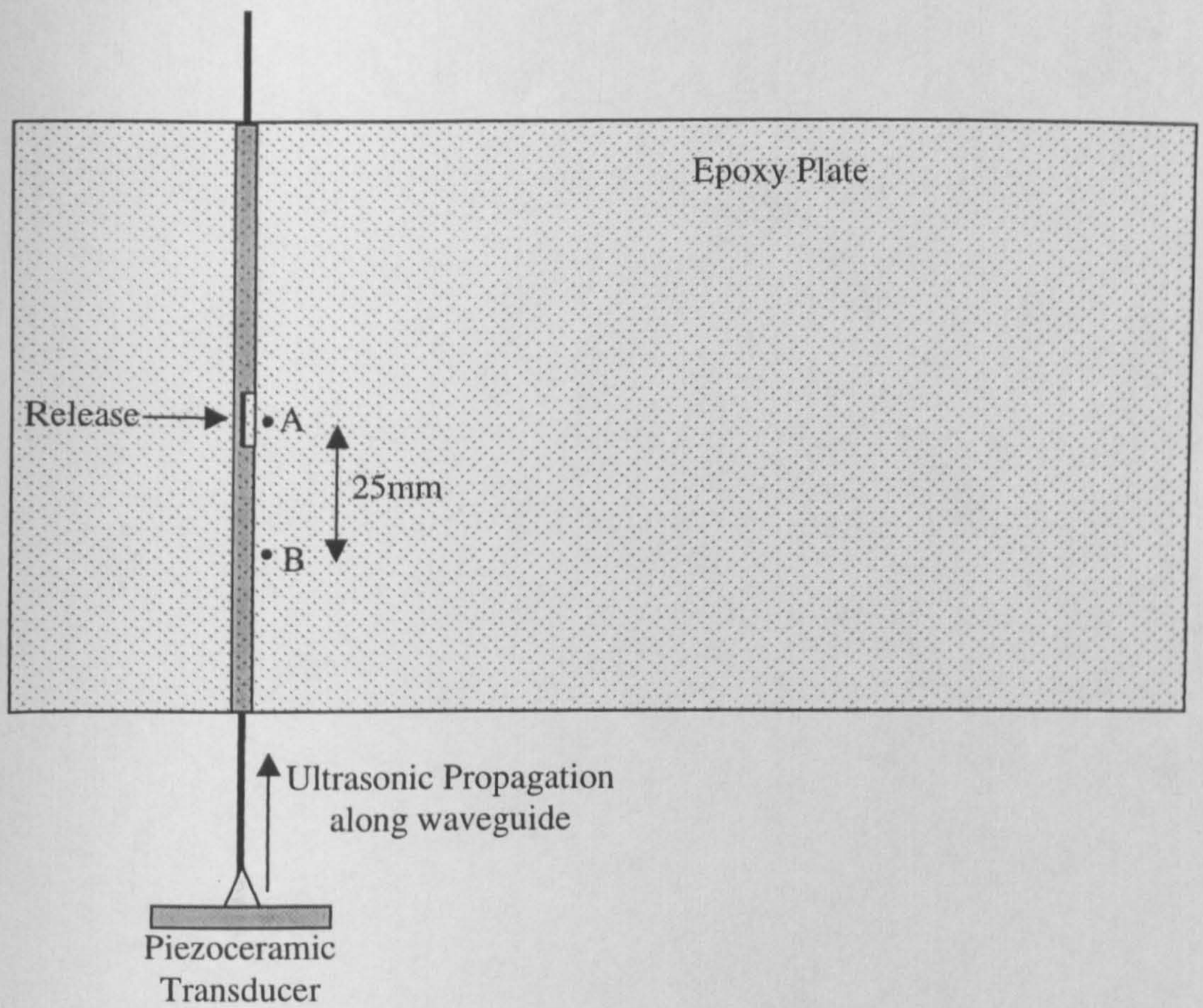

Figure 6.13: *Tube-Fibre Embedded Within a 5mm epoxy plate (not to scale)*

Delivering Ultrasound to a Release Point

Positions A and B, shown on Figure 6.13, represent two monitoring locations, on the surface of the plate, where signals were detected using the Hertzian probe transducer described in Chapter 5. Position A is located adjacent to the tube-fibre waveguide at the release area, while position B is located adjacent to the tube-fibre 25mm before the release area. The signals detected at positions A and B are presented in Figure 6.14, labelled trace A, and trace B respectively. It can be seen that the signal at B

arrives later in time than the signal at A and is smaller in magnitude despite being closer to the piezoceramic source transducer. Consequently the signal at B cannot correspond to energy leaking directly into the plate from the tube-fibre waveguide, but must be a result of energy leaking into the plate at A and subsequently propagating in the plate to B. That is, the additional time delay is due to propagation in the plate from A to B, and reduction in signal magnitude is due to attenuation in the plate. Furthermore, the Hertzian probe was utilised to detect signals on the plate surface above the entire length of the embedded waveguide. It was noted that the signal with both the greatest magnitude, and arriving first in time was detected at the release section. It can, therefore, be concluded that the tube-fibre waveguide is indeed confining the propagating ultrasound to the waveguide and releasing the energy into the surrounding media at the designated release location.

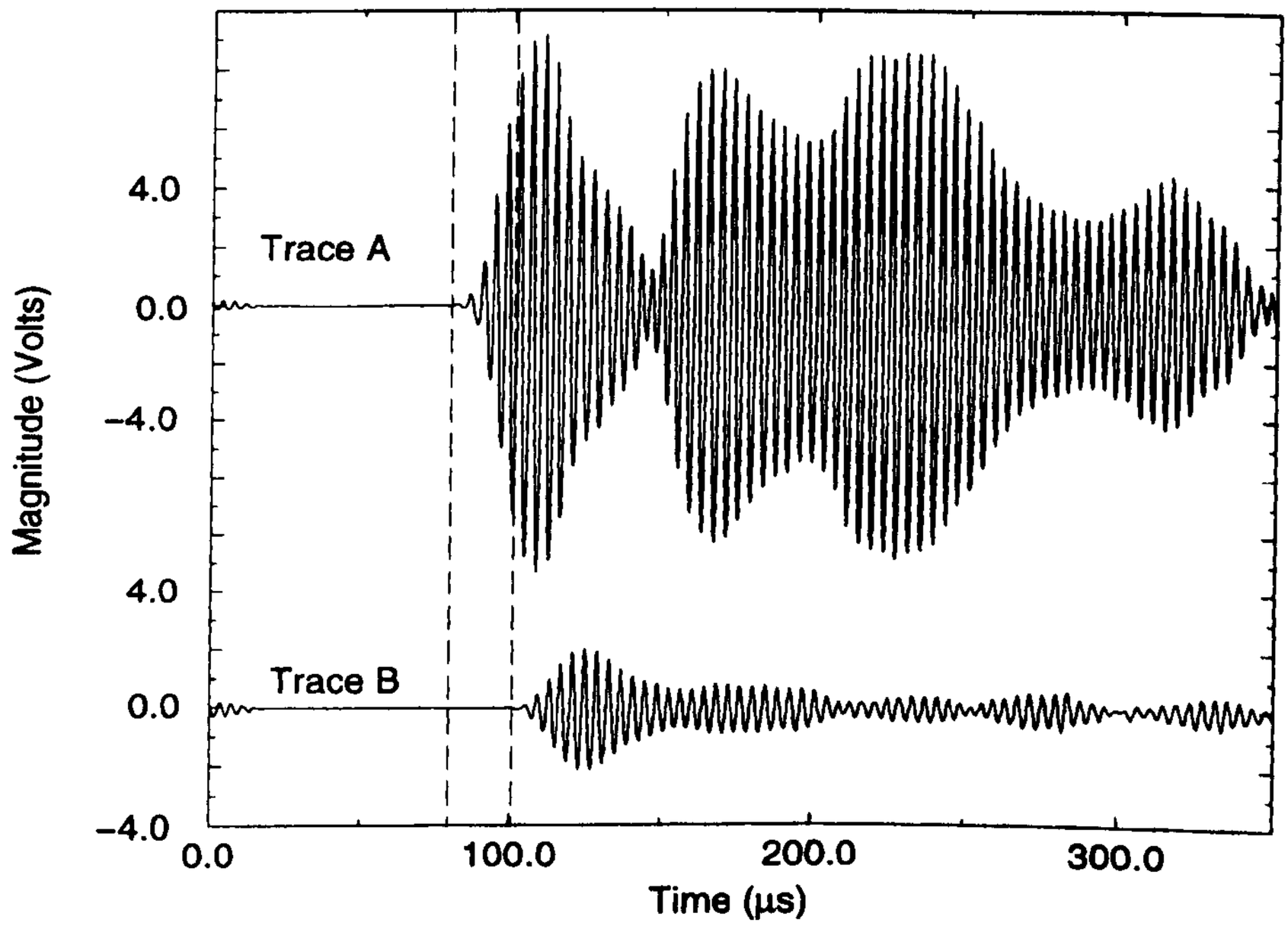

Figure 6.14: *Signals Delivered to an Epoxy plate via an Embedded Tube-Fibre Waveguide and Detected with a Hertzian Surface Probe*

6.2.3.4. Critical Evaluation of the Tube-Fibre Waveguide

It has been shown that housing a homogeneous fibre waveguide within a tube provides sufficient mechanical isolation from the surrounding media, and therefore permits non-leaky ultrasonic propagation along the waveguide. As such, removal of a section of the tubing enables the confined ultrasonic energy to be leaked into the surrounding media at a specified location. The tube-fibre configuration also permits guided propagation within the desired frequency range for Lamb wave propagation in composite plates (<1MHz). As discussed in Chapter 3, within this range only the three fundamental waveguide modes will be supported in small diameter fibre waveguides. Hence, uni-modal propagation in the waveguide is more readily achieved. A waveguide requirement still to be addressed is that of maintaining the host material's structural integrity. So far, a relatively large tube-fibre waveguide configuration has been considered i.e. an overall diameter of 0.86mm. Minimisation of this overall diameter to the order of 0.125mm would be required for non-invasive integration into carbon fibre reinforced composite components. While this issue has not been further investigated in the course of this Thesis, it is thought that the manufacture of such tube fibre waveguides is feasible, and therefore their integration into practical structural components has real potential. However, a problem that will result from miniaturisation of this configuration is that the surface area to volume ratio of the waveguide will increase. Consequently, the percentage of propagating energy present at the surface of the waveguide will increase, which in turn results in increased leakage from the waveguide to the tube sleeve housing at points of intimate contact. Nevertheless, it can be concluded that the tube-fibre waveguide

configuration provides the most promise for the desired embedded fibre Lamb wave monitoring system. Therefore, the ensuing Section aims to determine if an array of tube-fibre waveguides can be embedded within plate-type structures for Lamb wave generation and detection.

6.3. Embedded Tube-Fibre Lamb Wave Systems

The previous Section highlighted the suitability of the tube-fibre waveguide configuration for the proposed embedded Lamb wave monitoring system. Consequently, this Section investigates embedding such waveguides into hard-setting epoxy and CFRC plates for Lamb wave generation and detection. Firstly, a hard-set epoxy resin plate (shore 80, CY1300/HY1301) will be examined to confirm that embedded fibres are indeed capable of delivering periodic stress in order to generate Lamb wave modes within plates. Following this, tube-fibres will be embedded within a CFRC plate to demonstrate the sensor system incorporated into a 'realistic' structural component.

6.3.1. Hard Set Epoxy Resin Plate System

As discussed in Chapter 5, an array of fibre waveguides can be utilised to deliver periodic stress to plate-type structures, and through spatial selection, generate a desired Lamb wave mode. Therefore, eight copper waveguides, of equal length (400mm), and diameter 0.25mm, housed within aluminium tubes, of outer diameter

0.86mm and inner diameter 0.76mm, were embedded at half the thickness of an epoxy plate. Adjacent fibres were separated by half wavelength ($\Lambda/2$) spacing and therefore excited differentially. For each fibre a 6mm section of the aluminium housing was removed at half the fibres length, thereby creating a release location. Ultrasonic propagation was induced in the waveguides at both ends to maximise the amount of energy delivered to the structure. Similarly, four tube-fibre waveguides were utilised in reception except with Λ spacing (due to a shortage of aluminium tubing at the time of the experiment). The transmitter and receiver fibre arrays were separated by 133mm centre to centre. Figure 6.16 depicts the experimental arrangement in both end elevation and plan format.

Piezoceramic PZT5A disc transducers were employed to excite and receive the ultrasonic propagation in the waveguides utilising the polymer cone technique discussed in Chapter 4. Two discs were utilised in transmission, one for each differential excitation, and one disc was utilised in reception. The waveguides were adhered to the surface of each disc in a concentric ring to achieve the required uniform phase. Therefore, from the experimental analysis of Chapter 4 it is known that a significant amount of the F(1,1) mode (albeit to a lesser extent than the L(0,1) mode) will be generated in the waveguides since they were not centrally placed on the discs. In addition, the F(1,1) mode will also be detected if induced in the receiving waveguides. This effect will be utilised to highlight the problems introduced utilising a fibre-transducer interface design that excites more than one fibre mode, i.e. in this case L(0,1) and F(1,1).

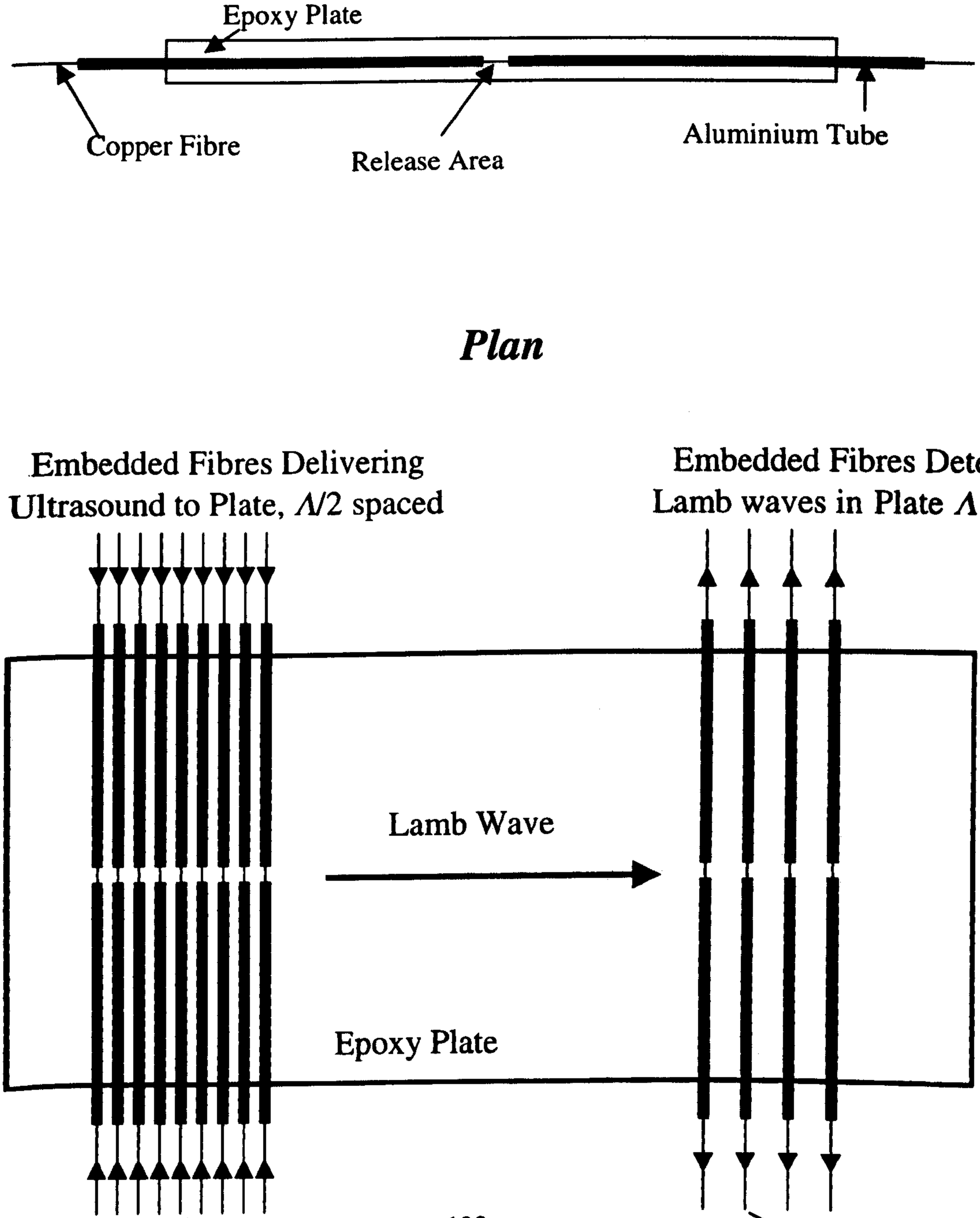

Figure 6.16: *Tube-Fibre Waveguides Array Embedded in an Epoxy Plate*

Since the fibre waveguides are embedded at half the plate thickness (i.e. symmetrically with respect to the plate's thickness) it seemed logical to design for the symmetrical S_0 mode. Furthermore, it has been documented that the symmetrical modes are more suited for long range monitoring applications [5]. Therefore, dispersion information on the epoxy load medium is required to establish an appropriate Frequency-Thickness-Product (FTP), and the required wavelength. Figures 6.17(a), and 6.17(b) display the relevant group and phase velocity data respectively.

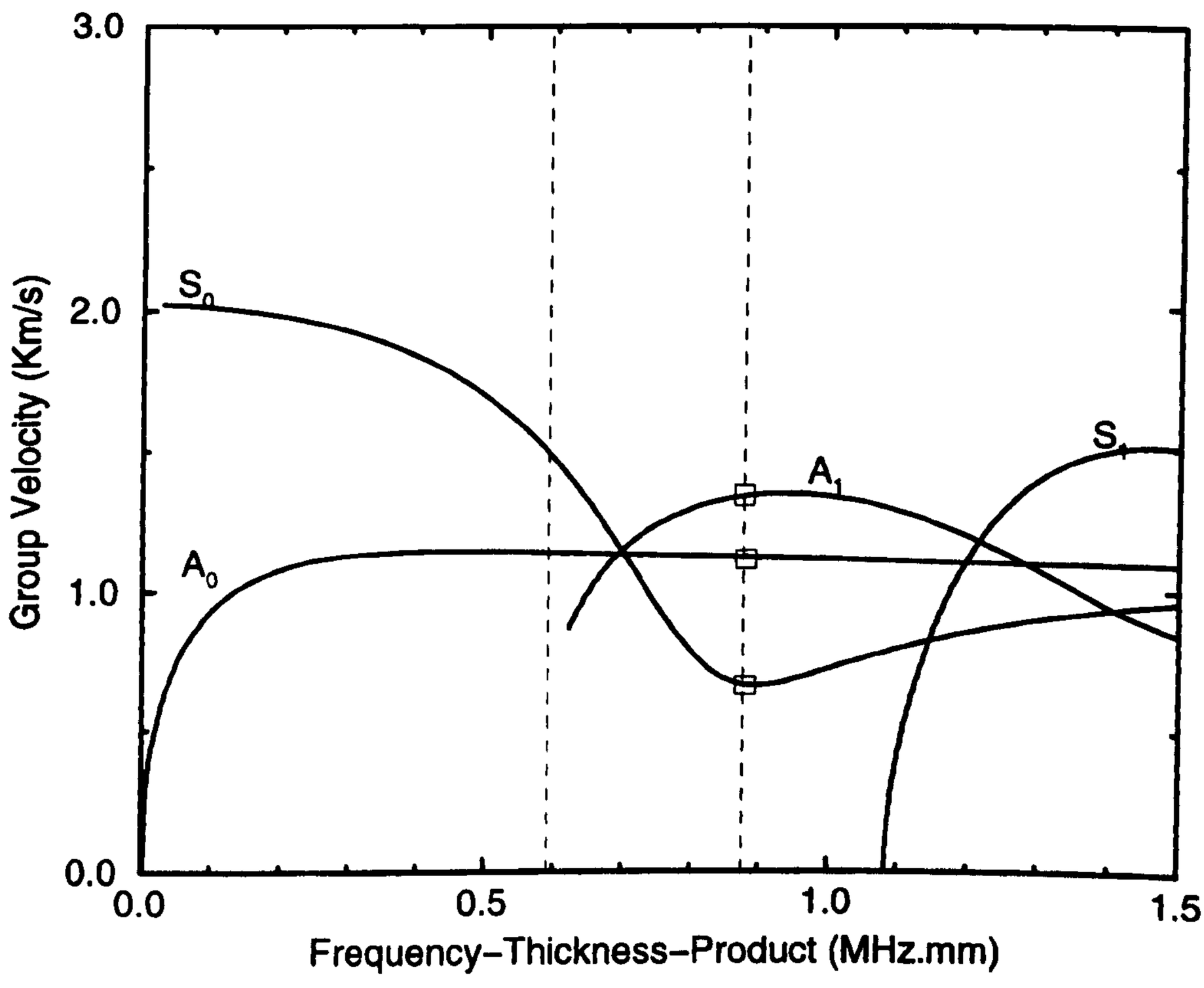

Figure 6.17(a) *Group Velocity Dispersion Curves for Hard Set Epoxy*

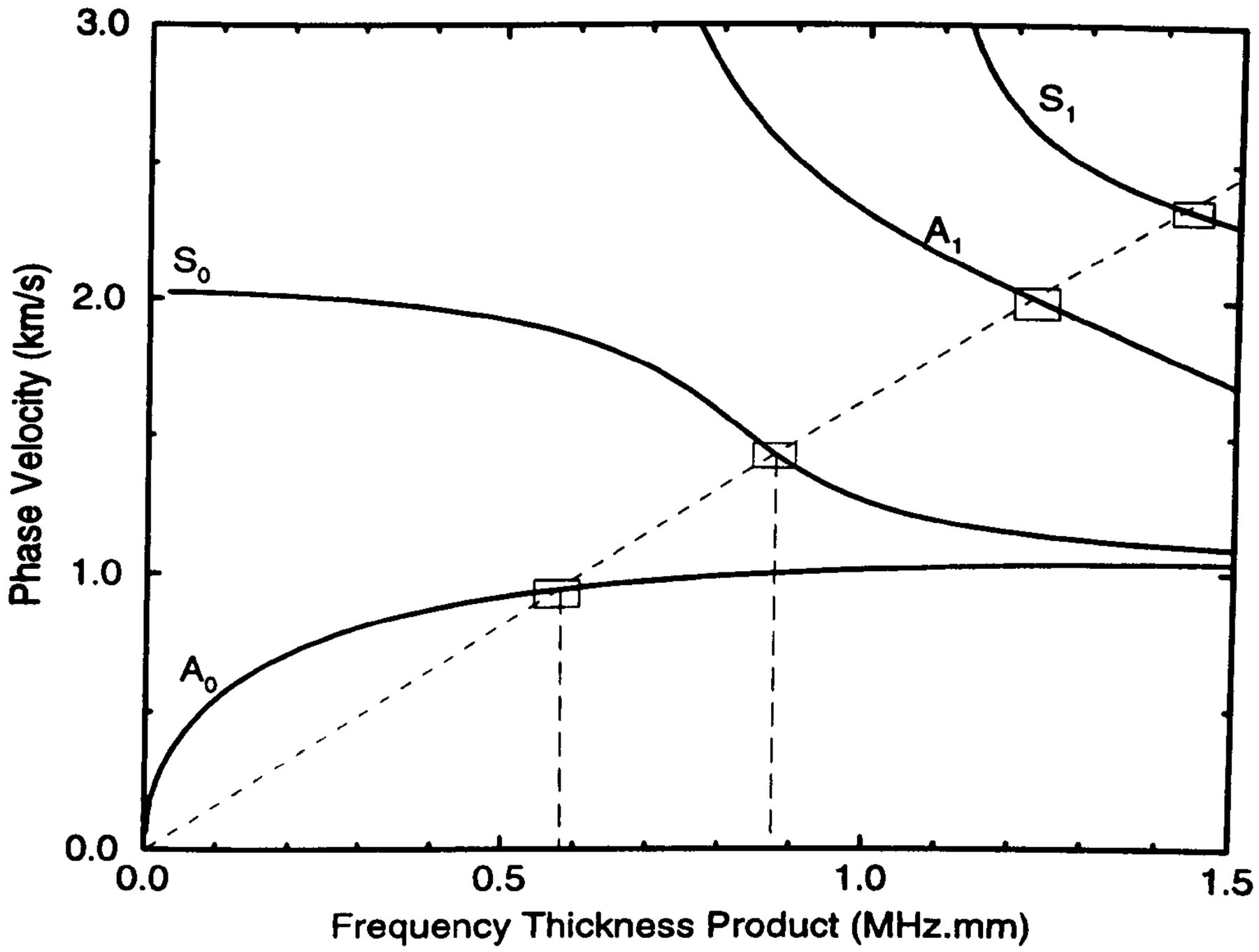

Figure 6.17(b): *Phase Velocity Dispersion Curves for Hard Set Epoxy*

When designing a Lamb wave system for long range structural monitoring, a requirement is to operate at an FTP where the desired mode is non-dispersive [5], that is, a flat region on the group velocity curve. This minimises pulse spreading and ensures that small changes in frequency do not result in propagation time variation. Therefore, a suitable region for S_0 mode Lamb wave operation in the epoxy load medium occurs at an FTP of 0.875MHzmm where the group velocity is at a minimum, see Figure 6.17(a). Consequently, a plate thickness of **3.5mm** and an operating frequency of **250kHz** would suffice. At this FTP it can be noted that the plate can also support the A_0 and A_1 modes. To select the appropriate wavelength spacing for S_0 operation consider the phase velocity data presented in Figure 6.17(b). At an FTP of 0.875MHz.mm, the phase velocity of the S_0 mode is $1457ms^{-1}$, yielding a wavelength of **5.8mm** at 250kHz. The broken diagonal line shown on the phase

velocity graph represents a line of equal wavelength. Consequently, at an FTP of 0.595MHzmm the wavelength for the A_0 mode is also 5.8mm. Therefore, an operating frequency of 170kHz in the same 3.5mm plate would match the wavelength spacing to the A_0 mode. It is noted, from the group velocity curve depicted in Figure 6.17(a), that the A_0 mode is also relatively non-dispersive at an FTP of 0.595MHzmm.

The embedded tube-fibre Lamb wave system was therefore designed with a wavelength of 5.8mm in a 3.5mm epoxy plate, and driven at both 250kHz for S_0 operation, and 170kHz for A_0 operation. The received signals for the two operating frequencies are displayed in Figures 6.18 and 6.19 respectively, where it can be seen that for both cases multiple mode excitation and reception is demonstrated. It is thought that this is due to the generation of non-axisymmetric modes in the waveguides. That is, the system design concept utilises fibre waveguides to deliver ultrasonic energy, carried by the L(0,1) mode. The axisymmetrical nature of this mode ensures that the rotational alignment of an embedded fibre is insignificant since the propagating mode exhibits uniform phase around the circumference of the waveguide at any given axial position. However, due to the non-centralised bonding of the waveguides to the piezoceramic disc transducers in this experiment, it is known that in addition to the dominant L(0,1) mode, a significant proportion of the F(1,1) mode will be generated in the waveguides. Since the rotational alignment of the waveguides is largely uncontrollable, the presence of the F(1,1) mode in the waveguides introduces random phasing at the release array. This effect will increase

the probability of anomalous Lamb wave modes (which can be supported at the FTP of operation) being generated, in this case the A_0 and A_1 modes.

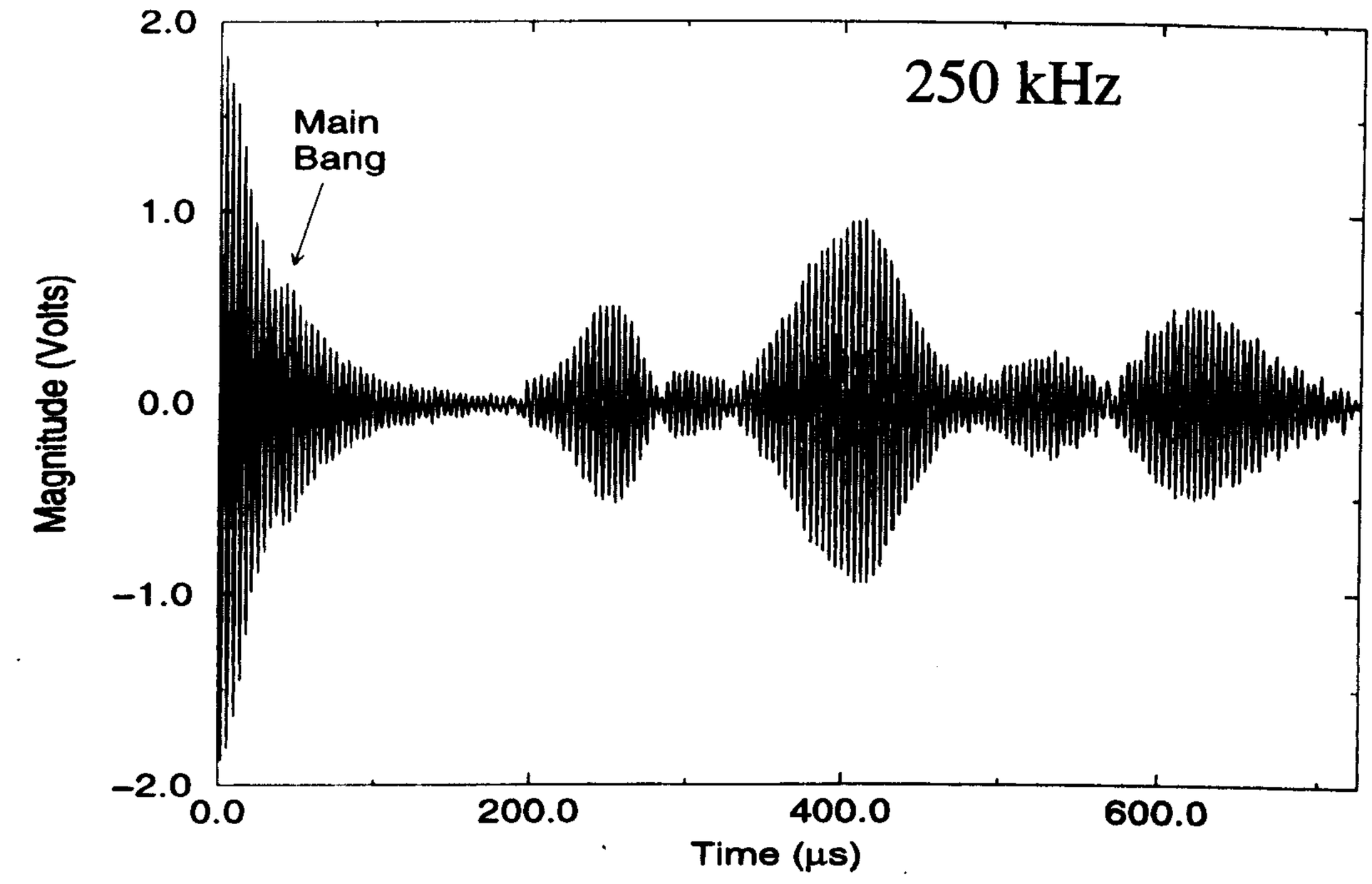

Figure 6.18: *Embedded Tube-Fibre Lamb Wave Signal Received at 250kHz*

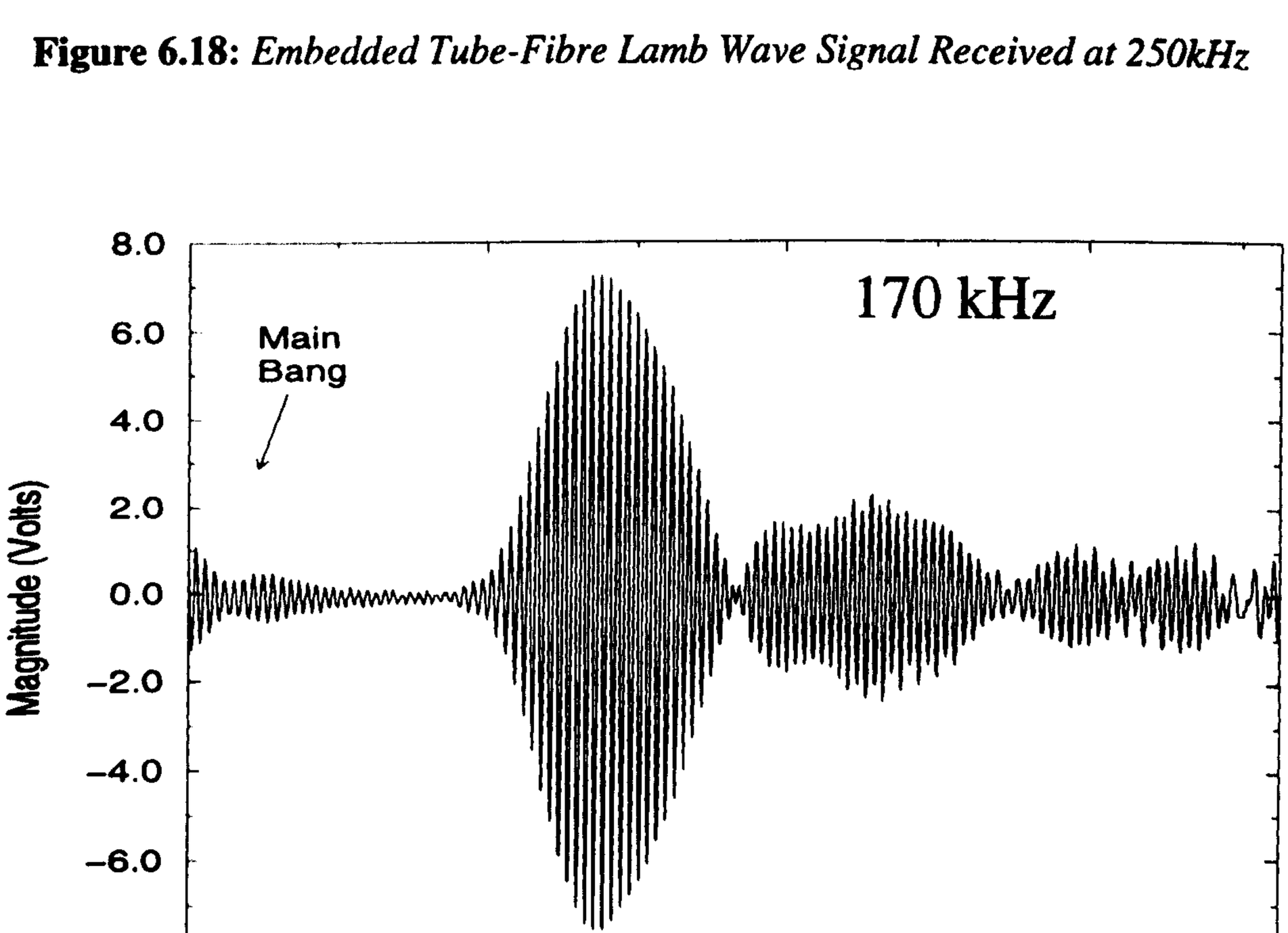

Figure 6.19: *Embedded Tube-Fibre Lamb Wave Signal Received at 170kHz*

Signal identification from propagation time information alone is complex since 2 waveguide modes are supported in the transmitting fibres, 3 Lamb wave modes in the plate, and 2 waveguide modes in the receive fibres (assuming no torsional modes), resulting in 12 possible propagation time combinations. Tables 6.2 and 6.3 display the various propagation times for operation at both 250kHz and 170kHz respectively. Note that the *WaveMaker-Duet* (Macro Design Ltd.) was utilised for signal generation, which triggers of the centre of the input signal. Therefore propagation times correspond to the centre of the mode packet.

Transmit mode / Receive mode	**Lamb Wave Mode S_0**	Lamb Wave Mode A_0	Lamb Wave Mode A_1
L(0,1) / L(0,1)	**303µs**	223µs	205µs
L(0,1) / F(1,1)	**428µs**	348µs	330µs
F(1,1) / L(0,1)	**428µs**	348µs	330µs
F(1,1) / F(1,1)	**553µs**	473µs	455µs

Table 6.2: *Propagation Time Combinations at 250kHz*

Transmit mode / Receive mode	Lamb Wave Mode S_0	**Lamb Wave Mode A_0**	Lamb Wave Mode A_1
L(0,1) / L(0,1)	194µs	**222µs**	314µs
L(0,1) / F(1,1)	351µs	**379µs**	471µs
F(1,1) / L(0,1)	351µs	**379µs**	471µs
F(1,1) / F(1,1)	508µs	**536µs**	628µs

Table 6.3: *Propagation Time Combinations at 170kHz*

It is evident that the identification of each Lamb wave mode present in the plate from propagation time information alone is inconclusive. Consequently, to establish if the system is preferentially generating the Lamb wave mode for which it was designed (S_0 at 250kHz, and A_0 at 170kHz), a two-dimensional Fast Fourier Transform (2DFFT) method, developed by Alleyne and Cawley [118], was employed. For this experiment a laser interferometer system (as described in by Hyslop *et al.* [116]) was utilised to record a series of digitised surface displacement time histories (2048 samples) at 128 discrete spatial intervals (δx=0.5mm) along the Lamb wave propagation path, as illustrated in Figure 6.20. On application of the 2DFFT (Equation 6.1), the temporal data yields frequency information (Hz) and the spatial data provides wavenumber information (1/m). Plotting the resultant data against theoretical dispersion curves permits the identification of the Lamb wave modes propagating along the plate.

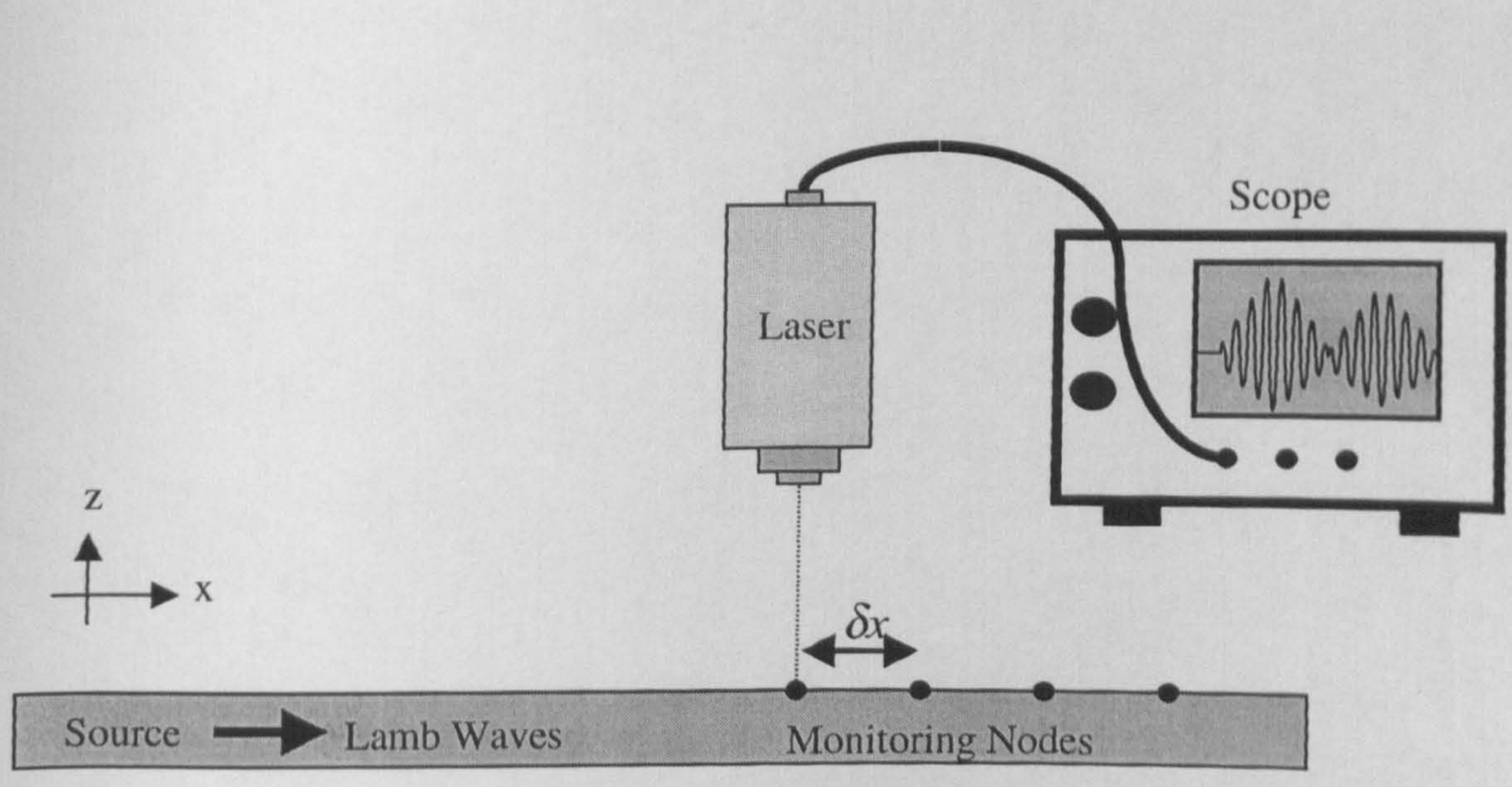

Figure 6.20: *Laser Vibrometer utilised in Reception to provide 2DFFT data*

$$H(k,f) = \int_{-\infty}^{+\infty}\int_{-\infty}^{+\infty} u(x,t)e^{-i(kx+\omega t)}dxdt \qquad \textbf{6.1}$$

Figures 6.21, and 6.22 display the information provided by the 2DFFT when the system was driven at 250kHz and 170kHz respectively. Figures 6.21(a) and 6.22(a) present the data as magnitude plots while Figures 6.21(b) and 6.22(b) present the same data as contour plots. It can be seen that when the system is operated at 250kHz all three Lamb wave modes have been generated (A_0, A_1, S_0), and that when operated at 170kHz the A_0, and S_0 modes are supported. Encouragingly, these results provide the significant revelation that S_0 mode excitation is dominant for operation at 250kHz (FTP=0.895MHz.mm), while A_0 mode excitation is dominant at 170kHz (FTP=0.595MHz.mm). This confirms the basic design methodology since the wavelength related spacing of the transmitting fibre-array at the FTP of interest yields the dominant mode.

However, the presence of the other Lamb wave modes is undesirable and considered to be a result of the contributions of the non-axisymmetrical F(1,1) fibre waveguide mode in the transmitting waveguides. It is thought that this mode introduces random phasing at the excitation fibre waveguide array, thereby increasing the generation of other supported Lamb wave modes. Consequently, this highlights the importance of uni-modal fibre waveguide operation, to reduce the excitation of additional Lamb wave modes in the plate.

Moreover, when utilising fibre waveguides to detect the Lamb wave activity in the plate both flexural and longitudinal modes excited in the receiving waveguides by the propagating Lamb waves will be detected. Importantly, the nature of the interaction between the generated Lamb waves and the coupling into the fibre waveguide modes is unknown. For example, the F(1,1) mode may be preferentially generated in the receiver waveguides by the S_0 Lamb wave mode. This problem needs to be addressed so that the reception technique utilised to detect the induced fibre waveguide mode can be designed to match the requirements of the system.

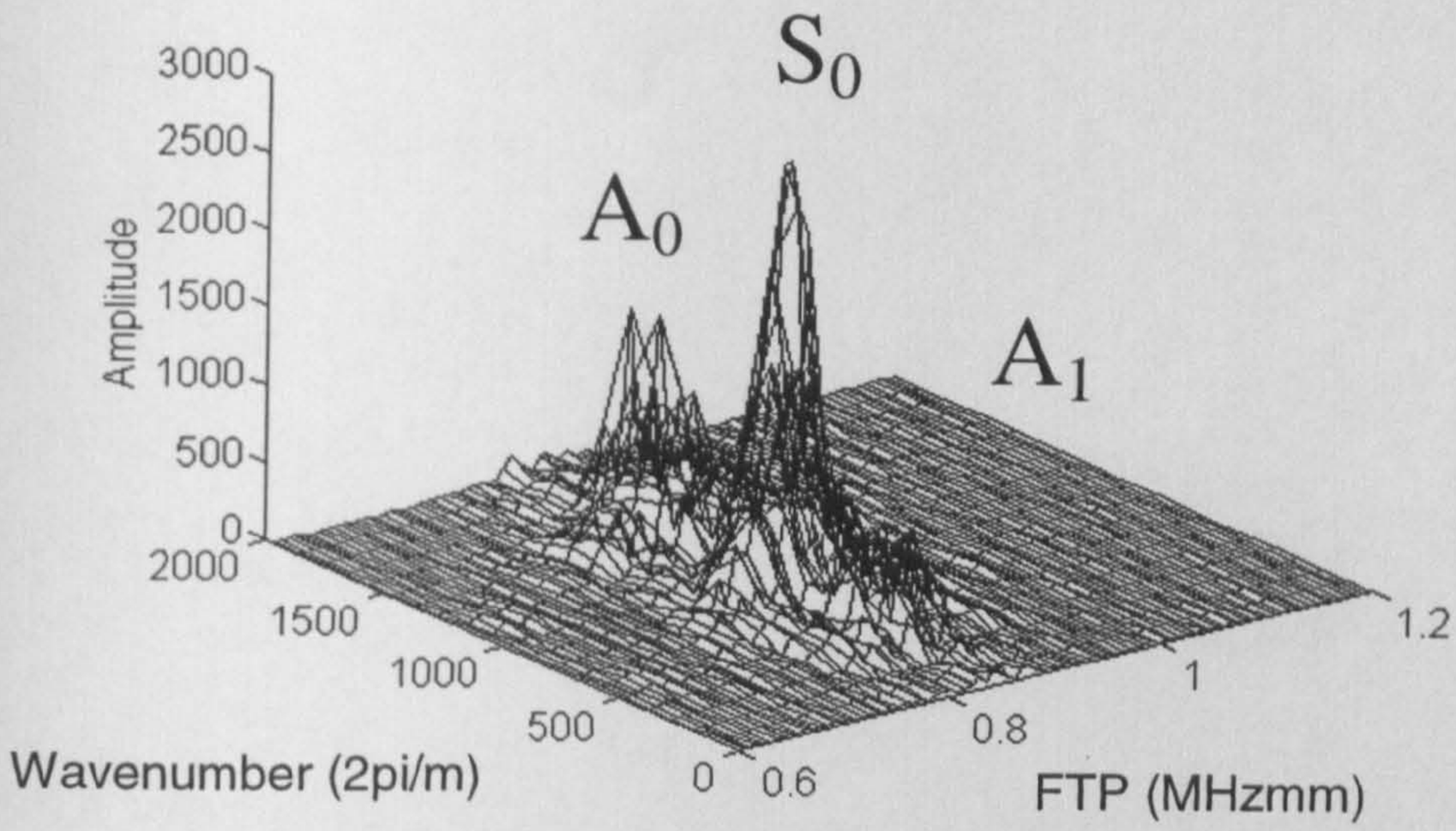

Figure 6.21(a): *2D FFT Magnitude Plot: 250kHz (FTP = 0.895MHzmm)*

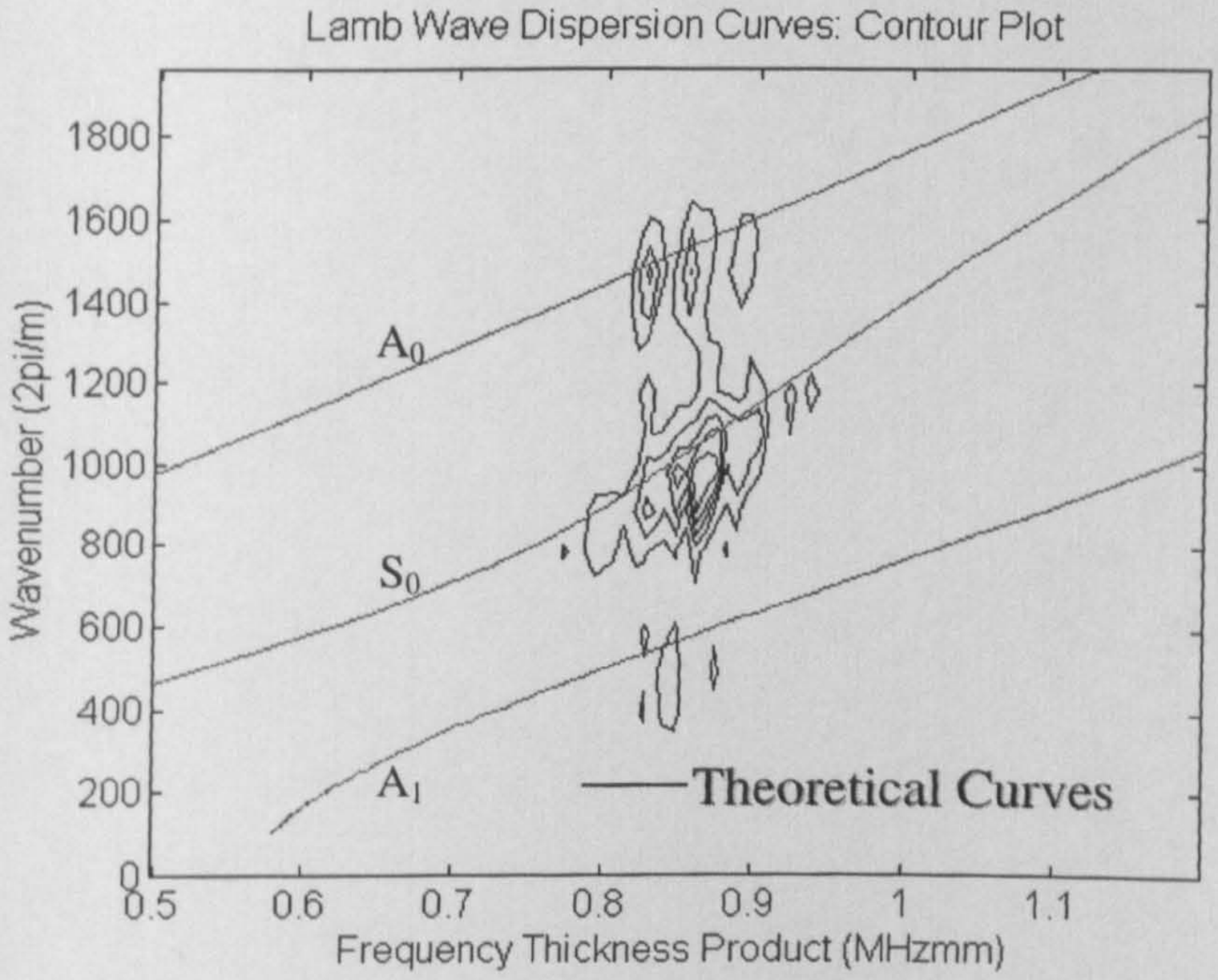

Figure 6.21(b): *2DFFT Contour Plot: 250kHz (FTP = 0.895MHzmm)*

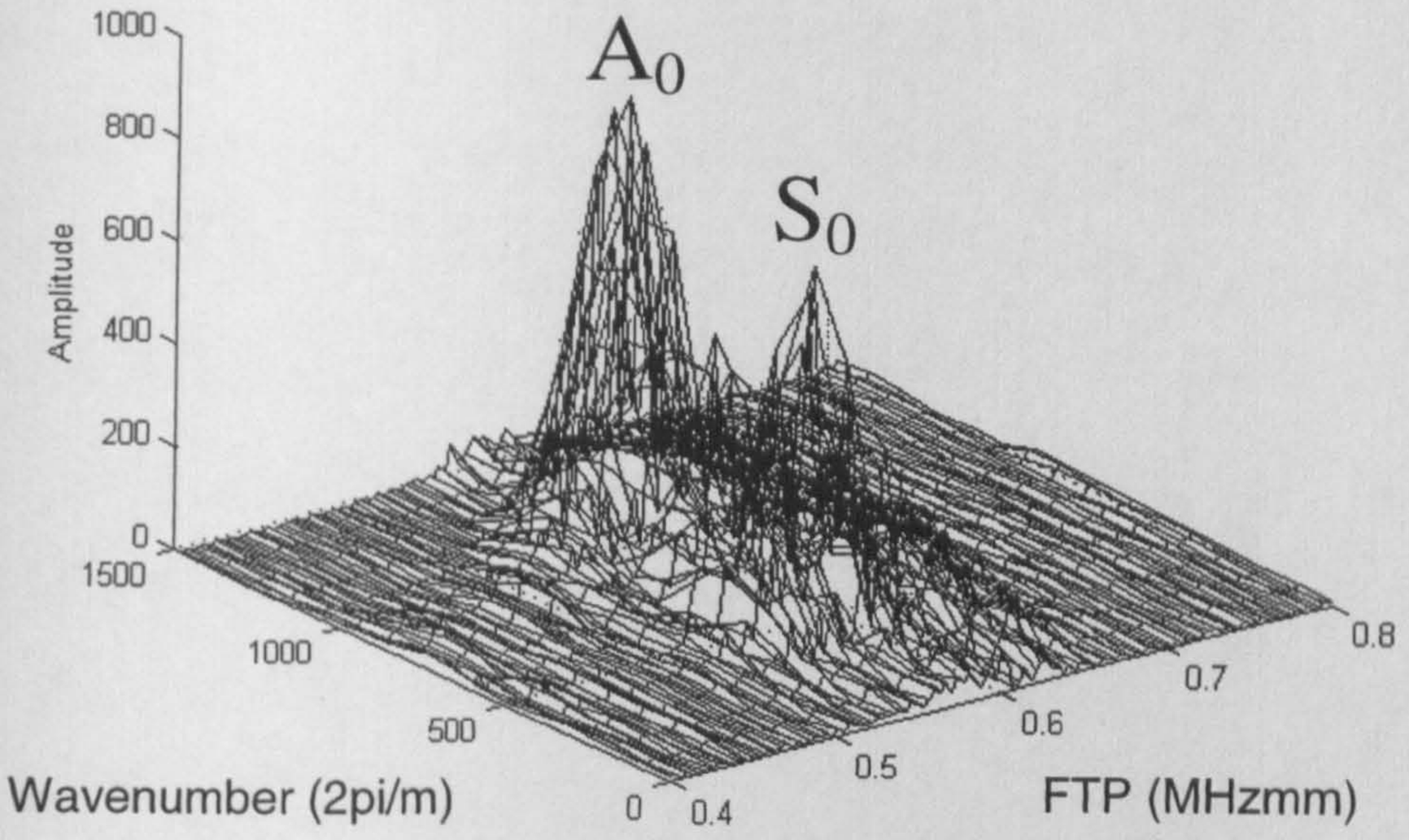

Figure 6.22(a): *2DFFT Magnitude Plot: 170kHz (FTP = 0.595MHzmm)*

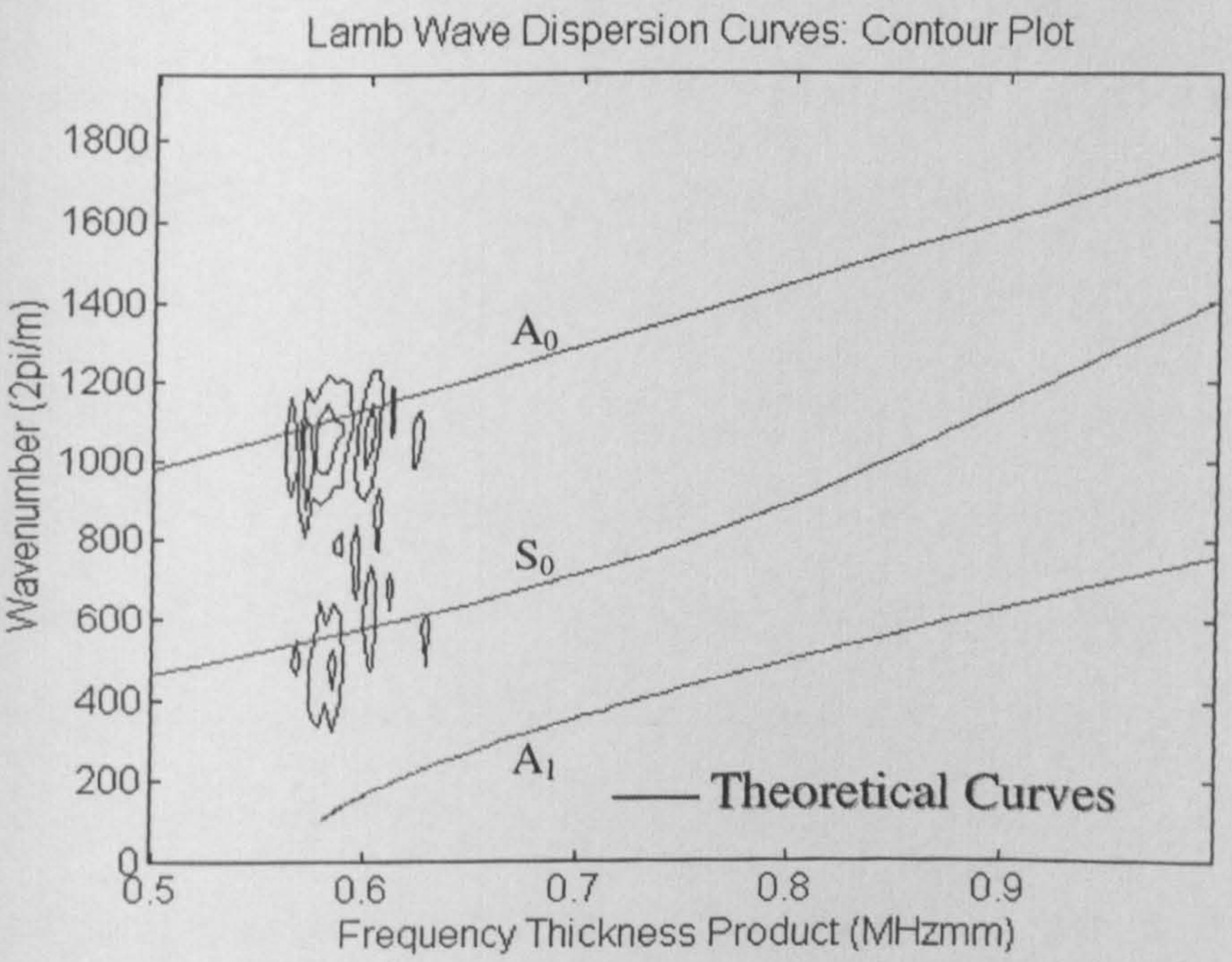

Figure 6.22(b): *2DFFT Magnitude Plot: 170kHz (FTP = 0.595MHzmm)*

6.3.2. Carbon Fibre Reinforced Composite Plate System

The previous Section has demonstrated that an embedded tube-fibre waveguide array can be utilised to generate Lamb waves. Moreover, the 2DFFT technique revealed that both the S_0 and A_0 Lamb wave modes were preferentially generated, when their wavelengths were matched to the array spacing. As previously mentioned, the symmetrical modes are more suited for long range monitoring applications, especially in lossy materials such as CFRC which will severely attenuate asymmetrical mode propagation. Therefore, this Section goes on to demonstrate an embedded, tube-fibre waveguide, Lamb wave system for S_0 operation in a unidirectional (UD) CFRC plate.

The CFRC plate was constructed utilising the procedure outlined in Figure 6.23. Firstly, a 1mm (8 ply) thick, UD, CFRC plate, of length 900mm, and width 125mm was manufactured. The carbon fibre (CF) direction is across the plate width, as indicated in Figure 6.23. The plate was subsequently cut into three sections of thickness 1mm, length 300mm, and width 125mm. Two of these sections were then adhered together with Araldite 20/19 epoxy, (hereafter referred to as epoxy), and grooves of width 0.9mm and depth 0.9mm were cut into the plate to accommodate the fibre waveguides. In order to simplify the embedding process only 4 waveguides (wavelength spaced) were utilised for transmission purposes and one waveguide for reception 80mm away. The waveguides were copper fibres of length 600mm, and diameter 0.25mm, housed within aluminium tubes of outer diameter 0.86mm, and inner diameter 0.76mm. These were prepared as before to create a release area (in this case 5mm long) half way along their length. Subsequently, the waveguides were

positioned in the grooves and covered with excess epoxy, and the top plate was lowered into place, also with additional epoxy applied to its underside. The composite plate configuration was then left to cure at room temperature for 48hours under a 30lbs load.

1. Fabricate 1mm UD CFRC

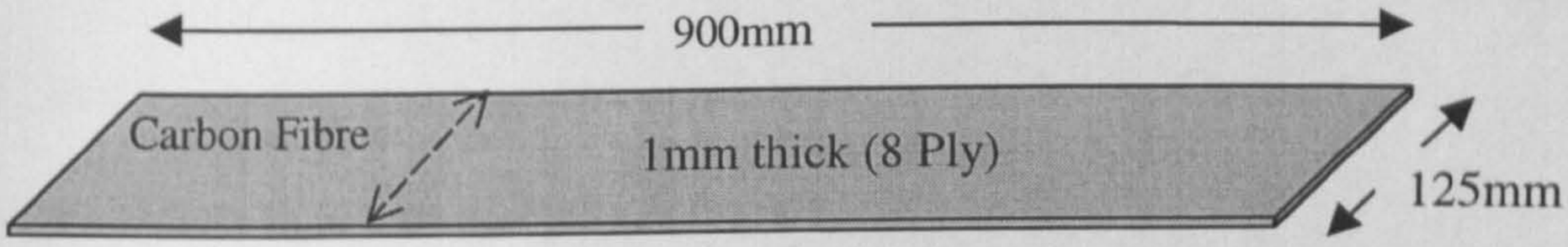

2. Cut into 3 equally sized plates

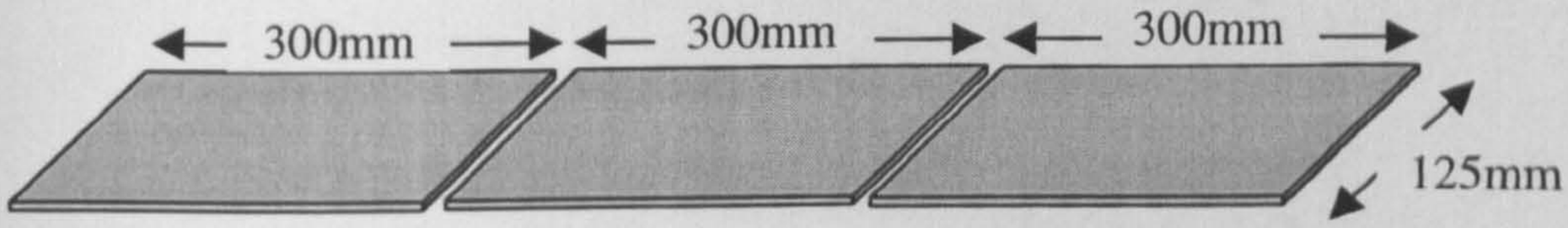

3. Adhere 2 Plates together and machine appropriately spaced grooves to Accommodate the fibre waveguides

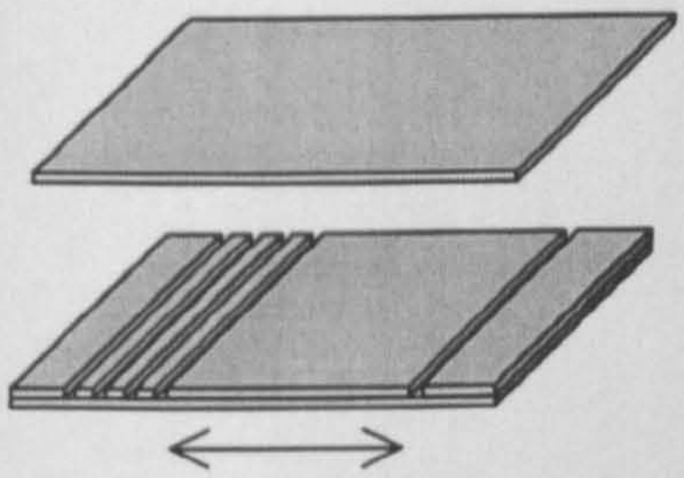

4. Adhere tube-fibre waveguides and top plate into position with excess epoxy

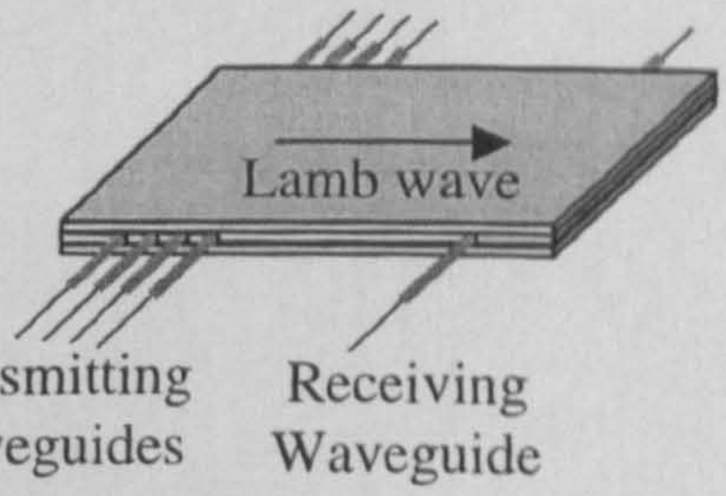

Figure 6.23: *Waveguide Embedding Process for the CFRC Plate*

In order to establish the appropriate wavelength spacing for S_0 operation, dispersion information on the load medium was required. Estimates of the Poisson ratio, density, and Young's modulus of elasticity for the UD prepreg material, both with, and against the CF direction, were available from the manufacturers (detailed in Appendix C). For the described system, the Lamb wave propagation is against the CF direction, and consequently the relevant parameters were entered into DISPERSE (described in Section 6.2.2.2.) to obtain Lamb wave dispersion information. It was assumed that, with respect to the Lamb wave propagation direction, the plate is a continuous 3mm homogenous layer. The resultant predicted group and phase velocity dispersion curves are presented in Figures 6.24(a) and 6.24(b) respectively.

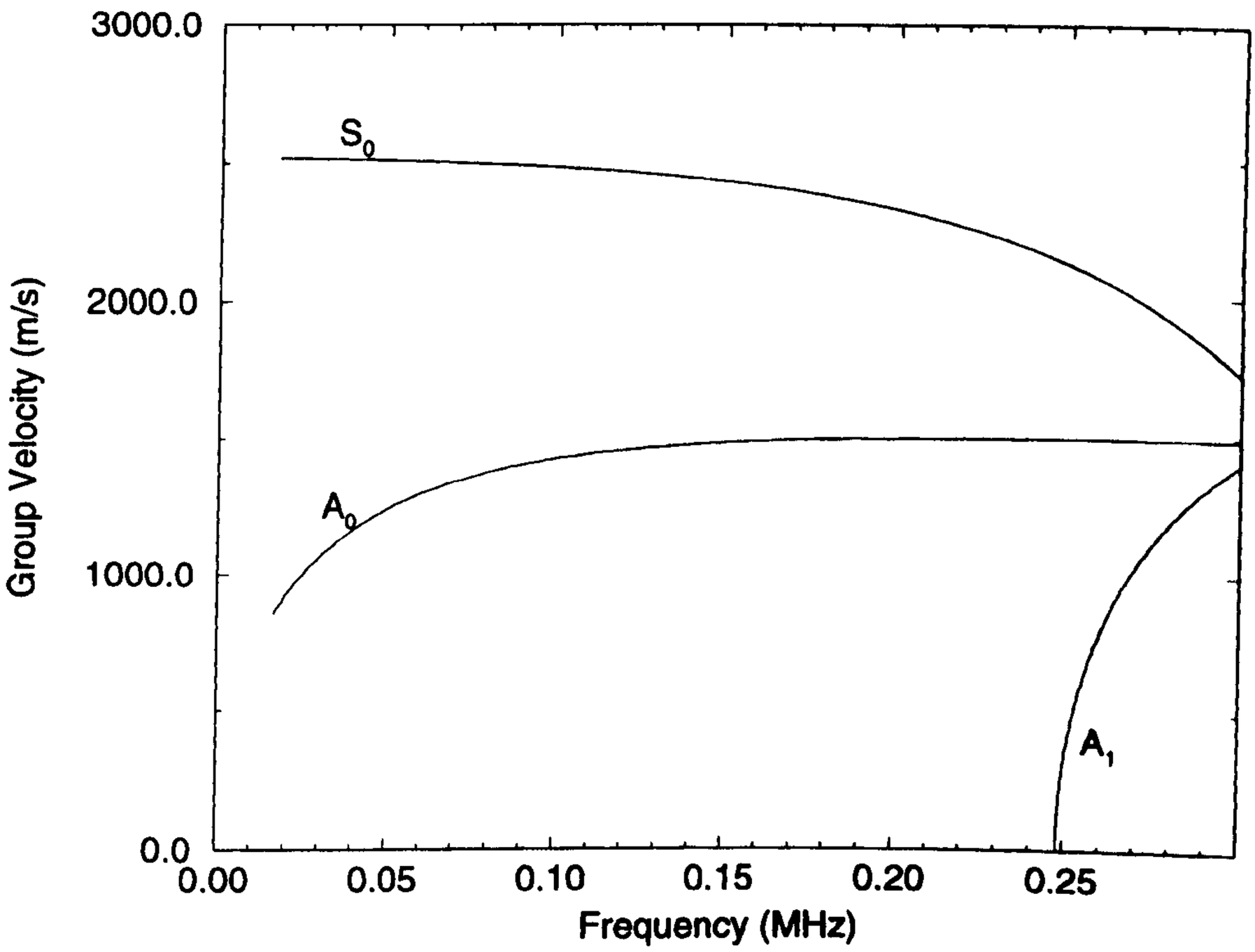

Figure 6.24(a): *Group Velocity Curves: 3mm UD CFRC plate (against CF)*

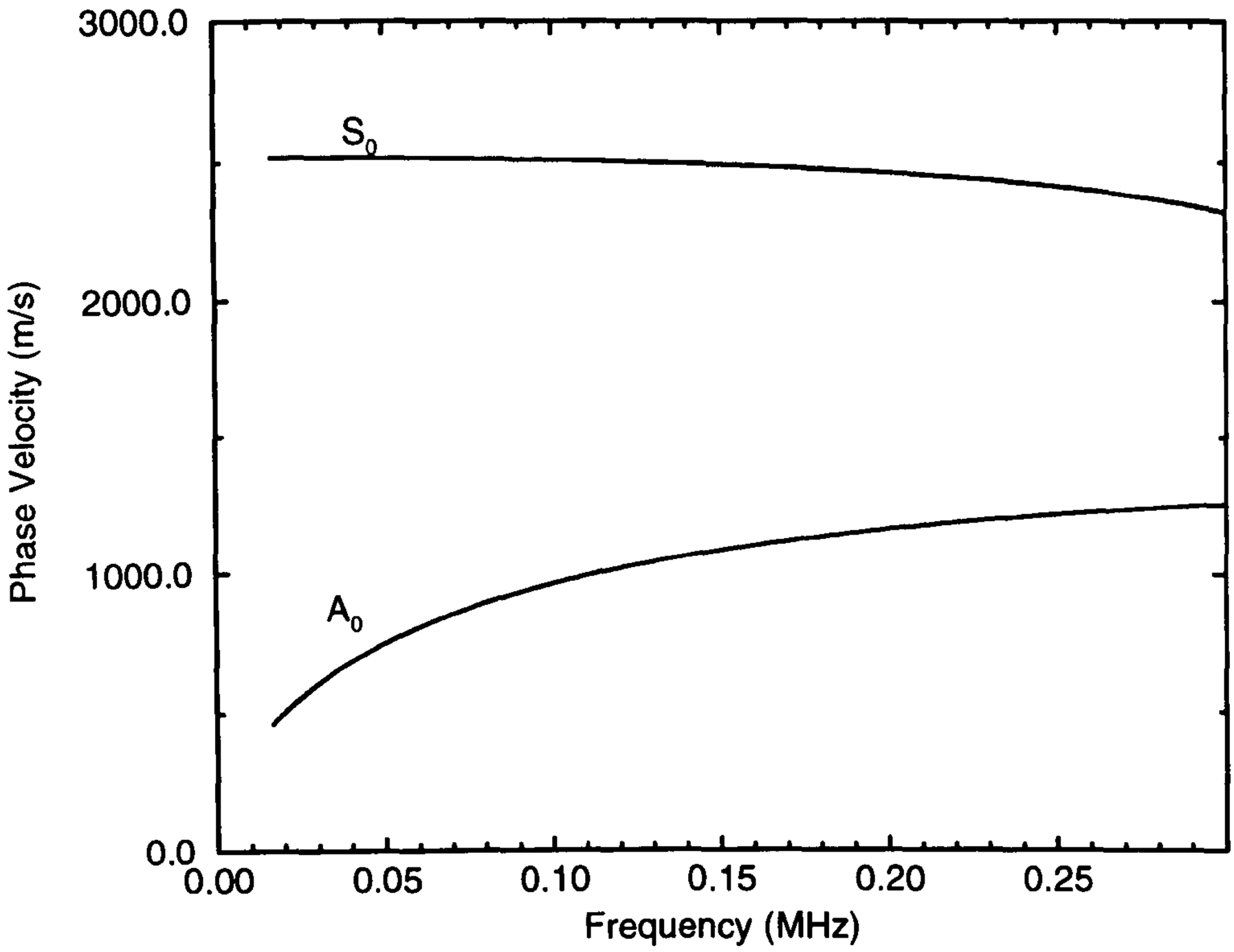

Figure 6.24(b): *Phase Velocity Curves: 3mm UD CFRC plate (against CF)*

In this experiment each fibre waveguide was attached (at one end only) to an individual piezoceramic disc transducer with a polymer cone. The design guidelines outlined in Section 4.11 were followed to maximise the amount of energy coupled into each waveguide and to obtain as high a SCNR as possible. This included bonding each individual waveguide centrally to a disc transducer to minimise the undesired contributions of the F(1,1) waveguide mode. Consequently, the system was designed for 250kHz since the 30mm diameter, PZT5A, 500kHz thickness mode piezoceramic disc transducers utilised have a strong radial harmonic at this frequency. It can be seen from Figure 6.24(a) that the S_0 mode is quite dispersive at this frequency, however, these transducers were employed since there was a large supply of them available in stock. It can be seen from Figure 6.24(b) that at 250kHz the phase velocity of the S_0 mode is 2413ms^{-1}, and therefore the wavelength is

9.6mm.

The transmitting piezoceramic discs were each excited with a 250kHz, 200Vp-p, 20 cycle, 'hanning windowed', toneburst, generated by the WaveMaker-Duet (Macro Design Ltd.), which was also employed as the receiver amplifier with a gain of 50dB. Recall that this signal generator triggers off the centre of the toneburst (i.e. the peak in the envelope), and consequently the propagation times are measured from the centre of the received wave packet. The dispersion curves illustrated in Figure 6.24(a) reveal that the S_0 mode has a group velocity of $2127ms^{-1}$ at 250kHz. Consequently, the propagation time for the S_0 mode in 94.4mm of the plate (i.e. the distance from the centre of the transmitting *array* to the receiving waveguide) is 45μs. In addition the propagation time in the transmitting wires (300mm), and the receiving waveguide (300mm) is 162μs for the L(0,1) mode, resulting in a total propagation time of 207μs. The received signal is displayed in Figure 6.25, where it can be seen that, as expected, the S_0 mode has been generated and detected, centred at approximately 207μs.

Subsequent signals in the received trace were identified as being reflections in the plate. This was achieved by simply applying localised pressure to the surface of the plate at various locations. This attenuates any acoustic propagation under that area and subsequently allows its identification. It should be noted that only a very small attenuation was witnessed when utilising this technique. This is because (unlike the asymmetrical modes, which are easily attenuated by applying surface pressure) the S_0 mode generated in this experiment has the majority of its energy confined to the

centre of the plate. However the attenuation is sufficient to identify the propagation path.

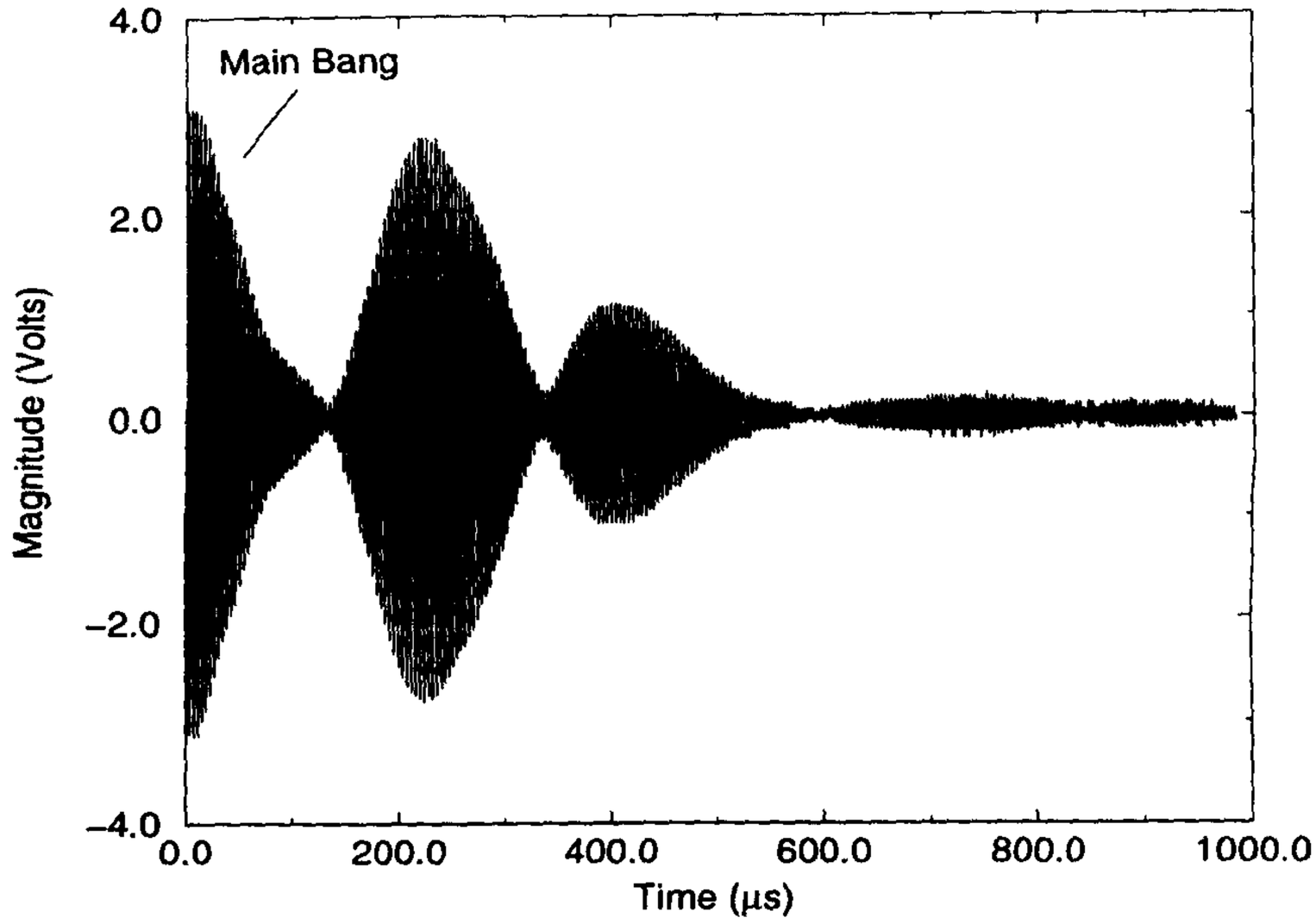

Figure 6.25: *Lamb Waves Generated and Received at 250kHz by tube-fibre waveguides in a 3mm UD CFRC plate.*

Since the elastic properties provided for the dispersion analysis were estimates on the prepreg material, the frequency of operation was swept to establish if the response could be improved. At 210kHz, a clearly identifiable mode has been preferentially generated and received in the plate, as illustrated in Figure 6.26. It can be confidently assumed that this dominant mode arriving at the beginning of the received trace is the S_0 mode since, it is the fastest propagating mode (would be expected to arrive first in the received trace), and is detected at approximately the predicted time. In addition, it is expected that any asymmetrical modes generated would be heavily attenuated by the propagation medium. It can be seen that this

mode does not 'ring out' for as many cycles as is did at 250kHz, this is because the piezoceramic discs are now operating off-resonance. Again, subsequent signals were identified as being reflections in the plate.

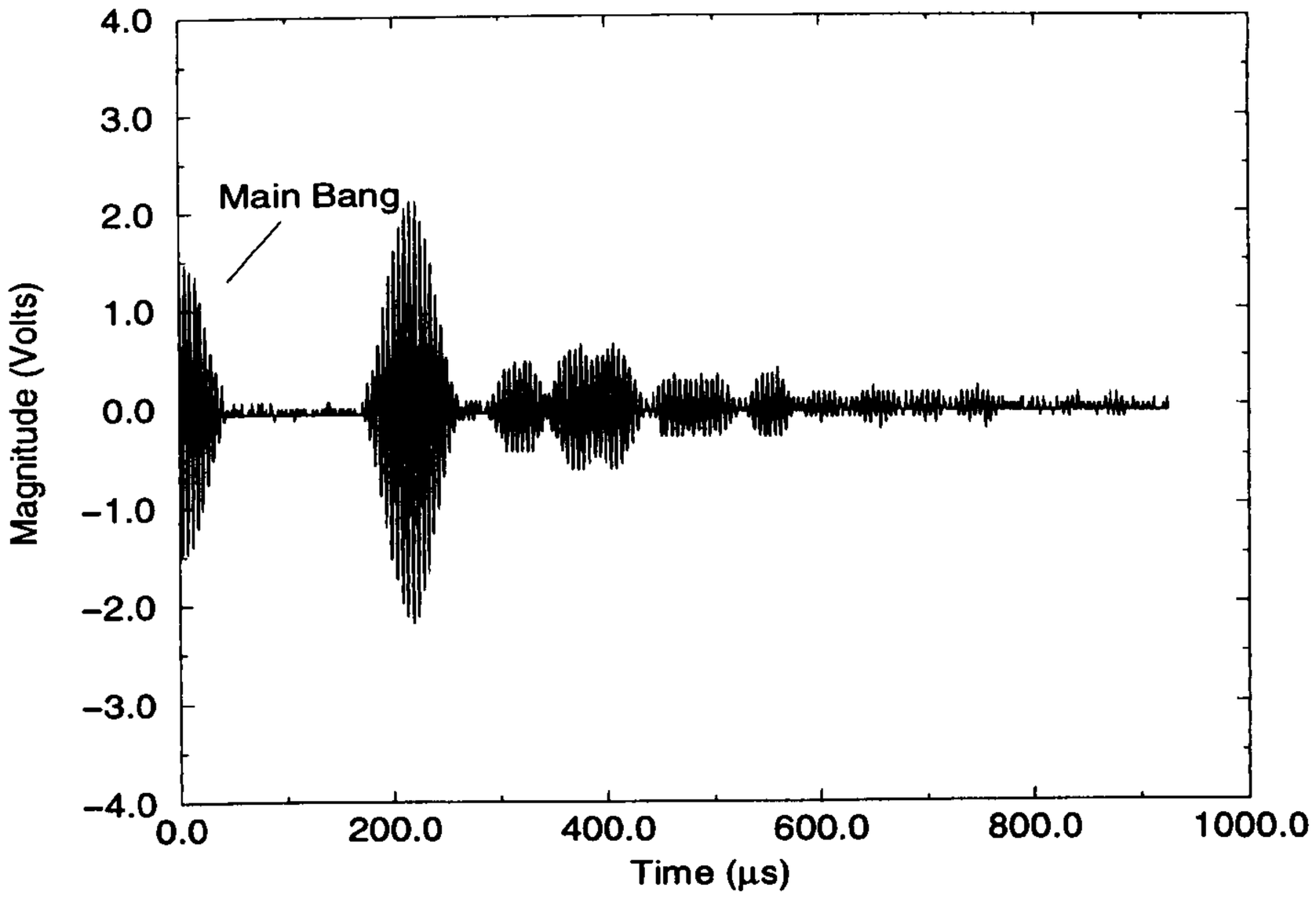

Figure 6.26: *Lamb Waves Generated and Received at 210kHz by tube-fibre waveguides in a 3mm UD CFRC plate.*

In order to isolate the S_0 mode from the subsequent reflections a gated analogue time switch circuit, as illustrated in Figure 6.27 was designed and built. As depicted in the diagram, the first monostable is triggered off a negative going edge (from the signal generator SYNC) to produce a pulse of duration T_1 from 0 seconds. The second monostable is then triggered with this output to produce a subsequent pulse that starts at time T_1 and stops at time T_2. This pulse controls the analogue gate, which is on (passes an analogue signal from its input to its output) for the duration of the control pulse. As illustrated in Figure 6.27, a resistor (R) and a capacitor (C) connected to the relevant pins of each monostable determine the times T_1 and T_2 by the relationship: T=0.7RC.

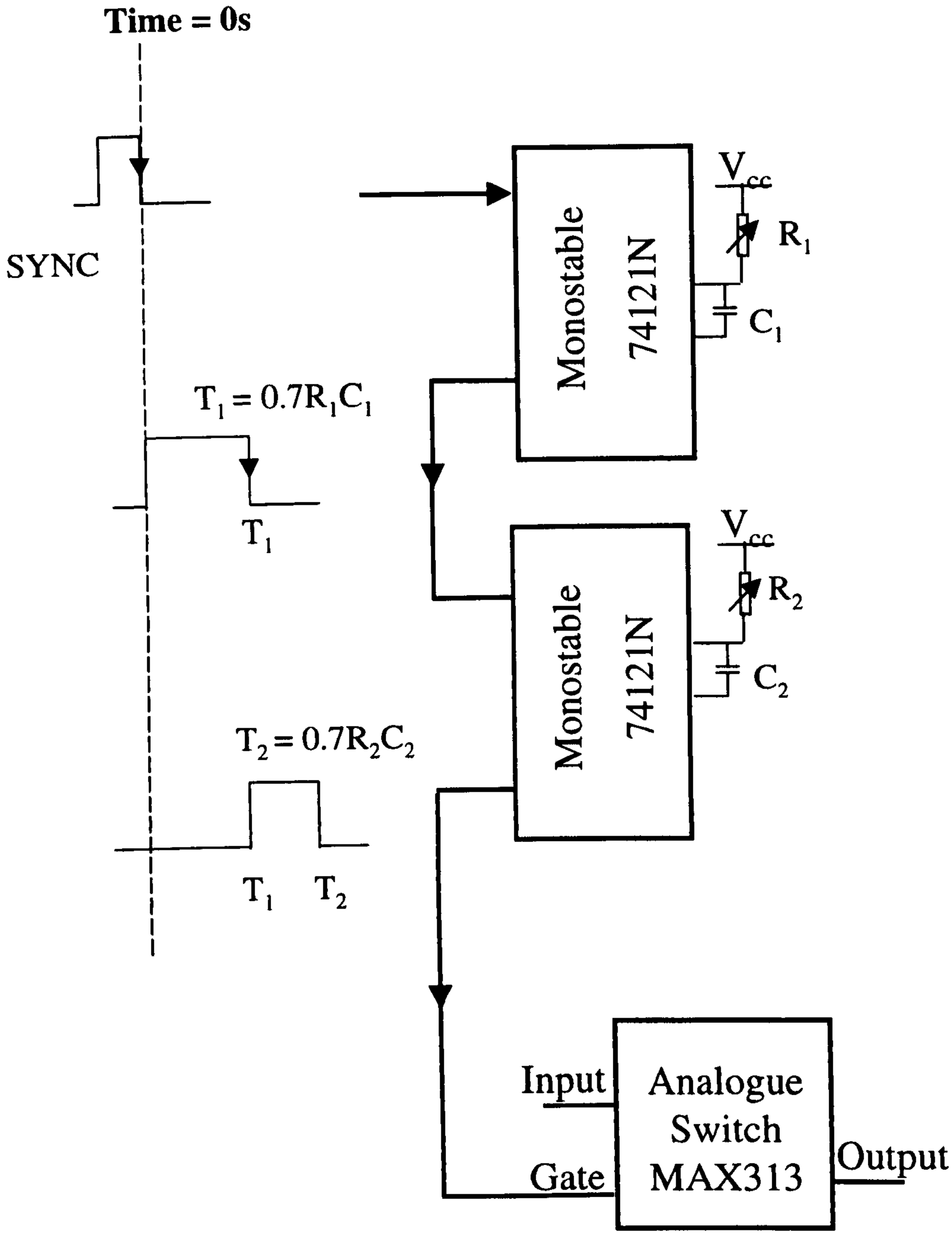

Figure 6.27: *Analogue Time Gate Circuit, with start and stop times established from two RC controlled Monostables*

The described analogue time gate circuit was then added to the system and calibrated to isolate the S_0 mode from the subsequent signals in the received trace at 210kHz. The resultant signal is displayed in Figure 6.28, where it can be seen that the S_0 mode has been successfully isolated. Utilising this circuit, the received signal purely comprises of the S_0 mode propagating from the transmitting tube-fibre array release area to the receiver tube-fibre waveguide. Consequently, this trace can be utilised as a signature to monitor the structural area between the transmitter and the receiver, where changes in the character of this signal will indicate a change in the integrity of this region.

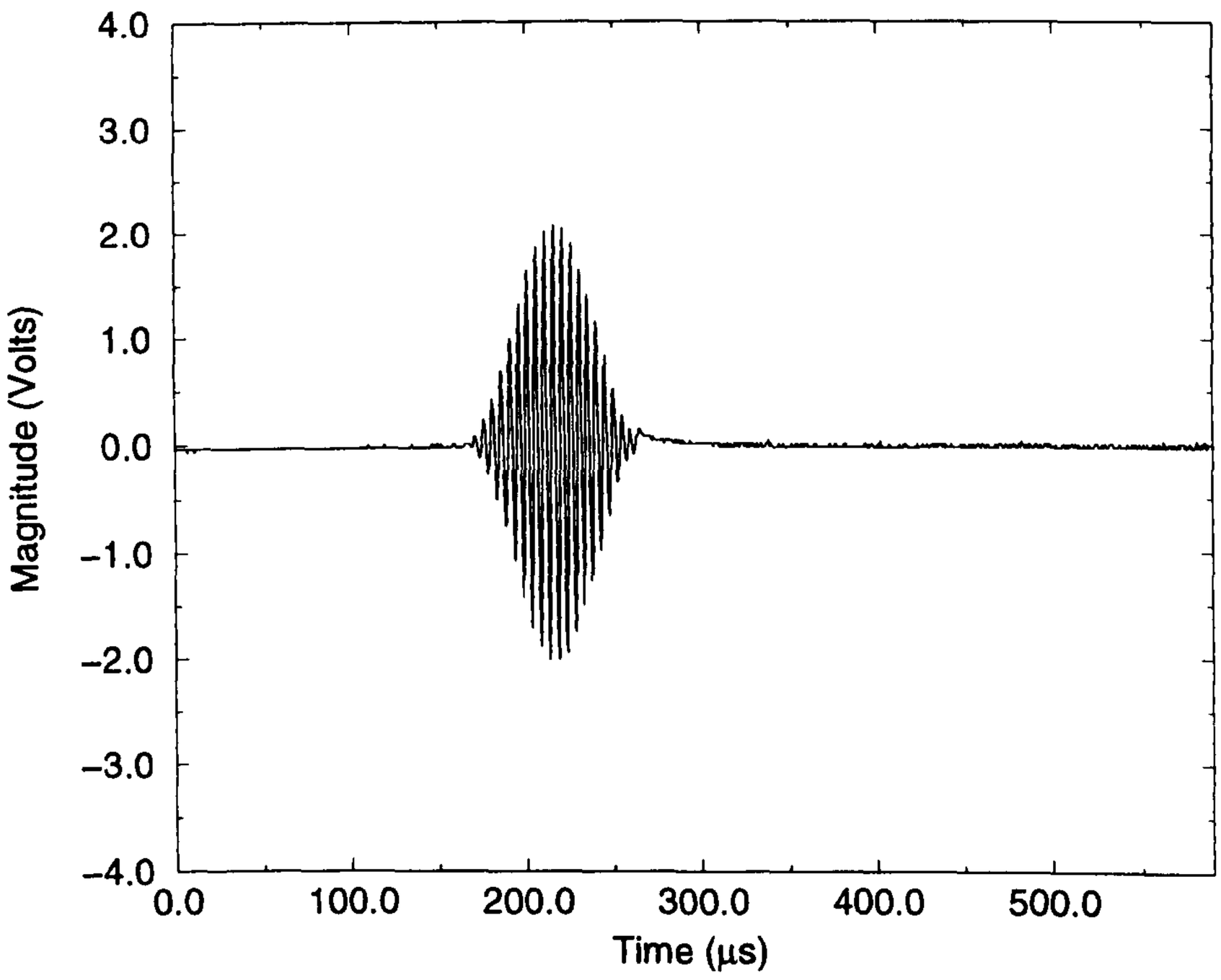

Figure 6.28: *Lamb Waves Generated and Received at 250kHz by tube-fibre waveguides in a 3mm UD CFRC plate with time gate circuit applied.*

6.4. Conclusions

This Chapter has discussed a novel condition monitoring system, which utilises embedded fibre waveguides for Lamb wave generation and detection. Initially, the system requirements of the waveguide were highlighted and subsequently various geometries were evaluated through theoretical, modelling, and experimental analysis. It was revealed that due to material parameter constraints, a homogeneous fibre waveguide configuration would not be suitable for this application due to uncontrollable leakage of the propagating ultrasound into the surrounding media. The clad fibre waveguide geometry was therefore considered in an attempt to confine the propagating ultrasound to the core of the guide. However, it was shown with dispersion analysis, that no core-guided mode could be generated within the desired frequency range for practical diameter sizes. Consequently, a homogenous fibre waveguide housed within a thin tube was proposed, and through experimental analysis, shown to meet the requirements of the system.

Utilising such waveguides, an embedded Lamb wave system was demonstrated in a 3.5mm hard-setting polymer plate. Here a transmitting and receiving array of tube fibre waveguides was embedded within the plate to generate and receive the S_0 Lamb wave mode at 250kHz. The received signal was shown to contain various modes of propagation. It was suggested that due to the coupling method utilised, the presence of non-axisymmetrical modes in the waveguides introduced random phasing at the transmitter array and subsequently other Lamb wave modes were generated. However, it was demonstrated (utilising a 2DFFT routine) that the system did indeed preferentially generate the S_0 mode at 250kHz. Moreover, by altering the frequency

of operation to 170kHz, to match the array spacing to that of the A_0 mode, it was shown that this mode could also be preferentially generated. Consequently, these results confirm the basic design methodology to be sound.

A unidirectional CFRC plate was fabricated with an embedded tube-fibre waveguide transmitter array, and single tube-fibre waveguide receiver. In an attempt to reduce the undesired influence of non-axisymmetrical modes in the waveguides, each individual fibre was coupled to a separate disc transducer, utilising the polymer cone design guidelines detailed in Chapter 4. Generation and reception of a clearly identifiable S_0 mode at 250kHz and 210kHz was demonstrated. Furthermore, an analogue time gate was presented and shown to be capable of isolating the S_0 mode from other anomalous modes and reflections in the received signal. Consequently, a uni-modal signature trace to monitor the integrity of the region between the embedded transmitter fibre waveguide array and receiver waveguide has been achieved.

Chapter 7

Conclusions and Recommendations for Further Work

7.1. Conclusions of Thesis

This Thesis has presented research concerned with the realisation of a novel condition monitoring system, which utilises active acoustic waveguide sensors to transport mechanical energy to and from plate-type structures. As such, the sensor concept strives to combine the robust, non-invasive, characteristics of passive optical fibre sensors with the long distance monitoring capabilities offered by alternative active ultrasonic sensor techniques. Significant progress towards the attainment of this concept has been detailed in the course of this Thesis.

Acoustic Fibre Waveguides

There are three families of elastic wave that can propagate along an isotropic cylinder, namely, longitudinal, torsional, and flexural. Through theoretical analysis, described in Chapter 3, the nature of these mode types has been discussed, and their dispersion characteristics presented. It was suggested that the longitudinal modes display the most suitable attributes for transporting acoustic energy for the described monitoring system. Primarily because knowledge of the phase of the propagating ultrasonic signal, as it is delivered to the load structure, is critical for successful interdigital excitation of a desired Lamb wave mode. The longitudinal modes are axisymmetric and consequently display uniform phase around the circumference of the waveguide at any axial position. This property simplifies the embedding process since the phase of the ultrasonic signal at the release location is purely a function of the mode's propagation distance and not

the rotational alignment of the embedded fibre, which is difficult to quantify for the small diameters of interest.

Waveguide Coupling Strategy

Following the identification of an appropriate waveguide mode, namely the fundamental longitudinal mode, Chapter 4 described a coupling technique for its generation and detection. Here, the initial ultrasonic energy was generated by electrical stimulation of a piezoceramic transducer and coupled into the waveguide via a polymer cone interface. Detailed theoretical analysis of this technique was presented showing that the polymer cone preferentially operates as a mechanical transformer converting lateral displacements at its base into longitudinal displacements at its apex, thereby inducing longitudinal wave propagation in the waveguide. Subsequently, it was shown that when the piezoceramic transducer is stimulated with a wideband voltage signal the lateral resonances of the piezoceramic transducer are more efficient coupled into the waveguide than its thickness mode. This effect was theoretically and experimentally demonstrated for both piezoceramic discs and plates. Furthermore, narrowband analysis of the system revealed that the geometry of the polymer cone considerably affects the coupling efficiency, with an optimum cone dimension existing for a given frequency of operation, and diameter of waveguide. Significantly, it was demonstrated that the load material does not influence the optimum cone geometry, and that the axial displacements generated in the waveguide become larger as its diameter is reduced corroborating the mechanical transformer hypothesis. Moreover, it was shown that the efficiency of the coupling increases with the Poisson ratio of the polymer, as would be

expected for a mechanism converting lateral displacements into longitudinal displacements.

Experimental analysis was then described to quantify the coupling strategy in terms of narrowband uni-modal operation. It was revealed that a SCNR of 25dB could be expected for L(0,1) mode operation when the polymer cone and waveguide (held within the polymer cone) were centrally adhered to the surface of a piezoceramic disc transducer being driven at a radial harmonic. Subsequently, the design parameters, listed below, were detailed for efficient L(0,1) mode operation utilising this technique.

- A piezoceramic material with strong lateral activity (high d_{31}) such as PZT5A should be utilised and excited at one of its lateral harmonics.

- A polymer bond with a high Poisson Ratio is favoured since the bond behaves as a mechanical transformer converting lateral displacements at its base into longitudinal displacements at its apex.

- For a given frequency, diameter of waveguide, and bond material an optimum cone geometry will exist to maximise the coupling efficiency, which can be established utilising FEA.

- The coupling arrangement should be configured as axisymmetrically as possible. That is, the fibre should be held centrally within the polymer cone, and the cone should be attached centrally on the surface of the piezoceramic disc.

Fibre Waveguides for Active Lamb Wave Sensing

This Thesis is concerned with the structural health monitoring of plate-type structures, and as discussed in Chapter 5, a recognised inspection technique capable of performing this function is that of Lamb wave propagation. Consequently, the application of fibre waveguides to deliver acoustic energy to and from plate-type structure for the subsequent generation and detection of Lamb waves was demonstrated. Initially, Chapter 5 discussed a surface mount strategy adopting a line array of fibre waveguides to deliver a series of periodic stresses to the surface of aluminium plates. Experimental and FEA results were reported, demonstrating the generation and detection of the S_0 and A_0 Lamb wave modes, and consequently confirming the viability of the concept. It was evident from the results presented that this form of surface excitation strongly favours A_0 Lamb wave mode operation as a result of the asymmetrical nature of the loading. Furthermore, the acoustic beam profile projected by a fibre waveguide line array was investigated using a theoretical model based on Huygens' Theorem. For comparison, experimental measurements were recorded utilising a dry contact Hertzian probe transducer. Good correlation was demonstrated between the theoretical predication and the experimentally measured response, both displaying a divergent acoustic beam propagating centrally away from the source, and significant side activity in the form of an interference pattern. The model predicted that the employment of a second line array parallel, and aligned with the first could be utilised to eradicate the side activity when separated by a half a wavelength of the generated Lamb wave mode.

Chapter 6 then went on to evaluate the employment of embedded fibre waveguides for Lamb wave generation and detection. This began with the waveguide requirements being stated for successful implementation of the system, which were as follows.

- Provide total elastic isolation for the ultrasound propagating along the waveguide from the surrounding structure.

- Be able to 'leak' the ultrasonic energy from the waveguide into the structure at a desired release location.

- Be capable of delivering a unimodal longitudinal (axisymmetric) acoustic mode.

- Operate within a practical frequency range for Lamb wave propagation in non-metallic plates i.e. < 1MHz

- Be non-invasive so that the structural integrity of the host is maintained.

Subsequently, various waveguide configurations were investigated in an attempt to meet the above requirements. Firstly, a homogeneous fibre waveguide was considered, however, it was established that core guided propagation could not be realised unless its shear wave velocity was less than that of the surrounding media within which it was embedded. Consequently, it was suggested that choice of waveguide material would be severely restricted for operation in non-metallic plates, such as CFRC whose shear wave velocities are typically very low. With this limitation in mind, the homogeneous fibre waveguide was considered impractical and subsequently eliminated from any further investigation.

The clad fibre waveguide geometry was then considered in an attempt to confine the propagating ultrasound to the core of the guide, with the cladding providing mechanical isolation from the surrounding media. It was revealed that, providing the shear wave velocity of the core is less than that of the cladding, such a configuration could support core-guided modes. Typically, these modes display a cut-off frequency, below which they behave as if they are propagating in a homogeneous medium (and are consequently leaky), and above which the propagating acoustic energy becomes increasingly concentrated to the core of the waveguide. However, dispersion analysis revealed that core-guided propagation could not be realised while maintaining the outlined requirements of the waveguide. That is, for the small fibre waveguide diameters required for unobtrusive integration into composite materials, the core-guided mode cut-off frequencies were beyond the practical operating range. Consequently, the clad fibre waveguide was also eliminated from the current application.

A homogenous fibre waveguide housed within a thin tube was therefore proposed. It was shown, using a copper fibre housed within an aluminium tube, that sufficient mechanical isolation could be realised, permitting non-leaky ultrasonic propagation along the waveguide. Experimental analysis also revealed that the removal of a section of the tubing enables the confined ultrasonic energy to be leaked into the surrounding media at a specified location. Importantly, the tube-fibre configuration permits guided propagation within the highlighted frequency range (<1MHz). Furthermore, within this range only the three fundamental waveguide modes will be supported in small diameter fibre waveguides, hence, uni-modal axisymmetrical propagation is more readily

achieved. This fibre waveguide configuration was therefore proposed for the implementation of the subsequent Lamb wave system.

Utilising a transmitting and receiving array of such waveguides, S_0 Lamb wave generation and detection in a 3.5mm hard-setting polymer plate at 250kHz was demonstrated. However, the received signal was shown to contain various Lamb wave modes of propagation, and it was suggested that this was the result of non-axisymmetrical modes in the waveguides introduced random phasing at the transmitter array. This highlighted the requirement for a uni-modal fibre waveguide coupling strategy. Utilising a laser vibrometer to acquire a discrete spatial series of surface displacement time histories, application of a 2DFFT routine revealed that the A_0 and A_1 modes were also generated in the plate. Significantly, it was established that the system did indeed preferentially generate the S_0 mode at 250kHz, for which it was designed. Moreover, by altering the frequency of operation to 170kHz, thereby matching the array spacing to that of the A_0 mode, it was shown that this mode was then be preferentially generated. It was concluded from these results that the basic design methodology was sound, and that the presence of non-axisymmetrical modes in the waveguides should be kept to a minimum if uni-modal Lamb wave generation is to be achieved.

Following this, the fabrication of a 3mm CFRC plate incorporating tube-fibre waveguides was described. Here the design guidelines outlined in Chapter 4 were followed to maximise the energy coupled into the waveguides and minimise the generation of the F(1,1) mode. S_0 Lamb wave mode generation and reception was

subsequently demonstrated at 250kHz and 210kHz over a propagation distance of 133mm. The results presented from this system were encouraging, confirming that fibre waveguides could be utilised to transport acoustic energy to and from composite materials for Lamb wave analysis. Moreover, the application of a time gated analogue filter permitted the isolation of the received S_0 mode from subsequent signals in the received trace. Consequently, the resultant signal is representative of ultrasonic propagation between the transmitting array to the receiving waveguide, and as such can be utilised to monitor that area.

Although Lamb waves can be utilised to identify the location and even characterise the nature of flaws, it is envisaged that the described system would be utilised to generate and receive various signature traces each capable of monitoring a particular section of the structure. Therefore, any changes in the received signal would highlight an irregularity in a particular area of the structure and subsequently flag the requirement for further NDE to quantify the severity of the flaw. Such a system would be aimed at reducing unnecessary maintenance costs, whereby the structure would demonstrate a degree of *intelligence* informing the structural engineer when it requires to be taken out of service for NDE, rather than maintenance being performed based on conservative estimates of failure. While this end goal is not immediately actionable, this Thesis has demonstrated the viability of the concept, and provided a significant contribution to its realisation.

7.2. Recommendations for Further Work

To further investigate the potential of this monitoring system concept, and address areas of concern discussed in the Thesis, the following recommendations are provided.

Improved Fibre Waveguide Coupling Techniques

The requirement for uni-modal propagation in the waveguide has been discussed, and in particular the L(0,1) mode has been recommended as the most suitable waveguide mode for the proposed application. It was suggested in Section 4.1 that a coupling strategy yielding a SCNR of 40dB should be aimed for to suppress erroneous waveguide modes to the random noise level. However, in Chapter 4 the polymer cone coupling technique was shown to generated the L(0,1) mode with an initial SCNR of only 17.4dB, and then with a refined axisymmetric layout an enhanced SCNR of 25dB. It is therefore suggested that further research should be performed on the development of an improved fibre waveguide coupling technique.

Initial work in this area has been carried out to develop an intrinsically axisymmetric transducer design for L(0,1) mode generation. The proposed transducer concept incorporates a spatial distribution to introduce wavelength selection and has consequently been termed an annular interdigital transducer (AIDT). This novel transducer concept utilises a series of radially excited piezoceramic annular elements, through which the waveguide is centrally bonded, to introduce a series of axisymmetrical stresses, as depicted in Figure 7.1. The element distribution is related to

the wavelength of the desired longitudinal mode for an improved spatial response. Subsequently, adjacent rings are separated (in the axial direction) by half the wavelength of the desired L(0,1) mode, and are driven 180° out-of phase at a radial mode frequency. Additionally, to improve the narrowband spatial response, the device is electrically apodised, whereby the voltage is applied with a Gaussian distribution weighted about the central elements, as indicated by Figure 7.1. A photograph of an AIDT is provided in Figure 7.2.

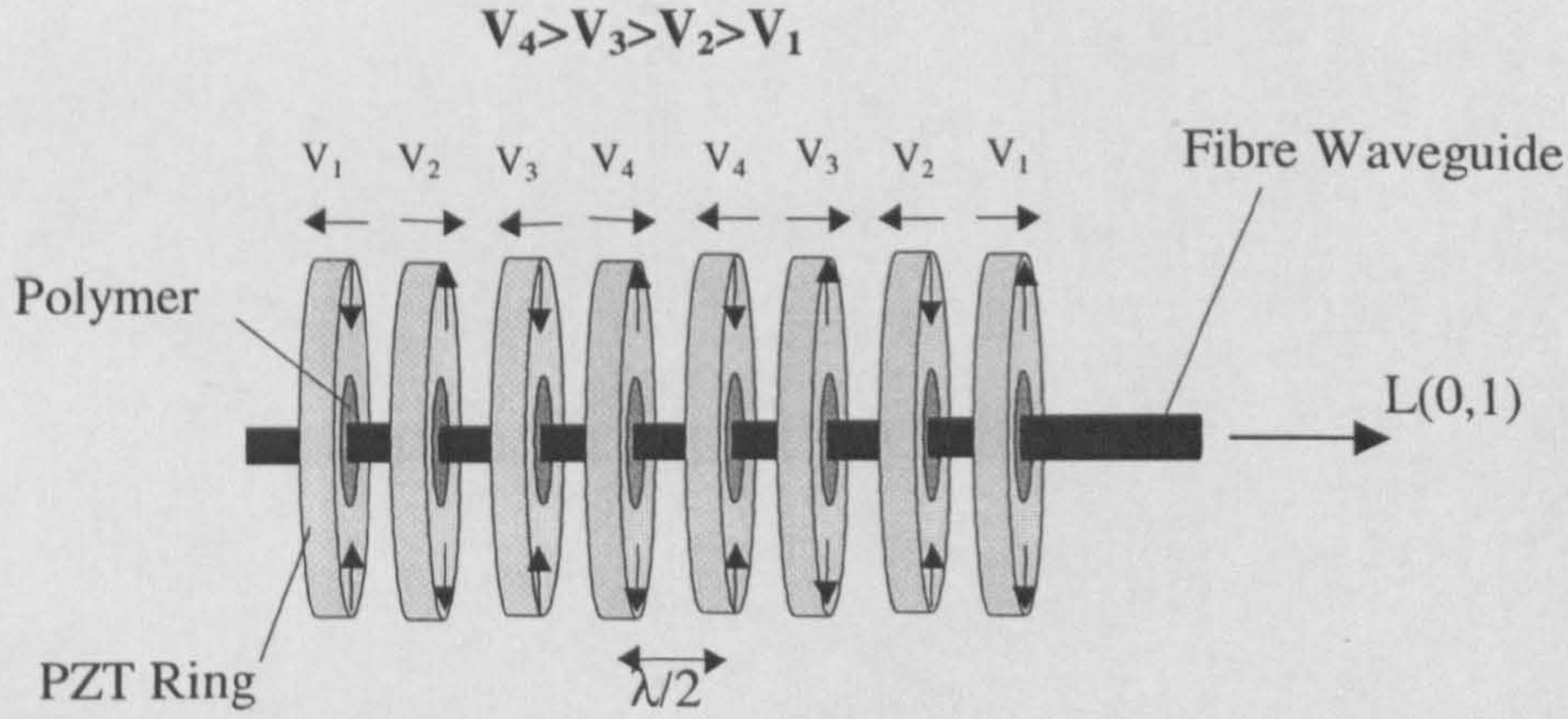

Figure 7.1. ***Annular Interdigital Transducer Configuration***

The AIDT was manufactured by filling a PZT5H annular disc transducer of thickness 10mm, outer diameter 20mm, and inner diameter 6.7mm with a hard-setting epoxy polymer. Once cured, a 0.5mm hole was drilled into the epoxy through the central axis of the device to accommodate the waveguide. The resultant transducer was sliced into a series of 0.6mm thick elements, which were individually electroded with silver paint, and then placed into a grooved cylindrical housing to achieve the appropriate spacing, as depicted in the photograph of Figure 5.16. A 0.5mm copper waveguide of length 1.2m

was then threaded through the elements and bonded into place with a fast setting epoxy resin.

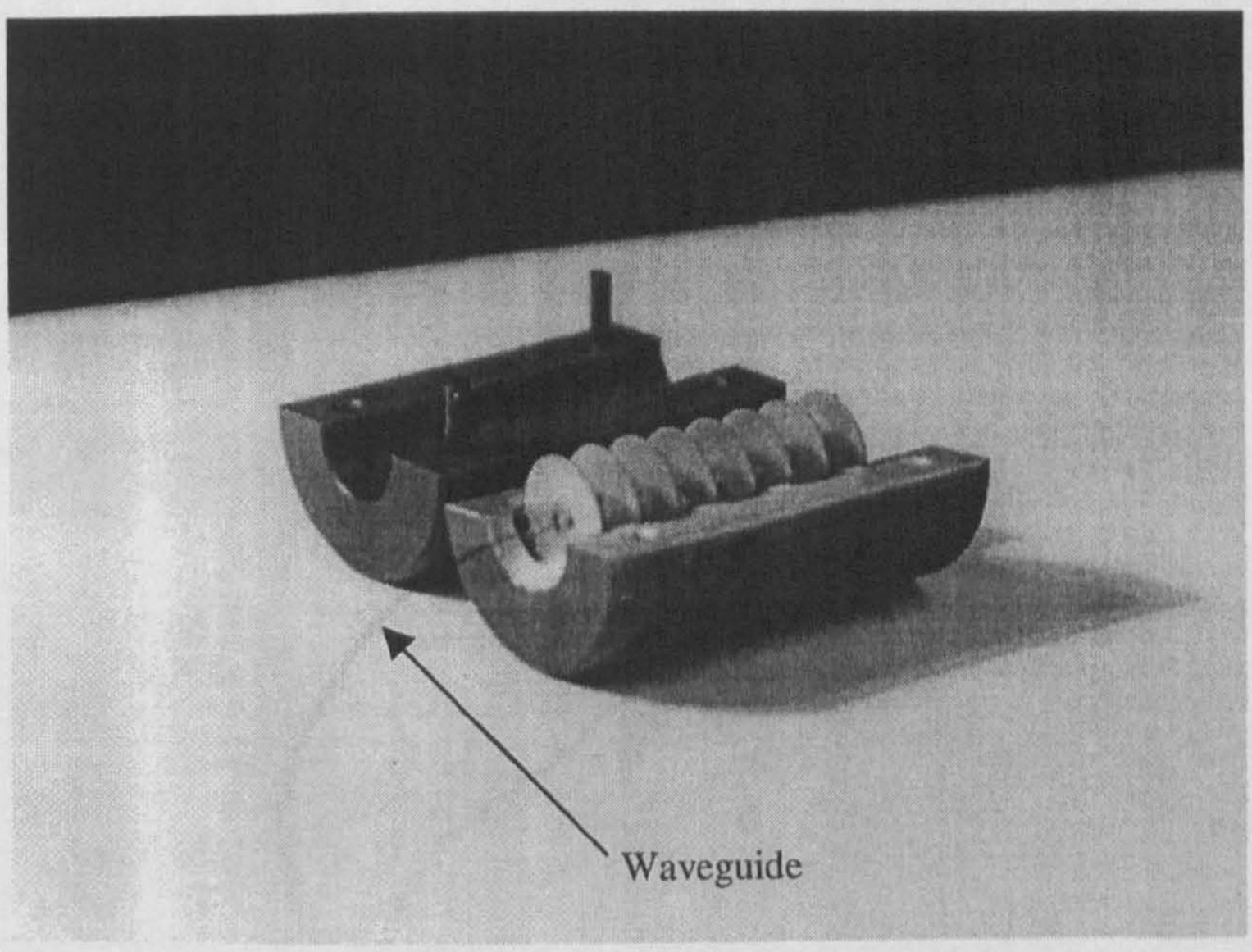

Figure 7.2: *Annular Interdigital Transducer Photograph*

The AIDT described was designed to generated the L(0,1) mode at 250kHz, and in this case the polymer cone coupling was utilised in reception to permit a comparison of the techniques in generation. The input voltages applied to the various elements of the AIDT were 20 cycle 'Hanning windowed' tonebursts with the following values: V1=3.5Vp-p, V2=13Vp-p, V3=32Vp-p, and V4=50Vp-p, and the receiver amplifier had a gain of 20dB. The received signal is shown in Figure 7.3, where it can be seen that the L(0,1) mode has been generated with an SNR of **36dB**, and a SCNR of **26dB**. Therefore, this transducer has been demonstrated to yield a marginally improved response to the polymer cone technique, with respect to the SCNR figure of merit.

Consequently, it can be seen that the design concept has potential, and therefore further work on its development is suggested for an improved performance. In particular FEA to establish the significance of parameters such as, the inner and outer ring diameters, number of elements, thickness of elements, and level of apodisation, which have not yet been investigated.

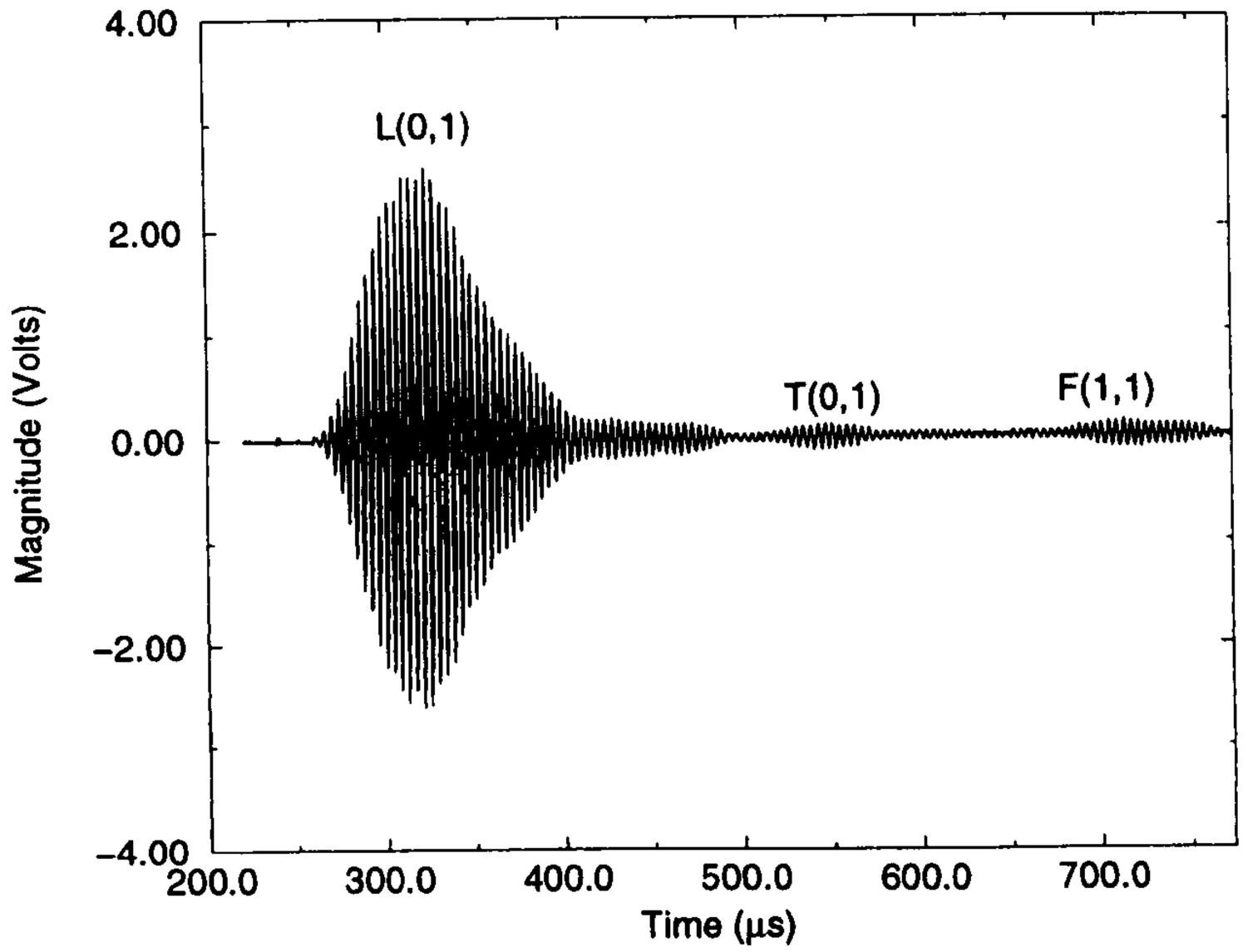

Figure 7.3: AIDT Generated Signal

While the AIDT design provides the potential to improve on the SCNR offered by the polymer cone coupling technique it is thought that the future of practical acoustic fibre waveguide transduction techniques lies with micro machining. Here precise transducer and interface designs, of comparable dimensions to the cross-section of the waveguide, should provide the opportunity to obtain greater control of the displacements imparted on the waveguide for selective mode generation. It is proposed that an investigation into this area should be performed.

Fibre Waveguide Array Analysis

In Chapter 5, it was shown *that* a Hertzian probe transducer could be utilised to measure the projected beam profile of a surface bonded fibre waveguide line array. *It is* proposed that further work in this area should be performed to quantify the beam profiles generated by various other array configurations. Furthermore, it is suggested that this technique be utilised to evaluate if selective phasing can be utilised to steer or focus the projected beam profile. It is thought that it would be beneficial to replace the Hertzian transducer method with a laser vibrometer scanning technique to automate the measurement procedure.

Quantify Embedded Fibre Waveguide as a Lamb Wave Receiver

In the course of this Thesis it has been proposed that the L(0,1) mode has the most suitable characteristics for ultrasonic delivery to the load plate. However, it is unclear if this is the best mode to be utilised in reception. Consequently, it is suggested that a study be carried out to determine which acoustic fibre waveguide mode is preferentially generated by each Lamb wave mode of interest. This is of importance for optimisation of the reception transducer-fibre interface design. It is suggested that experimental analysis could include the em*ployment* of uni-modal Lamb wave transducer techniques to selectively generate a particular mode. Using a single fibre waveguide as *the* receiver, time propagation analysis could be utilised to identify and quantify the induced waveguide modes.

Quantify Flaw Detection Capability

It is necessary to quantify the sensitivity of this system, with respect to the nature of the structural degradation it can detect. In particular, for application to the aerospace industry it is proposed that impact damage detection tests be performed on the system. Furthermore, it is proposed that a study be performed to established if an embedded fibre waveguide could be utilised as a passive sensor in CFRC materials to detect acoustic emission, which can result from matrix cracking, fibre breakage, or delamination.

Realisation of an Unobtrusive Embedded Fibre Waveguide System

A waveguide requirement still to be addressed is that of maintaining the host material's structural integrity. Consequently, it must be established if the tube-sleeved fibre waveguide configuration can be miniaturised to yield on overall diameter in the order of 125μm, i.e. comparable to that of optical fibres which have been successfully incorporated into structural components. Following this, it should be confirmed that the fibre waveguide requirements can still be maintained, and host integrity analysis should be performed on test pieces manufactured with such waveguides integrated into them.

Bibliography

[1] **Thurston, R. N.** 'Elastic Waves in Rods and Clad Rods', *J. Acoust. Soc. Am.*, **Vol. 64**, 1978, pp. 1-37.

[2] **Krautkramer, J., and Krautkramer, H.,** Ultrasonic Testing of Materials, 4th Edition, Springer-Verlag, Berlin, 1989

[3] **Hossack, J.A.,** 'Modelling Techniques For 1-3 Composite Transducers', Ph.D. Thesis, University of Strathclyde, Glasgow, Scotland, 1990.

[4] **Udd, E.,** 'Fibre Optic Smart Structures', *Proc. IEEE,* **Vol. 84 (1)**, 1996, pp 60-67

[5] **Monkhouse, R.S.C., Wilcox, P.D., and Cawley, P.,** 'Flexible interdigital PVDF Lamb Wave Transducers for the Development of Smart Structures', *Review of Progress in Quantitative Nondestructive Evaluation*, **Vol. 16**, Edited by Thompson D.O. and Chementi, D.E., Pelenum Press, New York, 1997, pp 877-884

[6] **Spillman, W.B. Jr,** 'Smart Structures', *Optical Engineering,* **Vol. 36 (7)**, 1997, pp 1835-1836

[7] **Culshaw, B. Gardiner, P.T., and McDonach, A., Eds.,** 'First European Conference on Smart Structures and materials,' *Proc. SPIE,* **Vol. 1777,** May 1992

[8] **Rogers, C. A.,** 'Intelligent Material Systems – The Dawn of a New Materials Age', *J. Intell. Mater. Syst. Struc.,* **Vol. 1**, 1993, pp 149-156

[9] **Spillman W.B. Jr, Sirkis, J.S., and Gardiner ,P.T.,** 'Smart Materials and Structures: What Are They?', *Smart Mater. Struct.,* **Vol. 5**, 1996, pp 247-254.

[10] **Culshaw, B,** Smart Structures and Materials, Artech House, Boston, 1996

[11] **Udd, E.,** 'Fibre Optic Smart Structures', *Proc. IEEE,* **Vol. 84 (6)**, 1996, pp 884-893

[12] **Spillman, W.B. Jr,** 'Sensing and Processing for Smart Structures', *Proc. IEEE,* **Vol. 84 (1)**, 1996, pp 68-77.

[13] **Measures, R. M.** 'Fibre Optic Strain Sensing', Fibre Optic Smart Structures, Chapter 8, Ed. Eric Udd, John Wiley & Sons, Inc., NY, 1995.

[14] **Lee, C.E., Taylor, H.F., Markus, A.M., and Udd, E.,** 'Optical-Fibre Fabry-Perot Embedded Sensor', *Opt. Lett.*, **Vol. 14**, 1989, pp 1225-1227

[15] **Alcoz, J.J., Lee, C.E., and Taylor, H.F.,** 'Embedded Fibre-Optic Fabry-Perot Ultrasound Sensor', *IEEE Transactions on Ultrasonics Ferroelectrics and Frequency Control,* **Vol. 37,** 1990, pp302-306

[16] **Valis, T., Hogg, D., and Measures, R.M.,** 'Composite Material Embedded Fibre-Optic Fabry-Perot Strain Gauge', *Proc. SPIE-Int. Soc. Opt. Eng.,* **Vol. 1370,** 1990, pp 154-157

[17] **Lee, C., and Taylor, H.F.,** 'Sensors for Smart Structures Based on the Fabry-Perot Interferometer', Fibre Optic Smart Structures, Chapter 9, Ed. Eric Udd, John Wiley & Sons, Inc., NY, 1995.

[18] **Measures, R.M.,** 'Advances Towards Fibre Optic Based Smart Structures', *Optical Engineering,* **Vol. 31 (1),** 1992, pp 34-47

[19] **Lee, C.E., Gibler, W.N., Atkins, R.A., Alcoz, J.J., and Taylor, H.F.,** 'Metal Embedded Fibre-Optic Fabry-Perot Sensors', *Opt. Lett.* **Vol. 16,** 1991, pp 1990-1992

[20] **Tang, L., Toa, X., and Choy, C-L.,** 'Effectiveness and Optimization of Fiber Bragg Grating Sensor as Embedded Strain Sensor', *Smart Mater. Struct.,* **Vol. 8,** 1999, pp 154-160.

[21] **Culshaw, B., Michie, C., Gardiner, P., and McGowan, A.,** 'Smart Structures and Applications in Civil Engineering', *Proc. IEEE,* **Vol. 84 (1),** 1996, pp 78-87

[22] **Jin, X.D., Sirkis J.S., Chung, J.K., and Venkat, V.S.,** 'Embedded In-Line Fibre Etalon/Bragg Grating Hybrid Sensor to Measure Strain and Temperature in a Composite Beam', *J. Intell. Mater. Syst. Struc.,* **Vol. 9**, 1998, pp 171-179.

[23] **Udd, E., Corona-Bittick, K., Slattery, K.T., Dorr, D.J., Crowe, C.R., Vandiver, T.L., and Evans, R.N.,** 'Fibre Grating Systems used to Measure Strain in Cylindrical Structures', *Optical Engineering,* **Vol. 36 (7)**, 1997, pp 1893-1900.

[24] **Masskant, R., Alavie, T., Measures, R.M., Tadros, G., Rizkalla, S.H., and Guha-Thakurta, A.,** 'Fibre-Optic Bragg Grating Sensors for Bridge Monitoring', *Cement and Concrete Composites,* **Vol. 19,** 1997, pp21-33

[25] **Davies, M.A., Bellemore, D.G., and Kersey, A.D.,** 'Distributed Fibre Bragg Grating Strain Sensing in Reinforced Concrete Structural Composites', *Cement and Concrete Composites,* **Vol. 19,** 1997, pp45-57

[26] **Pierce, S.G., Philip, W.R., Gachagan, A., McNab, A., Culshaw, B., and Hayward, G.** 'Surface Bonded and Embedded Optical Fibres As Ultrasonic Sensors', *Applied Optics,* **Vol. 35,** 1996, pp 5191-5197.

[27] **Carmen, G.P., and Sendeckyj G.P.,** 'Review of the Mechanics of Embedded Optical Sensors', *J. Composites Technol. Res.,* **Vol. 17**, 1995, pp 183-193.

[28] **Jeon B.S., Lee, J.L., Kin, J.K., and Huh, J.S.,** 'Low Velocity Impact and Delamination Buckling Behaviour of Composite Laminates with Embedded Optical Fibres', *Smart Mater. Struct.,* **Vol. 8**, 1999, pp 41-48

[29] **Singh, H., Sirkis, J.S., and Dasgupta, A.,** 'Micro-Interaction of Optical Fibres Embedded in Laminated Composites', *Fibre Optic Smart Structures and Skins IV, SPIE,* **Vol. 1588**, 1991, pp 76-85

[30] **Measures, R.M., Glossop, N.D.W., Lymer, J., LeBllance, M., West, J., Debois, S., Tsaw, W., and Tennyson, R.C.,** 'Structurally integrated fibre optic damage assessment system for composite materials', *Applied Optics.* **Vol. 28**, 1989, pp 2626-2633

[31] **Jenson, D.W. and Pascal, J.,** 'Degradation of graphite/bismaleimide laminate with multiple embedded fibre optic sensors', *Fibre Optic Smart Structures and Skins III, SPIE,* **Vol. 1370**, 1990, pp 228-237.

[32] **Haslach H.W., Whipple, K.G.,** 'Mechanincal Design of Embedded Optical Fibre Interferometric Sensors for Monitoring Simple Combined Loads', *Optical Engineering,* **Vol. 32 (3)**, 1993, pp 494-503.

[33] **Gang, M., and Yapeng, S.** 'The Coatings Optimisation of Embedded Fibre Optical Sensors under Thermal and Mechanical Load', *Acta Mechanica Solida Sinica,* **Vol. 9 (4)**, 1996, pp 319-329.

[34] **Hadjiprocopiou, M., Reed, G.T., Hollaway, L., and Thorne, A.M.,** 'Optimisation of Fibre Coating Properties for Fibre Optic Smart Structures', *Smart Mater. Struct.,* **Vol. 5**, 1996, pp 441-448

[35] **Chee, C.Y.K., Tong, L., and Steven, G.P.,** 'A Review on the Modelling of Piezoelectric Sensors and Actuators Incorporated in Intelligent Structures', *J. Intell. Mater. Syst. Struc.,* **Vol. 9,** 1998, pp3-19.

[36] **Kumar, S., Bhalla, A.S., Cross, L.E.** 'Smart Ceramics for Broadband Vibration Control', *J. Intell. Mater. Syst. Struc.,* **Vol. 5,** 1994, pp673-677.

[37] **Yang S.M., and Bian, J.J.,** 'Vibration Suppression Experiments On Composite Laminated Plates Using an Embedded Piezoelectric Sensor and Actuator', *Smart Mater. Struct.* **Vol. 5,** 1996, pp501-507.

[38] **Chiu, W.K., Galea, S.C, Zhang, H., Jones, R., and Lam, Y.C.** 'The use of Piezoelectric Thin Film Sensors for Structural Integrity Monitoring', *J. Intell. Mater. Syst. Struc.,* **Vol. 5,** 1994, pp683-693.

[39]. **Egusa, S. and Iwasawa, N.,** 'Piezoelectric Paints as one Approach to Smart Structural Materials with Health Monitoring Capabilities', *Smart Mater. Struct.* **Vol.7,** 1998, pp438-445.

[40] **Gachagan, A., Reynolds, P., Hayward, G., Monkhouse, R.S.C., and Cawley, P.,** 'Piezoelectric Materials for Application in Low Profile Interdigital Transducer Designs', *Proceedings of the IEEE Ultrasonics Symposium,* 1997, pp1025-1028

[41] **Gachagan A., Reynolds P., Hayward G., McNab A.,** 'Construction and Evaluation of a new generation of flexible ultrasonic transducers', *Proceedings of the IEEE Ultrasonics Symposium,* 1996, pp 853-856.

[42] **Moulin E., Assaad J., Delebarre C., Kaczmarek H., Balageas D.,** 'Piezoelectric Transducer Embedded in a Composite Plate: Application to Lamb Wave Generation', *J. Appl. Phys.,* **Vol. 82(5)** 1997, pp 2049-2055.

[43] **Wenger, M.P., Blanan, P., Shuford, R.J., and Das-Gupta, D.K.,** 'Characterisation and Evaluation of Piezoelectric Composite Bimorphs for *In-Situ* Acoustic Emission Sensors', *Polymer Engineering and Science,* **Vol.39(3),** 1996, pp508-518.

[43] **Varadan, V.V., Varadan, V.K., Boa, X., Ramanathan, S., and Piscotty, D.,** 'Wireless passive IDT strain microsensor', *Smart Mater. Struct.,* **Vol. 6**, 1997, pp 745-751

[45] **Kent R.M., and Ruddell, M.J.,** 'The In-Situ Sensor-Guided Process Characterisation of Advanced Composite Materials', *JOM-Journal of the Minerals Metals & Materials Society,* **Vol. 48 (9)**, 1996, pp 32-34.

[46] **Kent R.M.,** 'Laser interferometric analysis of fibre and composite material at elevated temperatures', *Report Prepared by SYSTRAN corporation for Wright Laboratory,* Materials Directorate, Ohio, Jan 1994

[47] **Kent, R.M.,** 'Investigation of Ceramic Composites Using Optical and Ultrasonic Testing Methods', *Report Prepared by SYSTRAN corporation for Wright Laboratory,* Materials Directorate, Ohio, Jan 1994

[48] **Ceysson, O., Risson, T., Salvia, M.,** 'Carbon Fibres: Sensor Components for Smart Structures', *Proc. SPIE – Int. Soc. Opt. Eng.,* **Vol. 2779**, 1996, pp 136-141.

[49] **Hayes, S., Liu, T., Brooks, D., Monteith, S., Ralph, B., Vickers, S., and Fernando, G.F.,** 'In-Situ self-sensing fibre reinforced composites', *Smart Mater. Struct.,* **Vol. 6**, 1997, pp 432-440.

[50] **Brockelsby C. F., Palfreeman J. S. Gibson R. W.,** Ultrasonic Delay Lines, London, Iliffe Books Ltd, 1963.

[51] **Meitzler A. H.,** 'Mode Coupling Occurring in the Propagation of Elastic Pulses in Wires', *J. Acoust. Soc. Am.,* **Vol. 33,** 1961, pp435-445

[52] **Abramson H.N.,** 'Flexural waves in elastic beams of circular cross-section', *J. Acoust. Soc. Am.,* **Vol. 33**, 1961, 435-445

[53] **Meeker T.R. and Meitzler A.H.,** 'Guided wave propagation in elongated cylinders and plates', in: *Physical Acoustics - Principles and Methods,* Vol 1A (Ed. Mason, W.P.) Academic Press, London UK 1964

[54] **Boyd G. D., Coldren L. A., Thurston R. N.,** 'Acoustic Waveguid with a Cladded Core Geometry', *Applied Physical Letters*, **Vol. 26,** 1975, pp31-34.

[55] **Boyd G. D., Coldren L. A., Thurston R. N.,** 'Acoustic Clad Fibre Delay Lines', *IEEE Transactions on Sonics and Ultrasonics,* **Vol. 24,** 1977, pp246-252

[56] **Risk W. P. Kino G. S.,** Acousto-optic polarization coupler and intensity modulator for birefringent fibre, *Opt. Lett.,* **Vol. 11,** 1986, pp48-50.

[57] **Risk W. P. Kino G. S.,** Acousto-optic fibre-optic frequency shifter using periodic contact with a copropagating surface acoustic wave, *Opt. Lett.,* **Vol. 11,** 1986, pp336-338.

[58] **Risk W. P. Kino G. S. Shaw H. J.,** Fibre-optic frequency shifter using a surface acoustic wave incident at an oblique angle, *Opt. Lett.,* **Vol. 11,** 1986, pp115-117.

[59] **Risk W. P. Kino G. S. Khuri-Yakub B. T.,** Tunable optical filter in fibre-optic form, *Opt. Lett.,* **Vol. 11,** 1986, pp578-580.

[60] **Kim B.Y. Blake J. N. Engan H. E. Shaw H.J.,** All-fibre acousto-optic frequency shifter, *Opt. Lett.,* **Vol. 11,** 1986 pp389 - 391.

[61] **Mason W. P.,** Physical Acoustics and the Properties of Solids, New York: Van Nostrand, 1958.

[62] **Engan H. E. Kim B. Y. Blake J. N. Shaw H. J.,** 'Propagation and Optical Interaction of Guided Acoustic Waves in Two-Mode Optical Fibres', *J. of Lightwave Technology,* **Vol. 6,** 1988, pp428-435

[63] **Lisboa O. Blake J. N. Oliveira J. E. B. Carrara S.L.A.,** 'New Configurations for an Optical Fibre Acousto-Optic Frequency Shifter', *Fibre Optic Sensors IV*, **SPIE Vol. 1267**, 1990, 17-23

[64] **Nicholson N. C., McDicken W.N., Anderson T.,** 'Waveguides in medical ultrasonics', *Ultrasonics,* **Vol. 26,** 1988, pp27-30

[65] **Woodward B. and Allen A.J.,** 'Importance of calibration in medical ultrasonics', *Brit. J. Radiol.,* **Vol. 47,** 1974, pp707-711

[66] **Woodward B.,** 'A waveguide pulse-echo system for ultrasonic absorption measurements in biological media', *J Biomed. Eng.*, **Vol. 5**, 1983, pp343-348

[67] **McDicken W. N. Anderson T.,** 'Ultasonic stylets for needles and catheters', *Ultrasound Med. Biol.,* **Vol. 10,** 1984, pp499-507.

[68] **Jen, C.-K., Legoux, J.-G.,** 'High Performance Clad Metallic Buffer Rods', *Proceedings of the IEEE Ultrasonics Symposium,* 1996, pp771-776

[69] **Jen, C.-K., Cao, B., Nguyen, K.T., Loong, C.A., Legoux, J.-G.,** 'On-Line Ultrasonic Monitoring of a Die-Casting Process Using Buffer Rods', *Ultrasonics,* **Vol. 35,** 1997, pp335-344.

[70] **Jen, C.-K., Chen, J.-Y., Hoa, S.V., Nguyen, K.T., Legoux, J.-G., and Herbert, H.,** 'Clad Buffer Rods for In-Situ Process Monitoring', *Proceedings of the IEEE Ultrasonics Symposium,* 1997, pp801-806

[71] **Chen, T.-F., Nguyen, K.T., Wen, S.-S.W., and Jen, C.-K.,** 'Temperature Measurement of Polymer Extrusion by Ultrasonic Techniquesg', *Meas. Sci. Technol.,* **Vol. 10,** 1999, pp139-145

[72] **Liu, Y., Lynnworth, L.C., and Zimmerman, M.A.,** 'Buffer Waveguides for Flow Measurement in Hot Fluids', *Ultrasonics,* **Vol. 36,** 1998, pp 305-315

[73] **Journeau, C., and Ducret, P.,** 'Towards in-situ ultrasonic transmission measurement of melt crusts above 2000°C', *Ultrasonics,* **Vol. 36,** 1998, pp 251-255

[74] **Sun, K.J., and Winfree, W.P.,** 'Propagation of Acoustic Waves in a Copper Wire Embedded in a Curing Epoxy', *Proceedings of the IEEE Ultrasonics Symposium,* 1987, pp 439-442.

[75] **Harrold, R.T., and Sanjana, Z.N.,** 'Acoustic Waveguide Monitoring of the Curing and Structural Integrity of Composite Materials', *Poly. Eng. Sci.,* **Vol. 26,** 1986, pp 367-372.

[76] **Yamaguchi, H., Yoshizawa, M., Tagawa, N., Moriya, T., and Yagi, S.-I.,** 'Ultrasonic Flaw Detection for High Impedance Materials Using a Transmission Line coupling Method', *Japanese J. Appl. Phys.* **Vol. 36,** 1997, pp 3287-3289.

[77] **Costley, R.D., Balasubramaniam K., Ingham, W.M., Simpson J.A., Shah, V.** 'Torsional Waveguide Sensor for Molten Materials', *Review of Progress in Quantitative Nondestructive Evaluation,* **Vol. 17**, Edited by Thompson D.O. and Chementi, D.E., Pelenum Press, New York, 1998, pp 859-866.

[78] **Degertekin, F.L., and Khuri-Yakub, B.T.,** 'Lamb Wave Excitation by Hertzian Contacts with Applications in NDE', *IEEE Transactions on Ultrasonics Ferroelectrics and Frequency Control,* **Vol. 44(4),** 1997, pp 769-779

[79] **Kolsky, H.,** Stress Waves in solid, New York, Dover Publications inc., 1963.

[80] **Redwood, M.,** Mechanical Waveguides, Pergamon Press, Oxford, 1960

[81] **Love, A. E. H.,** A Treatise on the Mathematical Theory of Elasticity, Dover Publications, New York, 1944.

[82] **Hayward, G.,** Forth Year Ultrasonic Course Notes, University of Strathclyde, Glasgow (1996).

[83] **Morse, P. M., and Freshbach, H.,** Methods of Theoretical Physics, Part I, McGraw-Hill Book Company Inc., 1953.

[84] **Zaky A.A., and Hawley**, R., Fundamentals of Electromagnetic Field Theory, Harrap & Co. Ltd, London 1974

[85] **Abramson, H.N.,** 'Flexural waves in elastic beams of circular cross-section', *J. Acoust. Soc. Am.*, 1961, **Vol. 33**, pp435-445

[86] **Hudson, G. E.,** 'Dispersion of Elastic Waves in Solid Circular Cylinders', *Phys. Rev.*, 1943 **Vol. 63,** pp46-51

[87] **Pochhammer, L.,** 'Uber die Fortpflanzungsgeschwindigkeiten Kleiner Schwingungen in einem Unbegrenzten Isotropen Kreiscylinder', *J. fur reine und angewandte Math.*, Crelle, 1876, **Vol. 81**, pp324-336

[88] **Chree, C,** 'The Equations of an Isotropic Elastic Solid in Polar and Cylindrical Co-ordinates, Their Solution and Application', *Trans. Cambridge, Philos. Soc.*, **Vol. 14,** 1889, pp250-369

[89] **Gray, Mathews, and Roberts**, A Treatise on Bessel Functions and Their Application to Physics, MacMillan and Co. Ltd., London 1922.

[90] **MATLAB,** distributed by The MathsWorks, Inc., Cochituate Place, 24 Prime Park Way, Natick, Mass. 01760

[91] **Bancroft, D.,** 'The Velocity of Longitudinal Waves in Cylindrical Bars', *Phys. Rev.*, **Vol. 59,** 1941, pp588-593

[92] **Achenbach, D.,** Wave Propagation in Elastic Solids, North-Holland Publishing Company, Amsterdam, 1973.

[93] **Booker, R. E. Sager, F. H.,** 'Velocity Dispersion of the Lowest-Order Longitudinal Mode in Finite Rods of Circular Cross Section', *J. Acoust. Soc. Am.*, **Vol. 49,** 1971, pp1491-1498.

[94] **Bennet J.,** Development of a Finite Element Modelling System for Piezocomposite transducers, *Ph.D Thesis,* University of Strathclyde, Glasgow, Scotland, UK, 1995

[95] **NAFEMS,** A Finite Element Primer, Department of Trade and Industry, National Engineering Laboratory, East Kilbride, Glasgow, 1986

[96] **PZFlex** distributed by Weidlinger Associates, 4410 El Camino Real, Suite 110, Los Altos, CA 94022.

[97] **Dogan, A., Uchino, K. and Newnham, R.E.,** 'Composite Piezoelectric Transducer with Truncated Conical Endcaps 'Cymbal', *IEEE Transactions on Ultrasonics, Ferroelectrics, and Frequency Control*, **Vol. 44(3)**, 1997, pp597-605.

[98] **Tressler, J.F., Cao, W., Uchino, K. and Newnham, R.E.,** 'Finite Element Analysis of the Cymbal-Type Flextensional Transducer', *IEEE Transactions on Ultrasonics, Ferroelectrics, and Frequency Control*, **Vol. 45(5)**, 1998, pp1363-1369.

[99] **Viktorov I. A.,** Rayleigh and Lamb waves: Physical Theory and Applications, New York, Plenum, 1967

[100] **Fraser, J., Khuri-Yakub B.T., Kino G.S.,** 'The Design of Efficient Broadband Wedge Transducers', *Appl. Phys. Lett.*, **Vol. 32**, 1978, pp698-700

[101] **Krautkramer, J. and Krautkramer H.,** Ultrasonic Testing of Materials, 4th Edition, Springer-Verlag, Berlin, 1990.

[102] **Kinsler, L.E., Frey, A.R., Coppens, A.B., Sanders, J.V.,** 'Fundamentals of Acoustics', 3rd Edition, John Wiley & Sons, New York, 1982.

[103] 'Morgan Matroc Data Book', Morgan Matroc Ldt., Transducer Products Division, Thornhill, Southampton, Hampshire, England.

[104] **Wilcox, P.D., Cawley, P., Lowe M.J.S.,** 'Acoustic Fields from PVDF interdigital transducers', *IEE Pro.-Sci. Meas. Technol.*, **Vol. 145,** 1998, pp250-259.

[105] **Farlow R., and Hayward G.,** 'An Automated Ultrasonic NDT Scanner Employing Aadvanced Air-Coupled 1-3 Connectivity Composite Transducers', *Insight,* **Vol. 38**, 1996, pp41-50

[106] **Luukkala, M., and Merilainen P.,** 'Metal plate testing using airborne ultrasound', *Ultrasonics,* 1973, pp218-221

[107] **Wright, W., Hutchins, D., Jansen, D., Schindel D.,** 'Air-Coupled Lamb Wave Tomography', *IEEE Transactions on Ultrasonics Ferroelectrics, and Frequency Control,* **Vol. 44(1),** 1997, pp53-59.

[108] **Kelly, S.P., Farlow, R., Hayward, G.,** 'Applications of Through-Air Ultrasound for Rapid NDE Scanning in the Aerospace Industry', *IEEE Transactions on Ultrasonics, Ferroelectrics, and Frequency Control,* **Vol. 43(4),** 1996, pp581-591.

[109] **Hutchins, D.A., Jansen, D.P., and Edwards, C.,** 'Lamb-Wave Tomography using non-contact transduction', *Ultrasonics,* **Vol. 31(2)**, 1993, pp. 97 – 103.

[110] **Pierce, S.G., and Culshaw, B.,** 'Laser Generation of Ultrasonic lamb Waves using Low Power Optical Sources', *IEE Proc.-Sci. Meas. Technol.*, **Vol. 145(5)**, 1998, pp224-249.

[111] **Pierce, S.G., Culshaw, B., and Shan, Q.,** 'Laser Generation of Ultrasound using a modulated continuous wave laser diode', *Appl. Phys. Lett.*, **Vol. 72(9)**, 1998, pp1030-1032.

[112] **Thompson, R.B.,** 'Physical Principals of Measurement with EMAT transducers', *Physical Acoustic,* edited by Mason, W.P., and Thurston R.N., (Academic Press, New York, 1990), **Vol. XIX,** pp179-275.

[113] **Landau, L., and Lifshitz, E.M.,** Theory of Elasticity, New York: Pergamon, 1959.

[114] **Degertekin F.L., and Khuri-Yakub, B.T.,** 'Hertzian Contact Transducers for Non-destructive Evaluation', *J. Acousti. Soc. Am.*, **Vol. 99**, 1996, pp299-308.

[115] **Gachagan, A., Hayward, G., McNab, A., Reynolds, P., Pierce, S. G., Philp, W. R., Culshaw, B,** 'Generation and Reception of Ultrasonic Guided Waves in Composite Plates Using Conformable Piezoelectric Transmitters and Optical Fibre Detectors', *IEEE Transactions on Ultrasonics, Ferroelectrics, and Frequency Control*, **Vol. 46**, 1999, pp72-81.

[116] **Hyslop, J., and Hayward, G.**: 'An Experimental and Theoretical Investigation into the Fluid-Loaded Performance of 1-3 Piezocomposite Transducer Array Structures: with Specific Regard to Device Surface Displacement and Beam Profile', *Proceedings of the IEEE Ultrasonics Symposium,* 1997, pp907-910,

[117] **Pavlakovic, B., Lowe, M., Alleyne D., and Cawley, P.,** 'Disperse: A General Purpose Program for Creating Dispersion Curves', *Review of Progress in Quantitative NDE,* Eds. Thompson, D.O., and Chimenti, D.E., Plenum Press, New York, **Vol. 16**, 1996, pp 185-192.

[118] **Alleyne, D., Cawley, P.,** 'A two dimensional fourier transform method for the measurement of propagating multimode signals', *J. Acoust. Soc. Am.*, **Vol. 89(3),** 1991, pp1159-1168.

Appendix A

Vector Calculus Relations in Cylindrical Co-ordinates

The following identities describe gradient (A1), divergence (A2), curl (A3), and the Laplacian operator (A4) in cylindrical co-ordinates [82].

$$\nabla V = \frac{\partial V}{\partial r}\mathbf{i}_r + \frac{1}{r}\frac{\partial V}{\partial \theta}\mathbf{i}_\theta + \frac{\partial V}{\partial z}\mathbf{i}_z \qquad \textbf{A1}$$

$$\nabla.\mathbf{F} = \frac{1}{r}\frac{\partial}{\partial r}(rF_r) + \frac{1}{r}\frac{\partial F_\theta}{\partial \theta} + \frac{\partial F_z}{\partial z} \qquad \textbf{A2}$$

$$\nabla \mathbf{x} \mathbf{F} = \left(\frac{1}{r}\frac{\partial F_z}{\partial \theta} - \frac{\partial F_\theta}{\partial z}\right)\mathbf{i}_r + \left(\frac{\partial F_r}{\partial z} - \frac{\partial F_z}{\partial r}\right)\mathbf{i}_\theta + \frac{1}{r}\left(\frac{\partial}{\partial r}(rF_\theta) - \frac{\partial F_r}{\partial \theta}\right)\mathbf{i}_z \qquad \textbf{A3}$$

$$\nabla^2 V = \frac{1}{r}\frac{\partial}{\partial r}\left(r\frac{\partial V}{\partial r}\right) + \frac{1}{r^2}\frac{\partial^2 V}{\partial \theta^2} + \frac{\partial^2 V}{\partial z^2} \qquad \textbf{A4}$$

Here V is a scalar and **F** is a vector.

Appendix B

Derivation of Relevant Bessel Function Relationships

Part I

The Bessel function of the first kind of order n, $J_n(x)$, can be expressed as follows [87].

$$J_n(x)=\sum_{s=0}^{\infty}\frac{(-1)^s}{\Pi(s)\Pi(n+s)}\left(\frac{x}{2}\right)^{n+2s} \qquad \textbf{B1}$$

Where $\Pi(s)$ represents Gauss's function, which is identical to $n!$ (product of 1 to n) for positive integer values of n.

Therefore, from B1 it follows that,

$$J_n(hr)=\sum_{s=0}^{\infty}\frac{(-1)^s}{\Pi(s)\Pi(n+s)}\left(\frac{hr}{2}\right)^{n+2s} \qquad \textbf{B2}$$

$J_n'(hr)$ is obtained by differentiating B2,

$$J_n'(hr)=\sum_{s=0}^{\infty}\frac{(-1)^s h(n+2s)}{\Pi(s)\Pi(n+s)}\left(\frac{1}{2}\right)^{n+2s}(hr)^{n+2s-1} \qquad \textbf{B3}$$

Therefore,

$$rJ_n'(hr)=\sum_{s=0}^{\infty}\frac{(-1)^s(n+2s)}{\Pi(s)\Pi(n+s)}\left(\frac{hr}{2}\right)^{n+2s} \qquad \textbf{B4}$$

$J_n''(hr)$ is obtained by differentiating Equation B3,

$$J_n''(hr)=\sum_{s=0}^{\infty}\frac{(-1)^s h^2(n+2s)(n+2s-1)}{\Pi(s)\Pi(n+s)}\left(\frac{1}{2}\right)^{n+2s}(hr)^{n+2s-2} \quad \textbf{B5}$$

Therefore, $$r^2 J_n''(hr)=\sum_{s=0}^{\infty}\frac{(-1)^s(n+2s)(n+2s-1)}{\Pi(s)\Pi(n+s)}\left(\frac{hr}{2}\right)^{n+2s} \quad \textbf{B6}$$

Equation B6 can be expressed as follows.

$$r^2 J_n''(hr) =\sum_{s=0}^{\infty}\frac{(-1)^s n^2}{\Pi(s)\Pi(n+s)}\left(\frac{hr}{2}\right)^{n+2s}-\sum_{s=0}^{\infty}\frac{(-1)^s(n+2s)}{\Pi(s)\Pi(n+s)}\left(\frac{hr}{2}\right)^{n+2s}+\sum_{s=0}^{\infty}\frac{(-1)^s 4s(n+s)}{\Pi(s)\Pi(n+s)}\left(\frac{hr}{2}\right)^{n+2s}$$

From Equations B2 and B4 this reduces to:

$$r^2 J_n''(hr)=n^2 J_n(hr)-rJ_n'(hr)+\sum_{s=0}^{\infty}\frac{(-1)^s 4s(n+s)}{\Pi(s)\Pi(n+s)}\left(\frac{hr}{2}\right)^{n+2s} \quad \textbf{B7}$$

Equation B7 can be further reduced,

$$r^2 J_n''(hr)=n^2 J_n(hr)-rJ_n'(hr)+(hr)^2\sum_{s=0}^{\infty}\frac{(-1)^s s(n+s)}{\Pi(s)\Pi(n+s)}\left(\frac{hr}{2}\right)^{n+2s-2}$$

$$=n^2 J_n(hr)-rJ_n'(hr)+(hr)^2\sum_{s=0}^{\infty}\frac{(-1)^s s}{\Pi(s)\Pi(n+s-1)}\left(\frac{hr}{2}\right)^{n+2s-2}$$

$$=n^2 J_n(hr)-rJ_n'(hr)+(hr)^2\sum_{s=1}^{\infty}\frac{(-1)^s}{\Pi(s-1)\Pi(n+s-1)}\left(\frac{hr}{2}\right)^{n+2s-2}$$

Now in the summation set $s = r + 1$; then

$$r^2 J_n''(hr) = n^2 J_n(hr) - rJ_n'(hr) - (hr)^2 \sum_{r=0}^{\infty} \frac{(-1)^r}{\Pi(r)\Pi(n+r)} \left(\frac{hr}{2}\right)^{n+r} \quad \textbf{B8}$$

Therefore substitution of Equation B2 into Equation B8 yields the following relationship.

$$r^2 J_n''(hr) = \left[n^2 - (hr)^2\right] J_n(hr) - rJ_n'(hr) \quad \textbf{B9}$$

Part II

From Equation B3 it can be seen that,

$$J_0'(hr) = \sum_{s=0}^{\infty} \frac{(-1)^s h(2s)}{\Pi(s)\Pi(s)} \left(\frac{1}{2}\right)^{2s} (hr)^{2s-1} \quad \textbf{B10}$$

Therefore $$J_0'(hr) = \frac{h}{hr} \sum_{s=0}^{\infty} \frac{(-1)^s (2s)}{\Pi(s)\Pi(s)} \left(\frac{hr}{2}\right)^{2s}$$

$$= \frac{hr}{r} \sum_{s=0}^{\infty} \frac{(-1)^s (s)}{\Pi(s)\Pi(s)} \left(\frac{hr}{2}\right)^{2s-1}$$

$$= h \sum_{s=1}^{\infty} \frac{(-1)^s}{\Pi(s-1)\Pi(s)} \left(\frac{hr}{2}\right)^{2s-1}$$

Now in the summation set s=r+1 thus,

$$J_0'(hr) = -h \sum_{r=0}^{\infty} \frac{(-1)^r}{\Pi(r)\Pi(r+1)} \left(\frac{hr}{2}\right)^{2r+1}$$

Therefore from Equation B2 it can be seen that,

$$J_0'(hr) = -hJ_1(hr) \quad \textbf{B11}$$

Part III

From Equation B3 it can be seen that

$$J_1'(hr)=\sum_{s=0}^{\infty}\frac{(-1)^s h(2s+1)}{\Pi(s)\Pi(s+1)}\left(\frac{1}{2}\right)^{2s+1}(hr)^{2s} \qquad \textbf{B12}$$

Therefore,

$$J_1'(hr)=\frac{1}{r}\sum_{s=0}^{\infty}\frac{(-1)^s(2s+1)}{\Pi(s)\Pi(s+1)}\left(\frac{hr}{2}\right)^{2s+1}$$

$$=\frac{1}{r}J_1(hr)+\frac{1}{r}\sum_{s=0}^{\infty}\frac{(-1)^s(2s)}{\Pi(s)\Pi(s+1)}\left(\frac{hr}{2}\right)^{2s+1}$$

$$=\frac{1}{r}J_1(hr)-\frac{2}{r}J_1(hr)+\frac{1}{r}\sum_{s=0}^{\infty}\frac{(-1)^s(2s+2)}{\Pi(s)\Pi(s+1)}\left(\frac{hr}{2}\right)^{2s+1}$$

$$=-\frac{1}{r}J_1(hr)+\frac{hr}{r}\sum_{s=0}^{\infty}\frac{(-1)^s(s+1)}{\Pi(s)\Pi(s+1)}\left(\frac{hr}{2}\right)^{2s}$$

$$=-\frac{1}{r}J_1(hr)+h\sum_{s=0}^{\infty}\frac{(-1)^s}{\Pi(s)\Pi(s)}\left(\frac{hr}{2}\right)^{2s}$$

Therefore,

$$J_1'(hr)=hJ_0(hr)-\frac{1}{r}J_1(hr) \qquad \textbf{B13}$$

Appendix C

Material Parameters

Ceramic

Ceramic	PZT5A	PZT5H	MPT
Stiffness (10^{10}Pa)			
C_{11}^E	12.03	12.72	14.92
C_{12}^E	7.52	8.02	3.68
C_{13}^E	7.51	8.47	3.24
C_{33}^E	11.09	11.74	12.76
C_{44}^E	2.11	2.30	5.52
C_{66}^E	2.26	2.35	5.65
Piezoelectric Stress (Cm^{-1})			
e_{13}	-5.4	-6.5	-0.953
e_{33}	15.8	23.3	10.24
e_{15}	12.3	17.0	5.25
Piezoelectric Strain ($10^{-12}CN^{-1}$)			
d_{31}	-171	-274	-21
d_{33}	374	593	91
d_{15}	585	741	95
Relative Permittivity			
ε_{11}^s	916	1700	263
ε_{33}^s	830	1470	210
ρ (kgm^{-1})	7750	7500	6900

Isotropic Materials

Material	Metals			*Polymers*	
	Copper	Aluminium	Steel	*Hardset CY1301/HY1300*	*Softset CY208/HY956*
E (10^9Pa)	120	67.6	210	4.03	2.0
ν	0.34	0.355	0.29	0.3791	0.393
ρ (kgm^{-3})	8900	2700	7890	1140	1150
C_l (ms^{-1})	4560	6420	5790	2565	1880
C_s (ms^{-1})	2250	3040	3100	1132	790

Nominal Values for Unidirectional Carbon Fibre Reinforced Composite

Material	Unidirectional CFRC	Unidirectional CFRC
	Against Carbon Fibre Direction	With Carbon Fibre Direction
E (10^9Pa)	9	138
ν	0.30	0.30
ρ (kgm^{-3})	1560	1560